Computational and Analytic Time-Dependent Ginzburg-Landau Theory for High-Resistivity High-Field Superconducting Josephson Junctions

BRADLEY PETER DIN

Computational and Analytic Time–Dependent Ginzburg–Landau Theory for High–Resistivity High–Field Superconducting Josephson Junctions

Bradley Peter Din

Abstract

In this thesis, we study the building block for the description of the granular structure of polycrystalline superconductors – the Josephson junction. We investigate the critical current density as a function of applied magnetic field both analytically and computationally, through the lens of time–dependent Ginzburg–Landau theory (TDGL) in 2D. We derive new analytic expressions for the order parameter distribution near interfaces of arbitrary material properties in 2D, validate them using TDGL simulations and use them to extract the effective upper critical field. These results represent a generalization of the famous work from Saint James and de Gennes to arbitrary grain boundary properties. We then extend this framework to include the transport current flowing across the grain boundary, and obtain analytic expressions for the maximum current density that can flow across the grain boundary, providing a generalization of the in–field work in the literature, to high resistivity grain boundaries. We provide a framework to predict the critical current density across the 2D grain boundary over the entire applied magnetic field range, again validated using TDGL simulations. Crucially, our derived expressions consider arbitrary width in detail, but require no additional free parameters, since the derivation formally includes the complexity near interfaces with arbitrary material parameters. We demonstrate how our analytic extension and treatment is necessary for systems with geometries and material parameters which are representative of commercial high–field superconducting materials. Finally, we address how to apply our understanding of a single Josephson junction to 3D polycrystalline materials.

Supervisors: Prof. Damian P. Hampshire and Dr. Budhika Mendis

Computational and Analytic Time–Dependent Ginzburg–Landau Theory for High–Resistivity High–Field Superconducting Josephson Junctions

Bradley Peter Din

A thesis presented for the degree of
Doctor of Philosophy

Department of Physics
Durham University
2024

Contents

List of Abbreviations

BCS Bardeen–Cooper–Schrieffer 2

FBH Fink–Blair–Hampshire 29

FBHZM Fink–Blair–Hampshire with zero mass 39

Fusion CDT EPSRC Centre for Doctoral Training in the Science and Technology of Fusion Energy 111

GL Ginzburg–Landau 4

HTS high–temperature superconductor 2

ISI insulator–superconductor–insulator 25

ITER International Thermonuclear Experimental Reactor 3

JET Joint European Torus 3

LTS low–temperature superconductor 2

MCF magnetic confinement fusion 3

MRI magnetic resonance imaging 4

NMR nuclear magnetic resonance 4

NSN normal–superconductor–normal 63

PCF parabolic cylinder function 22

REBCO rare-earth barium copper-oxide 2

SI superconductor–insulator 20

SN superconductor–normal 19

SNS superconductor–normal–superconductor 27

SQUID superconducting quantum interference device 4

TDGL time–dependent Ginzburg–Landau 5

Declaration

The work in this thesis is based on research carried out at Durham University Superconductivity Group, Department of Physics, University of Durham, England. No part of this thesis has been submitted elsewhere for any other degree or qualification, and it is the sole work of the author unless referenced to the contrary in the text. Some of the work presented in this thesis has been previously published in journals and presented at conferences - the relevant publications and conferences are listed below.

Publications

Automated Identification and Validation of the Optimal Number of Knowledge Profiles in Student Response Data.
B. P. Din, T. Nazaretsky, Y. Feldman–Maggor, and G. Alexandron; *Proceedings of the 16th International Conference on Educational Data Mining*, pp. 458–465 (2023)

Critical Current Densities through Josephson Junctions in Low Magnetic Fields.
B. P. Din, A. I. Blair, F. Schoofs and D. P. Hampshire; *IEEE Transactions on Applied Superconductivity*, vol. 32, no. 4, pp. 1-5, June 2022, Art no. 8000805 (2022)

Proximity-induced Upper Critical Field and Critical Current Density for Composite Superconductors with Normal Resistive Coatings and Barriers in High Magnetic Fields.
B. P. Din, D. P. Hampshire et. al. In progress for PRR.

Conference Presentations

Automated Identification and Validation of the Optimal Number of Knowledge Profiles in Student Response Data (Poster). B. Din, T. Nazaretsky, Y. Feldman–Maggor, G. Alexandron, EDM 2023, Bangalore, India (September 2023)

Modelling Josephson Junctions using Time–Dependent Ginzburg–Landau Theory (Oral). B. P. Din and D. P. Hampshire, Fusion CDT Student Conference 2022, York, UK (June 2022)

Critical Current Densities through Josephson Junctions in Low Magnetic Fields (Poster). B. P. Din, A. I. Blair, F. Schoofs, D. P. Hampshire, EUCAS 2021 (Virtual) (September 2021)

Modelling High-Field Superconductors using Time–Dependent Ginzburg–Landau Theory (Oral). B. P. Din and D. P. Hampshire, Fusion CDT Student Conference, York, UK (June 2021)

Applying Clem's Josephson Junction Model to Equiaxed Grains (Poster) B. P. Din, A. I. Blair, F. Schoofs, D. P. Hampshire, ASC 2020 (Virtual) (September 2020)

2nd May 2024

Bradley Peter Din

Statement of Copyright

Acknowledgements

I would like to start by thanking my partner Sophie for her unconditional love and her infinite patience through the many long days and various existential crises that occurred while getting this thesis complete. It is almost certain that this PhD would not have been possible without you by my side; partially due to fellow postgraduate competition, but mostly due to the unconditional emotional support you have given me. I would next like to thank my wonderful Mum and Nan for their love and encouragement throughout my life. Your support has undoubtedly shaped my mindset and approach to life, and I will be eternally grateful for the opportunities that you have provided and allowed me to get to where I am today. Particular thanks must also go to Matt Taylor for his unrelenting friendship over the many years, and for our assorted atypical adventures, ranging from Glasgow to cupcakes. You have all reminded me to be to be the best version of myself, and I am not sure that I would have had the confidence to even begin this journey without knowing that I had you to support me.

My next thanks must go to my supervisor, Professor Damian Hampshire, for his scientific wisdom and guidance throughout this long journey. I would like to thank the other members of the Durham University Superconductivity Group that I have been fortunate enough to know – Alex Blair, Andrew Smith, Jack Greenwood, Simon Chislett–McDonald, Adel Nader, Charles Gurnham, Rollo Hutson, Emma Gillard and Dan Scobbie. Special thanks must go to Charlie Haddon for his computational and mathematical wisdom – the value of our innumerable discussions of various problems in superconductivity cannot be measured. I would also like to especially thank Mark Raine, for his cool–headed advice, razor wit, and inspirational facial hair (perhaps only the lower–half). I shall particularly miss the post–COVID office environment; the inane chatter, competitive word games, and unwavering support. I have learnt a lot from you all – and I fortunately (accidentally) picked up some knowledge about superconductors along the way.

The computational simulations in this thesis simply would not have been possible without the expertise of Durham's Advanced Research Computing (ARC) services. Particular thanks must go to Karen Bower and Mark Dixon for their unconditional assistance, and for forgiving my commandeering of the supercomputers. I would also like to thank Giora Alexandron and colleagues at the Weizmann Institute of Science for making me feel so welcome during my time there – their philosophy to research (and taste for Middle Eastern food) has shaped my future outlook in many aspects of my life. Thanks must also go to assorted members of the Physics department who have inspired and motivated me over the years – in particular, I would like to

thank Douglas Halliday for his (severly extended) role as an academic (and personal) advisor. I would like to thank my fellow colleagues in the Fusion CDT and Ustinov College, for many interesting conversations about research frontiers in fusion and general postgraduate struggles. Finally, I would like to thank my close friends at home who have bolstered my spirits throughout the years – the list is simply too long to include. Special thanks must go to Liam Mckerracher and Tim Lafosse, for our endless virtual walkabouts that kept my sanity in check during COVID. Thank you to you all, for the reminder that nothing is more important than family and friendship.

This work has been carried out within the framework of the EUROfusion Consortium, funded by the European Union via the Euratom Research and Training Programme (Grant Agreement No 101052200 — EUROfusion). Views and opinions expressed are however those of the author(s) only and do not necessarily reflect those of the European Union or the European Commission. Neither the European Union nor the European Commission can be held responsible for them. This work made use of the Hamilton HPC Service Research Centre and the NVIDIA CUDA Centre (NCC) cluster at Durham University.

Dedication

This thesis is dedicated my three pillars:
SG, MD and PP.
Their unconditional love and support have seen me to the end, and made me the person I am today. I hope I did them proud.

Chapter 1

Introduction

1.1 Background

Superconductivity is perhaps the most tangible exhibition of quantum mechanics on a macroscopic scale. The roots of superconductivity had been brewing for over 100 years prior to its discovery in 1911. Advancements arose from gradual progression in the liquefaction of gases, starting from the work of Faraday in 1823 [1]. A turning point occurred in 1896 when James Dewar became the first person to successfully produce liquid hydrogen in his namesake cryogenic storage vacuum vessel. In 1908, Heike Kamerlingh Onnes was able to achieve the liquefaction of helium, granting access to the low temperatures needed to finally unveil superconductivity in 1911 [2]. He observed that the resistance of mercury dropped to zero at a particular transition temperature of approximately 4.2 K. This earned him the Nobel prize in 1913 and his colloquial title as the 'Father of Low-temperature Physics' [3]. Similar occurrences were found in other metals such as lead and tin, permitting persistent current flow without dissipation. Although unknown at the time, this was the first observation of the superconducting state. The developments in a theoretical framework of superconductivity were sporadic over the 20^{th} century, taking nearly half a century for any substantial understanding to emerge. The next important discovery by Walther Meissner in 1933 was the observation that superconductors exhibit perfect diamagnetism in the so-called 'Meissner state' [4]. This phenomena is distinct from a conductor with zero resistance. A perfect conductor will only resist a change to an external field in accordance with Lenz's law. If a conductor first contains a steady external magnetic field and is then cooled below the transition temperature to a zero resistance state, the magnetic field would be expected to stay the same. The Meissner effect in a superconductor is the active expulsion of magnetic flux from the bulk of the operating superconductor below a critical temperature. This is achieved through the spontaneous formation of currents near the surface of the superconductor that completely cancels the magnetic field in its interior. These two key properties are the defining signatures of superconductivity: zero electrical resistance and the expulsion of magnetic field.

Shortly after, the first theoretical description emerged from the work of the London brothers (Fritz and Heinz London) in 1935, providing an explanation of the Meissner effect [5]. However, the first major theoretical understanding of superconductivity emerged in the 1950s. The phenomenological theory from Vitaly Ginzburg and Lev Landau came in 1950 [6], combining the London equations with a field theory of second order phase transitions from Landau's earlier work. The microscopic theory

of John Bardeen, Leon Cooper and John Robert Schrieffer in 1957 provided the first comprehensive microscopic understanding of superconductivity [7], and eventually earned them a Nobel prize in 1972.

Unfortunately, theoretical formulations of superconductivity are far from complete. Bardeen–Cooper–Schrieffer (BCS) theory predicts that superconductivity should not exist above 30 K. This theory proved sufficient for many low–temperature superconductors (LTS), such as Nb_3Sn and NbTi. However, many materials have been found to become superconducting at significantly higher transition temperatures, with no widely accepted theory for their microscopic origin. Prior to 1986, the highest transition temperature observed was 23.3 K in Nb_3Ge [8]. However, a new class of metallic, oxygen deficient compounds, of the form $La_{2-x}Ba_xCuO_4$, were discovered to have transition temperatures at approximately 35 K. This sparked investigation into the previously overlooked usage of other rare-earth barium copper-oxide (REBCO) materials and more general layered cuprate superconductors. In 1987, the first high–temperature superconductor (HTS) of $YBa_2Cu_3O_{7-\delta}$ was discovered to have a transition temperature of 93 K [9]. This was the first superconductor with a transition temperature above that of liquid nitrogen, inviting an abundance of speculation for the possibility of 'room–temperature superconductivity'. Research to satisfy this expectation is still ongoing. Previous records stood at 203 K in 2015 [10] and 250 K in 2019 [11], using extremely pressurized (∼170 GPa) hydrogen sulfides and lanthanum hydrides respectively. More recent research using yttrium superhydrides obtained transition temperatures of 262 K at approximately 180 GPa [12]. However, these extreme pressures are clearly not practical for real applications. Most recently, a study has controversially claimed observations of a transition temperature at 294 K using nitrogen-doped lutetium hydride at approximately 10 kPa, near ambient temperatures and pressures [13]. Other researchers across the globe have tried and failed to recreate these results [14], casting doubt on the claims. However, independent measurements on the same original samples provided evidence for the predictions [15]. Most recently in July 2023, a study claimed success in synthesizing the first room–temperature superconductor at ambient pressure using a modified lead-apatite (LK-99) structure, with a transition temperature above 400 K [16, 17]. However, extraordinary claims require extraordinary proof; it is yet to be seen if these results are able to withstand scrutiny. Regardless of the validity of these claims, it is clear that the race to achieving room–temperature superconductivity, and harnessing the resulting transformative potential, is still ongoing.

The discovery of superconductivity unfortunately came with the caveat that it is not a state that is easily achieved. Perhaps the most well-known challenge is that of achieving low temperature since the superconducting state only persists below a specific critical temperature, T_c. However, for many applications, the cryogenic demands of superconductors are not their limiting factor. We face two other fundamental limits for the superconducting state. Shortly after his original discovery in 1914, Kamerlingh Onnes discovered that a sufficiently large magnetic field could destroy the phenomenon of zero resistance. Furthermore, the amount of current that may be carried by a superconductor is known to be finite, and a sufficiently large current density can also destroy superconductivity. In other words, beyond the upper critical magnetic field B_{c2} or above the critical current density J_c, the zero resistance state is destroyed. These two conditions more often than not form the primary bottleneck in commercial implementation for superconductors. Fortunately,

regardless of these limitations, the critical current density of a superconductor is several orders of magnitude larger than a typical conventional conductor such as copper.

1.2 Applications of Superconductivity

One could argue that the greatest modern challenge we currently face is the task of finding an efficient, sustainable and renewable energy source [18]. The technological evolution of mankind has been a remarkable phenomenon, but comes with a severe price in the form of an energy demand. The global energy usage is forecast to increase by 48% by 2040 [19]; as more technologies evolve, this will only increase further [20]. Furthermore, the supply of fossil fuels as the world's primary source is dwindling – a promising and sustainable candidate for a replacement is nuclear fusion energy; the same mechanism providing the energy powering our Sun. This was first eloquently proposed by Eddington in 1920 [21]. For a commercially viable application, the use of superconductors is essential – if one does not use superconductors in fusion reactors, then approximately a third of the produced energy will be wasted in supplying the cooling systems for the normal magnets - this is unfeasible for successful commercial fusion [22].

An overwhelming majority of modern fusion designs are based around magnetic confinement fusion (MCF) technology, such as in the Joint European Torus (JET) tokamak in Culham, UK or the International Thermonuclear Experimental Reactor (ITER) tokamak being built in Provence, France. The physical process involves magnetically confining a deuterium–tritium (D–T) plasma within a tokamak through the use of superconducting magnets, which achieves a sufficiently hot and dense plasma such that fusion occurs [23]. The power generated by a particular fusion reaction is proportional to B^4 [24]; increasing the magnetic field leads to improved plasma confinement and hence a higher power output. Thus, superconducting magnets are crucial for extended periods of tokamak operation, and the development of stronger superconducting magnets and cables with higher critical currents is a necessary step for the future of fusion energy [25]. This involves cable and magnet design, the continued improvement of superconducting materials, as well as solutions to large scale engineering problems, such as remountable joints [26, 27, 28]. Current tokamak designs are using cheaper LTS materials, which are readily commercially available and able to create a sufficiently high magnetic field for current state-of-the-art applications, such as the requirements for ITER [29, 22]. Conversely, there are an abundance of future designs looking to use HTS materials, which can provide access to significantly higher fields and current densities [30, 31, 32], including SPARC and ARC (Commonwealth Fusion Systems) [33], STEP (UK Atomic Energy Authority) [34], ST80–HTS (Tokamak Energy) [35], the stellarator FFHR–d1 (National Institute for Fusion Science, Japan) [36], and potentially EU DEMO [37, 38]. We provide the key parameters of some common superconducting materials in Table 1.1.

Applications that rely on high magnetic fields are not limited to fusion alone. A plethora of technologies can be achieved with sufficiently high magnetic fields and superconductors are by far the most efficient method of generating them. These include the fields required for tools in various disciplines, such as magnetic resonance

Material	T_c (K)	B_{c2} (T)	$\xi(0)$ (nm)	$\lambda(0)$ (nm)
Niobium Tin (Nb_3Sn)	17.8	29.5	2.73	93.5
Niobium Titanium (NbTi)	8.99	15.7	3.40	163
Magnesium Diboride (MgB_2)	38.6	9.20	7.01	97.1
Bi–2212 ($Bi_2Sr_2CaCu_2O_{8+\delta}$)	84.8	231	3.24	300
YBCO ($YB_2C_3O_{7-\delta}$)	90.0	120	1.29	135
Bi–2223 ($Bi_2Sr_2Ca_2Cu_3O_{10+\delta}$)	108	297	2.86	165

Table 1.1: A table of common superconducting materials and their characteristic properties [39]. For the anisotropic HTS materials, the upper critical field is provided with the field parallel to the c–axis together with the equivalent length scales. Yttrium Barium Copper Oxide (YBCO) has been shown in the table since it is the most common choice for rare–earth (ReBCO) superconductors. The subscript δ is a variable denoting the level of oxygen doping.

imaging (MRI) machines and nuclear magnetic resonance (NMR) spectroscopy [40], particle accelerators at CERN [41], and the magnetically levitated 'Maglev' train. This is by no means an exhaustive list, and optimizations may unlock more applications than one could imagine possible.

However, superconductors are not only used for the generation of high magnetic fields. The unique property of dissipationless current flow at low temperatures allows engineers to create more efficient technologies with massive energy benefits – for example, using superconductors in electrical motors can lead to a reduction of more than 50% of the typical Joule losses [42]. This increased efficiency also allows the potential for more compact devices to be made – this is crucial for future generations of 'greener' hydrogen–powered air travel [43], amongst many other engineering applications such as superconducting magnetic energy storage systems [44]. Superconductors have also found use in extreme metrology – the development of the superconducting quantum interference device (SQUID) led to the precise measurements of extremely weak magnetic fields [45, 46]. These devices provide a direct relationship between the frequency and the voltage involving only fundamental constants (the Planck constant and the elementary charge); subsequently, SQUIDs have been utilised to define the voltage standard since 1990 [47].

1.3 Thesis Outline

State of the art superconductors have a critical current density 2–3 orders of magnitude below the theoretical maximum. We are motivated to model macroscopic behaviour using traditional Ginzburg–Landau theory and its extensions. To optimize J_c, we must understand the mechanisms that operate and dependencies of J_c in polycrystalline high field superconductors. If successful, we can expect to predict how J_c depends on the applied magnetic field and the material properties such as grain size and grain boundary resistivity.

In this thesis, we will study the primary building block used to understand the current flow across grain boundaries in a real polycrystalline material – the Josephson Junction. We shall consider the importance of both the grain geometry and the specific material properties of the grain boundary in limiting the maximum current density that can flow through this building block. We will develop our understanding of these materials both analytically, through the formalism of Ginzburg–Landau (GL) theory, and computationally, by making use

of time–dependent Ginzburg–Landau (TDGL) simulations. In Chapter 2, we will review the fundamentals of superconductivity, with a particular focus on GL theory. We shall outline the key equations and mathematical frameworks used to describe superconductivity, and the existing analytic theory used to obtain the key technological parameters such as the effective upper critical field and the critical current density. In Chapter 3, we will review the numerical methods used throughout the TDGL simulations in this thesis. We shall outline the key outputs of our computation, and how these can be used to extract key information about vortex structure and dynamics, alongside the critical currents. In Chapter 4, we shall present novel analytic extensions to the theory presented in Chapter 2, accurately capturing the behaviour near grain boundaries of arbitrary properties. We will use these improved analytic calculations to provide a framework for obtaining predictions of the critical current density in 2D, for systems with arbitrary width and material properties. To our knowledge, this is the first complete framework that allows a description of how both the grain geometry and the grain boundary properties interact to limit the current flow in the system. Moreover, the analytic results do not require additional free parameters in order to describe the behaviour of the full 2D system; this is in contrast to existing theory which is primarily derived in the 1D limit. In Chapter 5, we shall validate our proposed analytic framework with TDGL simulations, for an assortment of different geometries ranging from narrow to wide Josephson junctions, with various different geometries and material properties. We also compare our new results to existing theory. In particular, we demonstrate how our analytic extensions are required for the description of geometries which are the most representative of real polycrystalline materials. Finally, in Chapter 6, we shall outline some possible future work and provide some concluding comments relevant to the optimization of both LTS and HTS materials.

Chapter 2

Review of Superconductivity Theory

2.1 Introduction

In this chapter, we first describe the fundamentals of BCS theory. We derive some basic results from the simplest form of the theory, and describe its applications and limitations in describing real superconductors. We then provide a justification for the GL free energy functional and describe the 2 equations that follow from it and characterise a superconducting material. We outline the basics of GL theory and the key characteristic length scales of superconductivity. Finally, we introduce the building block of polycrystalline superconductors – the Josephson junction. We describe the key theoretical frameworks that have been used to understand this building block, across a wide range of material parameters and geometries. In Sections 2.4 and 2.5.1, we explicitly include some details from the derivations in the literature so we can include the general solution for both strongly and weakly coupled junctions for later use in Chapters 4 and 5.

2.2 BCS Theory

The beauty of the BCS theory comes not from its completeness but its elegance. It holds the reassurance that many other key results, such as the London equations and penetration depth, coherence lengths, and GL theory, may be derived from it. BCS theory has quantitatively predicted fundamental behaviour of many 'conventional' low-temperature superconductors, such as a second-order phase transition at critical temperatures, the electronic specific heat dependence on temperature (and therefore the energy gap for individual particle–like excitations), the Meissner effect, infinite conductivity and the isotope effect [7, 48].

In 1950, Fröhlich proposed a fundamental mechanism for the theoretical understanding of superconductivity – the concept of electron–phonon interactions [49]. This mechanism forms an essential component of BCS theory, which suggests that superconductivity in a material is due to an attractive interaction between pairs of electrons, where the attraction is mediated by vibrations in the lattice, known as phonons. This interaction consequently creates a small net attraction between pairs of electrons, and provides an explanation for the isotope effect ($T_c \propto M^{-0.5}$). These bound electrons are commonly referred to as 'Cooper pairs'. Cooper's preliminary work in 1956 proved that the ground state of an electron gas is unstable if there is a net attraction between the electrons, such as in an effective phonon interaction [50].

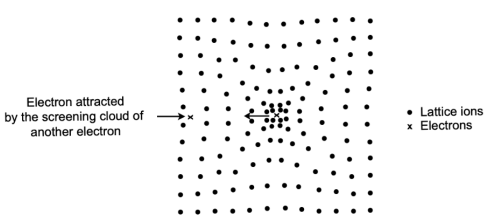

(a) The attractive interaction between two distant electrons due to the crystal lattice distortion [51].

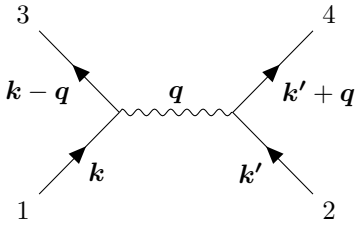

(b) An electron-phonon exchange, with the corresponding $V(\boldsymbol{k}, \boldsymbol{k'}, \boldsymbol{q})$.

Figure 2.1: Two diagrammatic representations of Cooper pair formation. Here, $\boldsymbol{q}$ is the phonon wavevector, while $\boldsymbol{k}$ and $\boldsymbol{k'}$ represent those for the two initial electrons.

This allows the electrons to form a bound state, despite having a total energy that is larger than zero.

This attractive interaction can be more intuitively understood by considering Figure 2.1. As the superconductor is cooled below the critical temperature, the thermal vibrations of the lattice (phonon energies) are decreased. The electrons are also less thermally agitated, and consequently, the electron-ion interaction is less disturbed. As electrons move through the lattice, surrounding ions are subject to Coulomb attraction, forming a positive charge cluster around the electron. This local deformation effectively screens distant electrons from the mutually repulsive charge of the electron, and hence a secondary electron may be attracted towards this positive charge. In essence, this is equivalent to the two electrons being attracted to one another. Below the critical temperature, this virtual attraction is not disturbed, and the electrons remain coupled together in what is known as a Cooper pair.

As an electron passes through a crystal ion lattice, the electron causes ion lattice vibrations, which can be represented as a quantised phonon. This may then be absorbed by another electron. The average maximum distance at which this phonon-coupled interaction takes place is called the coherence length. Overall, this interaction can be considered as an exchange of a phonon between two electrons, with the interaction taking the form

$$V(\boldsymbol{k}, \boldsymbol{k'}, \boldsymbol{q}) = \frac{g^2 \hbar\omega_q}{\left(\varepsilon_{k+q} - \varepsilon_k\right)^2 - \left(\hbar\omega_q\right)^2}. \tag{2.2.1}$$

Here, g is the phonon interaction coupling constant. $\boldsymbol{k}$ and $\boldsymbol{k'}$ represent the wavevectors of the two initial electrons and $\boldsymbol{q}$ is the phonon wavevector. Similarly, $\hbar\omega_q$ represents the energy of the phonon, while ε_i is the energy of the electron with wavevector i. For a negative, attractive potential, it is required that $|\varepsilon_{k+q} - \varepsilon_k| < \hbar\omega_q$. The key results of the BCS theory only demand that the electron interaction potential is attractive; the exact form of the potential is not necessary. To simplify matters, BCS formulated their theory with an isotropic, square well potential,

$$V_{k,k'} = \begin{cases} -V_0 & \text{if } |\varepsilon_k - \varepsilon_\mathrm{F}| < \hbar\omega_D \text{ and } |\varepsilon_{k'} - \varepsilon_\mathrm{F}| < \hbar\omega_D, \\ 0 & \text{otherwise.} \end{cases}. \tag{2.2.2}$$

The Debye energy of the lattice phonons is given by $\hbar\omega_D$ and V_0 is a constant parameterizing the strength of the interaction. Hence, the attractive potential only occurs for electrons within a small range of the Fermi surface energy. Whilst the electron–electron interaction is a smooth function of k and k', the response of electrons

at the Fermi level peaks when $k = -k'$ [52] – the interaction is most significant for electrons with opposite momenta.

The electron pairs in BCS theory are not strictly bosonic; since they are quite large, different pairs strongly overlap with one another – in this limit, it is not possible to describe an individual pair as a boson [19]. Nevertheless, the key insight from BCS theory is that Cooper pairs facilitate the formation of a coherent state, in which a macroscopic number of pairs are all in the same state [19]. Each pair condenses to the same quantum ground state below the Fermi surface*. Since each Cooper pair has an energy that is below the Fermi surface, their production is energetically favourable. This is the essence of the famous 'BCS energy gap', and results in the remarkable properties of superconductivity. In particular, any two electrons with energies close to the Fermi surface will experience an attractive potential and form a bound state. This may be written as a two-body wavefunction, where the interaction is negligible unless the electrons have opposite momentum [19]. One can imagine this as a situation where the centre-of-mass momentum is zero, and hence the overlap of the two electrons is maximized.

As an extension to Cooper's two electron description, BCS postulated that the entire Fermi surface would be unstable with respect to the creation of Cooper pairs. All electrons close to the Fermi surface will be bound into pairs, reducing the overall free energy. One can write a many-body wavefunction, which may be written as the normalised product [53]

$$|\Psi_{\mathrm{BCS}}\rangle = \prod_k \left(u_k^* + v_k c_{k,\uparrow}^\dagger c_{-k,\downarrow}^\dagger\right) |0\rangle_k \,. \tag{2.2.3}$$

Here, u_k and v_k represent complex amplitudes, while $|0\rangle_k$ and $|1\rangle_k$ denote unoccupied and occupied states respectively. The two are related through a creation operator which creates a pair of electrons of zero net momentum and opposite spins. The BCS theory then postulates an effective Hamiltonian and minimizes the corresponding energy; the details are described in resources such as [7], [53] or [19]. The result is an expression for the 'BCS gap equation',

$$N(0)V_0 \int_0^{\hbar\omega_D} \frac{1}{\sqrt{\varepsilon^2 + |\Delta|^2}} \tanh\left(\frac{1}{2k_bT}\sqrt{\varepsilon^2 + |\Delta|^2}\right) \mathrm{d}\varepsilon = 1. \tag{2.2.4}$$

The energy gap at the Fermi surface is denoted Δ and the density of energy states at the surface as $N(0)$. In practice, this integral is not analytically solvable. Taking the weak coupling approximation $N(0)V_0 \ll 1$ and $T \to 0$, the expression for Δ is given as

$$|\Delta|_{T=0} = \hbar\omega_D \exp\left(\frac{1}{N(0)V_0}\right). \tag{2.2.5}$$

Similarly, by taking the limit $T \to T_c$, where $\Delta \to 0$, one obtains [19]

$$2|\Delta|_{T=0} = 3.52 k_B T_c. \tag{2.2.6}$$

Eq. (2.2.5) provides insight into the isotope effect since the Debye energy is proportional to the inverse square of the isotopic mass as desired. Whilst this expression for the isotope effect is consistent with the observed behaviour for many superconductors, others deviate strongly [53]. It is unknown whether these

*The Fermi surface is the surface in momentum space separating occupied states from unoccupied states at 0 K, where single electrons outside of the Fermi sphere are 'excited'.

variations are a consequence of the assumptions made or suggest a radically difference mechanism altogether. One notable limitation is that the BCS theory cannot explain the existence of some specific classes of high–temperature superconductors, such as REBCO materials. Some extensions have attributed this to the assumption of a weak phonon-mediated interaction between electrons. Extensions to BCS exist which are more generic, such as Eliashberg's theory in 1960 [54], proving useful in high–temperature superconductivity discussions [55]. Some papers suggest that BCS theory provides no real understanding of superconductivity because of its inconsistencies and fundamental flaws [56, 57]. However, the BCS theory of superconductivity has strong experimental verification, and is generally accepted to include some of the important elements required in a correct theory of conventional superconductivity.

2.3 Ginzburg–Landau Theory

BCS theory is a detailed microscopic theory, but becomes unnecessarily cumbersome for describing the properties of real superconductors in magnetic fields. The phenomenological Ginzburg–Landau (GL) theory is generally preferred in this case. It is an extension of the previous work by the London brothers [5], and was shown to be derivable from microscopic BCS theory close to the transition temperature by Gor'kov in 1959 [58].

2.3.1 The Ginzburg–Landau Free Energy

Ginzburg and Landau proposed their theory in 1950 when the BCS microscopic theory had not yet been developed [6]. The GL theory is formulated in terms of a macroscopic complex order parameter and the vector potential. The magnitude of the order parameter is related to the density of the superconducting electrons; this is consistent with the view that the superelectrons are condensed to a single quantum state, where their collective behaviour is described by a single wavefunction [19]. Naturally, the vector potential describes the net magnetic field within the system and supercurrent density flowing through the superconductor [6]. The axiom of GL theory is captured in the free energy functional, motivated by considering superconductivity near the phase transition (critical) temperature, T_c [59]. By considering Landau's general theory of second order phase transitions and the required symmetry breaking across the normal/superconducting phase transition, the Helmholtz free energy functional can be written as a Taylor series expansion [60],

$$F - F_0 = \int \left[\alpha \left|\psi\right|^2 + \frac{1}{2}\beta \left|\psi\right|^4 + \frac{1}{2m} \left|\left(-i\hbar\boldsymbol{\nabla} - q\boldsymbol{A}\right)\psi\right|^2 + \frac{\boldsymbol{B}^2}{2\mu_0} \right] \mathrm{d}^3\boldsymbol{r}. \tag{2.3.1}$$

Here, α and β are temperature dependent parameters, whilst $q = -2e$ and $m = 2m_\mathrm{e}$, quantifying the charge and mass of the Cooper pair [60]. We have taken the symbol e here to be the (positive) fundamental constant, converse to some authors [53, 61]. In the normal phase, where $T > T_\mathrm{c}$, the superconducting state is broken, $\psi = 0$, and the free energy is simply the normal state energy in the absence of a magnetic field, denoted as F_0. The wavefunction is then normalised to the density of Cooper pairs (or equivalently, half the number of superelectrons). It is convenient to express this

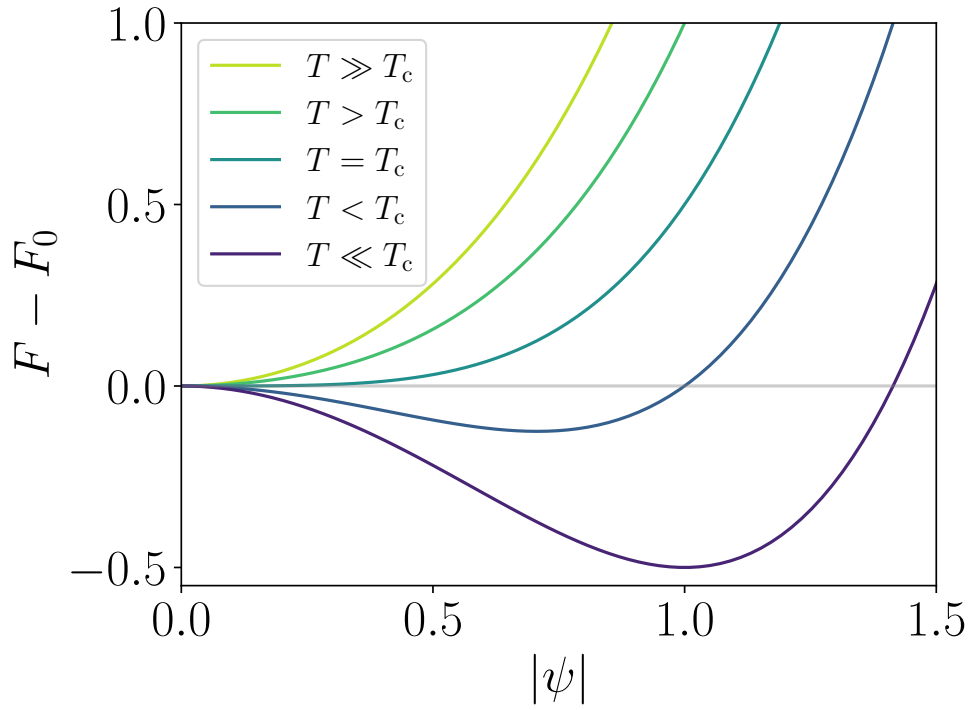

Figure 2.2: Free energy as a function of $|\psi|$ for a range of illustrative temperatures relative to T_c.

free energy in equivalent form

$$F - F_0 = \int \left[\alpha |\psi|^2 + \frac{1}{2}\beta |\psi|^4 + \frac{\hbar^2}{2m} |\mathcal{D}\psi|^2 + \frac{\boldsymbol{B}^2}{2\mu_0} \right] \mathrm{d}^3\boldsymbol{r}, \tag{2.3.2}$$

where the gauge covariant derivative operator is defined as

$$\mathcal{D}\psi = \left(\boldsymbol{\nabla} - \frac{iq}{\hbar} \boldsymbol{A} \right) \psi. \tag{2.3.3}$$

This free energy integral is taken over all space, and therefore represents the combined energy of the superconducting state and any external applied magnetic field. To obtain the equilibrium state of the order parameter in the absence of magnetic field or current; the order parameter is constant and therefore $\mathcal{D}\psi = 0$ [62]. Maximizing the resulting free energy yields

$$\frac{\partial F_s}{\partial |\psi|^2} = 0 \implies |\psi_0|^2 = -\frac{\alpha}{\beta}. \tag{2.3.4}$$

This equilibrium order parameter must be positive in the superconducting state and zero in the normal state. Therefore, it is required that *below* T_c, the minimum of the order parameter must be positive, and *above* T_c, the minimum of the order parameter must be zero. Consequently, Ginzburg and Landau proposed that $\alpha \propto (T - T_c)$, and that β to be positive on each side of the transition temperature, in order to ensure that the order parameter corresponding to the minimum energy is finite. Therefore, below T_c, there is a minimum in the free energy for a non-zero $|\psi|$, and the superconducting state is energetically preferable. Conversely, above T_c, the minimum of the free energy is exactly when $|\psi| = 0$, and so the normal state is energetically stable. This free energy variation is depicted in Fig. 2.2.

2.3.2 The Ginzburg–Landau Equations

The Ginzburg–Landau equations emerge from the minimisation of this free energy with respect to the order parameter and the magnetic field. By first varying Eq. (2.3.2) with respect to ψ^* to obtain the first GL equation (GL1), one obtains the result

$$\frac{1}{2m}\left(-i\hbar\boldsymbol{\nabla}-q\boldsymbol{A}\right)^2\psi+\left(\alpha+\beta\left|\psi\right|^2\right)\psi=0, \tag{2.3.5}$$

with a corresponding boundary condition

$$\boldsymbol{n}\cdot\left(-i\hbar\boldsymbol{\nabla}-q\boldsymbol{A}\right)\psi(\boldsymbol{r})=0, \tag{2.3.6}$$

where $\boldsymbol{n}$ is a unit normal to the surface. This is a non–linear Schrödinger equation, describing the spatial variation of the order parameter. The boundary condition is equivalent to the statement that no supercurrent flows through the boundary of the system, and was proposed by Ginzburg and Landau [63]. Similarly, one can vary Eq. (2.3.2) with respect to $\boldsymbol{A}$ to obtain the second GL equation (GL2),

$$\boldsymbol{J}_s=-\frac{iq\hbar}{2m}\left(\psi^*\boldsymbol{\nabla}\psi-\psi\boldsymbol{\nabla}\psi^*\right)-\frac{q^2}{m}|\psi|^2\boldsymbol{A}=\frac{q\hbar}{m}\mathrm{Im}\left[\psi^*\left(\boldsymbol{\nabla}-\frac{iq}{\hbar}\boldsymbol{A}\right)\psi\right]. \tag{2.3.7}$$

This equation describes the spatial variation of the supercurrent density. The challenge in describing the macroscopic state of the system is that these two equations are coupled; the order parameter and the vector potential must be solved for self–consistently.

2.3.3 Type I Superconductivity

GL theory predicts the existence of two fundamental length scales of a superconductor, which are consistent with the results from London theory [5]. The length scale describing the spatial variation of the magnitude of the order parameter – the superconducting coherence length – is defined as ξ_s [64]. Considering GL1 (Eq. (2.3.5)) in the absence of applied magnetic fields or transport currents in 1D leads to the equation

$$\frac{-\hbar^2}{2m}\frac{\partial^2\psi}{\partial x^2}+\left(\alpha+\beta\left|\psi\right|^2\right)\psi=0. \tag{2.3.8}$$

Using the Meissner value (Eq. (2.3.4)) as a natural normalisation for the order parameter, the coherence length can be written as [60]

$$\xi_\mathrm{s}^2=\frac{\hbar^2}{2m\left|\alpha\right|}. \tag{2.3.9}$$

This quantity is temperature dependent (through α) and monotonically increases as $T\to T_\mathrm{c}$; the order parameter magnitude varies more slowly.

Next, the length scale over which the electromagnetic effects (e.g. local magnetic field & current densities) vary throughout a superconductor – the superconducting penetration depth – is defined as λ_s. Consider GL2 (Eq. (2.3.7)) in a bulk superconductor. The gradient terms do not contribute and the order parameter solution takes the bulk equilibrium value (Eq. (2.3.4)), leading to the result [53]

$$\boldsymbol{J}_s=-\frac{q^2}{m}|\psi_0|^2\boldsymbol{A}=-\frac{4e^2}{m}|\psi_0|^2\boldsymbol{A}. \tag{2.3.10}$$

Taking the curl of each side leads to the intermediate result

$$\boldsymbol{\nabla} \times \boldsymbol{J}_s = -\frac{4e^2}{m}|\psi_0|^2 \boldsymbol{B}, \tag{2.3.11}$$

and making use of the (quasistatic) Ampère–Maxwell equation and vector identities leads to the differential equation

$$\boldsymbol{\nabla}^2 \boldsymbol{B} = \frac{4\mu_0 e^2}{m}|\psi_0|^2 \boldsymbol{B}. \tag{2.3.12}$$

This is a well–known double–differential equation. If one considers a geometry where a superconductor occupies the half–plane $x > 0$, and is subjected to a constant external field B_{app} in the z–direction, then the only bounded solution that exists is a simple exponential [60],

$$B_z(x) = B_{\text{app}} e^{-x/\lambda_s}, \tag{2.3.13}$$

where the superconducting penetration depth is defined to be [53]:

$$\lambda_{\text{s}}^2 = \frac{m}{4\mu_0 e^2 |\psi_0|^2}. \tag{2.3.14}$$

Clearly, the field is screening exponentially over the length scale of λ_{s}. This state is known as the 'Meissner state' – the applied field is completely excluded from the bulk of the superconductor, and the order parameter is completely homogeneous through the bulk. Here, it is convenient to also introduce the 'Ginzburg–Landau parameter', κ_{s}, as the ratio of these two length scales,

$$\kappa_{\text{s}} = \frac{\lambda_{\text{s}}}{\xi_{\text{s}}}. \tag{2.3.15}$$

We will discuss the importance of this length scale shortly.

The Meissner state exhibits perfect diamagnetism, and is one of the two key properties of superconductors; it arises naturally through the treatment of the GL free energy and resulting GL equations in the presence of sufficiently weak fields. However, as the field is increased, the Meissner state may not remain energetically favourable (i.e. may not be thermodynamically stable), relative to the normal state. In other words, the energy penalty required for screening becomes greater than the energy benefit from the condensation of electrons into Cooper pairs. The field at which this occurs is known as the thermodynamic critical field. At this field, the Gibbs free energies for the normal and superconducting states are equal. The Gibbs free energy is related to the Helmholtz energy discussed above by including the magnetization [53],

$$g = f - \mu_0 \boldsymbol{H} \cdot \boldsymbol{M} \implies G = F - \mu_0 \boldsymbol{H} \cdot \boldsymbol{m}. \tag{2.3.16}$$

Here, $\boldsymbol{M}$ is the magnetization and $\boldsymbol{m}$ is the corresponding magnetic moment:

$$\boldsymbol{m} = \int dV \boldsymbol{M} = \frac{1}{\mu_0} \int dV \left(\boldsymbol{B} - \mu_0 \boldsymbol{H}\right). \tag{2.3.17}$$

It is worth noting the same equations of motion for the order parameter and the supercurrent (GL1 and GL2) are obtained regardless of if one minimizes the Gibbs or the Helmholtz free energy [53] – nevertheless, it is important to use the correct Gibbs free energy. The Gibbs free energy corresponds to the equilibrium state at *constant applied field*, rather than the equilibrium state at *constant magnetic moment* obtained from the Helmholtz free energy. In the normal state, $\psi = 0$, and in the superconducting state, $\boldsymbol{B} = 0$ due to screening, and the volume of the system is

denoted as V [53]. The Gibbs free energy in both the normal state and in the superconducting state at this critical field is then written as

$$G_{\mathrm{s}} = V\left(f_0 - \frac{|\alpha|^2}{2\beta} + \frac{1}{2\mu_0}B_{\mathrm{app}}^2\right), \tag{2.3.18}$$

$$G_{\mathrm{n}} = V f_0. \tag{2.3.19}$$

Equating these two results leads to the identification of the thermodynamic critical field [53],

$$B_{\mathrm{c}}^2 = \frac{\mu_0 \alpha^2}{\beta}. \tag{2.3.20}$$

This critical field represents the field at which the Meissner state is unstable relative to the normal state – for any field above B_{c}, the superconducting state symmetry is broken, and for any field below B_{c}, the Meissner state is the most thermodynamically stable.

2.3.4 Type II Superconductivity

In contrast to Type I superconductors, which remain in the Meissner state until B_{c}, Type II superconductors remain in the Meissner state until a lower critical field, B_{c1}. After this field, the superconductor transitions into a 'mixed' state, where the superconducting bulk is penetrated by flux in quantized fluxons (or vortices). A fluxon consists of a core of normal material, which has a radius of approximately a coherence length. This normal region naturally has an applied field with a flux quanta of $\phi_0 = h/2e$ penetrating through it, and a local supercurrent that circulates around the core. These fluxon supercurrents may be extremely large relative to the other currents flowing within the superconductor.

The crossover between Type I and Type II superconductivity is encapulsated in the Ginzburg–Landau parameter κ_{s} (Eq. (2.3.15)). In their seminal paper, Ginzburg and Landau also present a calculation of the surface energy at the boundary of superconducting and normal phases, σ_{NS} [63, 65]. They found that a critical value of $\kappa_{\mathrm{s}} = \dfrac{1}{\sqrt{2}}$ is the demarcation between Type I and Type II behaviour. In summary:

$$\kappa \leq \frac{1}{\sqrt{2}} \implies \sigma_{\mathrm{NS}} > 0 \implies \text{Type I behaviour}, \tag{2.3.21}$$

$$\kappa > \frac{1}{\sqrt{2}} \implies \sigma_{\mathrm{NS}} < 0 \implies \text{Type II behaviour}. \tag{2.3.22}$$

The implications of having either positive or negative surface barriers are hugely impactful, and were not materially realized until Abrikosov's work in 1957 [66]. The energy benefit of allowing fluxons penetrate to the system (i.e. an increased number of surfaces) outweights the energy cost of screening, and so the mixed state is energetically favourable relative to the Meissner state. Therefore, the mixed state is a signature of a Type II superconductor. The difference in behaviour between Type I and Type II superconductors are summarized in Fig. 2.3.

An expression for the lower critical field can be derived by first demonstrating flux quantization. From the perspective of GL theory, this may be understood as the requirement that the wavefunction is single–valued [53]. We consider a multiply connected superconductor in an applied field [60]. By writing the complex

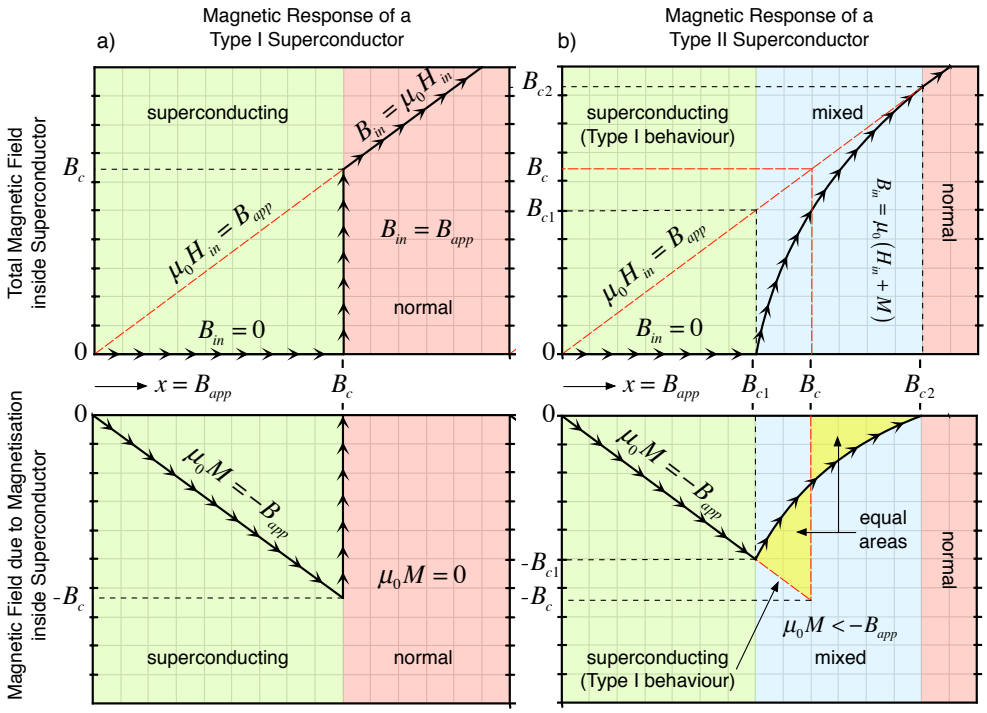

Figure 2.3: The magnetic response of Type I and Type II superconductors. Taken from [67].

wavefunction as a product of magnitude as phase in a standard way $\Psi = |\psi| e^{i\theta}$ and inserting this into GL2 (Eq. (2.3.7)), one obtains the result

$$\boldsymbol{J}_\mathrm{s} = |\psi|^2 \frac{q}{m} (\hbar \boldsymbol{\nabla} \theta - q \boldsymbol{A}) \,. \tag{2.3.23}$$

To obtain the quantization of flux, one considers the contour integral of each side of this expression. Taking the contours in a bulk superconductor, sufficiently far away from fluxons such that there is no screening, leads to the contour integral of the left hand side being zero [53]. Inserting the explicit charge $q = -2e$ then leads to the intermediate result

$$|\psi|^2 \frac{q}{m} (\hbar \boldsymbol{\nabla} \theta + 2eq \boldsymbol{A}) = 0. \tag{2.3.24}$$

Furthermore, since the order parameter must be single valued, the phase change must be an integer multiple of 2π,

$$\oint_C \boldsymbol{\nabla} \theta \cdot \mathrm{d}\boldsymbol{l} = 2\pi n. \tag{2.3.25}$$

Applying Stokes' theorem on the vector potential allows the remaining term to be identified as the total flux in the system. The flux quantum is then idenified as

$$\phi_0 = \frac{h}{q} = -\frac{h}{2e}. \tag{2.3.26}$$

This follows from taking $e > 0$ to be the fundamental constant and $q = -2e$. Other authors consider $e < 0$ to be the electron charge [53]. This flux quantization condition can be written as an integral of a closed contour in the superconductor,

$$\frac{m}{4e^2} \oint \frac{\boldsymbol{J}_s}{|\psi|^2} \cdot \mathrm{d}\boldsymbol{l} + \Phi = n\phi_0, \tag{2.3.27}$$

where Φ is the ordinary magnetic flux through the integral loop, and n is the number of vortices enclosed within the contour. In the Meissner state, where $|\psi|^2 \neq 0$ everywhere, there are no fluxons in the contour ($n = 0$).

To determine the lower critical field, one can perform a similar Gibbs energy analysis to the previous section. By equating the Gibbs free energy with a single fluxon in to the Gibbs free energy of the Meissner state, the lower critical field is given by the expression [68, 69]

$$B_{\mathrm{c1}} = \frac{\mu_0 \phi_0}{4\pi\lambda^2} \ln\kappa = \frac{B_{\mathrm{c}}}{\sqrt{2}\kappa} \ln\kappa. \tag{2.3.28}$$

For the high field superconductors considered in this thesis, κ is large and so B_{c1} is much smaller than B_{c} (n.b. Eq. (2.3.28)). The mixed state is therefore almost immediately energetically preferable other than in very low fields; understanding vortex dynamics is critical for understanding Type II superconductors.

Finally, the mixed state is preserved until the upper critical field, B_{c2}. As the field is increased, more fluxons are pushed into the bulk of the superconducting material, until the normal cores overlap and the superconducting state is destroyed completely. Abrikosov [66] investigated this phenomena close to the upper critical field, where the order parameter is close to zero. He began by looking for solutions of the linearised GL equation,

$$\frac{1}{2m^*} \left(-i\hbar\boldsymbol{\nabla} - q\boldsymbol{A}\right)^2 \psi + \alpha\psi = 0. \tag{2.3.29}$$

This is a Schrödinger equation for a particle of mass m^* and charge q in a uniform magnetic field, and can be identified as a quantum harmonic oscillator equation. Bounded solutions to this can exist only for a discrete set of fields. Abrikosov solved for the eigenvalues and obtain the upper critical field by finding the largest value permissible [53]. The resulting expression for the upper critical field is then given as [66]

$$B_{\mathrm{c2}} = \frac{\phi_0}{2\pi\xi^2} = \sqrt{2}\kappa B_{\mathrm{c}}. \tag{2.3.30}$$

Abrikosov's approach allows us to further probe the structure of the vortex lattice. The solution to the full GL equation (Eq. (2.3.5)) will be close to the solution to the linearised GL equation (Eq. (2.3.29)) when the applied field is close to the upper critical field. Hence, the full solution can be written as a perturbative expansion with the orthogonal linear combination, $\psi = \psi_L + \psi_1$. Working in the Landau gauge, Abrikosov then wrote the general periodic solution [53, 66, 70]

$$\psi(x,y) = \sum_{n=-\infty}^{\infty} C_n \exp(inky) \exp\left(-\frac{1}{2}\kappa^2 \left(x - \frac{nk}{\kappa^2}\right)^2\right), \tag{2.3.31}$$

where periodicity is accounted for in $C_n = C_{n+N}$. By defining a parameter β_A as

$$\beta_{\mathrm{A}} = \frac{\langle |\psi_L|^4 \rangle}{\langle |\psi_L|^2 \rangle^2} = \frac{\int |\psi_L|^4 \, \mathrm{d}^3\boldsymbol{r}}{\left(\int |\psi_L|^2 \, \mathrm{d}^3\boldsymbol{r}\right)^2}, \tag{2.3.32}$$

he optimized C_n and k to minimise the free energy. Abrikosov showed that β_A captures the complexity of the vortex lattice structure, and the minimisation of this parameter β_A is equivalent to minimising the free energy. He obtained a square vortex lattice solution by taking the $N = 1$ case, finding $\beta_A = 1.18$ [66]. This was later corrected by Kleiner: by taking $N = 2$, one obtains a lower energy solution with a triangular lattice and $\beta_A = 1.16$ [70]. This matches the experimental observations in homogeneous materials, where one can notice that vortices penetrate the mixed state, repel each other and form a hexagonal lattice with equal spacing $a_0 \propto B^{-\frac{1}{2}}$ [71]. However, in small or inhomogeneous systems, the arrangement of vortices can

be incredibly disordered due to defects and surface barriers. Abrikosov's work also provides field-dependent solutions for the average order parameter and field inside the superconductor [53]:

$$\left\langle \left|\psi_L\right|^2 \right\rangle = \frac{m_\mathrm{s}}{\mu_0 e\hbar}\frac{B_{\mathrm{c}2}-B_\mathrm{app}}{(2\kappa^2-1)\beta_\mathrm{A}}, \tag{2.3.33}$$

$$\langle B\rangle = B_\mathrm{app} - \frac{B_{\mathrm{c}2}-B_\mathrm{app}}{(2\kappa^2-1)\beta_A}, \tag{2.3.34}$$

where B_app is the externally applied magnetic field. These averages reflect the effect the fluxons have on reducing the order parameter and the field locally, and provide a more accurate approximation of the bulk superconducting electrode behaviour. As the field is decreased, the vortex lattice only nucleates in the bulk when this field is below $B_{\mathrm{c}2}$; very close to $B_{\mathrm{c}2}$, the lattice is closely packed and the average order parameter is very small. It is important to note here that the approach of Abrikosov considers an infinitely periodic system with no surface barriers. We will later explicitly consider how the role of surface barriers affects the superconducting state in Section 2.4.

2.3.5 The Nondimensional GL Equations

For the remainder of this thesis, we will consider the GL equations in normalised units, and adopt a tilde notation for dimensionless variables. We consider real systems with both superconducting electrodes and normal barriers. For efficient computational simulations, working in a non–dimensional form is almost a necessity. All material parameters (α, β and m) are normalized to that of the bulk superconductor. The order parameter will be considered in units of the equilibrium Meissner value, ψ_0, and the units of length are taken to be the coherence length, ξ_s. Inserting these into GL1 (Eq. (2.3.5)) provides a natural unit for the vector potential, $A_0 = \phi_0/2\pi\xi_\mathrm{s}$. The normalised version of GL1 now reads

$$\left[\frac{1}{\tilde{m}_\mathrm{n}}(\tilde{\boldsymbol{\nabla}} - i\tilde{\boldsymbol{A}})^2 + \tilde{\alpha}_\mathrm{n} - \tilde{\beta}_\mathrm{n}\left|\tilde{\psi}\right|^2\right]\tilde{\psi} = 0. \tag{2.3.35}$$

We introduced the notation $\tilde{m}_\mathrm{n} \equiv m_\mathrm{n}/m_\mathrm{s}$, to denote the ratio of the masses in the region of interest (n) and the superconducting region (s). Similar definitions have been made for $\tilde{\alpha}_\mathrm{n}$ and $\tilde{\beta}_\mathrm{n}$. Note that the region of interest may be superconducting (s) or normal (n), but the normalisation is with respect to the superconductor in the Meissner state. In the superconducting bulk electrode, the normalised material parameters ($\tilde{\alpha}_\mathrm{s}$, $\tilde{\beta}_\mathrm{s}$ and $\tilde{m}_\mathrm{s}$) are all by definition normalised to 1. Inserting these normalisations into GL2 ((2.3.7)) leads to a natural length scale for the current,

$$J_0 = \phi_0/2\pi\mu_0\kappa^2\xi_\mathrm{s}^3. \tag{2.3.36}$$

The normalised version of GL2 now reads

$$\tilde{\boldsymbol{J}}_\mathrm{s} = \tilde{m}_\mathrm{n}^{-1}\left[\frac{-i}{2}\left(\tilde{\psi}^*\tilde{\boldsymbol{\nabla}}\tilde{\psi} - \tilde{\psi}\tilde{\boldsymbol{\nabla}}\tilde{\psi}^*\right) - \left|\tilde{\psi}\right|^2\tilde{\boldsymbol{A}}\right] = \tilde{m}_\mathrm{n}^{-1}\mathrm{Im}\left[\tilde{\psi}^*(\tilde{\boldsymbol{\nabla}} - i\tilde{\boldsymbol{A}})\tilde{\psi}\right]. \tag{2.3.37}$$

Magnetic fields are normalised in units of the upper critical field, $B_{\mathrm{c}2}$. For completeness, the normalised GL free energy is written down as

$$\tilde{F} - \tilde{F}_0 = \int\left[-\tilde{\alpha}_\mathrm{n}\left|\tilde{\psi}\right|^2 + \frac{1}{2}\tilde{\beta}_\mathrm{n}\left|\tilde{\psi}\right|^4 + \sum_\mu \frac{1}{\tilde{m}_\mathrm{n}}\left|\left(\tilde{\partial}_\mu - i\tilde{A}_\mu\right)\tilde{\psi}\right|^2 + \kappa^2\tilde{B}^2\right]\mathrm{d}^3\tilde{\boldsymbol{r}}, \tag{2.3.38}$$

and the normalised Ampère–Maxwell equation is given as

$$\kappa_{\mathrm{s}}^2 \tilde{\boldsymbol{\nabla}} \times \tilde{\boldsymbol{\nabla}} \times \tilde{\boldsymbol{A}} = \tilde{\boldsymbol{J}}_{\mathrm{s}}. \tag{2.3.39}$$

The normalisations used throughout this thesis are summarized in Table 2.1.

Symbol	Units	Interpretation
$\boldsymbol{r}$	$\xi_{\mathrm{s}} = \hbar/\sqrt{-2m_{\mathrm{s}}\alpha_{\mathrm{s}}}$	Position vector
t	$\tau = \mu_0 \sigma_{\mathrm{N;s}} \lambda_{\mathrm{s}}^2$	Time
ψ	$\lvert\psi_0\rvert = \sqrt{-\alpha_{\mathrm{s}}/\beta_{\mathrm{s}}}$	Order parameter
$\boldsymbol{A}$	$A_0 = \phi_0/2\pi\xi_{\mathrm{s}}$	Magnetic vector potential
φ	$\varphi_0 = \phi_0/2\pi\tau$	Electrostatic potential
$\boldsymbol{B}$	$B_{\mathrm{c2}} = \phi_0/2\pi\xi_{\mathrm{s}}^2$	Magnetic induction
$\boldsymbol{E}$	$E_0 = \phi_0/2\pi\tau\xi_{\mathrm{s}}$	Electric field
$\boldsymbol{J}$	$J_0 = \phi_0/2\pi\mu_0\kappa^2\xi_{\mathrm{s}}^3$	Current density
F	$F_0 = \phi_0^2/8\pi^2\mu_0\kappa^2\xi_{\mathrm{s}}$	Free energy

Table 2.1: The normalisation parameters.

2.3.6 Gauge Invariant GL Equations

A common approach in literature is to include the phase explicitly within the GL equations (Eqs. (2.3.35) and (2.3.37)) [72, 73, 74, 75]. This holds the advantage that all of the variables involved are real quantities, and therefore invariant under gauge transformations. The wavefunction can be written in a standard way a product of magnitude and phase,

$$\tilde{\psi} = \lvert\tilde{\psi}\rvert e^{i\theta}, \tag{2.3.40}$$

where θ is a general phase that is not gauge–invariant. By defining a gauge invariant phase γ [73], where

$$\tilde{\boldsymbol{\nabla}}\gamma = \tilde{\boldsymbol{\nabla}}\theta - \tilde{\boldsymbol{A}}, \tag{2.3.41}$$

and imposing the condition that $\tilde{\boldsymbol{\nabla}} \cdot \tilde{\boldsymbol{J}}_{\mathrm{s}} = 0$, one obtains the general 'gauge invariant GL equations' [73]:

$$\left[\frac{1}{\tilde{m}_{\mathrm{n}}}\tilde{\boldsymbol{\nabla}}^2 - \frac{1}{\tilde{m}_{\mathrm{n}}}(\tilde{\boldsymbol{\nabla}}\gamma)^2 + \tilde{\alpha}_{\mathrm{n}} - \tilde{\beta}_{\mathrm{n}}\left\lvert\tilde{\psi}\right\rvert^2\right]\lvert\tilde{\psi}\rvert = 0, \tag{2.3.42}$$

$$\tilde{\boldsymbol{J}}_{\mathrm{s}} = \frac{1}{\tilde{m}_{\mathrm{n}}}\left\lvert\tilde{\psi}\right\rvert^2 \tilde{\boldsymbol{\nabla}}\gamma = \frac{1}{\tilde{m}_{\mathrm{n}}}\left\lvert\tilde{\psi}\right\rvert^2 \left(\tilde{\boldsymbol{\nabla}}\theta - \tilde{\boldsymbol{A}}\right). \tag{2.3.43}$$

2.3.7 Critical Currents

We have discussed how the critical temperature leads to the development of GL theory, and the resulting critical fields that emerged. The remaining parameter of interest; the current density; is perhaps the most technologically relevant. The critical current density (J_{c}) is typically the parameter that limits most technological applications. A higher critical current density allows for a larger magnetic field to be produced, or allows for a reduction of the amount of superconducting material necessary to achieve a given field, which is fundamental for the commercial viability of many applications [22].

The theoretical limit for the critical current density of a system is known as the *depairing current density*, J_{D} [60, 76]. This is the current density at which the kinetic

energy of the superelectrons is greater than their condensation energy, causing the Cooper pairs to break apart and the superconducting state to be destroyed. This current can be obtained by studying the gauge invariant GL equations presented in Eqs. (2.3.42) and (2.3.43). One can combine these by eliminating $\tilde{\boldsymbol{\nabla}}\gamma$ from each equation, to obtain a single equation,

$$\frac{1}{\tilde{m}_{\mathrm{n}}}\tilde{\boldsymbol{\nabla}}^2|\tilde{\psi}| + \tilde{\alpha}_{\mathrm{n}}|\tilde{\psi}| - \tilde{\beta}_{\mathrm{n}}|\tilde{\psi}|^3 - \frac{\tilde{m}_{\mathrm{n}}\tilde{\boldsymbol{J}}_{\mathrm{s}}^2}{|\tilde{\psi}|^3} = 0. \tag{2.3.44}$$

The upper bound on the current density can be found by considering Eq. (2.3.44) in a bulk superconductor in zero field. Consider a thin, narrow wire surrounded by an insulator – the order parameter is therefore constant in the wire and the current can only flow uniformly along the long axis of the wire. Therefore, Eq. (2.3.44) simplifies to read [60]

$$\tilde{J}_{\mathrm{s}}^2 = |\tilde{\psi}|^4\left(1 - |\tilde{\psi}|^2\right). \tag{2.3.45}$$

One can maximize this current with respect to $|\psi|$ and obtain the maximum lossless current that can flow within a superconductor. This current occurs when $|\psi|^2 = 2/3$ [60]. Inserting this value back into the above equation yields the result for the depairing current density,

$$J_{\mathrm{D}} = \frac{2}{3\sqrt{3}}J_0. \tag{2.3.46}$$

In zero field, below J_{D}, the current can flow with zero resistance. If the transport current is raised above J_{D}, the superconducting state is broken and the current flows with a typical Ohmic resistance. In contrast, if one considers a superconductor in the mixed state, then the critical current is the applied current which causes a continuous movement of vortices – this movement causes an electric field according to Maxwell's equations which leads to energy dissipation in the system.

In practice, superconductors are not homogeneous narrow single–crystalline wires – they are typically inhomogeneous, polycrystalline materials, containing an abundance of defects and grain boundaries. Fluxons are 'pinned' by defects and grain boundaries within the system – the critical current is therefore viewed as the applied current needed to free these fluxons from their pinned states. The critical current of real commercial superconductors are typically orders of magnitude below the theoretical limit [39]. The critical current densities of some commercial superconductors are shown in Fig. 2.4. Developing our analytic understanding and modelling real polycrystalline superconductor requires careful consideration of the system geometry, microstructure and material parameters of the system.

2.4 Interfaces and Surface Barriers

Many of the results discussed thus far are relevant for bulk superconducting materials. Although these are easy to describe analytically and capture important results for understanding real superconductors, they miss out the complexity that occurs near superconductor–normal (SN) interfaces. In this section, we present some results from Saint James and de Gennes describing the effect of an interface on the superconductor.

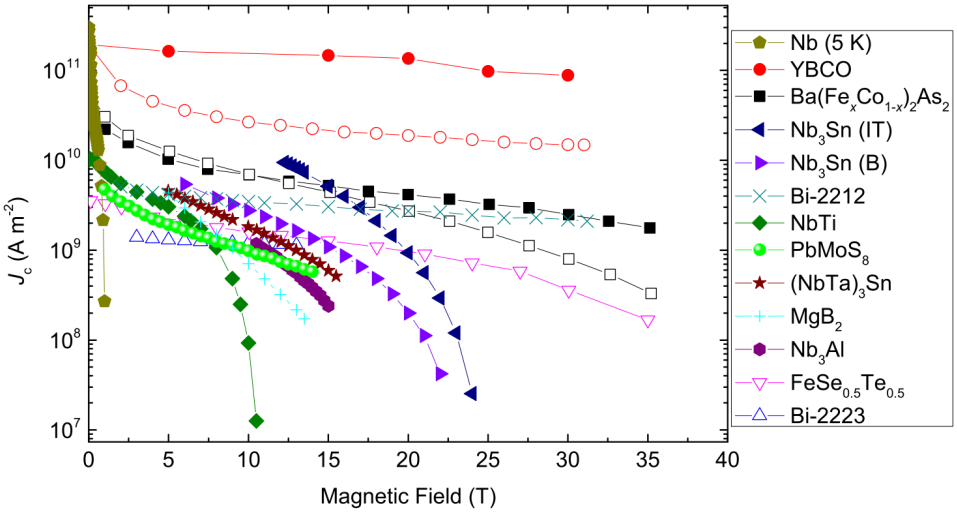

Figure 2.4: Critical current as a function of applied field for a variety of commercially used superconductors [39].

2.4.1 The Generalized GL Boundary Condition

By considering a single SN bilayer using microscopic theory, de Gennes proposed a generalization of the GL boundary condition (Eq. (2.3.6)) [77]:

$$\left(\tilde{\boldsymbol{\nabla}} - i\tilde{\boldsymbol{A}}\right)\tilde{\psi}\cdot\hat{\boldsymbol{n}} = \frac{1}{\tilde{b}}\tilde{\psi}. \tag{2.4.1}$$

Eq. (2.3.6) is correct for an interface between a superconductor and an insulator (an SI interface). With a SN interface, the order parameter (superelectrons) can penetrate some distance into the metal, inducing a weak superconducting effect in the normal barrier within a small region near the interface. Correspondingly, this leads to a decrease in the order parameter in the superconductor. This is known as the *proximity effect*. Here, b is known as the extrapolation length, characterizing the distance over which the order parameter drops to zero after passing through the boundary. In the extreme insulating limit, the order parameter drops to zero in the normal material almost instantly, and so $b \to \infty$ – this recovers the original GL boundary condition in Eq. (2.3.6), and the boundary condition is equivalent to having zero gradient at the interface. Conversely, for a perfect conductor, the superelectrons near the boundary can leak infinitely far into the normal region, and so $b \to 0$ and the order parameter is zero at the interface. One can consider a semi–infinite half plane in zero–field, where the SN interface is located at $x = 0$ and the superconductor is in the region $x > 0$. In this case, the boundary conditions are that the order parameter is zero at the interface and takes the Meissner value as $x \to \infty$. As a textbook example, the particular analytic solution to GL1 in this geometry is given by [69]

$$\tilde{\psi}(\tilde{x}) = \tanh\left(\frac{\tilde{x}}{\sqrt{2}}\right). \tag{2.4.2}$$

As expected, the order parameter in the electrode recovers over the length scale of the coherence length to the bulk Meissner value.

2.4.2 Superconductor–Insulator Interfaces

The previous results in Section 2.3.4 suggested that for fields above B_{c2}, the superconducting state is completely destroyed. This was derived in the case where

surface effects can be neglected – for infinite systems, as the field is reduced, the superconducting vortex lattice spontaneously arises when $B_{\mathrm{app}} = B_{\mathrm{c2}}$. Although this is true in the *bulk* of the superconducting electrode, interesting phenomena can arise when considering the presence of surface boundaries [78, 79].

2.4.2.1 Surface Nucleation Field for a Superconducting–Insulating Interface (SI)

We follow the approach outlined by Saint James and de Gennes, describing the nucleation of superconductivity near a surface, and the corresponding effect this interface has on the nucleation field. We will see how one can interpret this 'surface nucleation field' as an effective upper critical field, denoted as B_{c3}. Saint James and de Gennes consider a semi–infinite half–plane, with a superconducting electrode in the region where $x > 0$, and a vacuum (or extremely insulating normal metal) in the region where $x < 0$. They consider a uniform field applied in z–direction and make the choice of gauge [79]

$$\tilde{\boldsymbol{A}} = \tilde{A}_y \hat{\jmath}, \tag{2.4.3}$$

where

$$\tilde{A}_y(\tilde{x}) = \tilde{B}_{\mathrm{app}} \tilde{x}. \tag{2.4.4}$$

We note here than the net local field is not the same as the applied field – in the presence of a screening current, the field is spatially varying across the system. However, in the limit near the surface upper critical field, the order parameter is small everywhere, the screening currents are negligible and so the field is close to the applied field in the entire system. Saint James and de Gennes first consider the spatial variation of the order parameter in the x–direction, and write the order parameter in the standard way as a product of magnitude and phase where,

$$\tilde{\psi}(\tilde{x}, \tilde{y}) = |\tilde{\psi}(\tilde{x})| e^{i\phi(\tilde{x}, \tilde{y})}. \tag{2.4.5}$$

The presence of the insulating boundaries set some constraints on the current flow allowed throughout the system. No current is able to flow through the insulating surface, written as the first boundary condition

$$\tilde{J}_{\mathrm{s:x}} = 0. \tag{2.4.6}$$

Applying the condition of zero charge density ($\tilde{\boldsymbol{\nabla}} \cdot \tilde{\boldsymbol{J}} = 0$), leads to the second boundary condition,

$$\frac{\partial \tilde{J}_{\mathrm{s:y}}}{\partial \tilde{y}} = 0. \tag{2.4.7}$$

By applying these two boundary conditions (Eqs. (2.4.6) and (2.4.7)), the phase must be of the form [79]

$$\phi(\tilde{x}, \tilde{y}) = k_y \tilde{y}. \tag{2.4.8}$$

Substituting the wavefunction into GL1 (Eq. (2.3.35)) in the superconducting electrode leads to the result

$$\frac{\partial^2 |\tilde{\psi}|}{\partial \tilde{x}^2} - \left(k_y - \tilde{B}_{\mathrm{app}} \tilde{x}\right)^2 |\tilde{\psi}| + |\tilde{\psi}| - |\tilde{\psi}|^3 = 0. \tag{2.4.9}$$

In general, this is of the form of a non-linear Weber equation [80, Eq. 12.2.1], which has no known analytic solution. Saint James and de Gennes consider the system

with an applied field which is close to the surface nucleation field. In this limit, the order parameter magnitude will be small, and the non–linear term can be neglected. Rewriting the wavefunction in the form

$$\tilde{\psi}(\tilde{x},\tilde{y}) = C\tilde{f}(\tilde{x})e^{ik_y\tilde{y}}, \tag{2.4.10}$$

where the prefactor C is a constant and the resulting linearized equation can be written in the form

$$\frac{\partial^2\tilde{f}}{\partial\tilde{x}^2} - \left(k_y - \tilde{B}_{\mathrm{app}}\tilde{x}\right)^2\tilde{f} = 0, \tag{2.4.11}$$

which has solutions in terms of special functions known as parabolic cylinder functions (PCFs) [80, Section 12]*. By making the transformation of variables

$$t = \tilde{x}\sqrt{2\tilde{B}_{\mathrm{app}}} - k_y\sqrt{\frac{2}{\tilde{B}_{\mathrm{app}}}}, \tag{2.4.12}$$

the linearized equation is reduced to the form:

$$\frac{\partial^2\tilde{f}}{\partial t^2} - \left(-\frac{1}{2\tilde{B}_{\mathrm{app}}} + \frac{1}{4}t^2\right)\tilde{f} = 0. \tag{2.4.13}$$

This is one of the standard forms for a differential equation admitting PCF solutions (c.f. [80, Eq. 12.2.2]):

$$\frac{\partial^2\tilde{f}}{\partial t^2} - \left(a + \frac{1}{4}t^2\right)\tilde{f} = 0, \quad \text{where} \quad a = -\frac{1}{2\tilde{B}_{\mathrm{app}}}. \tag{2.4.14}$$

The PCF solutions, in general, may take real or complex arguments. For real x, the general solution is a pair of PCFs: $\{U(a,x), V(a,x)\}$ if $x > 0$, or $\{U(a,-x), V(a,-x)\}$ if $x < 0$ [80, Section 12.2(i)]). Since the electrode region is defined when $x > 0$, the general solution is therefore written as the superposition

$$\tilde{f}(\tilde{x}) = c_1 U(a,t) + c_2 V(a,t). \tag{2.4.15}$$

These cylinder functions can be expressed in terms of a number of other special functions, such as confluent hypergeometric functions (typically used for numerical evaluation) [80, Section 12.4].

To constrain this general solution, Saint James and de Gennes applied the two boundary conditions [79]

$$\tilde{f}(\tilde{x}\to\infty) = 0 \qquad \text{and} \qquad \left.\frac{\partial\tilde{f}}{\partial\tilde{x}}\right|_{\tilde{x}=0} = 0. \tag{2.4.16}$$

The first condition ensures that the order parameter is zero deep inside the bulk of the superconductor, whilst the second is the typical Neumann condition of zero gradient, appropriate at an insulating boundary as seen from Eq. (2.4.1). Since $U(a,z)\to 0$ as $z\to\infty$ and $V(a,z)\to\infty$ as $z\to\infty$ (as seen from [80, Figs. 12.3.3 and 12.3.4], or the asymptotic expansions in [80, Eqs. 12.9.1 and 12.9.2]), the first boundary condition requires that $c_2 = 0$. The particular solution is then written as

$$\tilde{f}(\tilde{x}) = c_1 U(a,t). \tag{2.4.17}$$

*Saint James and De Gennes refer to these special functions as 'Weber functions'; all modern texts instead call these 'parabolic cylinder functions'.

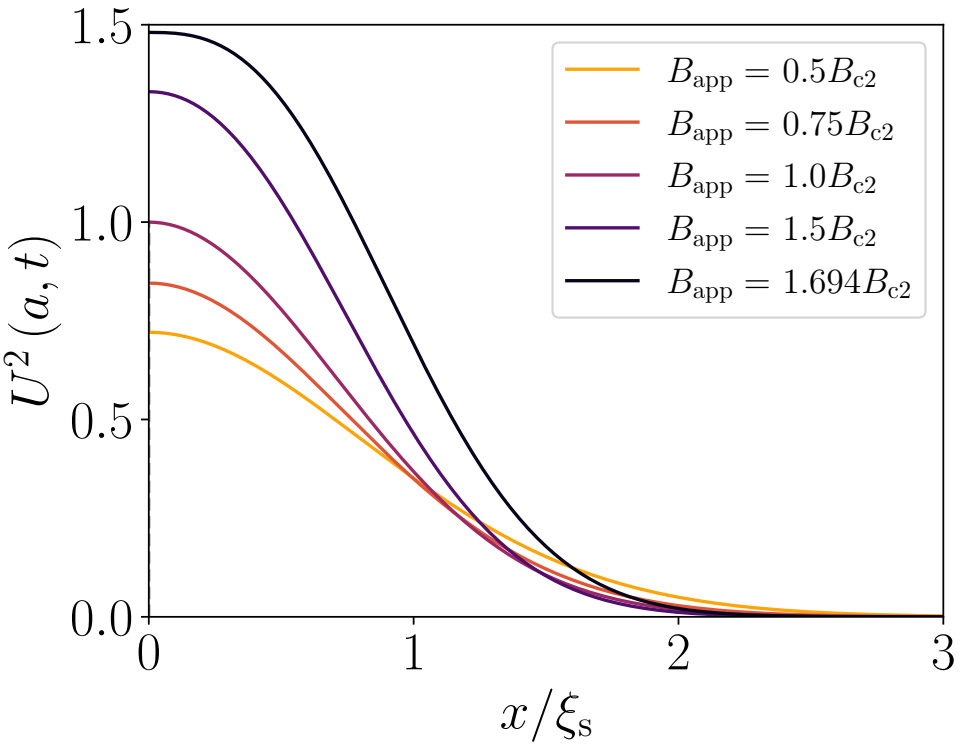

Figure 2.5: Examples of the parabolic cylinder functions (used in Eq. (2.4.17)) with the particular value of k_y that satisfies the boundary condition (Eq. (2.4.16)), for a range of applied magnetic fields. These cylinder functions describe the *spatial variation* of the order parameter solution – the *magnitude* is determined by the remaining constant prefactor in Eq. (2.4.17).

The remaining boundary condition in Eq. (2.4.16) provides an implicit equation for k_y. The derivative of these functions are defined through the recurrence relation [80, Eq. 12.8.3]*

$$U'(a,t) = \frac{1}{2}tU(a,t) - U(a-1,t). \tag{2.4.18}$$

Therefore, we find an implicit equation to determine the value of k_y for the particular solution,

$$\frac{1}{2}t_0 U\left(a,t_0\right) - U\left(a-1,t_0\right) = 0, \tag{2.4.19}$$

where t_0 is the spatial argument (Eq. (2.4.12)) evaluated at the interface; $t_0 = -k_y\sqrt{2/\tilde{B}_{app}}$. This equation is field dependent. As the applied field is increased, the value of k_y that satisfies the boundary condition changes. Moreover, the physical solution is unique so that there is a single value of k_y corresponding to a physical order parameter that meets the boundary condition.

Some examples of the parabolic cylinder functions at various field values are shown in Fig. 2.5. It is important to note here that the cylinder functions are responsible for describing the spatial variation of the order parameter magnitude. Since the equation is linear, the solution is only defined up to a constant prefactor [69] – the remaining prefactor c_1 in Eq. (2.4.17) determines the magnitude of these solutions. In practice, this prefactor must be determined by solving the full non–linear GL equations with the boundary conditions in Eq. (2.4.16) [78, 79]. In Chapter 4, we shall provide an analytic approach detailing how to constrain this remaining prefactor.

*There are three choices for the recurrence relations [80, Eqs. 12.8.1 to 12.8.4]; we chose to use this since it is the same form as used in Mathematica and other common resources in literature. The results are independent of the choice of recurrence relation.

As mentioned, Eq. (2.4.19) provides an implicit relationship between a and t_0, which provides the relationship between the applied field, $\tilde{B}_{\mathrm{app}}$, and the phase, k_y. As the applied field is increased, there is some maximum critical field, above which no implicit solution to Eq. (2.4.19) for k_y that satisfies the boundary condition is possible. In other words, beyond this critical field, there is no solution for the order parameter that satisfies the boundary conditions. Below this critical field, the superconducting state has nucleated within a small region on the order of a few coherence lengths, decaying to zero as it moves away from the interface. This field is the surface nucleation field, $B_{\mathrm{c}3}$. Between $B_{\mathrm{c}2}$ and $B_{\mathrm{c}3}$, the superconducting state can only nucleate and exist in this so–called 'sheath' region near the insulating interface. Below $B_{\mathrm{c}2}$, then the superconducting state can nucleate in the bulk region, as described by the Abrikosov results [66]. Strictly, the solutions presented here are valid only near the surface nucleation field where the order parameter is small.

In order to extract the surface nucleation field, we need to find the maximum field for which a solution exists. Eq. (2.4.13) can be viewed as an eigenvalue problem, and therefore this maximum field corresponds to the lowest eigenvalue for this particular potential. Saint James has shown this leads to [79, p. 86]

$$\left.\frac{\mathrm{d}a}{\mathrm{d}t}\right|_{t=t_0} = 0. \tag{2.4.20}$$

This condition holds at the critical values of a and t_0 that correspond to the maximum value of the applied field and the lowest eigenvalue, denoted as a_{c} and $t_{0,\mathrm{c}}$. Taking the derivative of Eq. (2.4.19) with respect to t_0 and using the condition in Eq. (2.4.20) yields the result

$$\frac{1}{2}\left(1+\frac{1}{2}t_{0,\mathrm{c}}^2\right)U\left(a_{\mathrm{c}},t_{0,\mathrm{c}}\right) - t_{0,\mathrm{c}}U\left(a_{\mathrm{c}}-1,t_{0,\mathrm{c}}\right) + U\left(a_{\mathrm{c}}-2,t_{0,\mathrm{c}}\right) = 0. \tag{2.4.21}$$

Eqs. (2.4.19) and (2.4.21) together form a set of coupled equations which specify the critical values a_{c} and $t_{0,\mathrm{c}}$. Using the recurrence relation [80, Eq. 12.8.1]

$$tU\left(a,t\right) - U\left(a-1,t\right) + (a+\tfrac{1}{2})U\left(a+1,t\right) = 0, \tag{2.4.22}$$

we can transform Eq. (2.4.21) to provide an explicit solution for the critical value of a_{c} that maximizes the field,

$$a_{\mathrm{c}} = -\frac{1}{4}t_{0,\mathrm{c}}^2. \tag{2.4.23}$$

Inserting this back into Eq. (2.4.19) leaves an implicit equation for $t_{0,\mathrm{c}}$:

$$\frac{1}{2}t_{0,\mathrm{c}}U\left(-\frac{1}{4}t_{0,\mathrm{c}}^2,t_{0,\mathrm{c}}\right) - U\left(-\frac{1}{4}t_{0,\mathrm{c}}^2-1,t_{0,\mathrm{c}}\right) = 0, \tag{2.4.24}$$

that leads to a value for $t_{0,c} \approx -1.09$. This gives the surface nucleation field for perfectly insulating boundary conditions given by [78]

$$\tilde{B}_{\mathrm{c}3} = -\frac{1}{2a_{\mathrm{c}}} = \frac{2}{t_{0,\mathrm{c}}^2} = 1.695. \tag{2.4.25}$$

We note that Saint James provided a framework using the integral representations of the cylinder functions (c.f. [80, Eq. 12.5.1]) which are equivalent to the complete cylinder function derivation presented here.

Finally, since the phase has been included explicitly here and the boundary condition is essentially a constraint on the phase, the supercurrent flowing in this system is also known. GL2 provides the spatial variation of the screening currents flowing [79],

$$\tilde{J}_{\mathrm{s:y}}\left(\tilde{x}\right) = \tilde{f}^2\left(\tilde{x}\right)\left(k_y - \tilde{B}_{\mathrm{app}}\tilde{x}\right). \tag{2.4.26}$$

Since k_y is positive, the sign of $\tilde{J}_{\mathrm{s:y}}(\tilde{x})$ changes and the screening currents are counter–rotating. This is a physical consequence of the order parameter being non–zero only in a thin region near the sheath; if x is sufficiently far away from the interface or $x < 0$, the order parameter is zero, the system is in the normal state and so the net field is B_{app}. The screening currents on each of these sides flow in opposite directions and compete, producing counter–flowing currents with a point of zero net current somewhere within the sheath. This is one of the beautiful results of Saint James and arises naturally from the direct inclusion of the phase. In Chapter 4, we will see how one can utilise these solutions as a basis to understand the order parameter variation across the entire field range. Moreover, the Saint James results presented here are derived for the specific case of insulating boundaries. We will later generalise these results to interfaces of arbitrary masses, providing the notion of an effective upper critical field which is dependent on the specific interface material parameters.

2.4.2.2 Effective Upper Critical Field for a Superconducting Slab with Insulating Coatings (ISI)

The framework for surface superconductivity above considers a SI interface in isolation, where the superconductor and the insulator were semi–infinite half–planes. A natural extension to this is to consider a finite system; Saint James and de Gennes also offered a framework to describe an insulator–superconductor–insulator (ISI) system, where the superconducting slab has a finite thickness, d_{s}. Consider the slab to be centered at $\tilde{x} = 0$, and each interface to be located at $\tilde{x} = \pm\tilde{d}_{\mathrm{s}}/2$. In the slab, the general solution is written as the superposition,

$$\tilde{f}(\tilde{x}) = c_{\mathrm{s1}} U(a,t) + c_{\mathrm{s2}} U(a,-t). \tag{2.4.27}$$

Eq. (2.4.27) can be seen as a symmetric combination of two solutions like Eq. (2.4.17), describing the variation of the order parameter near each respective interface. The relevant boundary conditions at the insulating interfaces are given as

$$\left.\frac{\partial \tilde{f}}{\partial \tilde{x}}\right|_{\tilde{x}=-\tilde{d}_{\mathrm{s}}/2} = 0 \qquad \text{and} \qquad \left.\frac{\partial \tilde{f}}{\partial \tilde{x}}\right|_{\tilde{x}=\tilde{d}_{\mathrm{s}}/2} = 0. \tag{2.4.28}$$

Again, this system has 3 unknowns (c_{s1}, c_{s2} and k_y) and 2 boundary conditions, and so one of the constant prefactors is left undetermined, consistent with the previous section. A similar approach is followed; one boundary condition will be used to constrain one of the prefactors in terms of the other, and the remaining boundary condition will determine the phase term, k_y. We adopt a prime notation, where prime denotes differentiation with respect to the spatial argument of the function:

$$\begin{aligned} U'(a,t) &= \frac{\partial U(a,t)}{\partial t}, \\ U'(a,-t) &= \frac{\partial U(a,-t)}{\partial(-t)}. \end{aligned} \tag{2.4.29}$$

If desired, the derivatives may be explicitly written out through the recurrence relation seen earlier ([80, Eq. 12.8.3]). However, this form is common in numerical evaluation, and in conjunction with the chain rule, allows for a particularly concise notation of the gradient boundary conditions. Using the first boundary condition in Eq. (2.4.28) at $x = -d_{\mathrm{s}}/2$ leads to the relation [78, 79]

$$c_{\mathrm{s2}} = \gamma_{\mathrm{s}} c_{\mathrm{s1}}, \tag{2.4.30}$$

where the variable γ_s is defined using Eq. (2.4.18) as

$$\gamma_\mathrm{s} = \left.\frac{U'(a,t)}{U'(a,-t)}\right|_{\tilde{x}=-\tilde{d}_\mathrm{s}/2} = \frac{\frac{1}{2}t_{-\tilde{d}_\mathrm{s}/2}U\left(a,t_{-\tilde{d}_\mathrm{s}/2}\right) - U\left(a-1,t_{-\tilde{d}_\mathrm{s}/2}\right)}{-\frac{1}{2}t_{-\tilde{d}_\mathrm{s}/2}U\left(a,-t_{-\tilde{d}_\mathrm{s}/2}\right) - U\left(a-1,-t_{-\tilde{d}_\mathrm{s}/2}\right)}. \quad (2.4.31)$$

Using the other boundary condition in Eq. (2.4.28) at $x = d_\mathrm{s}/2$ provides an implicit equation,

$$U'\left(a,t_{\tilde{d}_\mathrm{s}/2}\right) - \gamma_s U'\left(a,-t_{\tilde{d}_\mathrm{s}/2}\right) = 0. \quad (2.4.32)$$

Crucially, this implicit equation for k_y is independent of c_1. Eq. (2.4.32) contains all the necessary information about the thickness of the slab, and so can be used to identify the effective upper critical field as a function of thickness. Again, we could ramp up the field until no solution exists, or we can find the lowest eigenvalue as we did in the previous section by differentiating our implicit equation in Eq. (2.4.32) with respect to $t_{\tilde{d}_\mathrm{s}/2}$. From the definition of t in Eq. (2.4.12), we can notice that the two spatial coordinates at each interface ($t_{\tilde{d}_\mathrm{s}/2}$ and $t_{-\tilde{d}_\mathrm{s}/2}$) are simply related:

$$t_{-\tilde{d}_\mathrm{s}/2} = t_{\tilde{d}_\mathrm{s}/2} - \frac{\tilde{d}_\mathrm{s}}{\sqrt{-a}}. \quad (2.4.33)$$

Note that a is negative in order to guarantee a positive field and so the root remains well–defined. Therefore, we can replace any $t_{-\tilde{d}_\mathrm{s}/2}$ with $t_{\tilde{d}_\mathrm{s}/2}$, and then apply the same condition as in Eq. (2.4.21). Unfortunately there is not a simple explicit solution for a, since the parabolic cylinder functions themselves no longer cancel out precisely. Instead, the solution for the critical values of a_c and $t_{\tilde{d}_\mathrm{s}/2,\mathrm{c}}$ must be found numerically. The results are shown in Fig. 2.6. When the thickness of the superconducting layer is large, and the insulating edges are very far apart, the behaviour of the semi–infinite medium (shown in Section 2.4.2) is recovered, where $B^*_{\mathrm{c}2} = B_{\mathrm{c}3} = 1.695B_{\mathrm{c}2}$. However, as the thickness decreases, the enhanced superconducting sheath regions overlap and the effective upper critical field is dramatically increased. This is consistent with Tinkham's work on the parallel critical field for sufficiently thin films ($d_\mathrm{s} < 1.8\xi_\mathrm{s}$) [60], given by the equation

$$B_\parallel = \frac{\sqrt{12}\xi_\mathrm{s}}{d_\mathrm{s}}B_{\mathrm{c}2}. \quad (2.4.34)$$

This expression was first found by Ginzburg and Landau in their seminal paper [63, 81], and then generalised to arbitrary angle by Tinkham [82]. If the thickness is sufficient large such that the interfaces are sufficiently far away, then the Saint James results seen in Section 2.4.2 supersedes the Tinkham results [60]. Since the analytic effective upper critical field obtained from Eq. (2.4.32) contains the correct thickness dependence, one can explicitly see the crossover between these two limits as shown in Fig. 2.6.

2.5 Theory of SNS Josephson Junctions

The majority of modern superconductors used in technological applications, such as Nb_3Sn and the HTS materials are polycrystalline materials. Schematically, we can consider these materials as a series of superconducting grains (electrodes), surrounded by normal metal grain boundaries (barriers). In real materials, these grain boundaries are likely to have have a higher resistivity than the bulk electrode with a lower T_c [39, 83, 84] The network of grain boundaries may be complex, and the planes may be aligned at arbitrary angles to the applied magnetic field and current density.

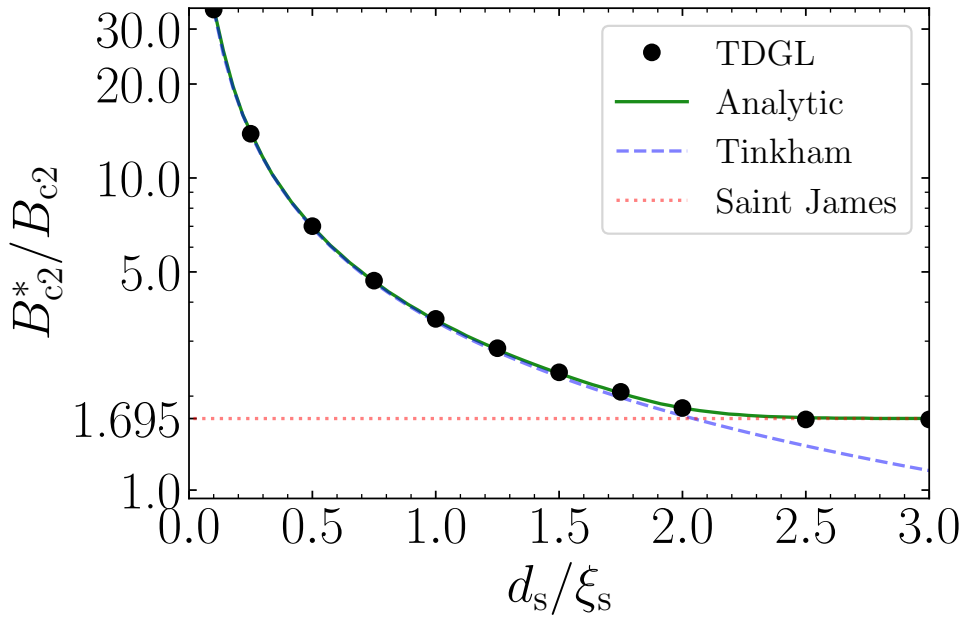

Figure 2.6: Effective upper critical field as a function of the superconducting thickness from the analytic form in Eq. (2.4.32) (solid green line), compared to the limiting values from Tinkham's parallel critical field (dashed blue line, Eq. (2.4.34)) and the semi–infinite Saint James result, $B^*_{c2} = B_{c3} = 1.695 B_{c2}$ (dashed red line, Section 2.4.2). TDGL slab data (solid circular markers) is shown for a range of superconducting thicknesses.

The grains themselves may span over a range of sizes and dimensions, and local defects may alter the material properties. Boundaries may intersect, introducing more complexity that must be accounted for. Understanding the behaviour of an entire polycrystalline superconductor is therefore an extremely difficult task – understanding the macroscopic critical current as a sum of microscopic pinning interactions has proved to be a challenge that has plagued the field for decades [85, 86, 87].

The central thesis of this work is that a fundamental building block that can be used to model polycrystalline materials is the Josephson junction [88]. Josephson junctions consist of two superconducting electrodes, separated by a barrier, which is typically a normal metal – these are known as superconductor–normal–superconductor (SNS) junction geometries [89, 90]. These geometries are particularly interesting since they can exhibit a tunnelling effect [91, 92, 93], even if the barrier itself is significantly insulating but thin enough for each electrode to be coupled together – de Gennes has famously shown that the maximum current that can flow across a junction exponentially decreases with the thickness of the normal barrier [77]. In other words, Cooper pairs and a dissipationless supercurrent can still flow across the junction.

Unfortunately, even though the concept of Josephson junctions has been considered for nearly half a century, the analytic framework that describes these systems is limited to only the simplest of geometries. A schematic of the system that we consider is shown in Fig. 2.7. We consider a square superconducting electrode of chemical width and length (w_s and l_s) and superconducting properties α_s, β_s and m_s. The superconductor is surrounded by a normal barrier (with a chemical junction thickness, d_n) in the x–direction, and a normal coating (with a chemical coating width of w_c) in the y–direction. In these regions, α_n, β_n and m_n describe the material properties of the normal barrier, whilst α_c, β_c and m_c describe the properties of the coating.

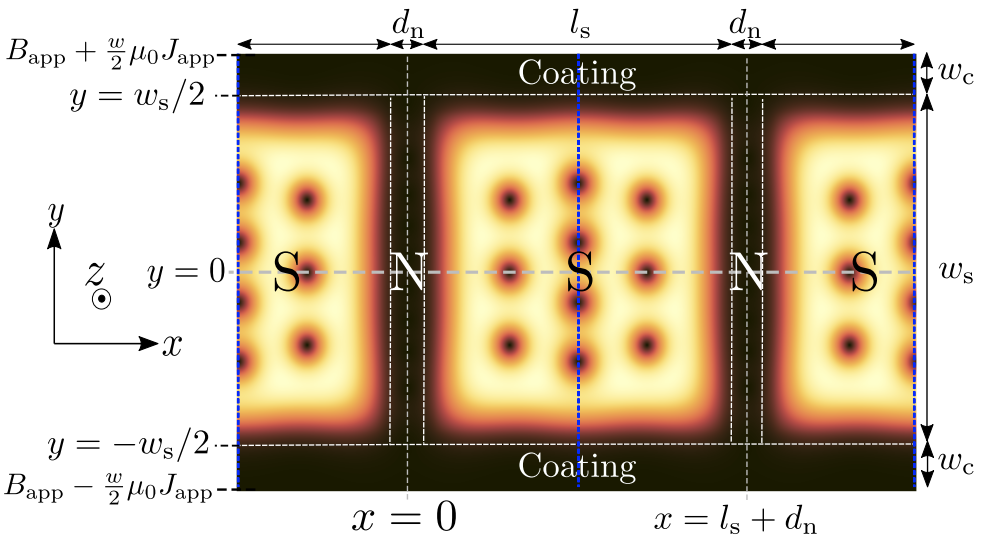

Figure 2.7: Schematic of the 2D computational domain used to model the Josephson junction system. The domain is subdivided into three sections - the superconducting region (S) the normal barrier (N), and a coating region (C). Each region has its own material parameters, normalised to the properties of the bulk superconducting electrode in the Meissner state. Periodic boundaries (shown as blue–dashed lines) are applied in the x–direction, and insulating boundary conditions are applied in the y–direction. The chemical width and length of the superconducting electrode are denoted as w_s and l_s, whilst the chemical thickness of the normal barrier is denoted as d_n. The width of the coating is denoted as w_c. Background: Order parameter magnitude is taken from an example TDGL simulation, highlighting the position of fluxons in the bulk electrode and their interactions with the surface boundaries.

As we saw in Section 2.3.5, we normalise materials properties parameters to those of the superconductor. For modelling polycrystalline materials, it is natural to take the material properties of the coating and barrier regions to be identical to each other. It stands to reason that if one wants to understand the entire macroscopic polycrystalline superconductor, one first needs to have a complete and accurate description of the simplest building block. Different analytic frameworks have been developed in various regions of phase space. We outline the relevant analytic theory and frameworks for the Josephson junction below.

2.5.1 Fink, Blair & Hampshire – Very Narrow Systems ($w_s \ll \xi_s$)

We first review the analytic results for the case where the superconducting electrodes are very narrow ($w_s \ll \xi_s$). This is equivalent to the assumption that there are no vortices in the system at all. If we consider systems with insulating boundary conditions, the general GL boundary condition (Eq. (2.4.1)) demands that the order parameter is independent of y, and therefore the problem reduces to one dimension only. We note that if we applied perfectly conducting boundary conditions, the order parameter would be zero across the width and the critical current would be identically zero since no supercurrent can flow. Fink first derived a zero–field analytic expression for the maximum current density that can flow across a junction [74]. His derivation began with the same gauge invariant framework in Section 2.3.6 to derive the depairing current in a homogeneous narrow wire, J_D – we therefore interpret this result as the equivalent for an inhomgeneous SNS system. We denote the maximum lossless current that can flow through the junction as J_{DJ}. Later, Blair & Hampshire extended these results to include applied magnetic fields, valid across the entire range of magnetic

field, up to the upper critical field [75]. Since Fink's results are captured in the zero–field limit of Blair, here we only describe the in–field derivation.

2.5.1.1 Fink–Blair–Hampshire (FBH) Framework

Blair begins by taking the contour integral of the GI phase defined in Eq. (2.3.41). By applying Stokes' theorem, he obtains

$$\oint \boldsymbol{\nabla}\gamma \cdot \mathrm{d}\boldsymbol{l} = \oint \boldsymbol{\nabla}\theta \cdot \mathrm{d}\boldsymbol{l} - \oint \tilde{\boldsymbol{B}} \cdot \mathrm{d}\boldsymbol{S}. \tag{2.5.1}$$

To ensure that the order parameter is single-valued, the contour integral of θ (first term on the RHS) is equal to $2\pi n$, where n is the number of vortices within the contour. In the very narrow limit, one can assume there are no fluxons in the system ($n = 0$), and so this term has no contribution. He assumes that the order parameter magnitude is symmetric about both the y and x–axes, and that the screening currents, and hence $\partial_y\gamma$, are antisymmetric about the y and x–axes. To first order, the transport current is uniform in the y–direction; there is a laminar flow of transport current in the x–direction. Since the supercurrent in the y–direction is assumed to be zero, Eq. (2.3.43) provides the result for the x–component of the supercurrent,

$$\tilde{J}_{s:x} = \frac{1}{\tilde{m}_\mathrm{n}} \left|\tilde{\psi}\right|^2 \partial_x\gamma(\tilde{y} = 0). \tag{2.5.2}$$

Inserting this back into Eq. (2.5.1), applying Stokes' theorem for a second time, and taking the length of the contours parallel to the x–axis to be sufficiently short leads to the result

$$\partial_x\gamma(\tilde{y}) = \frac{\tilde{J}_{s:x}}{|\psi|^2} + \tilde{B}_\mathrm{app}\tilde{y}. \tag{2.5.3}$$

Since the system is uniform in the y–direction, Blair utilises the mean value theorem and takes an average over the width of the system, replacing quantities by their averaged values:

$$\tilde{F} = \frac{1}{\tilde{w}_\mathrm{s}} \int_{-\tilde{w}_\mathrm{s}/2}^{\tilde{w}_\mathrm{s}/2} \left|\tilde{\psi}\right| \mathrm{d}\tilde{y}\,, \tag{2.5.4}$$

$$\langle \tilde{J}_{s:x} \rangle_y = \frac{1}{\tilde{w}_\mathrm{s}} \int_{-\tilde{w}_\mathrm{s}/2}^{\tilde{w}_\mathrm{s}/2} \tilde{J}_{s:x}\, \mathrm{d}\tilde{y} \equiv \langle \tilde{J}_\mathrm{app} \rangle_y. \tag{2.5.5}$$

Similarly, the average of the square of the result found in Eq. (2.5.3) is given as

$$\langle (\partial_x\gamma(\tilde{y}))^2 \rangle = \left(\frac{\tilde{B}_\mathrm{app}\tilde{w}_\mathrm{s}}{\sqrt{12}}\right)^2 + \frac{\tilde{m}_\mathrm{n}^2 \langle \tilde{J}_\mathrm{app} \rangle_y^2}{\tilde{F}^4}. \tag{2.5.6}$$

Inserting this result back into Eq. (2.3.42) yields a single equation,

$$\frac{1}{\tilde{m}_\mathrm{n}} \frac{\partial^2 \tilde{F}}{\partial \tilde{x}^2} + \left[\left(\tilde{\alpha}_\mathrm{n} - \frac{q^2}{\tilde{m}_\mathrm{n}} \right) - \tilde{\beta}_\mathrm{n} \tilde{F}^2 - \frac{\tilde{m}_\mathrm{n} \langle \tilde{J}_\mathrm{app} \rangle_y^2}{F^4} \right] \tilde{F} = 0, \tag{2.5.7}$$

where q^2 has been defined as

$$q^2 = \left(\frac{\tilde{B}_\mathrm{app}\tilde{w}_\mathrm{s}}{\sqrt{12}}\right)^2. \tag{2.5.8}$$

Eq. (2.5.7) represents a field dependent generalization of Eq. (2.3.44) – Fink's result is recovered in the limit where $q^2 = 0$. The expression for q^2 is related to the parallel

critical field for sufficiently thin films seen in Eq. (2.4.34) [60]. In effect, Blair's formalism treats the very narrow system as being within the overlapping sheath regions, with an enhanced upper critical field given by Eq. (2.4.34).

In order to extract an analytic solution, it is convenient to rescale the variables. Blair made the following substitutions [75]:

$$\tilde{F} = \tilde{\mathcal{F}}\sqrt{1-\frac{q^2}{\tilde{m}_{\rm n}\tilde{\alpha}_{\rm n}}}, \qquad \tilde{x} = \frac{\tilde{\mathcal{X}}}{\sqrt{1-\frac{q^2}{\tilde{m}_{\rm n}\tilde{\alpha}_{\rm n}}}}, \qquad \tilde{J} = \tilde{\mathcal{J}}\left(1-\frac{q^2}{\tilde{m}_{\rm n}\tilde{\alpha}_{\rm n}}\right)^{3/2}. \tag{2.5.9}$$

Inserting these into Eq. (2.5.7) leads to the result

$$\frac{1}{\tilde{m}_{\rm n}}\frac{\partial^2\tilde{\mathcal{F}}}{\partial\tilde{\mathcal{X}}^2} + \left[\tilde{\alpha}_{\rm n} - \tilde{\beta}_{\rm n}\tilde{\mathcal{F}}^2 - \frac{\tilde{m}_{\rm n}\langle\tilde{\mathcal{J}}_{\rm app}\rangle_y^2}{\mathcal{F}^4}\right]\tilde{\mathcal{F}} = 0. \tag{2.5.10}$$

This is the same equation that Fink considered, allowing Blair to use the same machinery to obtain an exact analytic solution [74]. In effect, the substitutions rescaled the variables to remove the field dependence, and provide the in–field observables $\tilde{F}$, $\tilde{x}$ and $\tilde{J}$.

2.5.1.2 Derivation of the General Mathematical Solution

Here we outline the literature derivation of the in–field solution for both strongly and weakly coupled junctions. FBH found a general solution to Eq. (2.5.10) in each region separately and then constrained them to be consistent at the boundary between them. Rewriting Eq. (2.5.10) with completely generic coefficients, gives

$$\frac{\partial^2\tilde{F}}{\partial\tilde{x}^2} + A\tilde{F} - B\tilde{F}^3 - C\frac{1}{\tilde{F}^3} = 0. \tag{2.5.11}$$

Integrate once to obtain the result

$$\left(\frac{\partial\tilde{F}}{\partial\tilde{x}}\right)^2 = \left(\tilde{F}^2-\tilde{F}_B^2\right)\left[-A+\frac{1}{2}B\left(\tilde{F}^2+\tilde{F}_B^2\right)+\frac{C}{\tilde{F}^2\tilde{F}_B^2}\right], \tag{2.5.12}$$

where $\tilde{F}_B$ will be constrained by the boundary conditions on the system. After making use of the chain rule to replace the derivative,

$$\left(\frac{\partial\tilde{F}^2}{\partial\tilde{x}}\right)^2 = 4\tilde{F}^2\left(\frac{\partial\tilde{F}}{\partial\tilde{x}}\right)^2, \tag{2.5.13}$$

Eq. (2.5.12) is then rewritten in the form

$$\left(\frac{\partial\tilde{F}^2}{\partial\tilde{x}}\right)^2 = 2\left(\tilde{F}^2-\tilde{F}_B^2\right)\left[\tilde{F}^2\left\{-2A+B\left(\tilde{F}^2+\tilde{F}_B^2\right)\right\}+\frac{2C}{\tilde{F}_B^2}\right]. \tag{2.5.14}$$

By making the substitution $\tilde{\Psi}^2 = \tilde{F}^2 - \tilde{F}_B^2$, Eq. (2.5.14) is transformed to read [74]

$$\left(\frac{\partial\tilde{\Psi}^2}{\partial\tilde{x}}\right)^2 = 2\Psi^2\left[\left(\tilde{\Psi}^2+\tilde{F}_B^2\right)\left\{-2A+B\left(\tilde{\Psi}^2+2\tilde{F}_B^2\right)\right\}+\frac{2C}{\tilde{F}_B^2}\right]. \tag{2.5.15}$$

Making use of the chain rule again, this is the rewritten into the important result

$$2\left(\frac{\partial\tilde{\Psi}}{\partial\tilde{x}}\right)^2 = \left(\tilde{\Psi}^2+\tilde{F}_B^2\right)\left\{-2A+B\left(\tilde{\Psi}^2+2\tilde{F}_B^2\right)\right\}+\frac{2C}{\tilde{F}_B^2}. \tag{2.5.16}$$

Crucially, this equation is only quadratic in $\tilde{\Psi}^2$. It is possible to factorise this equation into a standard form which admits solutions in terms of Jacobi elliptic functions (c.f. [80, Section 22.13(ii)]),

$$2\left(\frac{\partial\tilde{\Psi}}{\partial\tilde{x}}\right)^2 = \left(a^2/B - \tilde{\Psi}^2\right)\left(b^2 - B\tilde{\Psi}^2\right), \tag{2.5.17}$$

where expressions for a^2 and b^2 are identified as*:

$$a^2 = \left(A - \frac{3}{2}B\tilde{F}_B^2\right) + \sqrt{\left(-A + \frac{1}{2}B\tilde{F}_B^2\right)^2 - \frac{2BC}{\tilde{F}_B^2}}, \tag{2.5.18}$$
$$b^2 = \left(A - \frac{3}{2}B\tilde{F}_B^2\right) - \sqrt{\left(-A + \frac{1}{2}B\tilde{F}_B^2\right)^2 - \frac{2BC}{\tilde{F}_B^2}}.$$

Eq. (2.5.17) is a first-order, separable ODE. By separating variables and integrating each side, one can obtain the result

$$\frac{\tilde{x}}{\sqrt{2}} + k_2 = \int \mathrm{d}\Psi \, \frac{1}{\sqrt{\left(a^2/B - \tilde{\Psi}^2\right)\left(b^2 - B\tilde{\Psi}^2\right)}}, \tag{2.5.19}$$

where k_2 is the final integration constant. Without loss of generality, by the fundamental theorem of calculus, the indefinite integral on the right-hand side is replaced with the definite integral with limits from 0 to $\Psi(\tilde{x})$, absorbing any additional constants into the integration constant. After a small rearrangement, Eq. (2.5.19) now reads

$$\frac{\tilde{x}}{\sqrt{2}} + k_2 = \int_0^{\Psi(\tilde{x})} \mathrm{d}\Psi \, \frac{1}{\sqrt{b^2}\sqrt{\frac{a^2}{B}}\sqrt{\left(1 - \frac{B}{a^2}\tilde{\Psi}^2\right)\left(1 - \frac{B}{b^2}\tilde{\Psi}^2\right)}}. \tag{2.5.20}$$

In order to reduce this integral to a standard Legendre form, one makes the change of variables

$$\sin(\theta) = \sqrt{\frac{B}{a^2}}\Psi, \tag{2.5.21}$$

with the corresponding relations:

$$\mathrm{d}\Psi = \mathrm{d}\theta \sqrt{1 - \sin^2(\theta)}\sqrt{\frac{a^2}{B}},$$
$$\theta = \arcsin\left(\sqrt{\frac{B}{a^2}}\Psi\right).$$

Using these results in Eq. (2.5.20) leads to the an integrand of the form

$$\frac{\tilde{x}}{\sqrt{2}} + k_2 = \int_0^{\arcsin\left(\sqrt{\frac{B}{a^2}}\Psi(\tilde{x})\right)} \mathrm{d}\theta \, \frac{1}{\sqrt{b^2}\sqrt{1 - \frac{a^2}{b^2}\sin^2(\theta)}}. \tag{2.5.22}$$

By introducing the definition of the *incomplete elliptic integral of the first kind*, [80, Eq. 19.2.4] in both *modular* form (using modulus, k) and *parametric* form (using parameter, m):

$$F(\phi, k) = \int_0^{\phi} \frac{\mathrm{d}\theta}{\sqrt{1 - k^2\sin^2\theta}}, \qquad F(\phi|m) = \int_0^{\phi} \frac{\mathrm{d}\theta}{\sqrt{1 - m\sin^2\theta}}, \tag{2.5.23}$$

*The exact forms of a^2 and b^2 are slightly different to FBH because we have considered a slightly different factorisation, more convenient for the general equation. We could recover the Fink results precisely if we had applied the boundary conditions at an earlier stage to consider the same factorisation.

one can find the result:

$$\sqrt{b^2}\left(\frac{\tilde{x}}{\sqrt{2}}+k_2\right)=F\left(\arcsin\left(\sqrt{\frac{B}{a^2}}\Psi(\tilde{x})\right)\middle|m\right),\quad\text{where}\quad m=\frac{a^2}{b^2}. \tag{2.5.24}$$

The order parameter is inside the argument of this special function. By using the definition of the amplitude function as the inverse of the elliptic integral [80, Eqs. 22.16.10 and 22.16.11]:

$$x=F(\phi,k), \tag{2.5.25}$$

$$\mathrm{am}(x,k)=\phi, \tag{2.5.26}$$

Eq. (2.5.24) can be inverted to obtain

$$\arcsin\left(\sqrt{\frac{B}{a^2}}\Psi(\tilde{x})\right)=\mathrm{am}\left(\sqrt{b^2}\left(\frac{\tilde{x}}{\sqrt{2}}+k_2\right)\middle|\frac{a^2}{b^2}\right). \tag{2.5.27}$$

Finally, using the definition of the Jacobi elliptic function, $\mathrm{sn}(x,k)$, as the sine of the amplitude function [80, Eq. 22.16.1],

$$\mathrm{am}(x,k)=\arcsin\left(\mathrm{sn}(x,k)\right), \tag{2.5.28}$$

one can obtain the result

$$\sqrt{\frac{B}{a^2}}\Psi(\tilde{x})=\mathrm{sn}\left(\sqrt{b^2}\left(\frac{\tilde{x}}{\sqrt{2}}+k_2\right)\middle|\frac{a^2}{b^2}\right). \tag{2.5.29}$$

Taking the square of this result, replacing the previous substitution of $\tilde{\Psi}^2=\tilde{F}^2-\tilde{F}_B^2$, and rearranging, one finds the final general result

$$\tilde{F}^2=\tilde{F}_B^2+\frac{a^2}{B}\,\mathrm{sn}^2\left(\sqrt{b^2}\left(\frac{\tilde{x}}{\sqrt{2}}+k_2\right)\middle|\frac{a^2}{b^2}\right), \tag{2.5.30}$$

where the expressions for a and b are defined in Eq. (2.5.18). To reiterate, $\tilde{F}_B^2$ is an undetermined integration constant, which may be easily constrained by applying boundary conditions to Eq. (2.5.12), or by taking relevant derivatives of Eq. (2.5.30). The second integration constant k_2 is also be determined by applying the relevant boundary conditions.

2.5.1.3 Particular Solutions for the Electrodes and the Barrier

For simplicity, FBH consider only the region $x>0$, where the interface is located at $x=d_\mathrm{n}/2$, since the solutions where $x<0$ may be obtained by the symmetry of the system. Following Blair, we substitute the rescaled variables defined in Eq. (2.5.9) into the general results in Eqs. (2.5.18) and (2.5.30), such that the general solution describes real observable quantities.

We now take the general solution and calculate particular solutions for the order parameter first in the superconducting electrode and then in the barrier. The superconducting electrodes to the right in Fig. 2.7 is defined in the region $x\in[d_\mathrm{n}/2,l_\mathrm{s}/2]$. In the electrode, the coefficients are trivial, since $\tilde{\alpha}_\mathrm{n}$, $\tilde{\beta}_\mathrm{n}$ and $\tilde{m}_\mathrm{n}$ are equal to 1 in this region. Inserting the coefficients into the general solution in Eq. (2.5.18) leads to a_s^2 and b_s^2 being defined as [75]

$$a_\mathrm{s}^2=\mathcal{S}_1+\sqrt{\mathcal{S}_2},\quad b_\mathrm{s}^2=-\mathcal{S}_1+\sqrt{\mathcal{S}_2}, \tag{2.5.31}$$

where

$$\mathcal{S}_1 = \left(1 - \frac{3}{2}\frac{\tilde{F}_{\tilde{l}/2}^2}{1-q^2}\right), \tag{2.5.32}$$

$$\mathcal{S}_2 = \left(1 - \frac{1}{2}\frac{\tilde{F}_{\tilde{l}/2}^2}{1-q^2}\right)^2 - \frac{2\langle \tilde{J}_{\mathrm{app}}\rangle_{\mathrm{y}}^2}{(1-q^2)^2\tilde{F}_{\tilde{l}/2}^2}. \tag{2.5.33}$$

The particular solution for Eq. (2.5.30) then takes the form [80, Eq. 22.2.10]

$$\tilde{F}_{\mathrm{s}}^2(\tilde{x}) = \tilde{F}_{\tilde{l}/2}^2 - \left(1-q^2\right)\frac{b_{\mathrm{s}}^2 a_{\mathrm{s}}^2}{b_{\mathrm{s}}^2 + a_{\mathrm{s}}^2}\,\mathrm{sd}^2\left(\left(\frac{\tilde{l}_{\mathrm{s}}}{2} - \tilde{x}\right)\sqrt{1-q^2}\sqrt{\frac{a_{\mathrm{s}}^2 + b_{\mathrm{s}}^2}{2}}\,\middle|\,\frac{b_{\mathrm{s}}^2}{a_{\mathrm{s}}^2 + b_{\mathrm{s}}^2}\right). \tag{2.5.34}$$

We have transformed our original Jacobi elliptic function to ensure that it remains a well–defined function on the real line [94, Pg. 214, Table XIII]. This solution contains a remaining free constant, $\tilde{F}_{\tilde{l}/2}^2 = \tilde{F}_{\mathrm{s}}^2\left(\tilde{x} = \tilde{l}_{\mathrm{s}}/2\right)$, which represents the order parameter magnitude deep inside the electrode. To avoid the proliferation of subscripts, we implicitly understand that the $\tilde{l}$ in $\tilde{F}_{\tilde{l}/2}^2$ is the chemical length. This constant will be constrained by continuity of the two solutions across the interface.

Next, we consider the order parameter solution in the normal barrier. Importantly, the sign of $\tilde{\alpha}_{\mathrm{n}}$ is different to that in the electrode, and so the Jacobi elliptic function is transformed to ensure that it remains on the real line [94]. Again, by substituting the coefficients into Eq. (2.5.18), one can identify the two variables a_{n}^2 and b_{n}^2 to be [75]

$$a_{\mathrm{n}}^2 = \mathcal{N}_1 + \sqrt{\mathcal{N}_2}, \quad b_{\mathrm{n}}^2 = -\mathcal{N}_1 + \sqrt{\mathcal{N}_2}, \tag{2.5.35}$$

where

$$\mathcal{N}_1 = \left(\tilde{m}_{\mathrm{n}}\tilde{\alpha}_{\mathrm{n}} - \frac{3}{2}\tilde{m}_{\mathrm{n}}\tilde{\beta}_{\mathrm{n}}\frac{\tilde{F}_0^2}{1 - \dfrac{q^2}{\tilde{m}_{\mathrm{n}}\tilde{\alpha}_{\mathrm{n}}}}\right), \tag{2.5.36}$$

$$\mathcal{N}_2 = \left(-\tilde{m}_{\mathrm{n}}\tilde{\alpha}_{\mathrm{n}} + \frac{1}{2}\tilde{m}_{\mathrm{n}}\tilde{\beta}_{\mathrm{n}}\frac{\tilde{F}_0^2}{1 - \dfrac{q^2}{\tilde{m}_{\mathrm{n}}\tilde{\alpha}_{\mathrm{n}}}}\right)^2 - \frac{2\tilde{m}_{\mathrm{n}}^3\tilde{\beta}_{\mathrm{n}}\langle \tilde{J}_{\mathrm{app}}\rangle_{\mathrm{y}}^2}{\left(1 - \dfrac{q^2}{\tilde{m}_{\mathrm{n}}\tilde{\alpha}_{\mathrm{n}}}\right)^2\tilde{F}_0^2}. \tag{2.5.37}$$

The particular solution then takes the form [80, Eq. 22.2.10]

$$\tilde{F}_{\mathrm{n}}^2 = \tilde{F}_0^2 - \left(1 - \frac{q^2}{\tilde{m}_{\mathrm{n}}\tilde{\alpha}_{\mathrm{n}}}\right)\frac{a_{\mathrm{n}}^2}{\tilde{m}_{\mathrm{n}}\tilde{\beta}_{\mathrm{n}}}\,\mathrm{sc}^2\left(\sqrt{b_{\mathrm{n}}^2}\frac{\tilde{x}}{\sqrt{2}}\sqrt{1 - \frac{q^2}{\tilde{m}_{\mathrm{n}}\tilde{\alpha}_{\mathrm{n}}}}\,\middle|\,\frac{b_{\mathrm{n}}^2 + a_{\mathrm{n}}^2}{b_{\mathrm{n}}^2}\right). \tag{2.5.38}$$

This solution represents the order parameter magnitude in the normal barrier, and there is a remaining constant $\tilde{F}_0^2 = \tilde{F}_{\mathrm{n}}^2\left(\tilde{x} = 0\right)$, which represents the order parameter at the centre of the barrier. We have again transformed our original Jacobi elliptic function to ensure that it remains on the real line [94, Pg. 214, Table XIII].

Finally, the remaining constants $\tilde{F}_0^2$ and $\tilde{F}_{\tilde{l}/2}^2$ are constrained by imposing continuity of order parameter magnitude and current density across the interface. This is equivalent to ensuring that the following two conditions are met:

$$\tilde{F}_{\mathrm{n}}^2(\tilde{x})\big|_{\tilde{x}=\tilde{d}_{\mathrm{n}}/2} = \tilde{F}_{\mathrm{s}}^2(\tilde{x})\big|_{\tilde{x}=\tilde{d}_{\mathrm{n}}/2}, \tag{2.5.39}$$

$$\frac{1}{\tilde{m}_{\mathrm{n}}}\frac{\partial \tilde{F}_{\mathrm{n}}^2(x)}{\partial \tilde{x}}\bigg|_{\tilde{x}=\tilde{d}_{\mathrm{n}}/2} = \frac{\partial \tilde{F}_{\mathrm{s}}^2(\tilde{x})}{\partial x}\bigg|_{\tilde{x}=\tilde{d}_{\mathrm{n}}/2}. \tag{2.5.40}$$

Imposing these conditions leads to a general equation for interfacial order parameter, written as

$$\left(1-\frac{\tilde{\beta}_{\mathrm{n}}}{\tilde{m}_{\mathrm{n}}}\right)(\tilde{F}^2_{\tilde{d}_{\mathrm{n}}/2})^3-2\left(1-q^2-\frac{\tilde{\alpha}_{\mathrm{n}}}{\tilde{m}_{\mathrm{n}}}+\frac{q^2}{\tilde{m}^2_{\mathrm{n}}}\right)(\tilde{F}^2_{\tilde{d}_{\mathrm{n}}/2})^2 \tag{2.5.41}$$
$$+\left[(2(1-q^2)-\tilde{F}^2_{\tilde{l}/2})\tilde{F}^2_{\tilde{l}/2}+\frac{\tilde{F}^2_0}{\tilde{m}_{\mathrm{n}}}\left(-2\left(\tilde{\alpha}_{\mathrm{n}}-\frac{q^2}{\tilde{m}_{\mathrm{n}}}\right)+\tilde{\beta}_{\mathrm{n}}\tilde{F}^2_0\right)\right.$$
$$\left.+\frac{2\langle\tilde{J}_{\mathrm{app}}\rangle^2_y}{\tilde{F}^2_{\tilde{l}/2}}-\frac{2\langle\tilde{J}_{\mathrm{app}}\rangle^2_y}{\tilde{F}^2_0}\right]\tilde{F}^2_{\tilde{d}_{\mathrm{n}}/2}=0.$$

Note that there are now have three coupled equations with three unknowns ($\tilde{F}^2_{\tilde{l}/2}$, $\tilde{F}^2_0$, $\tilde{F}^2_{\tilde{d}_{\mathrm{n}}/2}$) – the order parameter solution in the superconducting electrode (Eq. (2.5.34)), the order parameter solution in the normal barrier (Eq. (2.5.38)), as well as the continuity conditions across the interface between them (Eq. (2.5.41).

2.5.1.4 Weakly Coupled Solutions for the Interfacial Order Parameter

FBH provide some simplifications which allow analytic forms to be more easily extracted by assuming that the junction is weakly coupled, such that only very small transport currents can pass through the junction and the order parameter magnitude in the bulk of the normal barrier is very small. In an applied magnetic field, the order parameter in the bulk of the electrode is proportional to the field. This sets $\tilde{F}^2_{\tilde{l}/2}\to 1-q^2$, $\tilde{F}^2_0\to 0$, and $\langle\tilde{J}_{\mathrm{app}}\rangle\to 0$. In this case, Eq. (2.5.41) can be solved for the solution

$$\tilde{F}^2_{\tilde{d}_{\mathrm{n}}/2}=\frac{-\tilde{\alpha}_{\mathrm{n}}\tilde{m}_{\mathrm{n}}+\tilde{m}^2_{\mathrm{n}}+q^2-\tilde{m}^2_{\mathrm{n}}q^2-\tilde{m}^2_{\mathrm{n}}\sqrt{\left(1-q^2-\frac{\tilde{\alpha}_{\mathrm{n}}\tilde{m}_{\mathrm{n}}-q^2}{\tilde{m}^2_{\mathrm{n}}}\right)^2-\left(1-\frac{\tilde{\beta}_{\mathrm{n}}}{\tilde{m}_{\mathrm{n}}}\right)\left(1-q^2\right)^2}}{\tilde{m}_{\mathrm{n}}\left(-\tilde{\beta}_{\mathrm{n}}+\tilde{m}_{\mathrm{n}}\right)}. \tag{2.5.42}$$

However, this result has a singularity when $\tilde{m}_{\mathrm{n}}=\tilde{\beta}_{\mathrm{n}}$. In this limit, the interfacial order parameter takes on the simple form,

$$\tilde{F}^2_{\tilde{d}_{\mathrm{n}}/2}=\frac{(1-q^2)^2}{2(1-\tilde{\alpha}_{\mathrm{n}})}. \tag{2.5.43}$$

2.5.1.5 Josephson Depairing Current Density, J_{DJ}

Finally, FBH use the order parameter to find J_{DJ} by finding the maximal current through the system using the condition

$$\frac{\partial\langle\tilde{J}_{\mathrm{app}}\rangle}{\partial\tilde{F}^2_0}=0. \tag{2.5.44}$$

This is similar to Eq. (2.4.20) in Section 2.4. Making use of the series expansions of the Jacobi elliptic functions in Eq. (2.5.38) within the limit of a weakly coupled junction (where the order parameter is small and the current that can flow through the junction is small) [80, Eqs. 22.10.7 and 22.10.9],

$$\mathrm{sn}\,(z,k)\approx\tanh z-\frac{k'^2}{4}(z-\sinh z\cosh z)\mathrm{sech}^2 z+O\left(k'^4\right), \tag{2.5.45}$$

$$\mathrm{dn}\,(z,k)\approx\mathrm{sech}\,z+\frac{k'^2}{4}(z+\sinh z\cosh z)\tanh z\,\mathrm{sech}\,z+O\left(k'^4\right), \tag{2.5.46}$$

and using the standard exponential expansions of the hyperbolic functions, the solution for the critical current density is then given by the equations:

$$J_{\mathrm{DJ}}(B_{\mathrm{app}}) = 4J_0(1-q^2)^{\frac{3}{2}}\frac{1-\sqrt{1-\tilde{s}\tilde{F}^2_{d/2}}}{\tilde{s}\tilde{v}}\exp\left(-\frac{\tilde{d}_{\mathrm{n}}}{\tilde{\xi}_{\mathrm{n}}}\right), \tag{2.5.47}$$

where

$$\tilde{F}^2_{\tilde{d}_{\mathrm{n}}/2} = \frac{\tilde{v}^2+1-\sqrt{\tilde{v}^2(2-\tilde{s})+1}}{\tilde{v}^2+\tilde{s}}, \tag{2.5.48}$$

and

$$\begin{aligned} q^2 &= \frac{\tilde{B}^2_{\mathrm{app}}\tilde{w}^2_{\mathrm{s}}}{12}, \qquad & \tilde{s} &= \frac{\tilde{\beta}_{\mathrm{n}}(1-q^2)}{(\tilde{\alpha}_{\mathrm{n}}-\frac{1}{\tilde{m}_{\mathrm{n}}}q^2)}, \\ \tilde{v} &= \tilde{m}_{\mathrm{n}}\tilde{\xi}_{\mathrm{n}}\sqrt{1-q^2}, \quad & \tilde{\xi}_{\mathrm{n}} &= \sqrt{\frac{1}{\tilde{m}_{\mathrm{n}}}\frac{1}{\left(-\tilde{\alpha}_{\mathrm{n}}+\frac{1}{\tilde{m}_{\mathrm{n}}}q^2\right)}}. \end{aligned} \tag{2.5.49}$$

Since this is the maximum current that can be passed through the junction, we refer to this as $\tilde{J}_{\mathrm{DJ}}$, the Josephson depairing current density. This result replicates the famous result from de Gennes that the critical current density through a junction depends exponentially on the barrier thickness [77].

2.5.1.6 General Solution for the Interfacial Order Parameter

If the conditions for weakly coupled junctions are not assumed, all three equations (Eq. (2.5.34), Eq. (2.5.38) and Eq. (2.5.41)) must be numerically solved self–consistently to find $\tilde{F}^2_{\tilde{l}/2}$, $\tilde{F}^2_0$ and $\tilde{F}^2_{\tilde{d}_{\mathrm{n}}/2}$. Here, we explicitly write down the general cubic solution to Eq. (2.5.41) that holds for both weakly and strongly coupled junctions,

$$\tilde{F}^2_{\tilde{d}_{\mathrm{n}}/2} = \frac{-\tilde{\alpha}_{\mathrm{n}}\tilde{m}_{\mathrm{n}}+\tilde{m}^2_{\mathrm{n}}+q^2-\tilde{m}^2_{\mathrm{n}}q^2-\tilde{m}^2_{\mathrm{n}}\sqrt{\mathcal{Z}}}{\tilde{m}_{\mathrm{n}}\left(-\tilde{\beta}_{\mathrm{n}}+\tilde{m}_{\mathrm{n}}\right)}, \tag{2.5.50}$$

where we have defined the argument of the square root as

$$\begin{aligned} \mathcal{Z} = &\left(1-q^2-\frac{\tilde{\alpha}_{\mathrm{n}}\tilde{m}_{\mathrm{n}}-q^2}{\tilde{m}^2_{\mathrm{n}}}\right)^2-\left(1-\frac{\tilde{\beta}_{\mathrm{n}}}{\tilde{m}_{\mathrm{n}}}\right)\left[\left(2(1-q^2)-\tilde{F}^2_{\tilde{l}/2}\right)\tilde{F}^2_{\tilde{l}/2}\right. \\ &\left.+\frac{\tilde{F}^2_0}{\tilde{m}_{\mathrm{n}}}\left(2\left(-\tilde{\alpha}_{\mathrm{n}}+\frac{q^2}{\tilde{m}_{\mathrm{n}}}\right)+\tilde{\beta}_{\mathrm{n}}\tilde{F}^2_0\right)+2\langle\tilde{J}_{\mathrm{app}}\rangle^2_y\left(\frac{1}{\tilde{F}^2_{\tilde{l}/2}}-\frac{1}{\tilde{F}^2_0}\right)\right]. \end{aligned} \tag{2.5.51}$$

This equation is the generalisation of Eq. (2.5.48). Again, this has a singularity when $\tilde{m}_{\mathrm{n}} = \tilde{\beta}_{\mathrm{n}}$. In this limit, the interfacial order parameter solution now reads

$$\tilde{F}^2_{\tilde{d}_{\mathrm{n}}/2} = \frac{\mathcal{T}_1-\mathcal{T}_2}{2\tilde{F}^2_{\tilde{l}/2}\tilde{F}^2_0(1-\tilde{\alpha}_{\mathrm{n}})}, \tag{2.5.52}$$

where we have defined the terms on the numerator as:

$$\mathcal{T}_1 = \tilde{F}^2_{\tilde{l}/2}\tilde{F}^2_0\left[(2\left(1-q^2\right)-\tilde{F}^2_{\tilde{l}/2})\tilde{F}^2_{\tilde{l}/2}+\tilde{F}^2_0\left(\tilde{F}^2_0-2\tilde{\alpha}_{\mathrm{n}}\left(1-\frac{q^2}{\tilde{\alpha}_{\mathrm{n}}}\right)\right)\right], \tag{2.5.53}$$

$$\mathcal{T}_2 = 2\left(\tilde{F}^2_{\tilde{l}/2}-\tilde{F}^2_0\right)\langle\tilde{J}_{\mathrm{app}}\rangle^2_y. \tag{2.5.54}$$

Notably, this represents a generalization of the work of FBH to include the case of strongly coupled junctions. This formalism provides a complete description of the interfacial order parameter in the presence of both an applied magnetic field and an applied transport current, for arbitrary normal barrier junction properties. Some example variations are shown in Figs. 2.8 and 2.9. Moreover, for any set of material parameters and applied magnetic field and transport current, there is a *unique* value of $\tilde{F}^2_{\tilde{l}/2}$, $\tilde{F}^2_0$ and $\tilde{F}^2_{\tilde{d}_{\mathrm{n}}/2}$ that satisfy the boundary conditions.

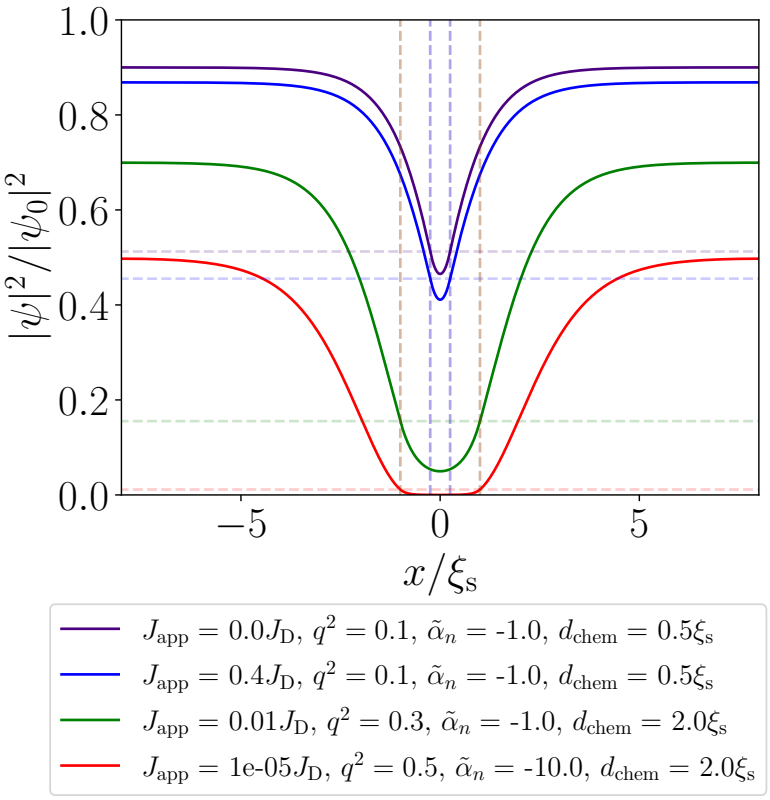

Figure 2.8: Spatial variation of the order parameter magnitude solutions presented in Eq. (2.5.34), Eq. (2.5.38) and Eq. (2.5.52). In all calculations, $\tilde{m}_n = 1.0$. The indigo/blue lines differ only by the presence of an applied current, demonstrating how the transport current affects the numerical solution. The green and red lines demonstrate the solutions for other arbitrary material parameter, including different fields, transport currents, and material parameters.

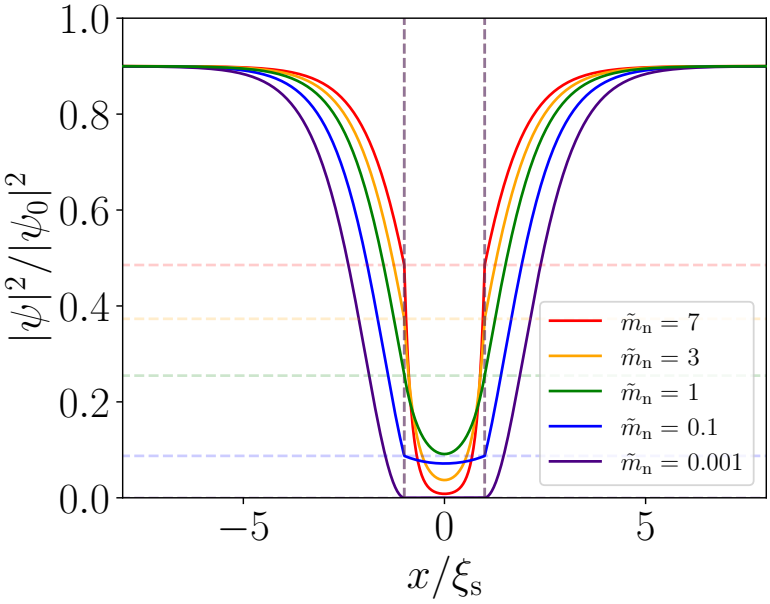

Figure 2.9: Spatial variation of the order parameter magnitude solutions presented in Eq. (2.5.34), Eq. (2.5.38) and Eq. (2.5.50), for a range of normal barrier masses/resistivities, $\tilde{m}_n$. For all calculations, the transport current is zero, $q^2 = 0.1$, $\tilde{\alpha}_n = -1.0$ and $d_n = 2.0\xi_s$.

2.5.2 Clem – Narrow Systems ($\xi_s < w_s < \lambda_s$)

The previous section was concerned with very narrow systems, where the width was sufficiently smaller than the coherence length and no fluxons could enter the system anywhere. If we consider narrow systems, where $\xi_s < w_s < \lambda_s$, then vortices are able penetrate the normal barrier even in very low fields. Naturally, the barrier itself is a normal material, with only a weak superconducting state due to the proximity effect. It is natural that this barrier is therefore easier for fluxons to penetrate into. By considering the gauge invariant GL equations in Section 2.3.6 and studying the voltage across the junction in low fields and currents (such that the phase is affected, but the magnitude of the order parameter remains unchanged), Josephson famously proposed his relation [95]

$$J = J_{\mathrm{DJ}} \sin\left(\Delta\gamma(\tilde{y})\right). \tag{2.5.55}$$

This formulation is written in terms of the phase difference across the junction, since only the difference in the phase of the order parameter is meaningful [93]. This equation provides a local expression for the supercurrent flowing across the junction at a given point y – here, $\Delta\gamma(\tilde{y})$ denotes the difference in the gauge invariant phase across the junction.

Full 2D solutions for this gauge invariant phase difference (GIPD) are provided by Clem [72]. Integrating Eq. (2.3.43) across the thickness of the junction provides an equation for the GIPD,

$$\Delta\gamma(\tilde{y}) = \theta(\tilde{d}_{\mathrm{n}}/2, \tilde{y}) - \theta(-\tilde{d}_{\mathrm{n}}/2, \tilde{y}) - \int_{-\tilde{d}_{\mathrm{n}}/2}^{\tilde{d}_{\mathrm{n}}/2} A_x \,\mathrm{d}x\,. \tag{2.5.56}$$

Here, θ is the typical phase of the wavefunction, which is not gauge invariant. Since the supercurrent is antisymmetric on each side of the junction, this phase is also antisymmetric, and hence Eq. (2.5.56) is rewritten to read

$$\Delta\gamma(\tilde{y}) = 2\theta(\tilde{d}_{\mathrm{n}}/2, \tilde{y}) - \int_{-\tilde{d}_{\mathrm{n}}/2}^{\tilde{d}_{\mathrm{n}}/2} A_x \,\mathrm{d}x\,. \tag{2.5.57}$$

Clem them solves for θ in the superconducting electrode by making the gauge choice $\tilde{\boldsymbol{A}} = -\tilde{B}_{\mathrm{app}}\tilde{y}\hat{\boldsymbol{x}}$ and imposing charge neutrality ($\tilde{\boldsymbol{\nabla}} \cdot \tilde{\boldsymbol{J}}_{\boldsymbol{s}} = 0$). Making the assumption of low coherence length results in Laplace's equation with the boundary conditions of zero supercurrent across the interfaces:

$$\tilde{\boldsymbol{\nabla}}^2\theta = 0, \tag{2.5.58}$$

$$\left.\frac{\partial\theta(\tilde{x},\tilde{y})}{\partial y}\right|_{\tilde{y}=\tilde{w}_s/2} = 0, \qquad \left.\frac{\partial\theta(\tilde{x},\tilde{y})}{\partial y}\right|_{\tilde{y}=-\tilde{w}_s/2} = 0, \tag{2.5.59}$$

$$\left.\frac{\partial\theta(\tilde{x},\tilde{y})}{\partial x}\right|_{\tilde{x}=\tilde{d}_{\mathrm{n}}/2} = -\tilde{B}_{\mathrm{app}}\tilde{y}, \qquad \left.\frac{\partial\theta(\tilde{x},\tilde{y})}{\partial x}\right|_{\tilde{x}=\tilde{l}_{\mathrm{s}}+\tilde{d}_{\mathrm{n}}/2} = -\tilde{B}_{\mathrm{app}}\tilde{y}. \tag{2.5.60}$$

The corresponding solution is found using separation of variables. Since it is a harmonic equation, the general solution of Laplace's equation is a product of hyperbolic and trigonometric functions [96]. With the odd inhomogeneous Neumann boundary conditions (Eq. (2.5.59)), the solution is written as a general series solution:

$$\theta(\tilde{x},\tilde{y}) = \sum_{n=0}^{\infty} \left[A_n \cosh(k_n x) + B_n \sinh(k_n x)\right] \sin\left(k_n \tilde{y}\right), \tag{2.5.61}$$

where

$$k_n = \frac{2\pi(n+1/2)}{\tilde{w}_s}. \tag{2.5.62}$$

The remaining Fourier coefficients are constrained by using remaining inhomogenous boundary conditions in Eq. (2.5.60). The particular solution is then given as

$$\theta(\tilde{x},\tilde{y}) = \frac{4\tilde{B}_{\rm app}}{\tilde{w}_s}\sum_{n=0}^{\infty}\frac{(-1)^{n+1}}{k_n^3}\frac{\sinh\left(k_n(\tilde{x}-\frac{\tilde{l}_s+\tilde{d}_n}{2})\right)}{\cosh\left(k_n\frac{\tilde{l}_s}{2}\right)}\sin\left(k_n\tilde{y}\right). \tag{2.5.63}$$

Inserting this phase result into Eq. (2.5.57) leads to the result

$$\Delta\gamma(\tilde{y}) = \Delta\gamma(0) + \tilde{B}_{\rm app}\tilde{y}\tilde{d}_n + \frac{8\tilde{B}_{\rm app}}{\tilde{w}_s}\sum_{n=0}^{\infty}\frac{(-1)^n}{k_n^3}\tanh\left(k_n\frac{\tilde{l}_s}{2}\right)\sin\left(k_n\tilde{y}\right). \tag{2.5.64}$$

Since the current is divergenceless ($\tilde{\boldsymbol{\nabla}}\cdot\tilde{\boldsymbol{J}}_{\boldsymbol{s}} = 0$), the spatial variation of the 2D supercurrent can be expressed as the curl of a stream function, $\tilde{\boldsymbol{J}}_{\boldsymbol{s}} = \tilde{\boldsymbol{\nabla}}\times\tilde{\boldsymbol{S}}$. From the phase solution in Eq. (2.5.63), a suitable stream function is given by Clem [72]: $\tilde{\boldsymbol{S}} = \tilde{S}(\tilde{x},\tilde{y})\hat{\boldsymbol{z}}$ where $\tilde{S}(\tilde{x},\tilde{y})$ is defined as [72]

$$\tilde{S}(\tilde{x},\tilde{y}) = \frac{\tilde{B}_{\rm app}}{2}\left|\tilde{\psi}\right|^2\left[\tilde{y}^2 + \frac{8}{\tilde{w}_s}\sum_{n=0}^{\infty}\frac{(-1)^{n+1}}{k_n^3}\frac{\cosh\left(k_n(\tilde{x}-\frac{\tilde{l}_s+\tilde{d}_n}{2})\right)}{\cosh\left(k_n\frac{\tilde{l}_s}{2}\right)}\cos\left(k_n\tilde{y}\right)\right]. \tag{2.5.65}$$

The most useful contribution arises when one utilises the result of the GIPD in the Josephson relation. Clem showed that the maximum current occurs when $\Delta\gamma(0) = \pm\pi/2$, and so the Josephson relation now reads

$$J_c(B) = \frac{1}{\tilde{w}_s}\lim_{\Delta\gamma(0)=\pm\pi/2}\left|\int_{-\tilde{w}_s/2}^{\tilde{w}_s/2} J_{\rm DJ}\left(\tilde{y}\right)\sin(\Delta\gamma(\tilde{y}))\,{\rm d}\tilde{y}\right|. \tag{2.5.66}$$

Physically, this is equivalent to shifting the fluxons around inside the junction until the net current across the junction is maximimzed. The beauty of the Clem formalism is that the oscillations in the magnetic field dependence of the critical current density are naturally captured, representing fluxons entering the junction system. The material parameters ($\tilde{\alpha}_n$, $\tilde{\beta}_n$, $\tilde{m}_n$) have no effect on the gauge invariant phase difference across the junction; all the material parameters are contained within $J_{\rm DJ}$, which is described in the FBH formulation in Section 2.5.1.

Eqs. (2.5.64) and (2.5.66) demonstrate that the spatial variation of the screening current and the resulting critical current density is very dependent on the aspect ratio of the superconducting electrode, l_s/w_s. Notably, when $l_s \ll w_s$ (i.e. the aspect ratio is small), the gauge invariant phase difference in Eq. (2.5.64) becomes linear in y. Physically, the vortices in the junction are equally spaced, and the magnetic field dependence of the critical current follows the familiar Fraunhofer diffraction [72],

$$J_c(B) = J_{\rm DJ}\left|\frac{\sin\left(\frac{\pi\Phi}{\phi_0}\right)}{\frac{\pi\Phi}{\phi_0}}\right|, \quad \text{where} \quad \Phi = \tilde{l}_s\tilde{w}_s\tilde{B}_{\rm app}. \tag{2.5.67}$$

In this limit, the field spacing between fluxons entering the junction ΔB are the identical, and given by the zeros of the Fraunhofer pattern: $\Delta B = \phi_0/\tilde{l}_s\tilde{w}_s$. Taking the limit where $\tilde{w}_s \to 0$ reproduces the very narrow results as seen in Section 2.5.1.

There is a clear optical analogy, where light is diffracted in a single slit to give a similar modulation of the light intensity; this pattern has been repeatedly observed experimentally [97].

Completely different behaviour is observed when the aspect ratio is large, i.e. $l_\mathrm{s} \gg w_\mathrm{s}$. In the limit that $l_\mathrm{s}/w_\mathrm{s} \to \infty$, the magnetic dependence can be approximated by a Bessel function solution,

$$J_\mathrm{c}(B) = J_\mathrm{DJ}\left|J_0\left(\frac{14\zeta(3)\tilde{B}_\mathrm{app}\tilde{w}_\mathrm{s}^2}{\pi^2\phi_0}\right)\right|. \tag{2.5.68}$$

Here, J_0 is the zeroth order Bessel function of the first kind and $\zeta(3)$ is Apéry's constant, where ζ is the Riemann zeta function. Here, the zeroes of the critical current are set by the well–known zeros the the Bessel function, but are not equally spaced, but approach a limiting value as $\tilde{B}_\mathrm{app} \to \infty$.

For arbitrary widths with insulating coatings, Blair–Hampshire carried over the standard narrow junction result for insulators (Eq. 2.5.47) and used

$$q^2 = \left(\frac{\tilde{B}_\mathrm{app}}{B^*_\mathrm{c2}}\right)^2. \tag{2.5.69}$$

In the case of normal coatings where $B^*_\mathrm{c2} = B_\mathrm{c2}$, they assumed

$$q^2 = \left(\frac{\tilde{B}_\mathrm{app}}{B_\mathrm{c2}}\right) \tag{2.5.70}$$

is a more appropriate form. This provides good agreement with results in literature from Abrikosov and Boyd, suggesting that the critical current in infinitely wide thin films is approximately $J_\mathrm{c} \simeq (1 - B_\mathrm{app}/B^*_\mathrm{c2})\, J_\mathrm{D}$.

Finally, we summarise the interior boundary conditions on the order parameter in Table 2.2. If one used the Abrikosov field approximation (rather than assuming that the field is uniformly the applied field), then the limiting values of the order parameter in the bulk of the electrode would be the appropriate values taken from this table. However, in typical systems where κ is large, and so the difference is the order parameter magnitude is proportional to $1/\beta_A \simeq 0.862$. This is important when considering very narrow or wide junctions – in a wide system, the field in the bulk of the electrode is not B_app. The internal field is lower than this due to screening and the averaging over the fluxons is captured through Abrikosov's work in Eq. (2.3.34).

2.5.2.1 FBH for Zero–Mass Normal Barriers

Finally, we address the limit of FBH with normal barriers of zero–mass (FBHZM), which will prove useful in future chapters. Eqs. (2.5.34), (2.5.38), and (2.5.50) are solved together to find self–consistent solutions for the magnitude of the order parameter with the specific parameters of $\tilde{\alpha}_\mathrm{n}$, $\tilde{B}_\mathrm{app}$ and $\tilde{J}_\mathrm{app}$ in the limit where $\tilde{m}_\mathrm{n} \to 0$. We use the form of q^2 in Eq. (2.5.69) with $B^*_\mathrm{c2} = B_\mathrm{c2}$. These zero–mass solutions are zero at the interface, with zero gradient. The limiting value in the bulk is then approximately $1 - \tilde{B}_\mathrm{app}$. Some examples are shown in Fig. 2.10.

2.6 Conclusions

In this section, we have built up the fundamental Ginzburg–Landau theory that is used as the backbone of this thesis. We have demonstrated how GL theory can be used to

Variable	Very Narrow	Wide
Length scale	w_s	a_0
Reduced field, q^2	$\left(\dfrac{B}{B^*_{\mathrm{c}2}}\right)^2$	$\dfrac{B}{B_{\mathrm{c}2}}$
AOPM, $F_{\tilde{l}/2}$	$\dfrac{\lvert\alpha_\mathrm{n}\rvert}{\beta_\mathrm{n}}\left(1-\left(\dfrac{B}{B^*_{\mathrm{c}2}}\right)^2\right)$ [60, Eq. 4.52]	$\dfrac{m}{\mu_0 e\hbar}\dfrac{B_{\mathrm{c}2}-B}{(2\kappa^2-1)\beta_\mathrm{A}}$ [53, Eq. 8.78]
HF–NAOPM, $\tilde{F}_{\tilde{l}/2}$	$1-\left(\dfrac{B}{B^*_{\mathrm{c}2}}\right)^2$	$\dfrac{2\kappa^2}{(2\kappa^2-1)\beta_\mathrm{A}}\left(1-\dfrac{B}{B_{\mathrm{c}2}}\right)$
LF–NAOPM, $\tilde{F}_{\tilde{l}/2}$	1	1
HF–RFNAOPM, $\tilde{\mathcal{F}}_{\tilde{l}/2}$	1	$\left\lvert\dfrac{2\kappa^2}{(2\kappa^2-1)\beta_\mathrm{A}}\right\rvert$
LF–RFNAOPM, $\tilde{\mathcal{F}}_{\tilde{l}/2}$	1	1

Table 2.2: Boundary conditions for the interior of the superconductor electrode, for a very narrow and a wide electrode. We provide expressions for the averaged order parameter magnitude squared (AOPM), the normalised order parameter magnitude squared (NAOPM) and the field–reduced NAOPM (FRNAOPM), as defined in Eq. (2.5.9). Expressions are given in both high–field (HF) and low–field (LF). Here, $\beta_\mathrm{A} = 1.16$ is the Abrikosov constant, derived by Kleiner [53].

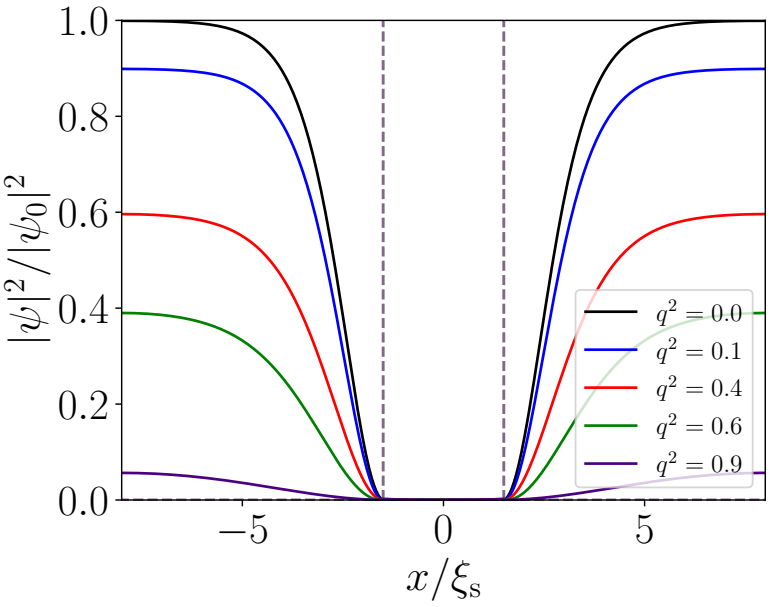

Figure 2.10: Spatial variation of the order parameter magnitude solutions presented in Eq. (2.5.34), Eq. (2.5.38) and Eq. (2.5.50), in the limit of zero–mass normal barriers, for a range of reduced field values, q^2. At the normal barrier, the gradient is zero; the order parameter magnitude is zero at the interface and throughout the normal region. For all calculations, the transport current is zero, $\tilde{m}_\mathrm{n} = 1 \times 10^{-3}$, $\tilde{\alpha}_\mathrm{n} = -10.0$ and $d_\mathrm{n} = 3.0\xi_\mathrm{s}$.

build our understand of the behaviour of superconductivity near interfaces, and how we can extract useful properties such as the critical current density. More relevant for real systems, we have outlined how GL theory can help us understand the building block of a polycrystalline superconductor – the Josephson junction. Many of the

results derived from GL theory have been shown to match experimental observations, despite materials being extremely far away from the limit close to the transition temperature [71, 74, 98, 99, 100, 101, 102]. In preparation for future chapters, we have presented our original derivations of previously obtained analytic results – we have derived the work of Saint James [78], Fink–Blair–Hampshire [74, 75] and Clem [72]. We note that many assumptions were made in the derivations for each analytic framework, and it is clear that some of these assumptions are unphysical for a real polycrystalline material; correcting and extending these analytic theories will be the focus of Chapter 4. First, we will see how we utilise the theory developed in this section to computationally model the time evolution of these Josephson junction systems.

Chapter 3

Numerical Methods For Modelling Superconductors

3.1 Introduction

Although GL theory (discussed in Chapter 2) can provide insights into simple geometries, it is difficult to derive useful results for real systems. Practical materials contain pinning landscapes that are much more complex than what can be described analytically, including point impurities and vacancies, networks of grain boundaries, and non–superconducting inclusions. Therefore, to understand real commercial materials, such as Nb_3Sn or REBCO, computational techniques must be utilised to solve these systems numerically.

The original Ginzburg–Landau equations consider only the case of thermodynamic equilibrium. Time–dependent Ginzburg–Landau (TDGL) theory is a natural generalization, and has been used for over 60 years to study the dynamic evolution of vortex structure in real systems [103, 104, 105]. It provides the temporal and spatial variation of the observable parameters, such as the superelectron density, the supercurrent flow and the magnetic field distributions. More relevant for commercial applications, it allows for the visualisation of the interaction of fluxons with pinning sites, and the effect this has on limiting parameters such as the critical current density [106]. Finite difference, finite element and finite volume approximations of TDGL theory have been used in many different studies [107, 108, 109, 110]. The finite element method (FEM) has an advantage in handling complex geometries, making use of smaller and unstructured mesh elements for higher accuracy and greater flexibility in irregularly shaped regions with steep gradients [111]. Moreover, it also allows adaptive mesh refinement and element–wise calculations, providing more efficient use of computational resources [111]. However, commercial FEM solvers (e.g. COMSOL) are typically closed-source, and identifying algorithmic error can be difficult. More importantly, FEM simulations for large 3D domains are extremely computationally expensive, even with the availability of HPC and massively parallel computing architecture. Therefore, finite difference approximations have been widely used for developing solvers of the TDGL equations within the wider research community [106], and has formed the backbone for computational research in this group [75, 84, 112, 113, 114, 115, 116, 117, 118].

In this chapter, we first outline the generalisation of GL theory to describe the time evolution of the superconducting state. We then briefly outline the main

computational solver used in this thesis – a general 2D semi–implicit CPU–based solver, where the material parameters ($\tilde{\alpha}_\mathrm{n}$, $\tilde{\beta}_\mathrm{n}$, $\tilde{m}_\mathrm{n}$) can vary spatially throughout the system. We note here that the computational foundations used in this thesis were previously developed by Blair – the details are more thoroughly described in his work [114, 115, 75]. We will describe the typical outputs of this solver, and how one can use it to usefully understand real polycrystalline materials, such as measuring the critical current density of real systems. Finally, we will briefly describe the limitations of this solver, and how one might overcome these limitations in order to understand larger and more realistic systems.

3.2 Time–Dependent Ginzburg–Landau Theory

GL theory was first extended to include time dependence by Schmidt in 1966 [103]. The validity of TDGL theory is far narrower than its original static counterpart; not only must we remain close to the critical temperature, but also require that deviations from equilibrium are suitably small – this is typically only achieved in gapless superconductors, where the relaxation process of the order parameter is slow compared to the characteristic electronic energy scales of the system [61]. The phenomenological form of TDGL theory is not unique in the literature [119]. Some other formulations have attempted to extend the validity of TDGL and generalize these results to include the energy gap and formally extend the range of validity of the TDGL equations [120, 121, 122, 123]. Nevertheless, the original formulation from Schmidt [103] has enjoyed much usage and success in investigating vortex dynamics of in both gapless and gapped superconductors in the mixed state [124].

To motivate the TDGL equations, an additional phenomenological parameter Γ is introduced, which parameterises how rapidly the order parameter relaxes into the equilibrium state from small perturbations from its equilibrium. The rate of relaxation depends on the deviation magnitude, and one can write [125]

$$-\Gamma\left(\frac{\partial}{\partial t}-\frac{iq}{\hbar}\varphi\right)\psi=\frac{\delta F_s}{\delta\psi^*}. \tag{3.2.1}$$

The term involving the scalar potential φ is required to maintain gauge invariance, and we recognise the right-hand side as the static first GL equation, given in Eq. (2.3.5) [126]. The generalisation for the supercurrent term accounts for the fact that a fraction of the current may be produced by normal electrons in the presence of an electric field. Hence, we can simply write a complete expression for the current as $\boldsymbol{J}_\mathrm{tot}=\boldsymbol{J}_\mathrm{s}+\boldsymbol{J}_\mathrm{n}+\boldsymbol{J}_\mathrm{app}$, where $\boldsymbol{J}_\mathrm{s}$ is the supercurrent defined in Eq. (2.3.7) and the normal current density $\boldsymbol{J}_\mathrm{n}$ is given by Ohm's Law [61],

$$\boldsymbol{J}_\mathrm{n}=\sigma_\mathrm{n}\boldsymbol{E}=-\sigma_\mathrm{n}\left(\frac{\partial\boldsymbol{A}}{\partial t}+\boldsymbol{\nabla}\varphi\right). \tag{3.2.2}$$

Here, σ_n is the normal-state conductivity [127]. Therefore, we can write down the normalized TDGL equations [103, 106, 114, 128]:

$$\eta\left(\frac{\partial}{\partial\tilde{t}}+i\tilde{\varphi}\right)\tilde{\psi}=\left[\frac{1}{\tilde{m}_\mathrm{n}}(\tilde{\boldsymbol{\nabla}}-i\tilde{\boldsymbol{A}})^2+\tilde{\alpha}_\mathrm{n}-\tilde{\beta}_\mathrm{n}\left|\tilde{\psi}\right|^2\right]\tilde{\psi}, \tag{3.2.3}$$

$$\frac{\partial\tilde{\boldsymbol{A}}}{\partial\tilde{t}}+\tilde{\boldsymbol{\nabla}}\tilde{\varphi}=-\kappa^2\tilde{m}_\mathrm{n}\tilde{\boldsymbol{\nabla}}\times\tilde{\boldsymbol{\nabla}}\times\tilde{\boldsymbol{A}}+\mathrm{Im}\left[\tilde{\psi}^*(\tilde{\boldsymbol{\nabla}}-i\tilde{\boldsymbol{A}})\tilde{\psi}\right], \tag{3.2.4}$$

where the parameter η is the ratio of characteristic time scales for the evolution of the electromagnetic field and the order parameter, $\eta=\Gamma/\tau$, which follows from the normalisations defined in Table 2.1.

3.3 2D Semi–Implicit TDGL Solver

The discretization has been thoroughly described in previous work [75, 116]. We shall outline the essential components here. In the limit of zero electric potential the TDGL equations are written in the form:

$$\eta\frac{\partial\tilde{\psi}}{\partial\tilde{t}} = \left[\frac{1}{\tilde{m}_{\mathrm{n}}}(\tilde{\boldsymbol{\nabla}} - i\tilde{\boldsymbol{A}})^2 + \tilde{\alpha}_{\mathrm{n}} - \tilde{\beta}_{\mathrm{n}}\left|\tilde{\psi}\right|^2\right]\tilde{\psi}, \tag{3.3.1}$$

$$\frac{\partial\tilde{\boldsymbol{A}}}{\partial\tilde{t}} = -\kappa^2\tilde{m}_{\mathrm{n}}\tilde{\boldsymbol{\nabla}}\times\tilde{\boldsymbol{\nabla}}\times\tilde{\boldsymbol{A}} + \mathrm{Im}\left[\tilde{\psi}^*(\tilde{\boldsymbol{\nabla}} - i\tilde{\boldsymbol{A}})\tilde{\psi}\right]. \tag{3.3.2}$$

The discretization of the TDGL equations still requires the preservation of gauge invariance – since without this, numerical instabilities and artefacts can arise that do not satisfy basic conservation laws, creating unphysical mechanisms in the discretized approximation [129]. Blair uses a modified version of the semi–implicit finite–difference spatial discretization scheme from Winiecki [130], which is based upon the explicit method from Gropp [131]. For explicit methods, the Courant–Friedrichs–Lewy (CFL) criterion must be satisfied, where the timesteps in the time evolution are inversely proportional to κ_{s} [130, 114]. In real materials, where κ_{s} may be large, the numerical calculations become prohibitively expensive – therefore, semi–implicit methods are much preferred for modelling useful polycrystalline superconductors. In order to retain gauge invariance, both the Gropp and Winiecki algorithms introduce an auxiliary vector field, $\boldsymbol{U}$. These are known as 'link variables', and provide a discretization of the vector potential $\boldsymbol{A}$.

We now briefly outline the spatial discretization used by Blair which includes spatial variation of the effective mass [115]. We shall consider only a 2D system, but this TDGL solver could simply be extended to 3D. The original 'U–ψ' method from Gropp defines the set of link variables U^x and U^y, and then evolves the set of $\{U, \psi\}$ [131]. Gropp introduces the unimodular link variables which can be written as [131]

$$\begin{aligned} U^x &= \exp\left(-i\int_{\tilde{x}_0}^{\tilde{x}}\tilde{A}^x(\tilde{x}', \tilde{y}, \tilde{z})\,\mathrm{d}\tilde{x}'\right), \\ U^y &= \exp\left(-i\int_{\tilde{y}_0}^{\tilde{y}}\tilde{A}^y(\tilde{x}, \tilde{y}', \tilde{z})\,\mathrm{d}\tilde{y}'\right), \end{aligned} \tag{3.3.3}$$

where $\{\tilde{x}_0, \tilde{y}_0\}$ are arbitrary reference points. The unimodularity of the link variables ($\overline{U} = U^{-1}$) provides an expression for the vector potential in the x-direction, $\tilde{A}^x$, as

$$\tilde{A}^x = \frac{1}{2i}\left(U^x\frac{\partial\overline{U}^x}{\partial\tilde{x}} - \overline{U}^x\frac{\partial U^x}{\partial\tilde{x}}\right), \tag{3.3.4}$$

with a similar expression for $\tilde{A}^y$. The vector potential is therefore expressed in terms of these link variables U, and the TDGL equations are rewritten in terms of these variables. Using the definition of the link variables, one obtains the relation

$$U^x\frac{\partial\overline{U^x}}{\partial x} = -\overline{U^x}\frac{\partial U^x}{\partial x}, \tag{3.3.5}$$

and making use of Eq. (3.3.4) allows the gauge derivative to be written in these link variables as [130]

$$\left(\tilde{\boldsymbol{\nabla}} - i\tilde{\boldsymbol{A}}\right)\tilde{\psi} = \sum_{\mu}\overline{U}^{\mu}\frac{\partial}{\partial\mu}\left(U^{\mu}\tilde{\psi}\right)\hat{\boldsymbol{e}}_{\mu}. \tag{3.3.6}$$

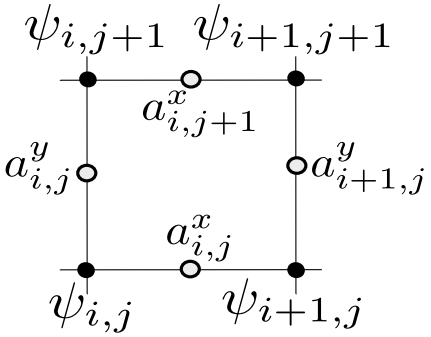

Figure 3.1: A unit cell used for TDGL computations. The order parameter is calculated on the discretized nodes (solid circles), whilst the link variables are defined on points halfway between nodes (open circles). The magnetic field in this cell is given by Eq. (3.3.12).

Here, μ is the set of spatial directions; $\mu = \{x, y\}$. The discretization of the kinetic term (the gauge invariant Laplacian) is then written as [130]

$$\left(\tilde{\boldsymbol{\nabla}} - i\tilde{\boldsymbol{A}}\right)^2 \tilde{\psi} = \sum_{\mu} \overline{U}^{\mu} \frac{\partial^2}{\partial \mu^2} \left(U^{\mu} \tilde{\psi}\right). \tag{3.3.7}$$

A schematic of a single cell of a discretized grid is shown in Fig. 3.1. The simulation space is first discretized in the x and y directions into a grid of nodes points, $\boldsymbol{r}_{i,j}$, where $i \in [1, n_x]$ and $j \in [1, n_y]$. These points are separated by spacing h_x and h_y respectively. The order parameter is calculated on each of these nodes, while these link variables are defined on points in–between these nodes. Each node has a specified set of material properties ($\tilde{\alpha}_{\mathrm{n}}$, $\tilde{\beta}_{\mathrm{n}}$ and η); the effective mass, $\tilde{m}_{\mathrm{n}}$, is defined on links between nodes along with the link variables. The discretized variables are written as [130]:

$$\tilde{\psi}_{i,j} = \tilde{\psi}\left(\boldsymbol{r}_{i,j}\right), \quad \tilde{\alpha}_{i,j} = \tilde{\alpha}_{\mathrm{n}}\left(\boldsymbol{r}_{i,j}\right), \quad \tilde{\beta}_{i,j} = \tilde{\beta}_{\mathrm{n}}\left(\boldsymbol{r}_{i,j}\right), \tag{3.3.8}$$

$$U^x_{i,j} = \overline{U}^{\mu}\left(\boldsymbol{r}_{i,j}\right) U^{\mu}\left(\boldsymbol{r}_{i,j} + h_x \hat{\imath}\right), \quad U^y_{i,j} = \overline{U}^{\mu}\left(\boldsymbol{r}_{i,j}\right) U^{\mu}\left(\boldsymbol{r}_{i,j} + h_y \hat{\jmath}\right). \tag{3.3.9}$$

The discretized effective mass in each direction is taken to be the average over the link [115]:

$$\begin{aligned} \left(\tilde{m}^{-1}_{i,j}\right)^x &= \frac{1}{h_x} \int_{\boldsymbol{r}_{i,j}}^{\boldsymbol{r}_{i,j} + \hat{\imath} h_x} \tilde{m}^{-1}_{xx} \, \mathrm{d}x, \\ \left(\tilde{m}^{-1}_{i,j}\right)^y &= \frac{1}{h_y} \int_{\boldsymbol{r}_{i,j}}^{\boldsymbol{r}_{i,j} + \hat{\jmath} h_y} \tilde{m}^{-1}_{yy} \, \mathrm{d}y. \end{aligned} \tag{3.3.10}$$

Winiecki uses a set of modified, but closely related, link variables. Instead of evolving the set of link variables $\boldsymbol{U}$ directly, he instead uses the modified link variables a [130],

$$\begin{aligned} a^x_{i,j} &= \int_{\boldsymbol{r}_{i,j}}^{\boldsymbol{r}_{i,j} + \hat{\imath} h_x} A^x(x', y, z) \, \mathrm{d}x', \\ a^y_{i,j} &= \int_{\boldsymbol{r}_{i,j}}^{\boldsymbol{r}_{i,j} + \hat{\jmath} h_y} A^y(x, y', z) \, \mathrm{d}y'. \end{aligned} \tag{3.3.11}$$

The original link variables in Eq. (3.3.3) can be written as the exponential of a real phase; $\{U\} = \{\exp\{-ia\}\}$. Using these real-valued modified link variables is less memory intensive than the original Gropp method since a complex-valued link variable must be represented by two real numbers. The electric field and magnetic

fields may be calculated from these link variables [114], given by

$$\begin{aligned} E^x_{i,j} &= -\frac{1}{h_x}\partial_t a^x_{i,j}, \quad E^y_{i,j} = -\frac{1}{h_y}\partial_t a^y_{i,j}, \\ B^z_{i,j} &= \frac{1}{h_x h_y}\left(a^x_{i,j} - a^x_{i,j+1} - a^y_{i,j} + a^y_{i+1,j}\right). \end{aligned} \tag{3.3.12}$$

The TDGL equations are now spatially discretized using second–order central differences in space. Using Eq. (3.3.7) and the modified link variables in Eq. (3.3.3), the first TDGL equation (Eq. (3.3.1)) is then spatially discretized as

$$\begin{aligned} \eta\frac{\partial\tilde{\psi}_{i,j}}{\partial\tilde{t}} &= \left(\tilde{\alpha}_{i,j} - \tilde{\beta}_{i,j}\left|\tilde{\psi}_{i,j}\right|^2\right)\tilde{\psi}_{i,j} \\ &+ \frac{1}{h_x^2}\left[\left(\tilde{m}^{-1}_{i-1,j}\right)^x e^{ia^x_{i-1,j}}\tilde{\psi}_{i-1,j} + \left(\left(\tilde{m}^{-1}_{i-1,j}\right)^x + \left(\tilde{m}^{-1}_{i,j}\right)^x\right)\tilde{\psi}_{i,j} + \left(\tilde{m}^{-1}_{i,j}\right)^x e^{-ia^x_{i,j}}\tilde{\psi}_{i+1,j}\right] \\ &+ \frac{1}{h_y^2}\left[\left(\tilde{m}^{-1}_{i,j-1}\right)^y e^{ia^y_{i,j-1}}\tilde{\psi}_{i,j-1} + \left(\left(\tilde{m}^{-1}_{i,j-1}\right)^y + \left(\tilde{m}^{-1}_{i,j}\right)^y\right)\tilde{\psi}_{i,j} + \left(\tilde{m}^{-1}_{i,j}\right)^y e^{-ia^y_{i,j}}\tilde{\psi}_{i,j+1}\right]. \end{aligned} \tag{3.3.13}$$

Making use of the field definition in Eq. (3.3.12) and vector identities, the two components of the second TDGL equation (Eq. (3.3.2)) are discretized as

$$\begin{aligned} \frac{\partial a^x_{i,j}}{\partial\tilde{t}} =& \operatorname{Im}\left[\tilde{\psi}^*_{i,j}e^{-ia^x_{i,j}}\tilde{\psi}_{i+1,j}\right] \\ &+ \kappa^2\left(\tilde{m}^{-1}_{i,j}\right)^x\left[a^x_{i,j+1} - 2a^x_{i,j} + a^x_{i,j-1} - a^y_{i+1,j} + a^y_{i,j} + a^y_{i+1,j-1} - a^y_{i,j-1}\right], \end{aligned} \tag{3.3.14}$$

$$\begin{aligned} \frac{\partial a^y_{i,j}}{\partial\tilde{t}} =& \operatorname{Im}\left[\tilde{\psi}^*_{i,j}e^{-ia^y_{i,j}}\tilde{\psi}_{i,j+1}\right] \\ &+ \kappa^2\left(\tilde{m}^{-1}_{i,j}\right)^y\left[a^y_{i+1,j} - 2a^y_{i,j} + a^y_{i-1,j} - a^x_{i,j+1} + a^x_{i,j} + a^x_{i-1,j+1} - a^x_{i-1,j}\right]. \end{aligned} \tag{3.3.15}$$

In all computational simulations considered in this thesis, ghost points are used to implement boundary conditions. These ghost points are not in the real computational domain; they are simply artificial points introduced to enforce the boundary condition in the finite difference approximation [132]. Periodic boundary conditions are implemented in the x–direction by introducing ghost points at 0 and $n_x + 1$ – this is equivalent to imposing the following conditions on the order parameter and the link variables [114, 130]:

$$\begin{aligned} \tilde{\psi}_{0,j} &= \tilde{\psi}_{n_x,j}, \quad \tilde{\psi}_{n_x+1,j} = \tilde{\psi}_{1,j}, \\ a^x_{0,j} &= a^x_{n_x,j}, \quad a^x_{n_x+1,j} = a^x_{1,j}, \\ a^y_{0,j} &= a^y_{n_x,j}, \quad a^y_{n_x+1,j} = a^y_{1,j}. \end{aligned} \tag{3.3.16}$$

Similarly, for the boundary conditions in the y–direction, insulating boundary conditions at the computational edge, which allow the applied field and the transport current to be easily imposed [75, 132]. The system is first initialized in the Meissner state ($\tilde{\psi} = 1$, $\tilde{B} = 0$) for reproducibility of simulations.

For evolving this set of variables forward in time, a modified Crank–Nicolson scheme is used [133], using a fixed time step, δt in units of τ [75]. However, since these equations are non–linear, an iterative method must be employed at each timestep. In real systems of interest, $\kappa^2 \gg \eta^-1$, and so the timescale for the evolution of the link variables is much shorter than the evolution of the order parameter. Therefore, a block Gauss–Seidel approach is applied to iteratively solve the fully coupled system [132].

The original application in Winiecki [130] solved for $\{\tilde{\psi}, a^x, a^y\}$ in three iterations at each timestep. The evolution of $\tilde{\psi}$ can be solved quickly using cyclic tridiagonal

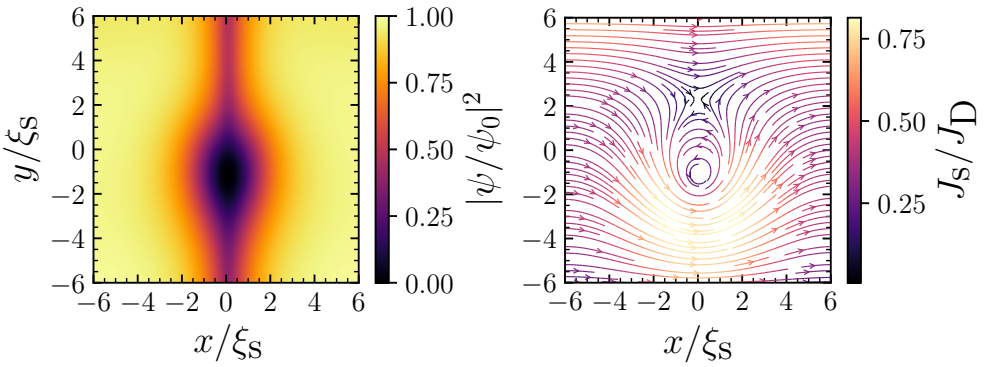

Figure 3.2: A snapshot of normalized order parameter magnitude (left) and supercurrent density (right) in a SNS junction with insulating boundary conditions at $B_{app} = 0.05B_{c2}$, $J_{app} = J_c = 0.415J_D$. The TDGL parameters are $l = w = 12.0\xi_s$, $d_{chem} = 0.5\xi_s$, $\tilde{\alpha}_n = -1.0$, $\tilde{m}_n = 1.0$, $\tilde{\beta}_n = 1.0$, $\kappa = 40.0$, $\delta t = 0.5\tau$ and $h_x = h_y = 0.1\xi_s$.

matrix and banded tridiagonal matrix solvers, for which efficient solution methods are available (e.g. the Sherman—Morrison algorithm provided in LAPACK) [132]. Since the evolution of $\{a^x, a^y\}$ are of similar magnitudes, this can lead to oscillatory behaviour of the iteration scheme with a block Gauss–Seidel approach and unreliability of convergence [114]. The modified Crank–Nicolson scheme instead solves for $\{a^x, a^y\}$ in a single step [114, 115, 75], making use of direct sparse matrix solvers such as the Intel MKL PARDISO solver [134]. For a given timestep, the order parameter is updated first, assuming all other variables unchanged from previous timestep. Then the link variables, $\{a^x, a^y\}$, are updated using the new $\tilde{\psi}$. The set of variables $\{\tilde{\psi}, a^x, a^y\}$ are continually iterated at each timestep until each variable has converged to within a specified absolute tolerance (set to 10^{-7} within this work).

In previous work [130], only a single iteration for each of $\{\tilde{\psi}, a^x, a^y\}$ was calculated at each timestep. For each of these iterations, fast tridiagonal matrix solvers can be used, that take $\mathcal{O}(n)$ steps to solve for the unknown link variables, where n is the number of links. In this case, the oscillatory behaviour and poor convergence of the block Gauss–Seidel approach can lead to the accumulation of numerical error, and therefore produces a decreased accuracy of the simulations [75]. In the limit of large κ, this error is negligible, since the link variables are determined by the applied magnetic field to first order, In this limit, the applied field is uniform, and so the oscillatory behaviour becomes negligible compared to the absolute tolerance. In general, we cannot assume that real materials are in this limit, and therefore we must solve for $\{a^x, a^y\}$ in one step directly. These direct solvers require, at worst, $\mathcal{O}(n^2)$ steps to solve [132] – this significantly limits the scalability of this method to 3–dimensions where there are many links to solve for. However, for our applications, this method is sufficient for studying the fundamental building block of a polycrystalline superconductor.

3.4 Computational Outputs

By allowing the spatial variation of all material parameters, one can arbitrarily create a mesh of superconducting/non–superconducting regions, and thus build a representation of real polycrystalline superconductors. In Fig. 2.7, we show an SNS Josephson junction system, used to model grain boundaries – one could also study other systems of interest, such as the inclusion of artificial pinning centres (i.e. a

bulk superconducting region with non–superconducting inclusions). For our SNS systems of interest, the computational system is defined in the region $x \in [-l/2, l/2]$, $y \in [-w/2, w/2]$, where $l = l_\mathrm{s} + d_\mathrm{n}$ and $w = w_\mathrm{s} + 2w_\mathrm{coat}$. Equiaxed grains have $w_\mathrm{s} = l_\mathrm{s}$.

The outputs from the methodology include the spatial dependence of the order parameter and the magnetic vector potential. These provide visualizations of useful physical phenomena, such as fluxon motion within the junction and the associated changes in the supercurrents. A snapshot of these outputs for a typical SNS system is shown in Fig. 3.2. Despite the transport critical current density being only $0.4J_\mathrm{D}$, the magnitude of the local supercurrent densities can be as large as $0.8J_\mathrm{D}$. The presence of the Josephson vortex itself within the junction causes large additional local current flows. The vortex itself is distorted within the junction, extending into a region much wider than the chemical thickness. Here, the junction is relatively thin and strongly coupled – we will see later in Chapter 5 how the properties of the junction affects the distribution of fluxons inside it.

As seen in Fig. 2.7, both the applied magnetic field (B_app) and applied transport current (J_app) are set by setting the local magnetic field at the edges of computational domain in the y–direction. The transport current in the x–direction is then set through Maxwell's equations from the magnetic field gradient in the y–direction across the system[106]. Both physically and computationally, the superconductor makes no distinction between a current–induced field or an externally applied magnetic field. Most significantly, representative values of the critical current density of the computational system can be extracted.

As discussed earlier, the system is initialized in the Meissner state. We slowly increase the applied field at a specified ramp rate, until it reaches the specified field of interest. To obtain a value for J_c, we then slowly increase the transport current and monitor the average electric field in the x direction within the system, $\langle \tilde{E}_x \rangle$ [106]. We apply Ekin's offset criterion method [135]; if $\langle \tilde{E}_x \rangle$ exceeds a critical electric field $\tilde{E}_\mathrm{c}$, then the system is held at this applied current value for a predetermined duration, t_hold, to allow transient effects to equilibriate. If the electric field persists beyond the duration of the hold time, then we interpret this as persistent fluxon motion — the critical current density, $\tilde{J}_\mathrm{c}$, is taken as the applied current density at this point. A typical simulation of both E and J as a function of time is shown in Fig. 3.3. Here, we can see the characteristic behaviour of a simulation. The field ramp at the start of the simulation leads to large electric fields generated in the system, which quickly dissipate as the specified field is reached, and an equilibrium state is achieved. As the transport current is applied, causing a change in the local magnetic field. This causes a transient spike in the electric field as the system is perturbed out of its equilibrium state, but again, these fields dissipate as the system reaches equilibrium. This creates an oscillatory behaviour in the average E–field as a function of time. Occasionally, the next step in the current is enough to cause a flux avalanche in the system – this was seen to occur twice in Fig. 3.3, at approximately 12,000 and 32,000 timesteps. However, this movement was not persistent; the system has found a new equilibrium state and the transient electric field dies down to below the criterion. As the applied current is increased even further, eventually, a current is found that causes a persistent electric field above the criterion – at this point, flux flow occurs where vortices are no longer pinned and free to move in the system, leading to a resistive and dissipative current flow and the breakdown of the superconducting state. These

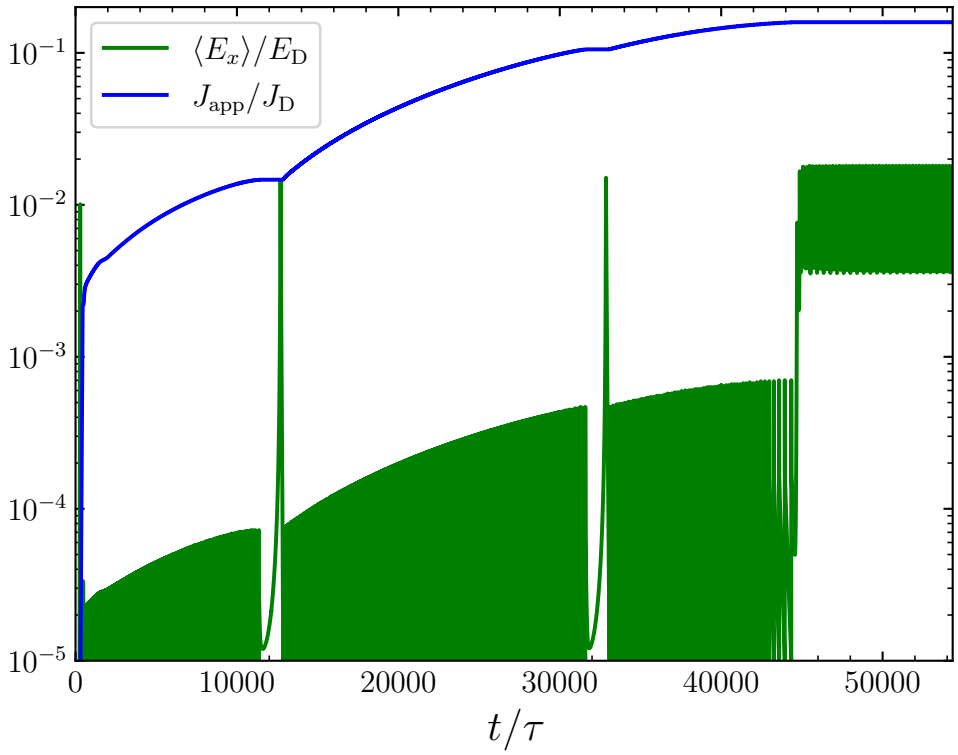

Figure 3.3: Normalised average electric field, $\langle \tilde{E}_x \rangle$, and normalised external applied current, $\tilde{J}_{app}$, as a function of normalised time for a typical TDGL simulation. The critical current density is determined when the electric field exceeds an electric field criterion ($E_c = 1 \times 10^{-5} E_D$) for a duration exceeding a specified hold time ($t_{hold} = 1 \times 10^4 \tau$). The applied current is constant during this hold time to allow the system to equilibriate. The TDGL parameters here are for a slab system with $B_{app} = 0.3 B_{c2}$, $l = w = 12.0\xi_s$, $\kappa = 5.0$, $\delta t = 0.1\tau$ and $h_x = h_y = 0.5\xi_s$.

observations are the motivation for using a hold time – we need to ensure that the applied current is truly the critical current, rather than just a transient spike as the system reequilibriates.

We can repeat this approach for any applied field, and therefore produce a trace of the critical current density as a function of applied magnetic field – an example simulation for an SNS junction system in the low–field regime is shown in Fig. 3.4. Here, we can observe the diffraction pattern of the magnetic field dependence of the critical current density, as described in Section 2.5.2. As $\tilde{\alpha}_n \to -\infty$, the junction becomes more weakly coupled and flux is able to enter the junction more easily. Because the in–field critical current density is the most important technological property, these $J_c(B)$ plots will become the focus of our analysis in Chapter 5.

3.5 Conclusions and Potential Improvements

In this chapter, we have described the computational methods used within this thesis to solve the TDGL equations in a 2D system, based on the algorithms described in [75]. Notably, we have identified limitations in previous fast and scalable solvers ([130]) that motivated the algorithm described in [75]. This algorithm improved convergence by solving for all components of the magnetic vector potential simultaneously using direct matrix solvers at each iteration, at the expense of scalability of the solver with system size. We briefly note that it is important to note the importance of choosing the grid

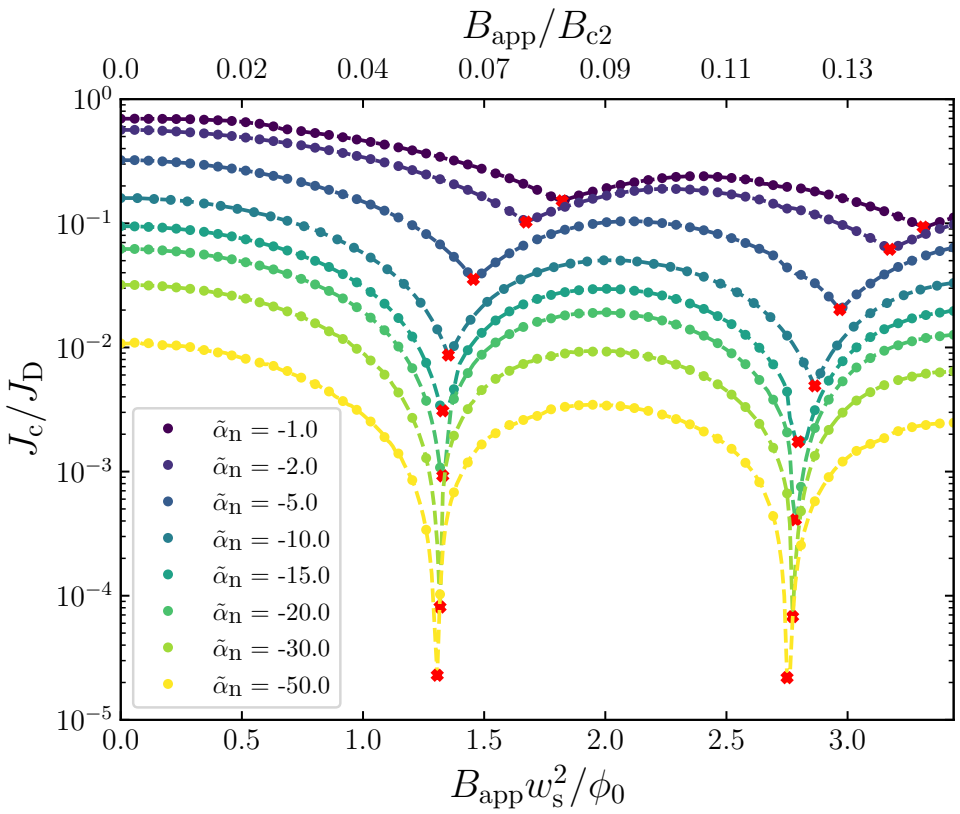

Figure 3.4: Critical current density as a function of applied magnetic field for a range of $\tilde{\alpha}_{\mathrm{n}}$ values in a SNS junction system with insulating boundary conditions. The TDGL parameters are $l = w = 12.0\xi_{\mathrm{s}}$, $d_{\mathrm{chem}} = 0.5\xi_{\mathrm{s}}$, $\tilde{m}_{\mathrm{n}} = 1.0$, $\tilde{\beta}_{\mathrm{n}} = 1.0$, $\kappa = 40.0$, $\delta t = 0.5\tau$ and $h_x = h_y = 0.1\xi_{\mathrm{s}}$. Red crosses denote the minima of J_c.

spacing carefully – if the resolution is too coarse (e.g. h_x and h_y are much larger than the normal coherence length), then the simulation is not able to accurately capture physics changing on these length scales [136]; these errors can be extremely large, and without careful consideration, could significantly alter the output of the simulations.

We note that Sadovskyy has developed a fast and scalable GPU–accelerated algorithm in the high κ limit, where the field distribution inside a superconductor is uniform and the two TDGL equations are simplified by neglecting the dynamics of the vector potential [128]. The concept of working in this limit has been known for decades [137], and has been used with great success to computationally model polycrystalline superconductors in both 2D and 3D [128, 75, 117]. Although the simplifications provided in the high κ limit lead to solvers which are efficient to model larger 3D systems, they are inherently restricted in the systems they can accurately model. Other methods of obtaining a similar computational performance for large 3D systems with general material parameters, such as multigrid methods [118], have been considered, but achieving a suitable performance in these solvers is complex. Nevertheless, Haddon has successfully implemented a multigrid TDGL solver for general material parameters (including finite κ_{s}) in the Coulomb gauge. Specifically, the multigrid method solves for the order parameter, the scalar potential and the vector potential, and can allow for much finer grids and stricter tolerances to be studied. For high resolution simulations, where the tolerance was set to be 10^{-10}, previous single grid methods such as the algorithm in [128] can take many thousands of iterations to reach convergence – the multigrid method converges in approximately 10

iterations. Not only is the accuracy of the simulations substantially increased, but the clocktime of the simulations is also significantly reduced [118], allowing simulations of realistic NbTi microstructure with realistic material parameters in large 3D systems.

We have described how the vortex state in the superconductor can be evolved in time with variable applied magnetic field and transport current. We have demonstrated the outputs of the solver, and in particular, have outlined how the critical current density may be extracted from these simulations using well–known experimental criteria. In the next chapters, we shall utilise the TDGL solver described here to investigate different Josephson junction systems of different material parameters and geometries. We will validate our computational results against textbook analytic results, such as the spatial distribution of the order parameter and the effective upper critical field. Most importantly, we will first computationally investigate the critical current densities that can flow through our junction systems, and use these results as a basis to extend existing analytic results to describe the critical current density as a function of applied magnetic field for both narrow and wide Josephson junctions.

Chapter 4

Normal Surface Barriers and Coatings with Arbitrary Material Properties

4.1 Introduction

Much of the theory presented in Sections 2.4 and 2.5.1 addressed the specific cases of superconducting–insulating interfaces. Although it is widely accepted that the resistivity of the grain boundaries is significantly higher than that of the superconducting grain [39, 83, 138], the framework presented in those sections does not account for the complexity that can occur near surfaces with finite mass.

In this chapter, we generalize the results of 1D Saint James and de Gennes to include interfaces of arbitrary mass. These results allow for a characterization of the order parameter near an interface of arbitrary materials. We provide an analytic framework to calculate the surface nucleation field or effective upper critical field ($\tilde{B}^*_{c2}$) for multicomponent geometries with normal materials with arbitrary mass. Although this has been numerically calculated in the literature [98, 139, 140], this is, to the best of our knowledge, the first analytic framework to capture the complexity near the interface. We also provide our analytic approach for determining the magnitude of the order parameter above B^*_{c2} (consistent with our TDGL computational results), and discuss an approximation to determine this constant over the entire field range. We use these results to determine the screening and Josephson depairing current density for arbitrary κ, and finally, outline the procedure we use to calculate the critical current density hereafter.

4.2 Effective Upper Critical Field for a Superconducting–Normal Interface (SN)

The systems discussed in Section 2.4.2 only considered geometries with insulating coatings. These are clearly not representative of real systems, where the resistivity of the grain boundaries is higher than the resistivity of the bulk electrode but finite [39, 83, 84]. Therefore, the proximity coupling of the normal metal to the superconductor plays a key role in the spatial variation of the order parameter and the critical current density in real materials [69, 141, 142]. This has been intensively studied both experimentally [143, 144, 145, 146, 147] and numerically (through the framework of a microscopic theory of superconductivity [148, 149]). We will use the same approach in Section 2.4.2, and solve the linearized form of

GL1 to describe the order parameter near the the normal barrier interface. We find parabolic cylinder functions in each region separately and then constrain them to ensure the order parameter magnitude and current is continuous across the interface. Crucially, we shall demonstrate that we not only capture the complex order parameter enhancement in the superconductor near the interface, but also describe the decay of the order parameter into the normal metal. This captures the proximity effect and accurately describes the order parameter variation near any arbitrary SN interface. The advantage of this framework, as shown in Section 2.4.2, is that we are then able to analytically obtain the surface nucleation field for an SN interface for arbitrary material properties.

We first consider a geometry that is similar to that described in Section 2.4.2, with an interface located at $x = 0$ and a superconducting half–plane in the region where $x > 0$. However, we shall now allow the region where $x < 0$ to be a normal metal, where the material parameters ($\tilde{\alpha}_\mathrm{n}$, $\tilde{m}_\mathrm{n}$ and $\tilde{\beta}_\mathrm{n}$) are completely arbitrary. We again consider a uniform field in the z–direction, using the same vector potential in Eq. (2.4.3), and (from symmetry) allow no current to flow across the surface, imposing the same conditions in Eqs. (2.4.6) and (2.4.7). Therefore, the wavefunction as a product of magnitude and phase is again written as in Eq. (2.4.10). Inserting this wavefunction into GL1 (Eq. (2.3.35) with arbitrary material parameters) and taking the linearized limit leads to the result

$$\frac{\partial^2 \tilde{f}}{\partial \tilde{x}^2} - \left(k_y - \tilde{B}_\mathrm{app}\tilde{x}\right)^2 \tilde{f} + \tilde{m}_\mathrm{n}\tilde{\alpha}_\mathrm{n}\tilde{f} = 0. \tag{4.2.1}$$

As before, we perform the change of variables in Eq. (2.4.12), and reduce this Weber equation to a standard form:

$$\frac{\partial^2 \tilde{f}}{\partial t^2} - \left(-\frac{\tilde{m}_\mathrm{n}\tilde{\alpha}_\mathrm{n}}{2\tilde{B}_\mathrm{app}} + \frac{1}{4}t^2\right)\tilde{f} = 0. \tag{4.2.2}$$

As in Chapter 2, Eq. (4.2.2) admits parabolic cylinder function solutions ($U(a,t)$, [80, Eq. 12.2.2]); the significant difference is that the parameter of the cylinder function, a, is now additionally dependent on the material parameters $\tilde{m}_\mathrm{n}$ and $\tilde{\alpha}_\mathrm{n}$. In particular, since $\tilde{\alpha}_\mathrm{n} = 1$ in the electrode and $\tilde{\alpha}_\mathrm{n} < 0$ in the normal region, this parameter will differ in sign between the two regions. We will find the general solutions in each region, and then constrain them to be continuous across the interface.

The solution in the superconducting electrode (where $x > 0$) is given as:

$$\tilde{f}_\mathrm{s}(\tilde{x}) = c_\mathrm{s} U(a_\mathrm{s}, t), \quad \text{where} \quad a_\mathrm{s} = -\frac{1}{2\tilde{B}_\mathrm{app}}, \tag{4.2.3}$$

where c_s is a constant prefactor. In the normal region, the solution is

$$\tilde{f}_\mathrm{n}(\tilde{x}) = c_\mathrm{n} U(a_\mathrm{n}, -t), \text{where} \quad a_\mathrm{n} = -\frac{\tilde{m}_\mathrm{n}\tilde{\alpha}_\mathrm{n}}{2\tilde{B}_\mathrm{app}}. \tag{4.2.4}$$

Note that a_n has a different sign to a_s since $\tilde{\alpha}_\mathrm{n} < 0$. Again, c_n is (at this stage) a constant prefactor, and k_y is the arbitrary phase factor.

We constrain these solutions so both the order parameter magnitudes and the supercurrent is continuous by imposing the two conditions:

$$\tilde{f}_\mathrm{n}(\tilde{x})\big|_{x=0} = \tilde{f}_\mathrm{s}(\tilde{x})\big|_{x=0}, \tag{4.2.5}$$

$$\frac{1}{\tilde{m}_\mathrm{n}}\frac{\partial \tilde{f}_\mathrm{n}^2(\tilde{x})}{\partial \tilde{x}}\bigg|_{x=0} = \frac{\partial \tilde{f}_\mathrm{s}^2(\tilde{x})}{\partial \tilde{x}}\bigg|_{x=0}. \tag{4.2.6}$$

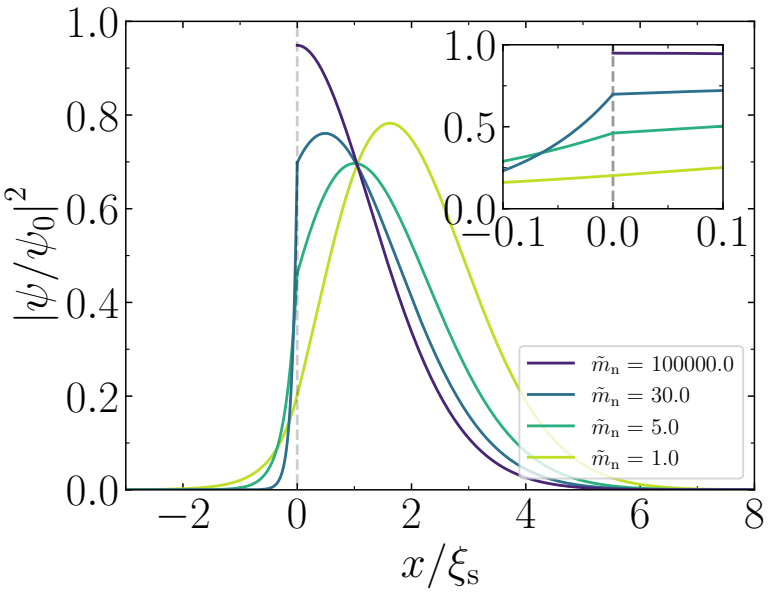

Figure 4.1: Examples of the parabolic cylinder functions (used in Eqs. (4.2.3) and (4.2.4)) with the specific value of k_y that satisfies the boundary condition (Eq. (4.2.9)), for a range of normal barrier masses. The figure inset demonstrates the behaviour close to the interface. All calculations are performed with $\tilde{B}_{\text{app}} = 0.1$ and $\tilde{\alpha}_n = -1.0$. The remaining constant prefactor has been determined by the procedure described in Section 4.3.

In the same way as in Section 2.4, one of the prefactors (c_s) is left undetermined. The first constraint of magnitude continuity (Eq. (4.2.5)) implies that

$$c_n U\left(a_n, -t_0\right) = c_s U\left(a_s, t_0\right), \tag{4.2.7}$$

where t_0 is again the spatial argument t evaluated at the interface. Therefore, by defining a variable γ, we can express c_n in terms of c_s:

$$c_n = \gamma c_s, \qquad \text{where} \qquad \gamma \equiv \frac{U\left(a_s, t_0\right)}{U\left(a_n, -t_0\right)}. \tag{4.2.8}$$

We use the second condition to constrain the phase by relating the gradients at the interface (Eq. (4.2.6)). Crucially, as in Section 2.4, this implicit equation is independent of the remaining prefactor, c_s. Making use of the chain rule and the recurrence derivative relation [80, Eq. 12.8.3], we find an implicit equation:

$$\frac{U\left(a_s, t_0\right)}{\tilde{m}_n U\left(a_n, -t_0\right)}\left[\frac{1}{2} t_0 U\left(a_n, -t_0\right) + U\left(a_n - 1, -t_0\right)\right] = \frac{1}{2} t_0 U\left(a_s, t_0\right) - U\left(a_s - 1, t_0\right). \tag{4.2.9}$$

The right hand side of this result is the same as in Section 2.4, and the previous results are clearly recovered in the limit that $\tilde{m}_n \to \infty$.

As before, this framework provides a description of the spatial variation of the order parameter. For any given value of the field and set of material parameters, there is a particular solution for k_y that satisfies the boundary condition in Eq. (4.2.9). Therefore, the order parameter is defined up to a constant prefactor by using Eqs. (4.2.3) and (4.2.4). We provide some examples of the resulting spatial variations for arbitrary mass in Fig. 4.1. Importantly, the implicit equation defined in Eq. (4.2.9) does not depend on the particular value of the remaining prefactor. This equation constrains the value of t_0 (and therefore, k_y) such that the solutions are continuous at the interface.

In principle, Eq. (4.2.9) can be used to determine the effective upper critical field for arbitrary mass. One could simply ramp up the field until no solution exists. However, we can again follow the procedure in Section 2.4 and extract a more explicit result. Again, by setting the derivative of Eq. (4.2.9) with respect to t_0 to zero and using the recurrence relation in Eq. (2.4.22), we maximize the field that allows a solution. This leads to another condition for the critical values of t_0, a_s and a_n:

$$a_{\mathrm{s,c}} + \frac{1}{4}t_{0,\mathrm{c}}^2 = \frac{1}{\tilde{m}_\mathrm{n}}\left[a_{\mathrm{n,c}} + \frac{1}{4}t_{0,\mathrm{c}}^2 - \frac{1}{2}t_0\left(\frac{U\left(a_\mathrm{n}-1,-t_0\right)}{U\left(a_\mathrm{n},-t_0\right)} + \frac{U\left(a_\mathrm{s}-1,t_0\right)}{U\left(a_\mathrm{s},t_0\right)}\right)\right. \tag{4.2.10}$$
$$\left. - \frac{U\left(a_\mathrm{s}-1,t_0\right)U\left(a_\mathrm{n}-1,-t_0\right)}{U\left(a_\mathrm{s},t_0\right)U\left(a_\mathrm{n},-t_0\right)} - \frac{U^2\left(a_\mathrm{n}-1,-t_0\right)}{U^2\left(a_\mathrm{n},-t_0\right)}\right].$$

However, since this equation contains the presence of both $U\left(a_\mathrm{s},t_0\right)$ and $U\left(a_\mathrm{n},-t_0\right)$ cylinder functions, this result unfortunately does not enjoy the same simplicity as in Section 2.4.2, where the cylinder functions precisely cancel out and an explicit solution for a_s in terms of t_0 can be identified. However, we can solve Eq. (4.2.9) and Eq. (4.2.10) numerically and identify the solutions for a_s and t_0. A comparison between TDGL and this analytic solution is shown in Fig. 4.2, and demonstrates excellent agreement. Moreover, we can see that in the limit where $\tilde{m}_\mathrm{n} \leq 1$, there is no surface sheath above $B_{\mathrm{c}2}$. In the limit where $\tilde{m}_\mathrm{n} \to \infty$, we recover the previous insulating result of $B_{\mathrm{c}3} = 1.695B_{\mathrm{c}2}$ from Saint James and de Gennes shown in Section 2.4.2.1.

The analytic results from Eq. (4.2.9) are not limited to dealing only with arbitrary mass – Fig. 4.2 demonstrates the application to a range of junction condensation parameter values. When the condensation parameter is large and negative, the elbow in the curve is much steeper; the normal material is more weakly coupled and the coherence length in this region is smaller (c.f. ξ_n, as defined in Eq. (2.5.49)); hence the system approaches the insulating limit quicker. Conversely, if the condensation parameter is smaller, the curve is broadened. Moreover, we can see that the transition begins at a higher mass for more negative condensation parameter magnitudes – Fig. 4.2 shows that the transition begins at $\tilde{m}_\mathrm{n} \simeq 11.0$ for $\tilde{\alpha}_\mathrm{n} = -10.0$. We have also checked that $\tilde{\alpha}_\mathrm{n} = -50.0$ exhibits a similar behaviour – the transition begins at $\tilde{m}_\mathrm{n} \simeq 5.0$, and is sharper than the $\tilde{\alpha}_\mathrm{n} = -10.0$ curve. We can understand this by considering the interfacial order parameter; as can be seen from Eq. (2.5.48), as $\tilde{\alpha}_\mathrm{n}$ is increased, the order parameter magnitude at the interface decreases, and therefore approaches the boundary condition for a lower mass material. As the mass is increased, then the interfacial order parameter is increased, and the sheath near interface approaches the insulating behaviour. Note that the specific value of $\tilde{\alpha}_\mathrm{n} = -1.0$ is not particularly special in any way, unlike the specific value of $\tilde{m}_\mathrm{n} = 1.0$, which serves as a demarcation between the presence/absence of surface effects. We note here that the calculation of $B_{\mathrm{c}2}^*$ does not depend on $\tilde{\beta}_\mathrm{n}$.

Instead of numerically solving Eq. (4.2.10) for the solution to a_s, we can instead find a good first approximation by taking the result of Eq. (2.4.23) (in the insulating limit). We can then insert this into the mass–dependent Eq. (4.2.9), and obtain a straightforward implicit equation in one unknown. It is then easy to numerically solve this, and therefore obtain a high mass limiting value of $\tilde{B}_{\mathrm{c}2}^*$. The results of this approximation are shown by the dashed lines in Fig. 4.2. The solid lines are the complete numerical solution, found from solving Eqs. (4.2.9) and (4.2.10) simultaneously which gives excellent agreement with TDGL data. The TDGL slab data had a thickness of $\tilde{d}_\mathrm{s} = 8.0$ – this is effectively in the semi–infinite limit, since each interface is sufficiently far away from one another such that there is no

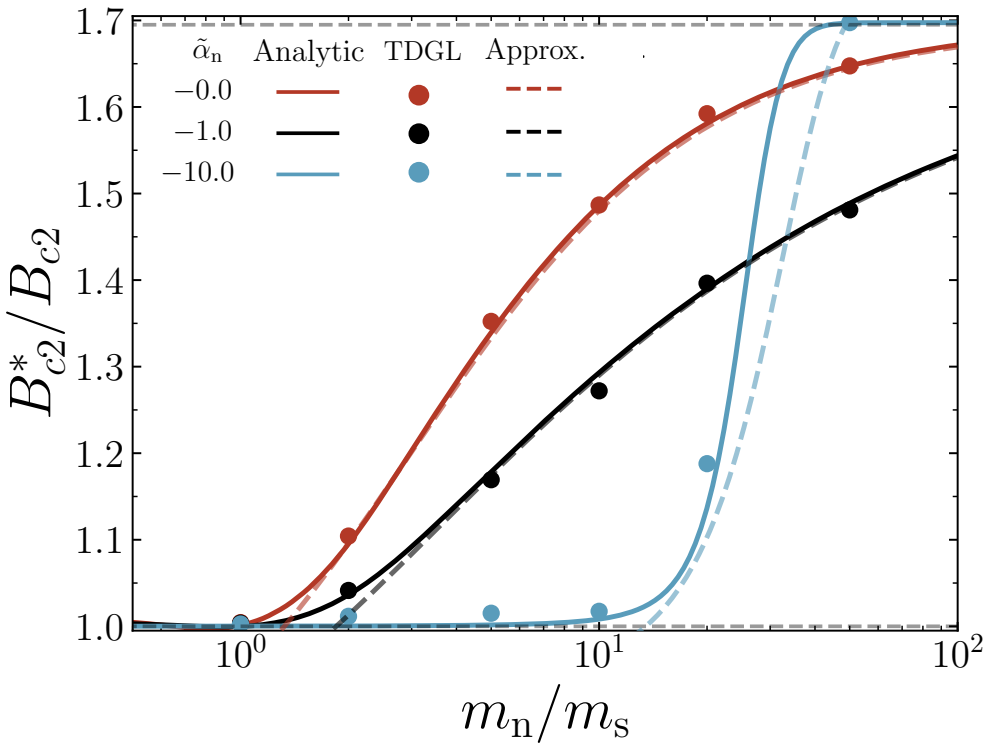

Figure 4.2: Effective upper critical field of an SN interface as a function of normal barrier mass, for a range of junction condensation parameter values, $\tilde{\alpha}_n$. The solid lines are the complete analytic results calculated from numerically solving Eqs. (4.2.9) and (4.2.10) simultaneously. The solid circles are TDGL slab data with $d_s = 8.0\xi_s$. The dashed lines are the analytic approximation obtained from inserting Eq. (2.4.23) into Eq. (4.2.9). For all TDGL simulations, $\tilde{\beta}_n = 1$.

interaction between the sheaths. We can see that, as expected, the approximation is very good when the masses are sufficiently large; here, the threshold is seen to be $\tilde{m}_n > 3.0$, and the approximation only becomes poor when $\tilde{m}_n < 2.0$. Real materials, such as Nb_3Sn, typically have grain boundaries with a resistivity of approximately $1 \times 10^{-7}\,\Omega\,m$ (although this is dependent on atomic Sn content and temperature) [150]; the ratio of the grain boundaries to grain resistivity has been found to range between 2 and 9 [151]. In microcrystalline and nanocrystalline YBCO, the ratio of grain boundary/grain resistivity is huge – it has been found to be 2×10^3 and 1.6×10^5 respectively [39]. This approximation provides a efficient way of obtaining $\tilde{B}^*_{c2}$ as a function of arbitrary material properties.

4.3 Order Parameter Magnitude – Determining the Prefactor

The framework in Section 4.2 described our approach for determining the spatial variation of the order parameter for arbitrary material parameters. The final issue preventing a complete description of the order parameter magnitude is the remaining constant prefactor. As mentioned in Section 2.4 by Saint James and de Gennes, this prefactor can only be found by solving the full non–linear equations numerically (i.e. including the cubic order parameter term). We present an analytic approach that formally captures this prefactor in the region between B_{c2} and B^*_{c2}. We will see how we can determine the remaining prefactor, c_s – this will be sufficient for any of the geometries considered in this section.

We closely follow the textbook Abrikosov approach [53, Section 8.5]. First we define

$\tilde{\psi}_{\mathrm{L}}$, the order parameter solution to the linearized GL1 equation in a generic material close to $\tilde{B}^{*}_{\mathrm{c2}}$:

$$\frac{1}{\tilde{m}_{\mathrm{n}}}\left(\tilde{\boldsymbol{\nabla}}-i\tilde{\boldsymbol{A}}_{\mathrm{c2}^{*}}\right)^{2}\tilde{\psi}_{\mathrm{L}}+\tilde{\alpha}_{\mathrm{n}}\tilde{\psi}_{\mathrm{L}}=0. \tag{4.3.1}$$

Here, we have denoted $\tilde{\boldsymbol{A}}_{\mathrm{c2}^{*}}$ as the vector potential for a magnetic field near $\tilde{B}^{*}_{\mathrm{c2}}$;

$$\tilde{\boldsymbol{A}}_{\mathrm{c2}^{*}}=\left(\tilde{B}^{*}_{\mathrm{c2}}\tilde{x}\right)\hat{\jmath}. \tag{4.3.2}$$

It is useful to define the operator $\mathcal{H}_0$, where

$$\mathcal{H}_0\tilde{\psi}_{\mathrm{L}}=0 \qquad \text{where} \qquad \mathcal{H}_0=\frac{1}{\tilde{m}_{\mathrm{n}}}\left(\tilde{\boldsymbol{\nabla}}-i\tilde{\boldsymbol{A}}_{\mathrm{c2}^{*}}\right)^{2}+\tilde{\alpha}_{\mathrm{n}}. \tag{4.3.3}$$

These are the solutions in the linearized limit, where the applied field is $\tilde{B}^{*}_{\mathrm{c2}}$. We write a general order parameter and the vector potential at some general field away from $\tilde{B}_{\mathrm{app}}$ as a small perturbation to the linearized solution:

$$\tilde{\psi}=\tilde{\psi}_{\mathrm{L}}+\tilde{\psi}_{1}, \tag{4.3.4}$$

$$\tilde{\boldsymbol{A}}=\tilde{\boldsymbol{A}}_{\mathrm{c2}^{*}}+\tilde{\boldsymbol{A}}_{1}. \tag{4.3.5}$$

Strictly, the field $\tilde{B}_{\mathrm{app}}$ should be close to $\tilde{B}^{*}_{\mathrm{c2}}$. To obtain a net applied field of $\tilde{B}_{\mathrm{app}}$, the small vector potential must be written as

$$\tilde{\boldsymbol{A}}_{1}=\left(\left(\tilde{B}_{\mathrm{app}}-\tilde{B}^{*}_{\mathrm{c2}}\right)\tilde{x}\right)\hat{\jmath}. \tag{4.3.6}$$

We note that these additional terms, $\tilde{\psi}_1$ and $\tilde{\boldsymbol{A}}_1$, are also small, and so we only include first order terms. We substitute these perturbative expansions into the full (non-linear) GL1 equation:

$$\frac{1}{\tilde{m}_{\mathrm{n}}}\left(\tilde{\boldsymbol{\nabla}}-i\tilde{\boldsymbol{A}}\right)^{2}\tilde{\psi}+\tilde{\alpha}_{\mathrm{n}}\tilde{\psi}-\tilde{\beta}_{\mathrm{n}}\left|\tilde{\psi}\right|^{2}\tilde{\psi}=0 \tag{4.3.7}$$

$$\begin{aligned}\implies &\frac{1}{\tilde{m}_{\mathrm{n}}}\left(\tilde{\boldsymbol{\nabla}}-i\left(\tilde{\boldsymbol{A}}_{\mathrm{c2}^{*}}+\tilde{\boldsymbol{A}}_{1}\right)\right)^{2}\tilde{\psi}_{\mathrm{L}}+\tilde{\alpha}_{\mathrm{n}}\tilde{\psi}_{\mathrm{L}}-\tilde{\beta}_{\mathrm{n}}\left|\tilde{\psi}_{\mathrm{L}}\right|^{2}\tilde{\psi}_{\mathrm{L}}\\ &\quad+\underbrace{\frac{1}{\tilde{m}_{\mathrm{n}}}\left(\tilde{\boldsymbol{\nabla}}-i\tilde{\boldsymbol{A}}_{\mathrm{c2}^{*}}\right)^{2}\tilde{\psi}_{1}+\tilde{\alpha}_{\mathrm{n}}\tilde{\psi}_{1}}_{\mathcal{H}_0\tilde{\psi}_1}=0\end{aligned} \tag{4.3.8}$$

$$\implies -\mathcal{H}_0\tilde{\psi}_1=\frac{1}{\tilde{m}_{\mathrm{n}}}\left(\tilde{\boldsymbol{\nabla}}-i\left(\tilde{\boldsymbol{A}}_{\mathrm{c2}^{*}}+\tilde{\boldsymbol{A}}_{1}\right)\right)^{2}\tilde{\psi}_{\mathrm{L}}+\tilde{\alpha}_{\mathrm{n}}\tilde{\psi}_{\mathrm{L}}-\tilde{\beta}_{\mathrm{n}}\left|\tilde{\psi}_{\mathrm{L}}\right|^{2}\tilde{\psi}_{\mathrm{L}}. \tag{4.3.9}$$

It is not immediately clear why this is useful, until we consider the orthonormality condition, denoted it as $\mathcal{O}$ [152]:

$$\mathcal{O}\equiv\int\tilde{\psi}^{*}_{\mathrm{L}}\mathcal{H}_0\tilde{\psi}_1\mathrm{d}^3\boldsymbol{r}=0. \tag{4.3.10}$$

This condition follows from the self–adjoint nature of the Hamiltonian operator $\mathcal{H}_0$; the solution to the homogenous equation must be orthogonal to the inhomogenous component of the differential equation. By identifying $\tilde{\psi}_{\mathrm{L}}$ as the solution to the linearized equation and $\mathcal{H}_0\tilde{\psi}_1$ as the inhomogeneous component, the two must be orthogonal in order for such a solution to exist. Therefore, using the expression for $\mathcal{H}_0\tilde{\psi}_1$, we find the orthonormality condition integral may be rewritten as:

$$\mathcal{O}=\int\tilde{\psi}^{*}_{\mathrm{L}}\left[\frac{1}{\tilde{m}_{\mathrm{n}}}\left(\tilde{\boldsymbol{\nabla}}-i\left(\tilde{\boldsymbol{A}}_{\mathrm{c2}^{*}}+\tilde{\boldsymbol{A}}_{1}\right)\right)^{2}\tilde{\psi}_{\mathrm{L}}+\tilde{\alpha}_{\mathrm{n}}\tilde{\psi}_{\mathrm{L}}-\tilde{\beta}_{\mathrm{n}}\left|\tilde{\psi}_{\mathrm{L}}\right|^{2}\tilde{\psi}_{\mathrm{L}}\right]\mathrm{d}^3\boldsymbol{r}. \tag{4.3.11}$$

Formally, this result contains all the information required [53]. However, in order to make the solution more explicit, some further manipulation is required. We rewrite the square in Eq. (4.3.11) to obtain

$$\mathcal{O}=\int\tilde{\psi}^{*}_{\mathrm{L}}\left[\frac{1}{\tilde{m}_{\mathrm{n}}}\left(\left(\tilde{\boldsymbol{\nabla}}-i\tilde{\boldsymbol{A}}_{\mathrm{c2}^{*}}\right)-i\tilde{\boldsymbol{A}}_{1}\right)^{2}\tilde{\psi}_{\mathrm{L}}+\tilde{\alpha}_{\mathrm{n}}\tilde{\psi}_{\mathrm{L}}-\tilde{\beta}_{\mathrm{n}}\left|\tilde{\psi}_{\mathrm{L}}\right|^{2}\tilde{\psi}_{\mathrm{L}}\right]\mathrm{d}^3\boldsymbol{r}=0. \tag{4.3.12}$$

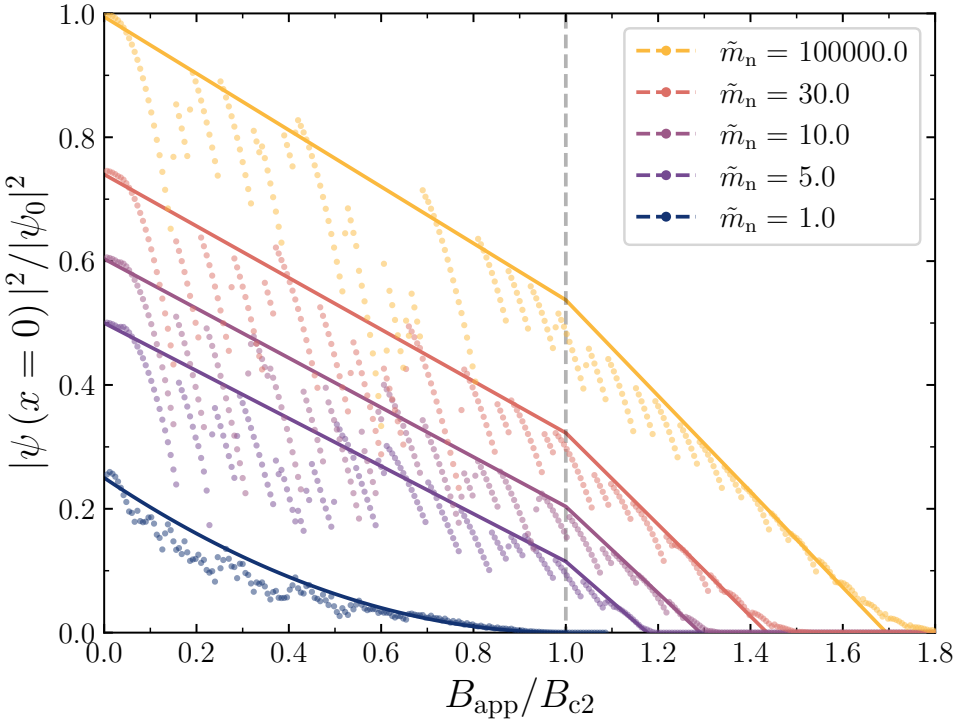

Figure 4.3: Interfacial order parameter magnitude as as function of field from TDGL data with arbitrary mass, compared to the analytic solution. We have taken a double–linear approach here; we used the rigorous approach in Eq. (4.3.22) from B^*_{c2} to B_{c2}, and then taken a linear fit down to the zero-field Fink value. When $\tilde{m}_n \leq 1$, there is no surface barrier, and so we have taken the FBH field dependent order parameter (Eq. (2.5.43)). In all simulations, we have set $\tilde{\alpha}_n = -1.0$ and $\tilde{\beta}_n = 1.0$.

Expanding the brackets and neglecting the contribution from the higher order small perturbation terms of order $\tilde{\boldsymbol{A}}_1{}^2$ yields the result

$$\mathcal{O} = \int \tilde{\psi}^*_L \left[\frac{1}{\tilde{m}_n} \left(\tilde{\boldsymbol{\nabla}} - i\tilde{\boldsymbol{A}}_{c2^*} \right)^2 \tilde{\psi}_L + \tilde{\alpha}_n \tilde{\psi}_L - \tilde{\beta}_n \left| \tilde{\psi}_L \right|^2 \tilde{\psi}_L \right. \\ \left. + \frac{-i}{\tilde{m}_n} \left\{ \left(\tilde{\boldsymbol{\nabla}} - i\tilde{\boldsymbol{A}}_{c2^*} \right) \cdot \tilde{\boldsymbol{A}}_1 \tilde{\psi}_L + \tilde{\boldsymbol{A}}_1 \cdot \left(\tilde{\boldsymbol{\nabla}} - i\tilde{\boldsymbol{A}}_{c2^*} \right) \tilde{\psi}_L \right\} \right] \mathrm{d}^3\boldsymbol{r} = 0. \tag{4.3.13}$$

We identify the first two terms as the zeroth order term in Eq. (4.3.3), $\mathcal{H}_0 \tilde{\psi}_L = 0$. Therefore, the remaining expression reads

$$\int \tilde{\psi}^*_L \left[\frac{-i}{\tilde{m}_n} \left\{ \left(\tilde{\boldsymbol{\nabla}} - i\tilde{\boldsymbol{A}}_{c2^*} \right) \cdot \tilde{\boldsymbol{A}}_1 \tilde{\psi}_L + \tilde{\boldsymbol{A}}_1 \cdot \left(\tilde{\boldsymbol{\nabla}} - i\tilde{\boldsymbol{A}}_{c2^*} \right) \tilde{\psi}_L \right\} \right] \mathrm{d}^3\boldsymbol{r} = \int \tilde{\beta}_n \left| \tilde{\psi}_L \right|^4 \mathrm{d}^3\boldsymbol{r}. \tag{4.3.14}$$

On the left hand side, we can use the chain rule on the first term and integrate by parts to identify the current density using GL2. Therefore, we obtain

$$\int 2\tilde{\boldsymbol{J}}_L \cdot \tilde{\boldsymbol{A}}_1 \mathrm{d}^3\boldsymbol{r} = \int \tilde{\beta}_n \left| \tilde{\psi}_L \right|^4 \mathrm{d}^3\boldsymbol{r}, \tag{4.3.15}$$

where $\tilde{\boldsymbol{J}}_L$ is the supercurrent associated with the linearized order parameter.

4.3.1 Solution between B_{c2} and B^*_{c2} for Arbitrary Mass

For the semi–infinite geometry considered, the only non-zero components in the LHS of Eq. (4.3.15) are in the y-direction. Explicitly using GL2 to write down the

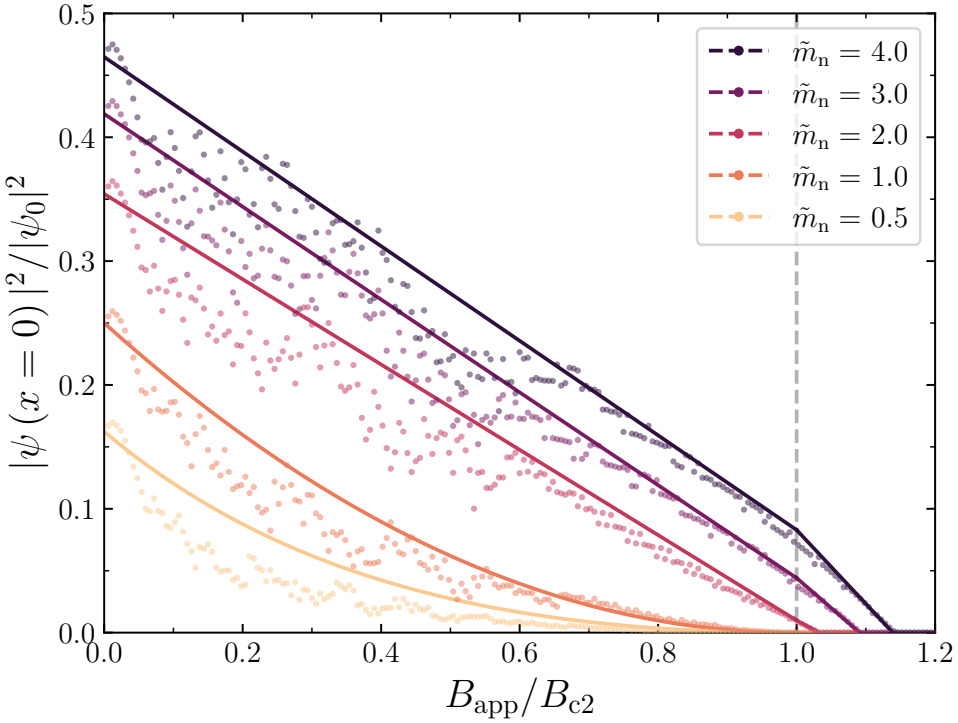

Figure 4.4: Interfacial order parameter magnitude as as function of field from TDGL data with arbitrary mass, compared to the analytic solution. We have taken a double–linear approach here; we used the rigorous approach in Eq. (4.3.22) from B^*_{c2} to B_{c2}, and then taken a linear fit down to the zero-field Fink value. When $\tilde{m}_{\mathrm{n}} \leq 1$, there is no surface barrier, and so we have taken the FBH field dependent order parameter (Eq. (2.5.42)). In all simulations, we have set $\tilde{\alpha}_{\mathrm{n}} = -1.0$ and $\tilde{\beta}_{\mathrm{n}} = 1.0$.

supercurrents in terms of the order parameter leads to the result:

$$\frac{2\left(B^*_{c2} - B_{\mathrm{app}}\right)}{\tilde{m}_{\mathrm{n}}} \int \left(k_{y,L} - B^*_{c2}\tilde{x}\right)\tilde{x}\left|\tilde{\psi}_{\mathrm{L}}\right|^2 \mathrm{d}^3\boldsymbol{r} = \int \tilde{\beta}_{\mathrm{n}}\left|\tilde{\psi}_{\mathrm{L}}\right|^4 \mathrm{d}^3\boldsymbol{r}. \tag{4.3.16}$$

Up until this point, the analysis has been independent of the specific form of the order parameter. We now define the order parameter in the linearized limit in each region as in Eq. (2.4.10):

$$\tilde{\psi}_{\mathrm{L}} = \left|\tilde{\psi}_{\mathrm{L}}\right| e^{ik_{y,\mathrm{L}}\tilde{y}}, \tag{4.3.17}$$

where we have used the cylinder function from the Saint–James derivation (Eqs. (4.2.3) and (4.2.4)) evaluated in the linear limit, near $\tilde{B}^*_{c2}$:

$$\left|\tilde{\psi}_{\mathrm{s,L}}\right| = C_{\mathrm{s}} \lim_{\tilde{B}\to\tilde{B}^*_{c2}} U\left(a_{\mathrm{s}}, t\right) \equiv C_{\mathrm{s}} U_{\mathrm{s,L}}, \tag{4.3.18}$$

$$\left|\tilde{\psi}_{\mathrm{n,L}}\right| = C_{\mathrm{n}} \lim_{\tilde{B}\to\tilde{B}^*_{c2}} U\left(a_{\mathrm{n}}, -t\right) \equiv C_{\mathrm{n}} U_{\mathrm{n,L}}. \tag{4.3.19}$$

Note that these C_{s} and C_{n} values are not the same as the c_{s} and c_{n} presented in Eqs. (4.2.3) and (4.2.4), since they include the prefactor presented in Eq. (2.4.10). The value of $k_{y,\mathrm{L}}$ is constrained by the boundary conditions in Eqs. (4.2.5) and (4.2.6), where $k_{y,\mathrm{L}}$ is treated as a constant (k_y evaluated near $\tilde{B}^*_{c2}$). Since these solutions decay to zero in the bulk, this approach is only valid above B_{c2}. Inserting this into Eq. (4.3.16) provides an explicit solution for the prefactor. Splitting the integral into

two for the electrode/normal regions respectively leads to the intermediate result:

$$2\left(B_{\mathrm{app}}-B_{\mathrm{c2}}^{*}\right)\left[\int_{0}^{\infty}\left(k_{y,\mathrm{L}}-B_{\mathrm{c2}}^{*}\tilde{x}\right)\tilde{x}\,C_{\mathrm{s}}^{2}U_{\mathrm{s,L}}^{2}\mathrm{d}\tilde{x}+\frac{1}{\tilde{m}_{\mathrm{n}}}\int_{-\infty}^{0}\left(k_{y,\mathrm{L}}-B_{\mathrm{c2}}^{*}\tilde{x}\right)\tilde{x}\,C_{\mathrm{n}}^{2}U_{\mathrm{n,L}}^{2}\mathrm{d}\tilde{x}\right] \tag{4.3.20}$$

$$=\int_{0}^{\infty}C_{\mathrm{s}}^{4}U_{\mathrm{s,L}}^{4}\mathrm{d}\tilde{x}+\tilde{\beta}_{\mathrm{n}}\int_{-\infty}^{0}C_{\mathrm{n}}^{4}U_{\mathrm{n,L}}^{4}\mathrm{d}\tilde{x}. \tag{4.3.21}$$

Again, using continuity to relate C_{s} to C_{n} as defined in Eq. (4.2.8) leads to an explicit result for C_{s}:

$$C_{\mathrm{s}}^{2}=\frac{2\left(B_{\mathrm{app}}-B_{\mathrm{c2}}^{*}\right)\left[S_{1}+\dfrac{\gamma^{2}}{\tilde{m}_{\mathrm{n}}}N_{1}\right]}{S_{2}+\tilde{\beta}_{\mathrm{n}}\gamma^{4}N_{2}}, \tag{4.3.22}$$

where we have defined the integrals

$$S_{1}=\int_{0}^{\infty}\left(k_{y,\mathrm{L}}-B_{\mathrm{c2}}^{*}\tilde{x}\right)\tilde{x}\,U_{\mathrm{s,L}}^{2}\mathrm{d}\tilde{x},\qquad N_{1}=\int_{-\infty}^{0}\left(k_{y,\mathrm{L}}-B_{\mathrm{c2}}^{*}\tilde{x}\right)\tilde{x}\,U_{\mathrm{n,L}}^{2}\mathrm{d}\tilde{x}, \tag{4.3.23}$$

$$S_{2}=\int_{0}^{\infty}U_{\mathrm{s,L}}^{4}\mathrm{d}\tilde{x},\qquad N_{2}=\int_{-\infty}^{0}U_{\mathrm{n,L}}^{4}\mathrm{d}\tilde{x}.$$

The interfacial order parameter is then found by taking this prefactor, and evaluating the cylinder function solutions at the interface ($x=0$). We have found this gives good results compared to TDGL data in the very high field regime, between B_{c2} and B_{c2}^{*} for arbitrary mass, as shown in Figs. 4.3 and 4.4.

4.3.2 Extending below B_{c2}

We also present an approximation to extend this approach to the full field range. Above B_{c2}, we have the solution from the rigorous Abrikosov approach described earlier in Section 4.3.1, providing a linear solution from B_{c2} to B_{c2}^{*}. However, below B_{c2}, we looked for solutions by first defining a generalized composite wavefunction as a sum of two contributions from the new Saint James solutions and from FBH with zero mass (ZM) (Section 2.5.2.1):

$$\tilde{\psi}=\tilde{\psi}_{\mathrm{SJ}}+\tilde{\psi}_{\mathrm{ZM}}. \tag{4.3.24}$$

Above B_{c2}, $\tilde{F}_{\tilde{l}/2}^{2}\left(\tilde{y}\right)$ is solely determined by the Saint James results (Section 4.2). The FBH solution with ZM has zero magnitude and gradient at the interface, and so does not contribute to the boundary condition of the Saint James solution. Furthermore, the limiting value in the bulk is proportional to $1-\tilde{B}_{\mathrm{app}}$, since the upper critical field for zero mass is precisely B_{c2}. Therefore this solution has no contribution above B_{c2}, and we recover the exact solution as required.

However, since the zero–mass terms do not tend to zero far away from the interface, this leads to unbounded cross terms in the additional integrals. Even if we ignore these unbounded terms (which are small close to B_{c2}), this approach still provides very poor agreement for the interfacial order parameter from TDGL, as seen in Fig. 4.6. We attribute this to the use of PCFs – clearly, the non–linear terms are now significantly important, and the solutions to the linearized equations (i.e. the PCFs) are no longer appropriate. Regardless, as we will see in Ch. 5, the use of this composite wavefunction provides excellent agreement with the spatial variation of the order parameter and the screening current.

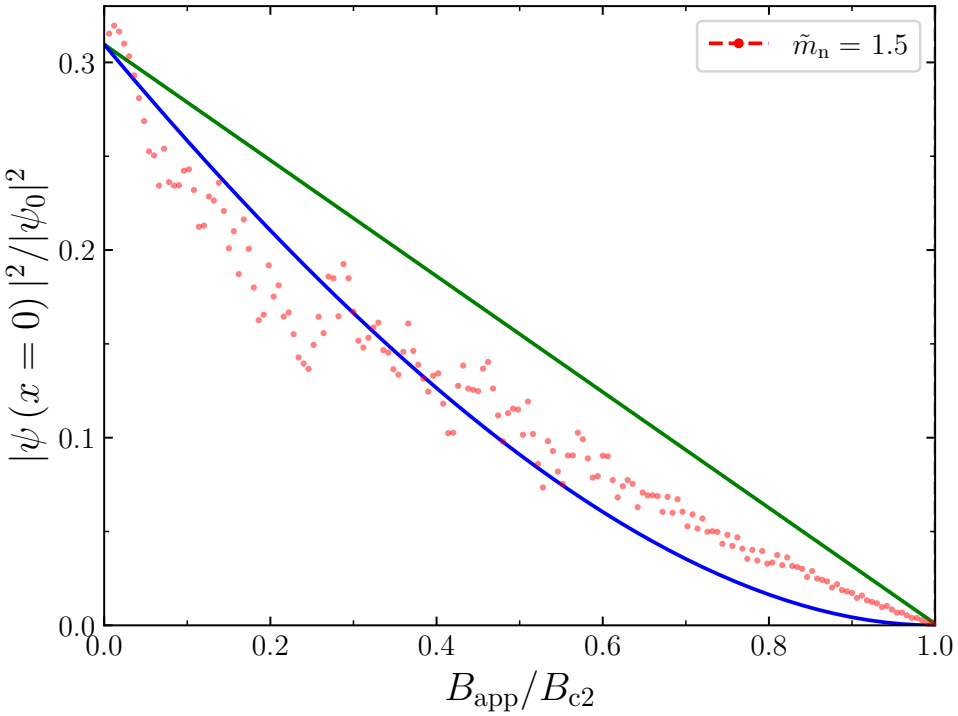

Figure 4.5: Interfacial order parameter magnitude as as function of field from TDGL data with an intermediate mass, compared to the two analytic solutions. The double–linear approach is shown in green; taking the rigorous approach in Eq. (4.3.22) from B^*_{c2} to B_{c2}, and then taken a linear fit down to the zero-field Fink value. The FBH field dependent order parameter (Eq. (2.5.42)) is shown in blue. In all simulations, we have set $\tilde{\alpha}_n = -1.0$ and $\tilde{\beta}_n = 1.0$.

Fortunately, from the TDGL data, we observe that the interfacial order parameter is broadly linear below B_{c2} as well. Since we know the precise zero–field interfacial order parameter from Fink, we propose using a simple empirical linear relationship between the value accurately calculated at B_{c2}, and the zero–field value from Fink. Therefore, we suggest a physically motivated 'double–linear' approximation, that provides two distinct regions with different gradients when the mass of the barrier is bigger than the mass of the electrode.

We note that if the mass of the barrier is less than the electrode ($\tilde{m}_n < 1.0$), then no surface barrier exists and the Saint James formalism is not appropriate for the order parameter description. In this case, we use the FBH in–field interfacial order parameter, which is shown to provide the correct non–linear field dependence. Comparisons between this approximation and TDGL is shown in Figs. 4.3 and 4.4, showing good agreement across the entire mass range. We note that the crossover is particularly sharp; when $\tilde{m}_n = 1.0$, the FBH non–linear field dependence provides a good fit, but when $\tilde{m}_n = 2.0$, the double–linear approximation is more appropriate. However, as shown in Fig. 4.5, there is a narrow range of masses ($1.0 < \tilde{m}_n < 2.0$) where neither are appropriate.

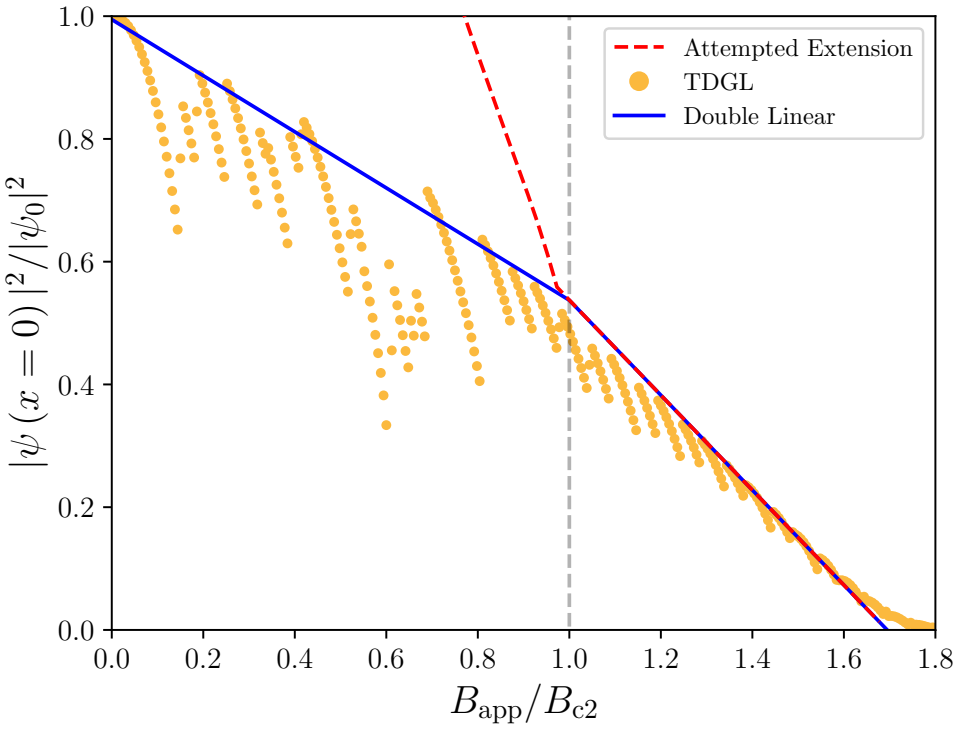

Figure 4.6: Interfacial order parameter magnitude as as function of field from TDGL data in the insulating limit, compared to the attempted extension to the analytic solution and the double–linear approach. The rigorous analytic attempt is shown as a red dashed line, using the composite wavefunction in Eq. (4.3.24) The double–linear approach is shown as the blue solid line; taking the rigorous approach in Eq. (4.3.22) from B_{c2}^{*} to B_{c2}, and then taken a linear fit down to the zero-field Fink value. In all simulations, we have set $\tilde{\alpha}_{\mathrm{n}} = -1.0$ and $\tilde{\beta}_{\mathrm{n}} = 1.0$.

4.4 Effective Upper Critical Field for a Superconducting Slab with Normal Coatings (NSN)

We now outline the derivation to describe the order parameter in a normal–superconductor–normal (NSN) system. This is an extension of the work in Section 2.4.2.2, where we considered an ISI slab geometry. Again, the superconducting slab has a finite thickness, d_{s}, is centered at $\tilde{x} = 0$, and the interfaces are located at $\tilde{x} = \pm\tilde{d}_{\mathrm{s}}/2$. However, the surrounding material in the regions $\tilde{x} > \tilde{d}_{\mathrm{s}}/2$ and $\tilde{x} < -\tilde{d}_{\mathrm{s}}/2$ is no longer a perfect insulator, but instead is a normal metal with a specified set of material parameters ($\tilde{\alpha}_{\mathrm{n}}$, $\tilde{m}_{\mathrm{n}}$ and $\tilde{\beta}_{\mathrm{n}}$). We proceed to define the solutions in each of the regions in the same way as Section 4.2. The solution in the superconducting region is [79]

$$\tilde{f}_{\mathrm{s}}(\tilde{x}) = c_{\mathrm{s1}} U\left(a_{\mathrm{s}}, t\right) + c_{\mathrm{s2}} U\left(a_{\mathrm{s}}, -t\right), \quad \text{if} \quad x \in [-d_{\mathrm{s}}/2, d_{\mathrm{s}}/2], \tag{4.4.1}$$

$$\text{where} \quad a_{\mathrm{s}} = -\frac{1}{2\tilde{B}_{\mathrm{app}}}.$$

Here, c_{s1} and c_{s2} are arbitrary constant prefactors. The solution in the normal material is

$$\tilde{f}_{\mathrm{nR}}(\tilde{x}) = c_{\mathrm{nR}} U\left(a_{\mathrm{n}}, t\right), \quad \text{if} \quad x \in [d_{\mathrm{s}}/2, \infty), \tag{4.4.2}$$

$$\tilde{f}_{\mathrm{nL}}(\tilde{x}) = c_{\mathrm{nL}} U\left(a_{\mathrm{n}}, -t\right), \quad \text{if} \quad x \in (-\infty, -d_{\mathrm{s}}/2], \tag{4.4.3}$$

$$\text{where} \quad a_{\mathrm{n}} = -\frac{\tilde{m}_{\mathrm{n}}\tilde{\alpha}_{\mathrm{n}}}{2\tilde{B}_{\mathrm{app}}}.$$

Here, c_{nL} and c_{nR} are again arbitrary prefactors (where L and R denote the left and right–hand side interfaces). The boundary conditions to constrain the behaviour at the interface are more general than the conditions for the ISI system presented in Section 2.4.2.2; we must consider not only the gradients at the interface, but also the magnitudes. Therefore, to ensure the necessary continuity of our solutions in each region, we impose the four conditions:

$$\tilde{f}_{\mathrm{nL}}\big|_{\tilde{x}=-\tilde{d}_{\mathrm{s}}/2} = \tilde{f}_{\mathrm{s}}\big|_{\tilde{x}=-\tilde{d}_{\mathrm{s}}/2}\,, \tag{4.4.4}$$

$$\tilde{f}_{\mathrm{nR}}\big|_{\tilde{x}=\tilde{d}_{\mathrm{s}}/2} = \tilde{f}_{\mathrm{s}}\big|_{\tilde{x}=\tilde{d}_{\mathrm{s}}/2}\,, \tag{4.4.5}$$

$$\frac{1}{\tilde{m}_{\mathrm{n}}}\frac{\partial \tilde{f}_{\mathrm{nL}}^2}{\partial \tilde{x}}\bigg|_{\tilde{x}=-\tilde{d}_{\mathrm{s}}/2} = \frac{\partial \tilde{f}_{\mathrm{s}}^2}{\partial \tilde{x}}\bigg|_{\tilde{x}=-\tilde{d}_{\mathrm{s}}/2}\,, \tag{4.4.6}$$

$$\frac{1}{\tilde{m}_{\mathrm{n}}}\frac{\partial \tilde{f}_{\mathrm{nR}}^2}{\partial \tilde{x}}\bigg|_{\tilde{x}=\tilde{d}_{\mathrm{s}}/2} = \frac{\partial \tilde{f}_{\mathrm{s}}^2}{\partial \tilde{x}}\bigg|_{\tilde{x}=\tilde{d}_{\mathrm{s}}/2}\,. \tag{4.4.7}$$

We have 4 boundary conditions and 5 unknowns (c_{s1}, c_{s2}, c_{nL}, c_{nR}, and k_y); as before, we will constrain k_y by finding the lowest eigenfunction (or by deriving a new equation that gives the condition for that eigenfunction, as in Eq. (4.2.10)). In addition, we have the constant prefactor that can be constrained by external means, e.g. by solving the non–linear equations or using the approach in Section 4.3.2. To explicitly follow the approach taken in the ISI system, we will:

(i) Use Eq. (4.4.4) to constrain c_{nL} in terms of c_{s1} and c_{s2},

(ii) Use Eq. (4.4.5) to constrain c_{nR} in terms of c_{s1} and c_{s2},

(iii) Use Eq. (4.4.6) to constrain c_{s2} in terms of c_{s1},

(iv) Use Eq. (4.4.7) to obtain an implicit equation for k_y (independent of c_{s1}).

We now proceed to implement these conditions in the same way as in Section 2.4.2.2. The first two conditions imposing continuity of magnitude are straightforward; we obtain:

$$c_{\mathrm{nL}} = c_{\mathrm{s1}}\frac{U\left(a_{\mathrm{s}}, t_{-\tilde{d}_{\mathrm{s}}/2}\right)}{U\left(a_{\mathrm{n}}, -t_{-\tilde{d}_{\mathrm{s}}/2}\right)} + c_{\mathrm{s2}}\frac{U\left(a_{\mathrm{s}}, -t_{-\tilde{d}_{\mathrm{s}}/2}\right)}{U\left(a_{\mathrm{n}}, -t_{-\tilde{d}_{\mathrm{s}}/2}\right)}, \tag{4.4.8}$$

$$c_{\mathrm{nR}} = c_{\mathrm{s1}}\frac{U\left(a_{\mathrm{s}}, t_{\tilde{d}_{\mathrm{s}}/2}\right)}{U\left(a_{\mathrm{n}}, t_{\tilde{d}_{\mathrm{s}}/2}\right)} + c_{\mathrm{s2}}\frac{U\left(a_{\mathrm{s}}, -t_{\tilde{d}_{\mathrm{s}}/2}\right)}{U\left(a_{\mathrm{n}}, t_{\tilde{d}_{\mathrm{s}}/2}\right)}. \tag{4.4.9}$$

The next conditions involving the derivative are more involved; similarly to Section 2.4.2.2, we shall make use of the prime notation in Eq. (2.4.29). The first gradient condition considers the system at $x = -d_{\mathrm{s}}/2$, and will constrain c_{s2}. The gradient of the normal region is straightforward:

$$\frac{\partial \tilde{f}_{\mathrm{nL}}^2}{\partial \tilde{x}}\bigg|_{\tilde{x}=-\tilde{d}_{\mathrm{s}}/2} = 2\tilde{f}_{\mathrm{nL}}\frac{\partial \tilde{f}_{\mathrm{nL}}}{\partial \tilde{x}}\bigg|_{\tilde{x}=-\tilde{d}_{\mathrm{s}}/2} = -2\sqrt{2\tilde{B}_{\mathrm{app}}}c_{\mathrm{nL}}^2 U(a_{\mathrm{n}}, -t)U'(a_{\mathrm{n}}, -t)\bigg|_{\tilde{x}=-\tilde{d}_{\mathrm{s}}/2} \tag{4.4.10}$$

$$= -2\sqrt{2\tilde{B}_{\mathrm{app}}}c_{\mathrm{nL}}^2 U\left(a_{\mathrm{n}}, -t_{-\tilde{d}_{\mathrm{s}}/2}\right)U'\left(a_{\mathrm{n}}, -t_{-\tilde{d}_{\mathrm{s}}/2}\right).$$

The gradient in the superconductor is similarly given as

$$\begin{aligned}\frac{\partial \tilde{f}_{\mathrm{s}}^2}{\partial \tilde{x}} &= 2\tilde{f}_{\mathrm{s}}\frac{\partial \tilde{f}_{\mathrm{s}}}{\partial \tilde{x}} = 2\sqrt{2\tilde{B}_{\mathrm{app}}}\tilde{f}_{\mathrm{s}}\left[c_{\mathrm{s}1}U'\left(a_{\mathrm{s}},t\right)-c_{\mathrm{s}2}U'\left(a_{\mathrm{s}},-t\right)\right] \\ &= 2\sqrt{2\tilde{B}_{\mathrm{app}}}\left[c_{\mathrm{s}1}U\left(a_{\mathrm{s}},t\right)+c_{\mathrm{s}2}U\left(a_{\mathrm{s}},-t\right)\right]\left[c_{\mathrm{s}1}U'\left(a_{\mathrm{s}},t\right)-c_{\mathrm{s}2}U'\left(a_{\mathrm{s}},-t\right)\right] \\ &= 2\sqrt{2\tilde{B}_{\mathrm{app}}}\Big[c_{\mathrm{s}1}^2U\left(a_{\mathrm{s}},t\right)U'\left(a_{\mathrm{s}},t\right)-c_{\mathrm{s}2}^2U\left(a_{\mathrm{s}},-t\right)U'\left(a_{\mathrm{s}},-t\right) \\ &\qquad +c_{\mathrm{s}1}c_{\mathrm{s}2}\left[U\left(a_{\mathrm{s}},-t\right)U'\left(a_{\mathrm{s}},t\right)-U\left(a_{\mathrm{s}},t\right)U'\left(a_{\mathrm{s}},-t\right)\right]\Big].\end{aligned} \tag{4.4.11}$$

Evaluating this result (Eq. (4.4.11)) at the interface at $x=-d_{\mathrm{s}}/2$, replacing the definition of c_{nL} (Eq. (4.4.8)) into Eq. (4.4.10), and inserting these two results back into the gradient continuity (Eq. (4.4.6)) leads to a quadratic in $c_{\mathrm{s}2}$. This has the simple solution

$$c_{\mathrm{s}2}=\frac{-b+\sqrt{b^2-4ac}}{2a}, \tag{4.4.12}$$

where

$$a=\frac{1}{\tilde{m}_{\mathrm{n}}}U'\left(a_{\mathrm{n}},-t_{-\tilde{d}_{\mathrm{s}}/2}\right)\frac{U^2\left(a_{\mathrm{s}},-t_{-\tilde{d}_{\mathrm{s}}/2}\right)}{U\left(a_{\mathrm{n}},-t_{-\tilde{d}_{\mathrm{s}}/2}\right)}-U\left(a_{\mathrm{s}},-t_{-\tilde{d}_{\mathrm{s}}/2}\right)U'\left(a_{\mathrm{s}},-t_{-\tilde{d}_{\mathrm{s}}/2}\right), \tag{4.4.13}$$

$$\begin{aligned}b=c_{\mathrm{s}1}\Big[&\frac{2}{\tilde{m}_{\mathrm{n}}}U'\left(a_{\mathrm{n}},-t_{-\tilde{d}_{\mathrm{s}}/2}\right)\frac{U\left(a_{\mathrm{s}},t_{-\tilde{d}_{\mathrm{s}}/2}\right)U\left(a_{\mathrm{s}},-t_{-\tilde{d}_{\mathrm{s}}/2}\right)}{U\left(a_{\mathrm{n}},-t_{-\tilde{d}_{\mathrm{s}}/2}\right)} \\ &-U\left(a_{\mathrm{s}},t_{-\tilde{d}_{\mathrm{s}}/2}\right)U'\left(a_{\mathrm{s}},-t_{-\tilde{d}_{\mathrm{s}}/2}\right)+U\left(a_{\mathrm{s}},-t_{-\tilde{d}_{\mathrm{s}}/2}\right)U'\left(a_{\mathrm{s}},t_{-\tilde{d}_{\mathrm{s}}/2}\right)\Big],\end{aligned} \tag{4.4.14}$$

$$c=c_{\mathrm{s}1}^2\left[\frac{1}{\tilde{m}_{\mathrm{n}}}U'\left(a_{\mathrm{n}},-t_{-\tilde{d}_{\mathrm{s}}/2}\right)\frac{U^2\left(a_{\mathrm{s}},t_{-\tilde{d}_{\mathrm{s}}/2}\right)}{U\left(a_{\mathrm{n}},-t_{-\tilde{d}_{\mathrm{s}}/2}\right)}+U\left(a_{\mathrm{s}},t_{-\tilde{d}_{\mathrm{s}}/2}\right)U'\left(a_{\mathrm{s}},t_{-\tilde{d}_{\mathrm{s}}/2}\right)\right]. \tag{4.4.15}$$

The solution can be written more transparently; by defining $b'=b/c_{\mathrm{s}1}$ and $c'=c/c_{\mathrm{s}1}^2$, we can extract an overall factor of $c_{\mathrm{s}1}$ explicitly and obtain

$$c_{\mathrm{s}2}=\gamma_{\mathrm{s}}c_{\mathrm{s}1}, \tag{4.4.16}$$

where we have defined

$$\gamma_{\mathrm{s}}=\frac{-b'+\sqrt{b'^2-4ac'}}{2a}. \tag{4.4.17}$$

We note here that the positive root is required to be taken in order to ensure that the γ_{s} is positive. Note that with this result for $c_{\mathrm{s}2}$ in Eq. (4.4.16), the previous results for c_{nL} and c_{nR} (in Eqs. (4.4.8) and (4.4.9)) are now solely determined in terms of $c_{\mathrm{s}1}$. Finally, we obtain an implicit equation for k_y using the final boundary condition in Eq. (4.4.7). The gradient in the normal region is written as

$$\begin{aligned}\left.\frac{\partial \tilde{f}_{\mathrm{nR}}^2}{\partial \tilde{x}}\right|_{\tilde{x}=\tilde{d}_{\mathrm{s}}/2} &= \left.2\tilde{f}_{\mathrm{nR}}\frac{\partial \tilde{f}_{\mathrm{nR}}}{\partial \tilde{x}}\right|_{\tilde{x}=\tilde{d}_{\mathrm{s}}/2} = \left.2\sqrt{2\tilde{B}_{\mathrm{app}}}c_{\mathrm{nR}}^2U(a_{\mathrm{n}},t)U'(a_{\mathrm{n}},t)\right|_{\tilde{x}=\tilde{d}_{\mathrm{s}}/2} \\ &= 2\sqrt{2\tilde{B}_{\mathrm{app}}}c_{\mathrm{nR}}^2U\left(a_{\mathrm{n}},t_{\tilde{d}_{\mathrm{s}}/2}\right)U'\left(a_{\mathrm{n}},t_{\tilde{d}_{\mathrm{s}}/2}\right).\end{aligned} \tag{4.4.18}$$

Squaring the result for c_{nR} in Eq. (4.4.9) and inserting the result for $c_{\mathrm{s}2}$ in Eq. (4.4.16) yields:

$$\begin{aligned}\left.\frac{\partial \tilde{f}_{\mathrm{nR}}^2}{\partial \tilde{x}}\right|_{\tilde{x}=\tilde{d}_{\mathrm{s}}/2} = 2\sqrt{2\tilde{B}_{\mathrm{app}}}c_{\mathrm{s}1}^2\frac{U'\left(a_{\mathrm{n}},t_{\tilde{d}_{\mathrm{s}}/2}\right)}{U\left(a_{\mathrm{n}},t_{\tilde{d}_{\mathrm{s}}/2}\right)}\Big[&U^2\left(a_{\mathrm{s}},t_{\tilde{d}_{\mathrm{s}}/2}\right)+\gamma_{\mathrm{s}}^2U^2\left(a_{\mathrm{s}},-t_{\tilde{d}_{\mathrm{s}}/2}\right) \\ &+2\gamma_{\mathrm{s}}U\left(a_{\mathrm{s}},t_{\tilde{d}_{\mathrm{s}}/2}\right)U\left(a_{\mathrm{s}},-t_{\tilde{d}_{\mathrm{s}}/2}\right)\Big].\end{aligned} \tag{4.4.19}$$

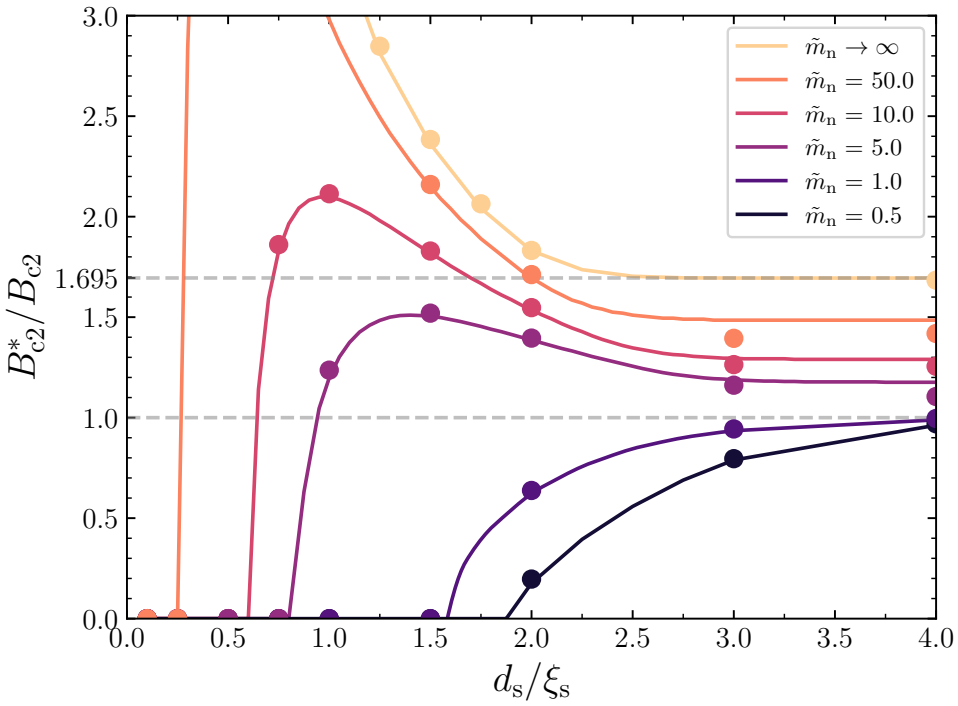

Figure 4.7: Effective upper critical field of an NSN superconducting slab as a function of the slab's thickness, for a range of normal barrier masses. The numerical lines are calculated from Eq. (4.4.7) (using Eqs. (4.4.20) and (4.4.19)). The TDGL slab data are shown as closed circles markers with $w_{\text{coat}} = 3.0\xi$. In all simulations, we have set $\tilde{\alpha}_n = -1.0$ and $\tilde{\beta}_n = 1.0$.

We have already found the gradient in the superconductor (in Eq. (4.4.11)) – evaluating this at $x = d_s/2$ and again inserting the result for c_{s2} in Eq. (4.4.16) yields:

$$\begin{aligned}\left.\frac{\partial \tilde{f}_s^2}{\partial \tilde{x}}\right|_{\tilde{x}=\tilde{d}_s/2} = 2\sqrt{2\tilde{B}_{\text{app}}}c_{s1}^2 \Big[& U\left(a_s, t_{\tilde{d}_s/2}\right) U'\left(a_s, t_{\tilde{d}_s/2}\right) \\ & -\gamma_s^2 U\left(a_s, -t_{\tilde{d}_s/2}\right) U'\left(a_s, -t_{\tilde{d}_s/2}\right) \\ & -\gamma_s U\left(a_s, t_{\tilde{d}_s/2}\right) U'\left(a_s, -t_{\tilde{d}_s/2}\right) \\ & +\gamma_s U\left(a_s, -t_{\tilde{d}_s/2}\right) U'\left(a_s, t_{\tilde{d}_s/2}\right)\Big] .\end{aligned} \tag{4.4.20}$$

Inserting these results (Eqs. (4.4.19) and (4.4.20)) into the boundary condition in Eq. (4.4.7) leads to an implicit equation that is independent of the remaining prefactor as required. We can proceed to identify the effective upper critical field, B^*_{c2}, as a function of the thickness of the superconducting slab for arbitrary mass in a similar way to Section 4.2, by identifying the lowest eigenvalue. We first note that just as in Section 2.4.2.2, Eqs. (4.4.19) and (4.4.20) contain both $t_{\tilde{d}_s/2}$ and $t_{-\tilde{d}_s/2}$; as before, these can be easily related using the definition of t, shown in Eq. (2.4.33). Therefore, by following the same process in Section 2.4.2.2, we can find the lowest eigenvalue corresponding to the effective upper critical field.

The B^*_{c2} results are shown in Fig. 4.7, demonstrating excellent agreement between TDGL data and the analytic result described above. As the thickness becomes large, we approach the same semi–infinite behaviour seen in the previous section (Section 4.2). The extreme insulating limit has been described already in Section 2.4.2.2 and seen in Fig. 2.6 – the formalism here reduces correctly in the limit that $\tilde{m}_n \to \infty$, and

our analytic form follows the inverse thickness dependence as seen from Tinkham's parallel critical field result (Eq. (2.4.34)). For $\tilde{m}_{\rm n} > 1$, where the normal barrier has a higher mass than the bulk and therefore a region of enhanced superconductivity is observed, the same intuition for Tinkham's result holds; reducing the thickness causes these enhancement regions to overlap, leading to an inverse thickness dependence for increase in $B^*_{\rm c2}$. As the superconducting region becomes infinitely thin ($d_{\rm s} \to 0$), it is clear that $B^*_{\rm c2} \to 0$, since there is no superconducting region at all. However, as can be seen from the spatial variations of the order parameter magnitude in Fig. 4.1, the breadth of the sheath increases as $\tilde{m}_{\rm n}$ decreases (i.e. the enhancement region becomes more spread out). This has a corresponding effect on the thickness dependence on $B^*_{\rm c2}$; as the thickness is decreased, $B^*_{\rm c2}$ initially increases as the sheaths overlap, but then begin to decrease as the thickness becomes very small. Both the position of this turnover (i.e. the critical thickness for the maximum $B^*_{\rm c2}$), and the sharpness of the transition are dependent on the mass, as can be seen from the $\tilde{m}_{\rm n} = 5.0$, $\tilde{m}_{\rm n} = 10.0$ and $\tilde{m}_{\rm n} = 50.0$ data in Fig. 4.7. For larger masses, since the breadth of the sheath is narrower, it remains close to the semi–infinite limit until much smaller thicknesses. Similarly, the transition as $B^*_{\rm c2} \to 0$ is sharper, since the coupling to the normal region becomes weaker and the behaviour approaches that of Tinkham's parallel critical field result (Eq. (2.4.34)).

For $\tilde{m}_{\rm n} < 1$, no such enhancement occurs. Therefore, when $\tilde{m}_{\rm n} < 1$, $B^*_{\rm c2}$ monotonically drops as the thickness is decreased. As $\tilde{m}_{\rm n} \to 0$, the order parameter at the interface approaches zero (c.f. Eq. (2.3.6)); therefore, the rate of this decrease is faster with lower masses, as can be seen from comparison of the $\tilde{m}_{\rm n} = 1$ and $\tilde{m}_{\rm n} = 0.5$ data in Fig. 4.7.

The slab results in this section naturally find use in the description of thin films with normal metal layers of arbitrary parameters. In the next section, we will apply the mathematical machinery developed here to describe the geometry more relevant to polycrystalline materials.

4.5 Effective Upper Critical Field for a Josephson Junction (SNS)

In this section, with a view to the development of our understanding of polycrystalline materials, we return to our typical Josephson junction geometry. The mathematical framework is almost identical to that considered in Section 4.4. We consider an SNS system, where the normal barrier now has a finite thickness, $d_{\rm n}$. We have three regions of interest: the left superconducting electrode, $x =\in (-\infty, -d_{\rm n}/2]$; the normal barrier, defined in $x =\in [-d_{\rm n}/2, d_{\rm n}/2]$; and the right superconducting electrode, defined in $x =\in [d_{\rm n}/2, \infty)$. The origin of the system (the centre of the normal barrier) is located as $x = 0$, and the interfaces are located at $\tilde{x} = \pm\tilde{d}_{\rm n}/2$. As usual, the normal junction has arbitrary material parameters, $\tilde{\alpha}_{\rm n}$, $\tilde{m}_{\rm n}$ and $\tilde{\beta}_{\rm n}$.

The mathematical approach is almost identical to Sections 4.2 and 4.4; in fact, one can identify a clear symmetry in the system, by exchanging $a_{\rm s} \leftrightarrow a_{\rm n}$, $c_{\rm nL} \leftrightarrow c_{\rm sL}$, $c_{\rm nR} \leftrightarrow c_{\rm nR}$, $c_{\rm s1} \leftrightarrow c_{\rm n1}$ and $c_{\rm s2} \leftrightarrow c_{\rm n2}$*. Nevertheless, we shall again obtain the

*The intermediate results for the differential equations in the applications of the boundary conditions is identical with this set of exchanges. However, the quadratic solution for the definition of $\gamma_{\rm s}$ in Eq. (4.4.17) is not identical.

solution in each region and constrain them to be continuous. First, the solution in each of the superconducting regions are given by:

$$\tilde{f}_{\mathrm{sR}}(\tilde{x}) = c_{\mathrm{sR}} U\left(a_{\mathrm{s}}, t\right), \quad \text{if} \quad x \in [d_{\mathrm{n}}/2, \infty), \tag{4.5.1}$$

$$\tilde{f}_{\mathrm{sL}}(\tilde{x}) = c_{\mathrm{sL}} U\left(a_{\mathrm{s}}, -t\right), \quad \text{if} \quad x \in (-\infty, -d_{\mathrm{n}}/2], \tag{4.5.2}$$

$$\text{where} \quad a_{\mathrm{s}} = -\frac{1}{2\tilde{B}_{\mathrm{app}}}.$$

Here, t is the familiar variable defined in Eq. (2.4.12), and both c_{sL} and c_{sR} are arbitrary constant prefactors. In the normal region, we will have a solution which effectively describes the spatial variation away from each of the two interfaces. We write the particular solution as a superposition:

$$\tilde{f}_{\mathrm{n}}(\tilde{x}) = c_{\mathrm{n1}} U\left(a_{\mathrm{n}}, t\right) + c_{\mathrm{n2}} U\left(a_{\mathrm{n}}, -t\right), \quad \text{if} \quad x \in [-d_{\mathrm{n}}/2, d_{\mathrm{n}}/2], \tag{4.5.3}$$

$$\text{where} \quad a_{\mathrm{n}} = -\frac{\tilde{m}_{\mathrm{n}}\tilde{\alpha}_{\mathrm{n}}}{2\tilde{B}_{\mathrm{app}}}.$$

Here, c_{n1} and c_{n2} are again arbitrary prefactors. The boundary conditions are similar to those seen in Section 4.4; they are given as:

$$\tilde{f}_{\mathrm{sL}}\big|_{\tilde{x}=-\tilde{d}_{\mathrm{n}}/2} = \tilde{f}_{\mathrm{n}}\big|_{\tilde{x}=-\tilde{d}_{\mathrm{n}}/2}, \tag{4.5.4}$$

$$\tilde{f}_{\mathrm{sR}}\big|_{\tilde{x}=\tilde{d}_{\mathrm{n}}/2} = \tilde{f}_{\mathrm{n}}\big|_{\tilde{x}=\tilde{d}_{\mathrm{n}}/2}, \tag{4.5.5}$$

$$\frac{1}{\tilde{m}_{\mathrm{n}}}\frac{\partial \tilde{f}_{\mathrm{n}}^2}{\partial \tilde{x}}\bigg|_{\tilde{x}=-\tilde{d}_{\mathrm{n}}/2} = \frac{\partial \tilde{f}_{\mathrm{sL}}^2}{\partial \tilde{x}}\bigg|_{\tilde{x}=-\tilde{d}_{\mathrm{n}}/2}, \tag{4.5.6}$$

$$\frac{1}{\tilde{m}_{\mathrm{n}}}\frac{\partial \tilde{f}_{\mathrm{n}}^2}{\partial \tilde{x}}\bigg|_{\tilde{x}=\tilde{d}_{\mathrm{n}}/2} = \frac{\partial \tilde{f}_{\mathrm{sR}}^2}{\partial \tilde{x}}\bigg|_{\tilde{x}=\tilde{d}_{\mathrm{n}}/2}. \tag{4.5.7}$$

As before, we have 4 boundary conditions and 5 unknowns (c_{sL}, c_{sR}, c_{n1}, c_{n2}, and k_y). Explicitly, we will ensure continuity of our solutions in the follow way:

(i) Use Eq. (4.5.4) to constrain c_{sL} in terms of c_{n1} and c_{n2},

(ii) Use Eq. (4.5.5) to constrain c_{sR} in terms of c_{n1} and c_{n2}

(iii) Use Eq. (4.5.6) to constrain c_{n2} in terms of c_{n1},

(iv) Use Eq. (4.5.7) to obtain an implicit equation for k_y (independent of c_{n1}).

We now proceed as before: by implementing the first two boundary conditions which impose continuity of magnitude (Eqs. (4.5.4) and (4.5.5)), we constrain c_{sL} and c_{sR} to be:

$$c_{\mathrm{sL}} = c_{\mathrm{n1}}\frac{U\left(a_{\mathrm{n}}, t_{-\tilde{d}_{\mathrm{n}}/2}\right)}{U\left(a_{\mathrm{s}}, -t_{-\tilde{d}_{\mathrm{n}}/2}\right)} + c_{\mathrm{n2}}\frac{U\left(a_{\mathrm{n}}, -t_{-\tilde{d}_{\mathrm{n}}/2}\right)}{U\left(a_{\mathrm{s}}, -t_{-\tilde{d}_{\mathrm{n}}/2}\right)}, \tag{4.5.8}$$

$$c_{\mathrm{sR}} = c_{\mathrm{n1}}\frac{U\left(a_{\mathrm{n}}, t_{\tilde{d}_{\mathrm{n}}/2}\right)}{U\left(a_{\mathrm{s}}, t_{\tilde{d}_{\mathrm{n}}/2}\right)} + c_{\mathrm{n2}}\frac{U\left(a_{\mathrm{n}}, -t_{\tilde{d}_{\mathrm{n}}/2}\right)}{U\left(a_{\mathrm{s}}, t_{\tilde{d}_{\mathrm{n}}/2}\right)}. \tag{4.5.9}$$

Next, we apply Eq. (4.5.6) to constrain c_{n2} in terms of c_{n1}. Taking the relevant derivatives and using the defintion of c_{sL} in Eq. (4.5.8) leads to the quadratic solution for c_{n2}:

$$c_{\mathrm{n2}} = \frac{-b + \sqrt{b^2 - 4ac}}{2a}, \tag{4.5.10}$$

where*

$$a = U'\left(a_{\mathrm{s}}, -t_{-\tilde{d}_{\mathrm{n}}/2}\right)\frac{U^2\left(a_{\mathrm{n}}, -t_{-\tilde{d}_{\mathrm{n}}/2}\right)}{U\left(a_{\mathrm{s}}, -t_{-\tilde{d}_{\mathrm{n}}/2}\right)} - \frac{1}{\tilde{m}_{\mathrm{n}}}U\left(a_{\mathrm{n}}, -t_{-\tilde{d}_{\mathrm{n}}/2}\right)U'\left(a_{\mathrm{n}}, -t_{-\tilde{d}_{\mathrm{n}}/2}\right), \tag{4.5.11}$$

$$\begin{aligned} b = c_{\mathrm{n}1}\Big[&2U'\left(a_{\mathrm{s}}, -t_{-\tilde{d}_{\mathrm{n}}/2}\right)\frac{U\left(a_{\mathrm{n}}, t_{-\tilde{d}_{\mathrm{n}}/2}\right)U\left(a_{\mathrm{n}}, -t_{-\tilde{d}_{\mathrm{n}}/2}\right)}{U\left(a_{\mathrm{s}}, -t_{-\tilde{d}_{\mathrm{n}}/2}\right)} \\ &- \frac{1}{\tilde{m}_{\mathrm{n}}}U\left(a_{\mathrm{n}}, t_{-\tilde{d}_{\mathrm{n}}/2}\right)U'\left(a_{\mathrm{n}}, -t_{-\tilde{d}_{\mathrm{n}}/2}\right) + \frac{1}{\tilde{m}_{\mathrm{n}}}U\left(a_{\mathrm{n}}, -t_{-\tilde{d}_{\mathrm{n}}/2}\right)U'\left(a_{\mathrm{n}}, t_{-\tilde{d}_{\mathrm{n}}/2}\right)\Big], \end{aligned} \tag{4.5.12}$$

$$c = c_{\mathrm{n}1}^2\left[U'\left(a_{\mathrm{s}}, -t_{-\tilde{d}_{\mathrm{n}}/2}\right)\frac{U^2\left(a_{\mathrm{n}}, t_{-\tilde{d}_{\mathrm{n}}/2}\right)}{U\left(a_{\mathrm{s}}, -t_{-\tilde{d}_{\mathrm{n}}/2}\right)} + \frac{1}{\tilde{m}_{\mathrm{n}}}U\left(a_{\mathrm{n}}, t_{-\tilde{d}_{\mathrm{n}}/2}\right)U'\left(a_{\mathrm{n}}, t_{-\tilde{d}_{\mathrm{n}}/2}\right)\right]. \tag{4.5.13}$$

Again, we can extract an overall factor of $c_{\mathrm{n}1}$ explicitly; by defining $b' = b/c_{\mathrm{n}1}$ and $c' = c/c_{\mathrm{n}1}^2$, we obtain

$$c_{\mathrm{n}2} = \gamma_{\mathrm{n}} c_{\mathrm{n}1}, \tag{4.5.14}$$

where we have defined

$$\gamma_{\mathrm{n}} = \frac{-b' + \sqrt{b'^2 - 4ac'}}{2a}. \tag{4.5.15}$$

Again, we note that the positive root is required to ensure the solution is positive. Finally, we obtain an implicit equation for k_y by using the final boundary condition in Eq. (4.5.7). The gradient in the normal region is written as

$$\begin{aligned} \left.\frac{\partial \tilde{f}_{\mathrm{n}}^2}{\partial \tilde{x}}\right|_{\tilde{x}=\tilde{d}_{\mathrm{n}}/2} = 2\sqrt{2\tilde{B}_{\mathrm{app}}}c_{\mathrm{n}1}^2\Big[&U\left(a_{\mathrm{n}}, t_{\tilde{d}_{\mathrm{n}}/2}\right)U'\left(a_{\mathrm{n}}, t_{\tilde{d}_{\mathrm{n}}/2}\right) \\ &-\gamma_{\mathrm{n}}^2 U\left(a_{\mathrm{n}}, -t_{\tilde{d}_{\mathrm{n}}/2}\right)U'\left(a_{\mathrm{n}}, -t_{\tilde{d}_{\mathrm{n}}/2}\right) \\ &-\gamma_{\mathrm{n}} U\left(a_{\mathrm{n}}, t_{\tilde{d}_{\mathrm{n}}/2}\right)U'\left(a_{\mathrm{n}}, -t_{\tilde{d}_{\mathrm{n}}/2}\right) \\ &+\gamma_{\mathrm{n}} U\left(a_{\mathrm{n}}, -t_{\tilde{d}_{\mathrm{n}}/2}\right)U'\left(a_{\mathrm{n}}, t_{\tilde{d}_{\mathrm{n}}/2}\right)\Big]. \end{aligned} \tag{4.5.16}$$

By squaring the result for c_{sR} in Eq. (4.5.9), the relevant gradient in the electrode is given by:

$$\begin{aligned} \left.\frac{\partial \tilde{f}_{\mathrm{sR}}^2}{\partial \tilde{x}}\right|_{\tilde{x}=\tilde{d}_{\mathrm{n}}/2} = 2\sqrt{2\tilde{B}_{\mathrm{app}}}c_{\mathrm{n}1}^2\frac{U'\left(a_{\mathrm{s}}, t_{\tilde{d}_{\mathrm{n}}/2}\right)}{U\left(a_{\mathrm{s}}, t_{\tilde{d}_{\mathrm{n}}/2}\right)}\Big[&U^2\left(a_{\mathrm{n}}, t_{\tilde{d}_{\mathrm{n}}/2}\right) \\ &+\gamma_{\mathrm{n}}^2 U^2\left(a_{\mathrm{n}}, -t_{\tilde{d}_{\mathrm{n}}/2}\right) \\ &+2\gamma_{\mathrm{n}} U\left(a_{\mathrm{n}}, t_{\tilde{d}_{\mathrm{n}}/2}\right)U\left(a_{\mathrm{n}}, -t_{\tilde{d}_{\mathrm{n}}/2}\right)\Big]. \end{aligned} \tag{4.5.17}$$

Again, inserting these two results into the boundary condition in Eq. (4.5.7) leads to an implicit equation that is independent of the remaining constant prefactor as required. We can again proceed to identify the effective upper critical field, $B_{\mathrm{c}2}^*$, as a function of the thickness of the normal barrier for arbitrary mass in a similar way to Section 4.4. Making use of the relationship between $t_{\mathrm{d}/2}$ and $t_{-\mathrm{d}/2}$ from Eq. (2.4.33), one can easily solve for the lowest eigenvalue numerically as we did in Section 2.4.2.2. therefore obtaning the effective upper critical field for the SNS system.

*These coefficients share symmetry with the previous coefficients found in Eqs. (4.4.13), (4.4.14) and (4.4.15). Each cylinder function is as expected by the set of exchanges described earlier, but the factor of the inverse mass now affects the 'complementary' set of terms in each coefficient.

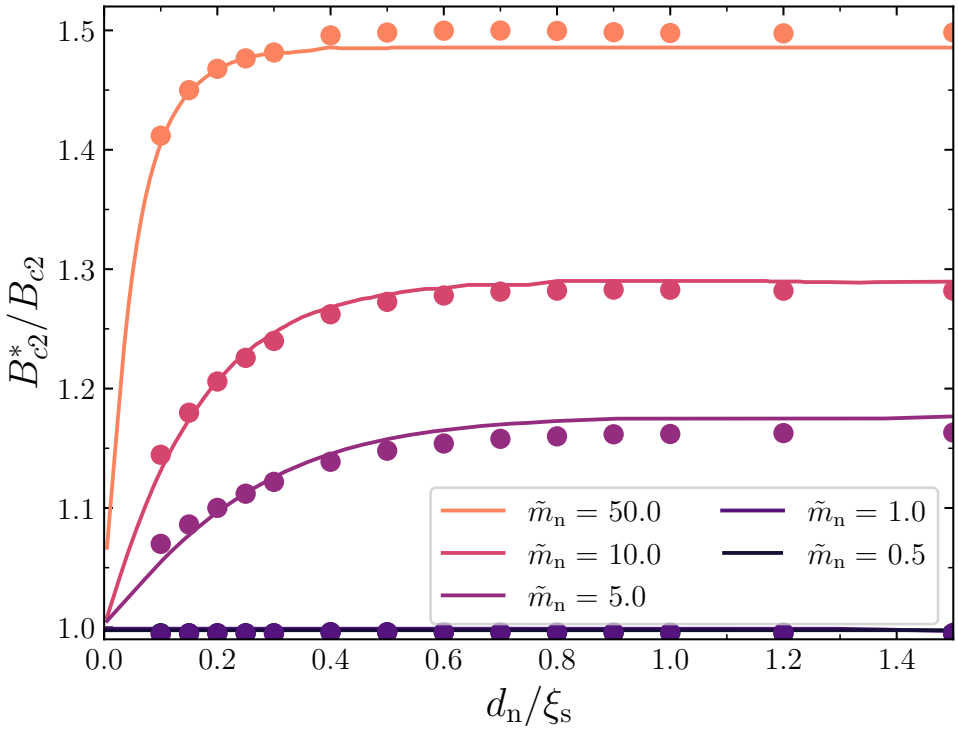

Figure 4.8: Effective upper critical field of an SNS Josephson junction as a function of normal barrier thickness, for a range of normal barrier masses. The analytic lines are calculated from Eq. (4.4.7) (using Eqs. (4.5.16) and (4.5.17)). Associated TDGL data is shown as closed markers. The TDGL simulations had a chemical length of $8.0\xi_\mathrm{s}$, with a coating of thickness $w_\mathrm{c} = 3.0\xi_\mathrm{s}$ and mass $\tilde{m}_\mathrm{c} = 1.0$. In all simulations, we have set $\tilde{\alpha}_\mathrm{n} = -1.0$ and $\tilde{\beta}_\mathrm{n} = 1.0$.

The B^*_{c2} results are shown in Fig. 4.8 for a range of normal barrier thicknesses and masses, and compared to corresponding TDGL data. The TDGL simulations all used coatings with a mass $\tilde{m}_\mathrm{c} = 1.0$ to prevent any corner effects. Small barrier thicknesses ($d_\mathrm{n} \leq 0.3$) had a grid step of $0.05\xi_\mathrm{s}$ to ensure sufficient resolution of the order parameter – all other simulations used a typical resolution of $0.1\xi_\mathrm{s}$.

Again, we can see excellent agreement between the analytic results and the TDGL simulations. In the limit that $d_\mathrm{n} \to 0$, as required, the system approaches a bulk superconductor, and the effective upper critical field tends towards the standard Abrikosov result, B_{c2}. We note that the barrier approaches the thick limit very rapidly, where there is no interference between the two sides of the barrier – we recover the single interface limits seen in Section 4.2. This is useful (in the remaining chapters) because it shows that we can consider the two interfaces in a high mass barrier of a Josephson junction to be non–interacting. The transition between the thin and thick barrier limits is smooth, but the sharpness of the transition is mass–dependent. This can be understood by considering the length scale for the order parameter in the normal region, ξ_n – as $\tilde{m}_\mathrm{n}$ increases, ξ_n decreases due to the shorter scattering length. Therefore, barriers with a larger value of $\tilde{m}_\mathrm{n}$ must be much thinner before the two sides of the barriers interact and decrease the net effective upper critical field. For the $\tilde{m}_\mathrm{n} = 50.0$ data, this sharp transition is visible, whilst the transition is much broader for the lower mass data. Notably, for $\tilde{m}_\mathrm{n} \leq 1.0$, there is no sheath and so the effective upper critical field is B_{c2} for any normal barrier thickness. We briefly note that the TDGL data for large separation (i.e. $\tilde{d}$ large) for large mass (specifically, $\tilde{m}_\mathrm{n} = 50.0$) differs by approximately 5% between the NSN simulations (Fig. 4.7) and

the SNS simulations here (Fig. 4.8) – specifically, we found values of 1.418 and 1.497 for NSN and SNS systems respectively. We can attribute this difference to numerical error due the fact that the normal coherence length is inversely proportional to the mass (c.f. Eq. (2.5.49)), and it becomes harder to capture changes on the relevant length scale.

4.6 Josephson Depairing Current Density

None of the work in the previous sections has considered the application of transport current through the system; ultimately, we will utilise these results in the determination of the critical current through a resistive grain boundary. Within wide systems in 2D, the current flow in the bulk of the electrode is localized to near the edges of the system. However, if the normal barrier is sufficiently resistive, then the current density can flow across the entire width of the system even if the system is above B_{c2}, due to the emergence of the sheath. If we assume the grain boundaries are sufficiently weakly coupled, then we can consider the current injection into the junction to be uniform across the width of the system – irrespective of what happens deep in the electrode bulk (far away from the junction), we can intuitively picture the current flow re–equilibriating along the entire width.

The treatment of the boundaries of arbitrary mass presented in the previous section captured the behaviour of this sheath – the next step in obtaining critical currents is to include the transport current that can flow across the barrier as a function of the applied magnetic field and material parameters. Above B_{c2}^*, the entire system is normal. At B_{c2}^*, there is a solution for the wavefunction in the system, with some equilibrium critical superelectron kinetic energy. Below B_{c2}^*, the equilibrium superelectron kinetic energy is lower than the previously determined maximum; we can then apply a transport current – the critical current will then be determined as the maximum current we can put through the junction at a given field.

4.6.1 Complete Analytic Solutions for the Josephson Depairing Current Density

The broad approach of the analytic framework remains similar to Section 2.4. We consider a similar vector potential to Eq. (2.4.3) but include a transport current to flow across the barrier in the x–direction following Blair. We take the wavefunction again to be

$$\tilde{\psi}(\tilde{x},\tilde{y}) = |\tilde{\psi}(\tilde{x})|e^{ik_y\tilde{y}}. \tag{4.6.1}$$

and the vector potential as

$$\tilde{\boldsymbol{A}} = \tilde{B}_{\mathrm{app}}\tilde{x}\hat{\jmath} - A_0\hat{\imath}, \tag{4.6.2}$$

where as we shall see, A_0 is associated with the applied transport current. Using the general expression for the gauge-invariant current density gives,

$$\tilde{\boldsymbol{J}}_{\boldsymbol{s}} = \frac{1}{\tilde{m}_{\mathrm{n}}}\left|\tilde{\psi}\right|^2\left((k_y - \tilde{B}_{\mathrm{app}}\tilde{x})\hat{\jmath} + \tilde{A}_0\hat{\imath}\right). \tag{4.6.3}$$

where we can use the notation $|\tilde{\psi}(\tilde{x})| = C\tilde{f}(\tilde{x})$. We describe the x-component of the current density as the applied current J_{app} and the y-component as the screening

current. This leads to

$$\tilde{J}_{\mathrm{app}} = \frac{1}{\tilde{m}_{\mathrm{n}}} \left|\tilde{\psi}\right|^2 (\tilde{x})\, \tilde{A}_0. \tag{4.6.4}$$

Inserting GL–II (Eq. 4.6.3) into GL–I yields the equation

$$\frac{\partial^2 \left|\tilde{\psi}\right|}{\partial \tilde{x}^2} - \left(k_y - \tilde{B}_{\mathrm{app}}\tilde{x}\right)^2 \left|\tilde{\psi}\right| - \left(\frac{\tilde{m}_{\mathrm{n}}\tilde{J}_{\mathrm{app}}}{\left|\tilde{\psi}\right|^2}\right)^2 \left|\tilde{\psi}\right| + \tilde{m}_{\mathrm{n}}\tilde{\alpha}_{\mathrm{n}} \left|\tilde{\psi}\right| + \tilde{m}_{\mathrm{n}}\tilde{\beta}_{\mathrm{n}} \left|\tilde{\psi}\right|^3 = 0. \tag{4.6.5}$$

Unfortunately there is simply no general solution to Eq. (4.6.5). Necessarily, we look for solutions in the weak coupling limit: we assume that the main effect on the order parameter from the flowing current is determined primarily where the order parameter is lowest. For the electrode, this is the order parameter at the interface between the electrode and the barrier, $\left|\tilde{\psi_s}\right|_{d/2}$ (which we can also write as $\left|\tilde{\psi_n}\right|_{d/2}$). For the barrier, this is at its centre, given by $\left|\tilde{\psi_n}\right|_0$. Therefore in the superconducting region, we approximate GL–I as

$$\frac{\partial^2 \tilde{f}_{\mathrm{s}}}{\partial \tilde{x}^2} - \left(k_y - \tilde{B}_{\mathrm{app}}\tilde{x}\right)^2 \tilde{f}_{\mathrm{s}} - \left(\frac{\tilde{J}_{\mathrm{app}}}{\left|\tilde{\psi_n}\right|^2_{d/2}}\right)^2 \tilde{f}_{\mathrm{s}} + \tilde{f}_{\mathrm{s}} = 0, \tag{4.6.6}$$

and in normal barrier region as

$$\frac{\partial^2 \tilde{f}_{\mathrm{n}}}{\partial \tilde{x}^2} - \left(k_y - \tilde{B}_{\mathrm{app}}\tilde{x}\right)^2 \tilde{f}_{\mathrm{n}} - \left(\frac{\tilde{m}_{\mathrm{n}}\tilde{J}_{\mathrm{app}}}{\left|\tilde{\psi_n}\right|^2_0}\right)^2 \tilde{f}_{\mathrm{n}} + \tilde{m}_{\mathrm{n}}\tilde{\alpha}_{\mathrm{n}}\tilde{f}_{\mathrm{n}} = 0. \tag{4.6.7}$$

Both of these last two equations are again of the form of a Weber equation, which provides a generalisation of the results in Sec. 4.2 that includes the applied transport current. For the SNS system of interest, we find the similar solutions for the order parameter magnitude in the left and right electrode (as given in Eqs. (4.5.1) and (4.5.2)), and in the normal barrier (as given in Eq. (4.5.3)). First, the solution in each of the superconducting regions are given by:

$$\tilde{f}_{\mathrm{sR}}(\tilde{x}) = c_{\mathrm{sR}} U\left(a_{\mathrm{s}}, t\right), \quad \text{if} \quad x \in [d_{\mathrm{n}}/2, \infty), \tag{4.6.8}$$

$$\tilde{f}_{\mathrm{sL}}(\tilde{x}) = c_{\mathrm{sL}} U\left(a_{\mathrm{s}}, -t\right), \quad \text{if} \quad x \in (-\infty, -d_{\mathrm{n}}/2], \tag{4.6.9}$$

$$\text{where} \quad a_{\mathrm{s}} = -\frac{1}{2\tilde{B}_{\mathrm{app}}} \left(1 - \left(\frac{\tilde{J}_{\mathrm{app}}}{\left|\tilde{\psi_n}\right|^2_{d/2}}\right)^2\right).$$

Again, t is the familiar variable defined in Eq. (2.4.12), and both c_{sL} and c_{sR} are arbitrary constant prefactors. In the normal region, we write the particular solution as the superposition:

$$\tilde{f}_{\mathrm{n}}(\tilde{x}) = c_{\mathrm{n1}} U\left(a_{\mathrm{n}}, t\right) + c_{\mathrm{n2}} U\left(a_{\mathrm{n}}, -t\right), \quad \text{if} \quad x \in [-d_{\mathrm{n}}/2, d_{\mathrm{n}}/2], \tag{4.6.10}$$

$$\text{where} \quad a_{\mathrm{n}} = -\frac{1}{2\tilde{B}_{\mathrm{app}}} \left(\tilde{m}_{\mathrm{n}}\tilde{\alpha}_{\mathrm{n}} - \left(\frac{\tilde{m}_{\mathrm{n}}\tilde{J}_{\mathrm{app}}}{\left|\tilde{\psi_n}\right|^2_0}\right)^2\right).$$

Again, c_{n1} and c_{n2} are again arbitrary constants. However, we note that (by construction) these solutions are written in terms of the order parameter magnitudes at the centre of the normal barrier and at the interface ($\left|\tilde{\psi_n}\right|_{d/2}$ and $\left|\tilde{\psi_n}\right|_0$) – strictly, these should be calculated from the non–linear equations. In the weakly coupled limit, we can approximate these with their values as calculated from the linearized

equations. However, these will depend on a_s and a_n themselves, and therefore will no longer allow one to obtain an explicit solution for the prefactors written in terms of one another as we did in Section 4.5. To overcome this and render the problem analytically tractable, we again make the assumption of being in the weakly coupled limit, so the current is small enough that the order parameter at the centre of the junction does not change significantly in the presence of transport current, and therefore, both $\left|\tilde{\psi_n}\right|_{d/2}$ and $\left|\tilde{\psi_n}\right|_0$ are calculated in the zero–current limit. This assumption is comparable to the weak–coupling approximation in Fink [74], and is necessary to retain the explicit nature of the problem. Therefore, we can rewrite the two variables (a_s and a_n):

$$\begin{aligned} a_\mathrm{s} &= -\frac{1}{2\tilde{B}_\mathrm{app}}\left(1-\left(\frac{\tilde{J}_\mathrm{app}}{\tilde{f}^2_{\mathrm{n},\tilde{d}_\mathrm{n}/2}}\right)^2\right), \\ a_\mathrm{n} &= -\frac{1}{2\tilde{B}_\mathrm{app}}\left(\tilde{m}_\mathrm{n}\tilde{\alpha}_\mathrm{n}-\left(\frac{\tilde{m}_\mathrm{n}\tilde{J}_\mathrm{app}}{\tilde{f}^2_{\mathrm{n},0}}\right)^2\right), \end{aligned} \tag{4.6.11}$$

where the specific values of $\tilde{f}_{\mathrm{n},\tilde{d}_\mathrm{n}/2}$ and $\tilde{f}_{\mathrm{n},0}$ are calculated in zero transport current.

In order to make use of these general equations, we need to know the order parameter at the centre of the junction. From the framework in Section 4.3 (the 'double–linear' approach), we know the order parameter at the interface. We can then use the derived Saint James order parameter distribution to calculate the order parameter throughout the normal barrier, and subsequently can identify the order parameter in the centre of the junction. A comparison between the calculated $\left|\tilde{\psi_n}\right|_0$ and TDGL simulation is shown in Fig. 4.9 for a wide range of masses. We can see good agreement between the TDGL simulations and the calculated Saint James order parameter - by construction, the solutions agree well near $B^*_{\mathrm{c}2}$ for all masses. For very low masses (e.g. $\tilde{m}_\mathrm{n} = 0.5$), the order parameter in the normal barrier is very small (as a consequence of the boundary conditions, c.f. Eq. (2.4.1)), and so we see particularly poor agreement in low and intermediate fields. Another possible cause may be in the choice of method for the calculation of the order parameter for cases in the low mass limit: as presented in Section 4.3, the interfacial order parameter is simply the Fink–Blair result – and in this case, the Saint James order parameter distribution may not be an appropriate framework for calculating the order parameter at the centre of the barrier. However, for the cases of interest, we see good agreement across the entire field range, apart from in extremely low fields (as expected) – our approach of using the Saint James order parameter to describe the centre of the junction is therefore validated for any set of barrier geometries and material properties.

To find criticality where $\tilde{J}_\mathrm{app} = \tilde{J}_\mathrm{c}$, we use the same approach that was used in Section 4.5 for an SNS junction to find B^*_{c2} (i.e. where effectively $J_\mathrm{app} = 0$). We find the maximum current density that can flow, by setting B_app (to be less than B^*_{c2}) in the general form of a_s and a_n, and solve to find J_c. The 'complete analytic solutions' for J_c for the SNS junction were found by solving Eqs. (4.5.4) to (4.5.7). This results in exactly the same equations as in Section 4.5 – after manipulating the boundary conditions, we are left with a single implicit equation in one unknown, as defined in Eq. (4.5.7), making use of Eqs. (4.5.16) and (4.5.17). The crucial difference is that now we are using the general forms (that include transport current) of a_s and a_n (Eq. (4.6.11)). In a similar way to the $B^*_{\mathrm{c}2}$ calculation (where we maximized the field), we can similarly find the maximal J_app that admits a solution to find J_c.

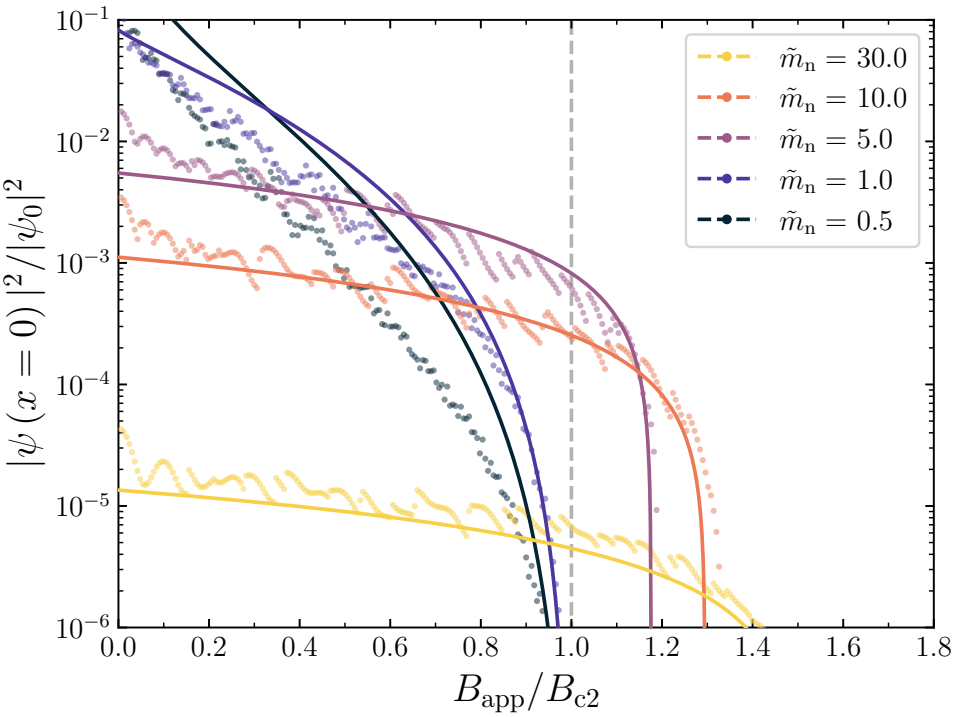

Figure 4.9: Order parameter magnitude at the centre of the normal barrier as as function of field from TDGL data with arbitrary mass, compared to the analytic solution from Saint James. We have used the double–linear approach (c.f. Section 4.3) to calculate the order parameter at the interface for arbitrary mass, and then used the SNS Saint James order parameter to calculate the order parameter distribution in the normal barrier (c.f. Section 4.5). In all simulations, we have set $\tilde{d}_{\mathrm{n}} = 2.0$, $\tilde{\alpha}_{\mathrm{n}} = -1.0$ and $\tilde{\beta}_{\mathrm{n}} = 1.0$.

4.6.1.1 Reduction to Previous Results in Literature

A rather simplistic approximation for J_{c} can be found by assuming that the screening current in the superconducting electrode is broadly unaffected by the applied current which in constant magnetic field, is equivalent to assuming the gradient in the phase in the y–direction is the same in both the electrode and the barrier is unaffected by the applied current. Taking leading terms from Eq. (4.6.6) and using Eq. (2.4.12) gives

$$k_y^2 = \left(t_{0,c}\sqrt{\frac{\tilde{B}_{c2}^*}{2}}\right)^2 = \left(t_{0,c}\sqrt{\frac{\tilde{B}}{2}}\right)^2 + \left(\frac{\tilde{m}_{\mathrm{n}}\tilde{J}_{\mathrm{app}}}{\left|\tilde{\psi}_{\mathrm{n}}\right|_0^2}\right)^2. \tag{4.6.12}$$

Since we are in the weak-coupling limit, we take the insulating result $t_{0,c}^2 \approx 2/B_{c2}^*$ from Section 2.4 and rearrange to give

$$\tilde{J}_{\mathrm{DJ}}\left(\tilde{B}_{\mathrm{app}}\right) = \frac{1}{\tilde{m}_{\mathrm{n}}}\left|\tilde{\psi}_{\mathrm{n}}\right|_0^2\sqrt{1-\tilde{b}}, \tag{4.6.13}$$

where we have defined the reduced field variable, $\tilde{b} = \tilde{B}_{\mathrm{app}}/\tilde{B}_{\mathrm{c2}}^*$. Although this result is approximate at best, comparing it with that of Abrikosov and Boyd (c.f. Section 2.5.2) shows it is consistent with the surface barrier producing marked increases in J_{c} close to B_{c2}^*.

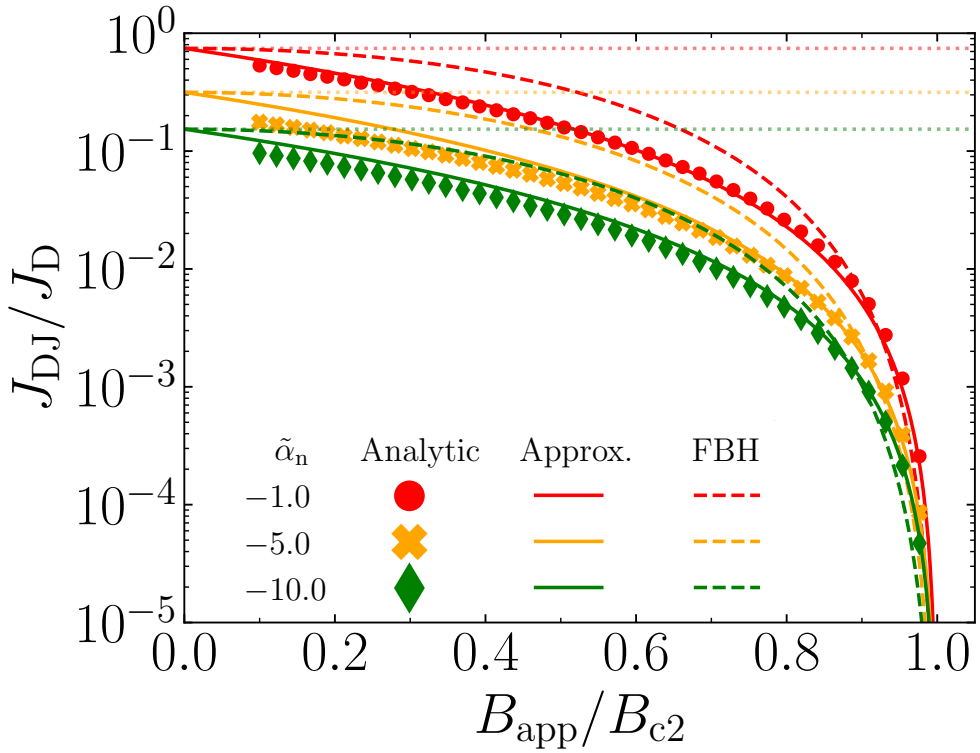

Figure 4.10: Josephson depairing current density as a function of applied magnetic field, for a range of normal barrier thicknesses with $\tilde{\alpha}_{\mathrm{n}} = -1.0$, $\tilde{m}_{\mathrm{n}} = 1.0$, and $\tilde{\beta}_{\mathrm{n}} = 1.0$. The complete analytic solutions (solid symbols) are calculated by numerically solving Eq. (4.5.7) (using Eqs. (4.5.16) and (4.5.17)) using the general forms of a_{n} and a_{s} (Eq. (4.6.11)) for the maximal current density. The FBH solution (dashed line) is calculated from Eqs. (2.5.47) and (2.5.69); the faint horizontal dotted line shows the zero–field Fink value. The approximate functional forms of the analytic solution (Eq. (4.6.14), with n taken from Table 4.1) are shown as solid lines.

4.6.2 Approximations of the Josephson Depairing Current Density

Although this prescription is relatively easy to solve numerically, we can improve the clarity of these results by providing a simple analytic approximation of our solution. In zero–field, we expect to recover the Fink result (c.f. Section 2.5.1). Since our solution is formally derived in the linearized limit, it is strictly valid near B^*_{c2}. As seen from Eq. (4.6.13) and Fig. 4.9, the field dependence of the analytic solution changes with the material parameters. Although our analytic solution has a clear $1-\tilde{b}$ dependence, the additional field dependence within $\left|\tilde{\psi}_{\mathrm{n}}\right|_0$ is not obvious. Therefore, we suggest that the functional form can be approximated over the entire field range by the empirical equation

$$\tilde{J}_{\mathrm{DJ}}\left(\tilde{B}_{\mathrm{app}}\right) = \tilde{J}_{\mathrm{Fink}}\left(1 - \frac{\tilde{B}_{\mathrm{app}}}{\tilde{B}^*_{\mathrm{c2}}}\right)^n = \tilde{J}_{\mathrm{Fink}}\left(1-\tilde{b}\right)^n, \tag{4.6.14}$$

where $\tilde{J}_{\mathrm{Fink}}$ is calculated from Eq. (2.5.47) in the zero–field limit ($q^2 = 0$). We fit this functional form to the results of the complete analytic calculations in Section 4.6.1. We present the results of these fits in Tabs. 4.1a and 4.1b for $\tilde{m}_{\mathrm{n}} = 1.0$ and $\tilde{m}_{\mathrm{n}} = 10.0$ respectively. It can be seen that n is a function of the material parameters.

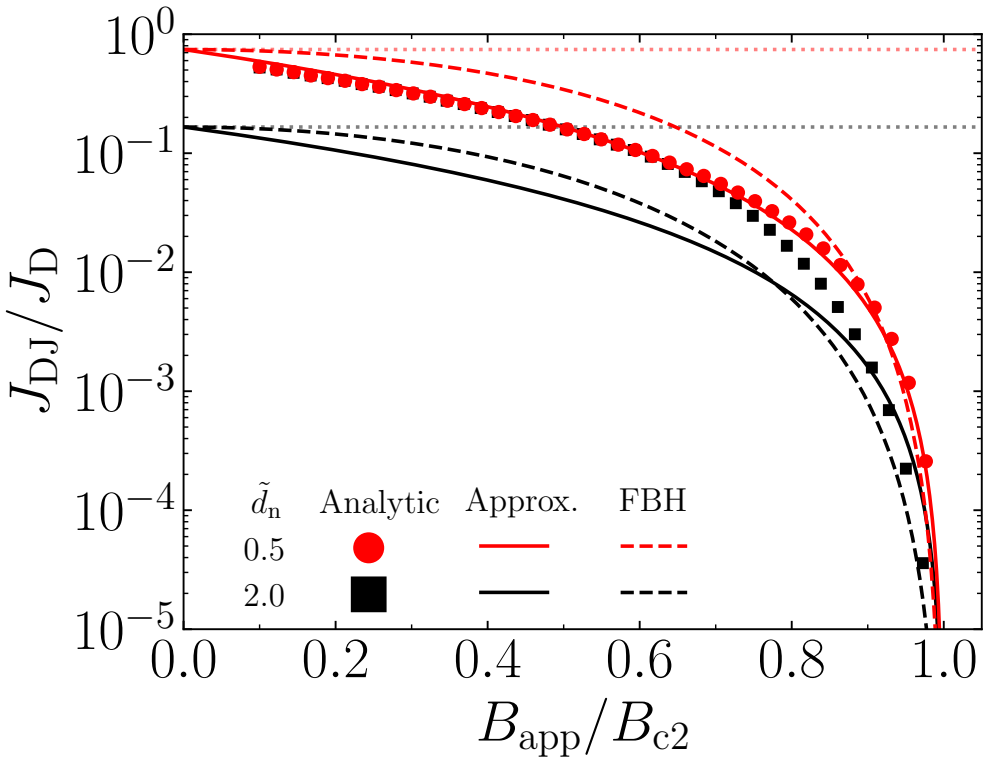

Figure 4.11: Josephson depairing current density as a function of applied magnetic field, for a range of normal barrier thicknesses with $\tilde{\alpha}_{\mathrm{n}} = -1.0$, $\tilde{m}_{\mathrm{n}} = 1.0$ and $\tilde{\beta}_{\mathrm{n}} = 1.0$. The complete analytic solutions (solid symbols) are calculated by numerically solving Eq. (4.5.7) (using Eqs. (4.5.16) and (4.5.17)) using the general forms of a_{n} and a_{s} (Eq. (4.6.11)) for the maximal current density. The FBH solution (dashed line) is calculated from Eqs. (2.5.47) and (2.5.69); the faint horizontal dotted line shows the zero–field Fink value. The approximate functional forms of the analytic solution (Eq. (4.6.14), with n taken from Table 4.1) are shown as solid lines.

$\tilde{\alpha}_{\mathrm{n}}$ \ $\tilde{d}_{\mathrm{n}}$	0.5	2.0
-1.0	2.17	2.01
-5.0	2.19	2.02
-10.0	2.13	2.18

(a) The values of n for $\tilde{m}_{\mathrm{n}} = 1.0$

$\tilde{\alpha}_{\mathrm{n}}$ \ $\tilde{d}_{\mathrm{n}}$	0.5	2.0
-1.0	0.60	0.50
-5.0	0.46	0.50
-10.0	0.39	0.50

(b) The values of n for $\tilde{m}_{\mathrm{n}} = 10.0$

Table 4.1: Fitted values for the power n in the functional form presented in Eq. (4.6.14) for an assortment of material parameters. The functional form has been fitted to the complete analytic solutions (solid symbols) are calculated by numerically solving Eq. (4.5.7) (using Eqs. (4.5.16) and (4.5.17)) using the general forms of a_{n} and a_{s} (Eq. (4.6.11)) for the maximal current density.

4.6.3 Comparing the Complete Solution with FBH and the Functional Form

Comparisons of the complete analytic solutions (solid markers) to both the FBH result (dashed lines) and the fitted functional form (solid lines) are shown in Figs. 4.10 to 4.13. The new analytic solutions follows the calculations presented in Section 4.6.1 – J_{DJ} at each field point was obtained by finding the maximum current that still permits a solution, by inserting the general forms of a_{s} and a_{n} (as defined in Eq. (4.6.11)) and then solving Eqs. (4.5.4) to (4.5.7). We also note that the dependence of the form $\left(1 - \tilde{b}\right)$ (that is more appropriate for 2D systems [153, 154]) has been derived, rather

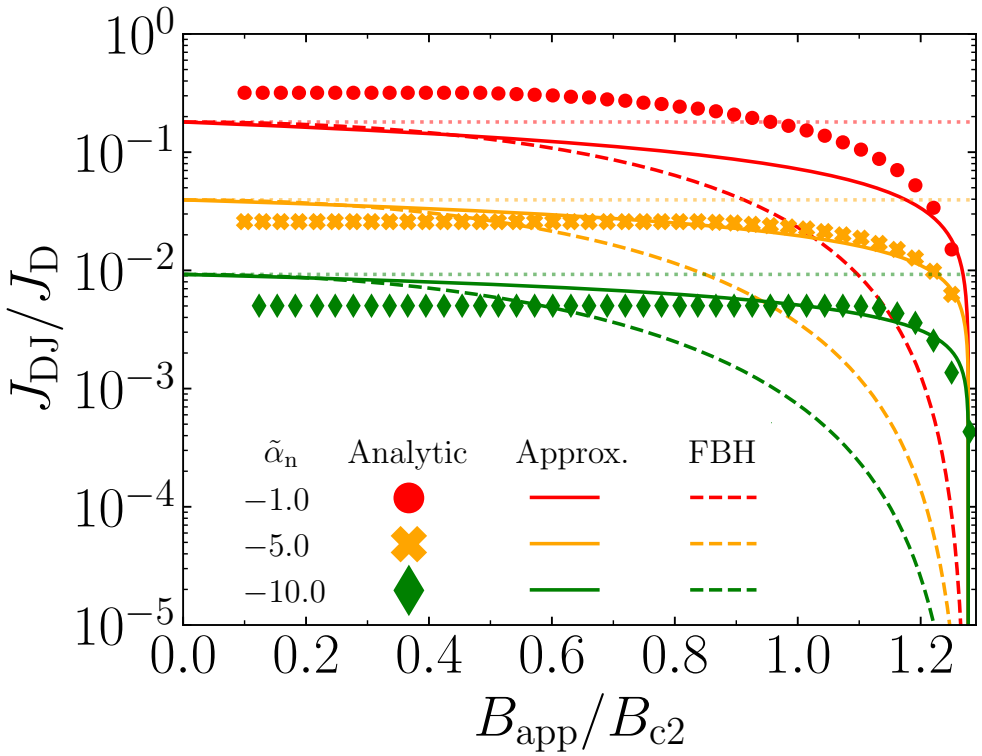

Figure 4.12: Josephson depairing current density as a function of applied magnetic field, for a range of junction condensation parameters with $\tilde{d}_{\mathrm{n}} = 0.5$, $\tilde{m}_{\mathrm{n}} = 10.0$ and $\tilde{\beta}_{\mathrm{n}} = 1.0$. The complete analytic solutions (solid symbols) are calculated by numerically solving Eq. (4.5.7) (using Eqs. (4.5.16) and (4.5.17)) using the general forms of a_{n} and a_{s} (Eq. (4.6.11)) for the maximal current density. The FBH solution (dashed line) is calculated from Eqs. (2.5.47) and (2.5.69); the faint horizontal dotted line shows the zero–field Fink value. The approximate functional forms of the analytic solution (Eq. (4.6.14), with n taken from Table 4.1) are shown as solid lines.

than simply proposed and inserted as in the 1D FBH calculations of Eqs. (2.5.47) and (2.5.69). The FBH solution uses the key results presented in Section 2.5.1.1, making use of Eqs. (2.5.47) and (2.5.69). However, since FBH only considers insulating boundaries in 1D, it contains no information about the effective upper critical field for arbitrary mass; the field dependence of the FBH results is therefore calculated using Eq. (2.5.69), where the effective upper critical field has been determined exactly from our results in Section 4.5. Finally, the functional approximation shown in Eq. (4.6.14) was found by fitting to the results of the complete analytic calculations, and ensures that the solution is physically reasonable over the entire field range.

Figs. 4.10 and 4.11 consider the case where $\tilde{m}_{\mathrm{n}} = 1.0$, and we see reasonable agreement with the results of FBH. However, Figs. 4.12, and 4.13 show some of the central results of this thesis – namely that for high mass barriers, the surface barrier plays a central role and the current density close to B^*_{c2} is very significantly enhanced. In this case, our complete analytic solution is markedly different from the FBH solution – as we will see in Chapter 5, is required for the accurate description of the critical current in the high–field regime.

We briefly note that the $\tilde{m}_{\mathrm{n}} = 1.0$, $\tilde{d}_{\mathrm{n}} = 2.0$ case shown in Fig. 4.11 does not provide as good agreement as seen for $\tilde{m}_{\mathrm{n}} = 10.0$, $\tilde{d}_{\mathrm{n}} = 2.0$ as seen in Fig. 4.13. We have attributed this to the corresponding same low–mass discrepancy as seen in Fig. 4.9, where the calculation of the order parameter magnitude in the barrier (using Eq.

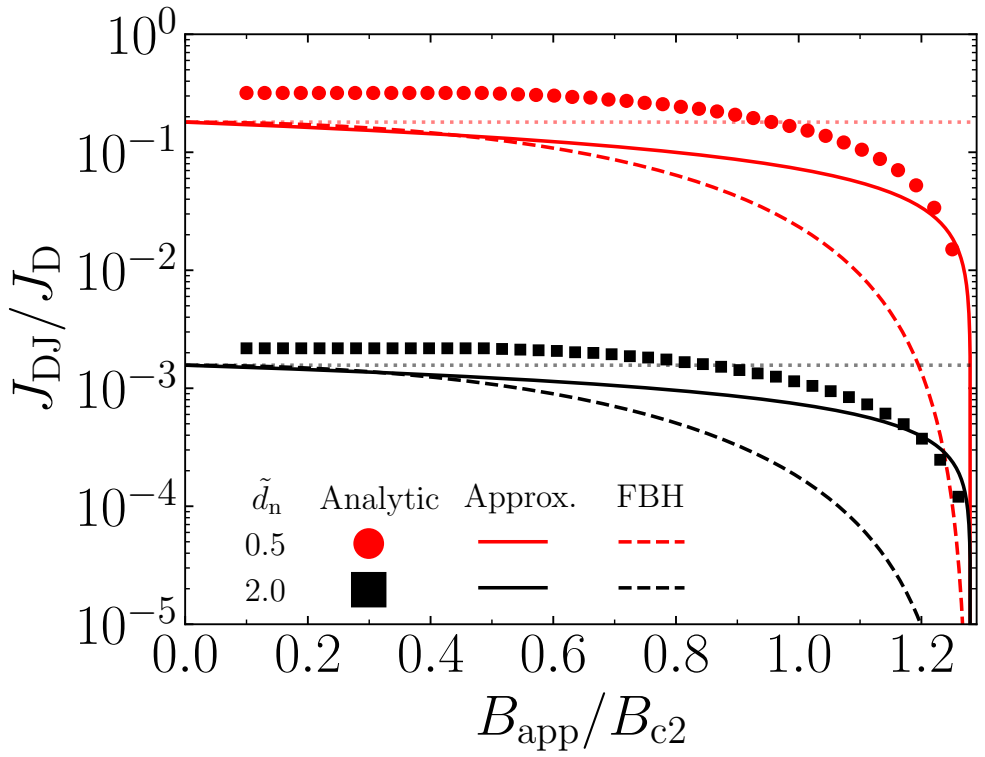

Figure 4.13: Josephson depairing current density as a function of applied magnetic field, for a range of normal barrier thicknesses with $\tilde{\alpha}_{\mathrm{n}} = -1.0$, $\tilde{m}_{\mathrm{n}} = 10.0$ and $\tilde{\beta}_{\mathrm{n}} = 1.0$. The complete analytic solutions (solid symbols) are calculated by numerically solving Eq. (4.5.7) (using Eqs. (4.5.16) and (4.5.17)) using the general forms of a_{n} and a_{s} (Eq. (4.6.11)) for the maximal current density. The FBH solution (dashed line) is calculated from Eqs. (2.5.47) and (2.5.69); the faint horizontal dotted line shows the zero–field Fink value. The approximate functional forms of the analytic solution (Eq. (4.6.14), with n taken from Table 4.1) are shown as solid lines.

(4.5.3), with the corresponding boundary conditions found from Eq. (4.4.7) using Eqs. (4.5.16) and (4.5.17)) systematically overestimates the TDGL data. We suggest that for low mass barriers, where the junctions are strongly coupled, the order parameter magnitude is significantly large enough such that the linear nature of the Saint James approach loses some accuracy. No such problem occurs when the mass is large, so we do not see this discrepancy in Fig. 4.13.

We note here that the zero–field value from Fink is known to be correct; this is shown as faint horizontal lines in all of Figs. 4.10 to 4.13. The FBH result is only formally correct in very narrow systems – our new treatment is required to extend our description accurately to wide junctions. However, by omitting the non–linear term, the accuracy of the cylinder functions decreases rapidly in low fields, and can exceed the Fink zero–field value (particularly for high mass barriers). Therefore, to find an approximation across the entire field range, in Chapter 5 we will choose to use the functional form approximation, which allows a smooth interpolation between the high–field end and the zero–field Fink value.

4.6.3.1 Dependencies of the Complete Analytic Solution

Figs. 4.10 to 4.13 demonstrates the $\tilde{m}_{\mathrm{n}}$, $\tilde{\alpha}_{\mathrm{n}}$, and $\tilde{d}_{\mathrm{n}}$ dependencies of the analytic solution. We can understand this physical behaviour by considering the spatial variation of the order parameter in the normal region (c.f. Fig. 4.1). If we consider a

single SN interface, then we can gain some intuition into the dependencies of $\tilde{f}_0$ (and therefore, $\tilde{J}_{\mathrm{DJ}}$) on the material parameters. If the barrier is thicker, then the centre of the barrier is further into the normal region – the order parameter in the centre of the barrier is therefore smaller. Similarly, if $\tilde{m}_{\mathrm{n}}$ is larger, or $\tilde{\alpha}_{\mathrm{n}}$ is larger and more negative, then the coupling is much weaker and the length scale ξ_{n} is shorter (c.f. Eq. (2.5.49)), and so the order parameter decays faster in the normal region – again, the order parameter at the centre of the junction is reduced. From Eq. (4.6.11), as $f_{\mathrm{n},0}$ is reduced, then the maximum critical current that can pass through the barrier is then smaller, as expected.

Although the dependencies of the solutions on the field and assorted material parameters are not physically surprising (and clearly observed in Figs. 4.10 to 4.13), they are not obviously transparent from the complete mathematical solution in Section 4.6.1. We shall explicitly consider the structure of Eq. (4.6.13) (i.e. parabolic cylinder function used to calculate $f_{\mathrm{n},0}$) in order to gain a clearer insight into the behaviour of the analytic solutions.

First, it is clear that as $B \to B^*_{\mathrm{c2}}$, $\tilde{f}_0^2 \to 0$ in this limit by construction. Therefore, from Eq. (4.6.11), it is clear that $\tilde{J}_{\mathrm{DJ}}$ also tends to zero as expected – a smaller order parameter in the barrier directly correlates to a degraded ability to carry a transport current. Next, to see the explicit dependence of $\tilde{J}_{\mathrm{DJ}}$ on the material parameters ($\tilde{m}_{\mathrm{n}}$, $\tilde{\alpha}_{\mathrm{n}}$ and d_{n}), we must consider a representation of the parabolic cylinder functions in terms of the Kummer confluent hypergeometric functions of the first kind [155]; these are another set of special functions, which are defined through a well–defined infinite series [80, Eq. 13.2.2]. The leading terms of the parabolic cylinder functions are given as [80, Eq. 12.4.1]

$$U\left(a,x\right) = e^{-\frac{x^2}{4}} 2^{-\frac{1}{2}\left(a+\frac{1}{2}\right)} \left[\frac{\sqrt{\pi}}{\Gamma\left(\frac{a}{2}+\frac{3}{4}\right)} - \frac{\sqrt{2\pi}}{\Gamma\left(\frac{a}{2}+\frac{1}{4}\right)} x \right] + \mathcal{O}\left(x^2\right). \tag{4.6.15}$$

The first result for us is that Eq. (4.6.15) is proportional to $2^{-\frac{1}{2}\left(a+\frac{1}{2}\right)}$; as $\tilde{m}_{\mathrm{n}}$ is increased or $\tilde{\alpha}_{\mathrm{n}}$ become larger and more negative, then a_{n} increases (c.f. Eq. (4.6.11)). Therefore, $\tilde{f}_{\mathrm{n},0}$ decreases, and consequently $\tilde{J}_{\mathrm{DJ}}$ is reduced as required. Finally, we address the thickness dependence. Physically, we can note that the order parameters decay exponentially away from each side of the barrier; therefore, as the thickness of the barrier is increased, $\tilde{f}_{\mathrm{n},0}$ correspondingly decreases – Eq. (4.6.15) provides the exponential dependence on the normal barrier thickness required, reproducing the results from de Gennes [77], Fink [74] and Blair [75].

4.7 Generalized Clem: Arbitrary κ_s and Width

The framework of Clem presented in Section 2.5.2 is useful since it is the only analytic approach we have that captures the behaviour of fluxons entering the junction. However, it is flawed in that it makes the assumption of zero coherence length - the order parameter instantaneously recovers to the bulk Meissner value, and the field and current flow is assumed to be uniform across the width. This is not accurate for real polycrystalline materials, where the grain size is typically much larger than the penetration depth, and therefore the current flows locally near the edges of the junction. In this section, we generalize Clem's results to include the finite spatial

variation of the magnetic vector potential which leads to the correct spatial variation of screening currents. We also explicitly include the order parameter magnitude and obtain an explicit solution of the spatial variation of the phase. Furthermore, we additionally describe identify the variation of the transport current in geometries with arbitrary κ_{s} and $\tilde{w}_{\mathrm{s}}$.

4.7.1 General Screening Current Solutions

Following Clem's work, we shall retain the London approximation, assuming that the spatial variation of the order parameter is small. We rewrite GL2 (Eq. (2.3.43)) in the London gauge, by making a gauge transformation such that there is no explicit phase dependence:

$$\tilde{\boldsymbol{J}}_{\boldsymbol{s}} = -\frac{1}{\tilde{m}_{\mathrm{n}}} \left|\tilde{\psi}\right|^2 \tilde{\boldsymbol{A}}. \tag{4.7.1}$$

We then use Maxwell's equation (Eq. (2.3.39)) to write the current density in terms of the vector potential,

$$\tilde{\boldsymbol{J}}_{\boldsymbol{s}} = \kappa_{\mathrm{s}}^2 \boldsymbol{\nabla} \times \boldsymbol{\nabla} \times \boldsymbol{A} = -\frac{1}{\tilde{m}_{\mathrm{n}}} \left|\tilde{\psi}\right|^2 \tilde{\boldsymbol{A}}, \tag{4.7.2}$$

and apply a vector identity to yield a Helmholtz equation,

$$\boldsymbol{\nabla}^2 \boldsymbol{A} = \frac{\left|\tilde{\psi}\right|^2}{\tilde{m}_{\mathrm{n}} \kappa_{\mathrm{s}}^2} \tilde{\boldsymbol{A}}. \tag{4.7.3}$$

Now, the boundary conditions imposed on the current may be equivalently written in terms of the vector potential. We define a superconducting electrode with a square geometry of arbitrary width and length, where $x \in [-L/2, L/2], y \in [-W/2, W/2]$. We require that no screening current crosses the boundary interfaces and the applied field at each edge is the specified applied magnetic field. For the x–component, we have

$$A_x\left(\tilde{x}, \tilde{y}\right)\big|_{\tilde{x}=\pm L/2} = 0, \tag{4.7.4}$$

$$\left.\frac{\partial A_x\left(\tilde{x}, \tilde{y}\right)}{\partial \tilde{y}}\right|_{\tilde{y}=\pm W/2} = -\tilde{B}_{\mathrm{app}}. \tag{4.7.5}$$

The solution for the vector potential (i.e. the current flow) has to be antisymmetric in y, and symmetric in x. Therefore, we write a general solution to the Helmholtz equation as the Fourier series,

$$\tilde{A}_{\mathrm{x}}\left(\tilde{x}, \tilde{y}\right) = \sum_{n,m} C_{n,m} \cos\left(k_x \tilde{x}\right) \sin\left(k_y^* \tilde{y}\right). \tag{4.7.6}$$

At this stage, $C_{n,m}$, k_x and k_y^* are undefined constants which may be real or complex. We will see later that they are all required to be real. Applying the first boundary condition in Eq. (4.7.4) constrains k_x:

$$k_x = \frac{(2n+1)\pi}{L}. \tag{4.7.7}$$

This ensures the correct perioidicity in the x–direction. Inserting this result back into the original Helmholtz equations constrains k_y^* in terms of this k_x:

$$\left(k_x\right)^2 + \left(k_y^*\right)^2 = -\frac{\left|\tilde{\psi}\right|^2}{\tilde{m}_{\mathrm{n}} \kappa_{\mathrm{s}}^2} \implies k_y^* = \sqrt{-\frac{\left|\tilde{\psi}\right|^2}{\tilde{m}_{\mathrm{n}} \kappa_{\mathrm{s}}^2} - \left(\frac{(2n+1)\pi}{L}\right)^2}. \tag{4.7.8}$$

It is clear that this is a purely imaginary term. Inserting this back into our general solution, and using that $\sin(ix) = i\sinh(x)$ provides:

$$\tilde{A}_{\mathrm{x}}\left(\tilde{x},\tilde{y}\right) = \sum_n C_n \cos\left(k_x\tilde{x}\right)\sinh\left(k_y\tilde{y}\right) \tag{4.7.9}$$

where we have defined the variable $k_y = ik_y^*$ as:

$$k_y = \sqrt{\frac{\left|\tilde{\psi}\right|^2}{\tilde{m}_{\mathrm{n}}\kappa_{\mathrm{s}}^2} + \left(\frac{(2n+1)\pi}{L}\right)^2}. \tag{4.7.10}$$

Finally, we use the last boundary condition in Eq. (4.7.5) to constrain the Fourier coefficients. This equation provides the condition:

$$-\tilde{B}_{\mathrm{app}} = \sum_n C_n \cos\left(k_x\tilde{x}\right) k_y \cosh\left(k_y\frac{W}{2}\right). \tag{4.7.11}$$

We then use typical Fourier methods to extract the coefficients, and shall make use of the identity

$$\int_{-L/2}^{L/2} \cos\left(\frac{(2n+1)\pi}{L}\tilde{x}\right)\cos\left(\frac{(2m+1)\pi}{L}\tilde{x}\right)\mathrm{d}x = \delta_{nm}\frac{L}{2}. \tag{4.7.12}$$

Multiplying each side of Eq. (4.7.11) by $\cos\left(\frac{(2m+1)\pi}{L}\tilde{x}\right)$ and integrating in the x–direction yields

$$-\int_{-L/2}^{L/2} \tilde{B}_{\mathrm{app}}\cos\left(\frac{(2n+1)\pi}{L}\tilde{x}\right)\mathrm{d}x = C_n\frac{L}{2}k_y\cosh\left(k_y\frac{W}{2}\right). \tag{4.7.13}$$

The remaining integral can be easily evaluated:

$$-\int_{-L/2}^{L/2} \tilde{B}_{\mathrm{app}}\cos\left(\frac{(2n+1)\pi}{L}\tilde{x}\right)\mathrm{d}x = \tilde{B}_{\mathrm{app}}\frac{(-1)^{n+1}2L}{(2n+1)\pi}. \tag{4.7.14}$$

Finally, Eq. (4.7.13) can be rearranged for the explicit Fourier coefficients. We find the final result

$$C_n = \frac{4\tilde{B}_{\mathrm{app}}(-1)^{n+1}}{(2n+1)\pi k_y\cosh\left(k_y\frac{W}{2}\right)}. \tag{4.7.15}$$

We now have a general solution for the vector potential which includes κ dependence:

$$\tilde{A}_{\mathrm{x}}\left(\tilde{x},\tilde{y}\right) = \sum_n \frac{4\tilde{B}_{\mathrm{app}}(-1)^{n+1}}{(2n+1)\pi k_y\cosh\left(k_y\frac{W}{2}\right)}\cos\left(k_x\tilde{x}\right)\sinh\left(k_y\tilde{y}\right), \tag{4.7.16}$$

$$k_x = \frac{(2n+1)\pi}{L}, \qquad k_y = \sqrt{\frac{\left|\tilde{\psi}\right|^2}{\tilde{m}_{\mathrm{n}}\kappa_{\mathrm{s}}^2} + \left(\frac{(2n+1)\pi}{L}\right)^2}.$$

This solution converges rapidly. In the limit of large κ, we recover a linear vector potential as presented by Clem. The solution for the y–component can be obtained similarly – the boundary conditions are

$$A_y\left(\tilde{x},\tilde{y}\right)\big|_{\tilde{y}=\pm W/2} = 0, \tag{4.7.17}$$

$$\left.\frac{\partial A_y\left(\tilde{x},\tilde{y}\right)}{\partial\tilde{x}}\right|_{\tilde{x}=\pm L/2} = \tilde{B}_{\mathrm{app}}, \tag{4.7.18}$$

$$\tilde{A}_{\mathrm{y}}\left(\tilde{x},\tilde{y}\right) = \sum_n \frac{4\tilde{B}_{\mathrm{app}}(-1)^{n}}{(2n+1)\pi k_x\cosh\left(k_x\frac{L}{2}\right)}\cos\left(k_y\tilde{y}\right)\sinh\left(k_x\tilde{x}\right), \tag{4.7.19}$$

$$k_y = \frac{(2n+1)\pi}{W}, \qquad k_x = \sqrt{\frac{\left|\tilde{\psi}\right|^2}{\tilde{m}_{\mathrm{n}}\kappa_{\mathrm{s}}^2} + \left(\frac{(2n+1)\pi}{W}\right)^2}.$$

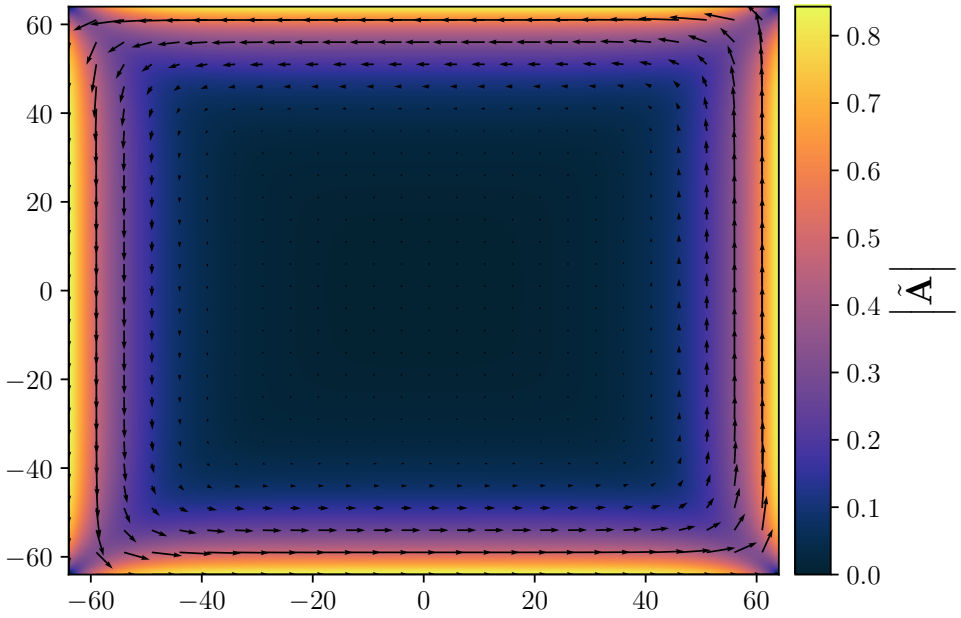

Figure 4.14: Screening current spatial variation from Eqs. (4.7.9) and (4.7.15), at $\tilde{B}_{\mathrm{app}} = 0.5B_{\mathrm{c2}}$, with an equiaxed electrode of dimensions $128 \times 128\xi_{\mathrm{s}}$. Arrows indicate the direction and magnitude of the screening currents at each point. The magnitude of the order parameter is taken to be spatially constant, with a value of $1 - \tilde{B}_{\mathrm{app}}$.

This solution can also be obtained by symmetry (exchanging $\tilde{x} \leftrightarrow \tilde{y}$, with an additional minus sign originating from the different boundary condition in Eq. (4.7.18) and $L \leftrightarrow W$). An example of the vector potential magnitude and the variation of the screening currents is shown in Fig. 4.14, demonstrating the exponential dependence of the screening currents on the penetration depth.

By construction, the field will be set at the applied field at the edge, and decay exponentially in the bulk. In practice, as seen from Eq. (2.3.34), the field in the bulk should be the average Abrikosov field. For materials where κ_{s} is large, the difference between $\tilde{B}_{\mathrm{app}}$ and $\tilde{B}_{\mathrm{Abr}}$ is relatively small; the small change in the field only requires a small screening current magnitude. If we set the field at the edge to be $\tilde{B}_{\mathrm{app}} - \tilde{B}_{\mathrm{Abr}}$, and add a uniform field of $\tilde{B}_{\mathrm{Abr}}$ everywhere, then we get the boundary conditions that we are searching for – the field is the applied field at the edge; the field in the bulk is the Abrikosov field; and both the spatial variation and the magnitude of the screening currents and the field are now correctly determined according to GL2 and Maxwell's equations. Moreover, in the limit where $w_{\mathrm{s}} \simeq \lambda_{\mathrm{s}}$ (i.e. in the narrow limit where the junction is not sufficiently wide), the decay length may be long enough to prevent decay to zero - therefore, our bulk value is higher than the Abrikosov prediction, as expected.

4.7.2 General Transport Current Solutions

The transport current flows only in the x–direction, rather than the 2D screening currents – our Helmholtz equation is then significantly easier to solve since it is now only 1–dimensional. We are only concerned with the calculation of $\tilde{J}_{\mathrm{s:x}}(\tilde{y})$. The degree to which this flow is laminar in the y–direction is dictated by the width of the system and the penetration depth. In the presence of an applied current, our

boundary conditions are written as an asymmetric field gradient across the junction:

$$\tilde{B}(\tilde{y} = \pm\tilde{w}/2) = \pm\frac{\tilde{w}}{2}\frac{\langle \tilde{J}_{\rm app}\rangle_y}{\kappa_{\rm s}^2}. \tag{4.7.20}$$

Making use of Maxwell's equation and vector identities, Eq. (4.7.3) can be rewritten to read

$$\tilde{\boldsymbol{\nabla}}^2\tilde{\boldsymbol{B}} = \frac{\left|\tilde{\psi}\right|^2}{\tilde{m}_{\rm n}\kappa_{\rm s}^2}\tilde{\boldsymbol{B}} \tag{4.7.21}$$

This has a solution as a sum of exponentials, with the particular solution reading

$$\tilde{B}(\tilde{y}) = \frac{\tilde{w}\langle \tilde{J}_{\rm app}\rangle_y}{2\kappa_{\rm s}^2}\frac{\sinh\left(\dfrac{\tilde{y}\left|\tilde{\psi}\right|}{\sqrt{\tilde{m}_{\rm n}}\kappa_{\rm s}}\right)}{\sinh\left(\dfrac{\left|\tilde{\psi}\right|\tilde{w}}{2\sqrt{\tilde{m}_{\rm n}}\kappa_{\rm s}}\right)}. \tag{4.7.22}$$

We can use Maxwell's equation (Eq. (2.3.39)) to get the current, yielding the spatial variation of the transport current:

$$\tilde{J}_{\rm sx}(\tilde{y}) = \frac{\tilde{w}\langle \tilde{J}_{\rm app}\rangle_y\left|\tilde{\psi}\right|}{2\sqrt{\tilde{m}_{\rm n}}\kappa_{\rm s}}\frac{\cosh\left(\dfrac{\tilde{y}\left|\tilde{\psi}\right|}{\sqrt{\tilde{m}_{\rm n}}\kappa_{\rm s}}\right)}{\sinh\left(\dfrac{\left|\tilde{\psi}\right|\tilde{w}}{2\sqrt{\tilde{m}_{\rm n}}\kappa_{\rm s}}\right)}. \tag{4.7.23}$$

4.8 Extending Critical Current Density Calculations from 1D to 2D

It is well–known that decreasing the grain size in a superconducting system increases $J_{\rm c}$ [156, 157, 158]. The traditional picture is due to pinning; the smaller grains allow more grain boundaries to be present, and therefore the fluxons are pinned more strongly. However, in our context of junctions in wide systems, most of the current flows along the edges of the grains. Therefore, decreasing the grain size only brings the edges together, which doesn't significantly change the amount of current that can flow, but does increases the critical current density. Therefore, understanding how the current flows (and therefore, the order parameter) near the grain boundaries is pivotal in the description of $J_{\rm c}$; an understanding of the spatial variation of the order parameter near an interface becomes invaluable.

The framework so far has focused primarily on the calculation of the upper critical field for arbitrary material properties. Although useful, the primary technological limitation is the critical current density. In Section 4.6, we developed a framework for the calculation of the Josephson depairing current, which is inherently a 1D concept. Here, we shall extend these new results to provide an analytic description of the critical current density, $J_{\rm c}$, within a wide junction; the treatment varies according to the properties of the normal barrier or the coating. We shall treat three cases of interest: i) $\tilde{m}_{\rm n} \leq 1.0$, $\tilde{m}_{\rm c} \geq 1.0$, ii) $\tilde{m}_{\rm n} \leq 1.0$, $\tilde{m}_{\rm c} \leq 1.0$, and iii) $\tilde{m}_{\rm n} > 1.0$, $\tilde{m}_{\rm c} \geq 1.0$. The remaining case which we have not considered is when $\tilde{m}_{\rm n} > 1.0$, $\tilde{m}_{\rm c} \leq 1.0$ – in this case, the current flow will shunt around the resistive normal barrier, which is not an interesting case for real systems.

Fig. 4.15 shows a flowchart of the procedure we will follow to determine the critical current in 2D, for a SNS junction with arbitrary material properties. Our calculation

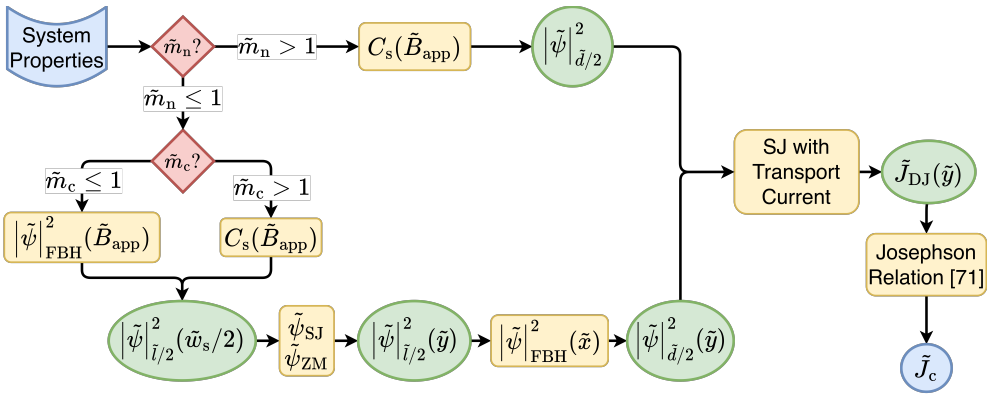

Figure 4.15: Flowchart for calculating the analytic prediction of the critical current density in 2D. The treatment is different depending on the mass of the normal barrier, $\tilde{m}_n$, and the mass of the coating, $\tilde{m}_c$. Here, C_s is the constant prefactor (Section 4.3), and $|\tilde{\psi}|$ is the normalised order parameter magnitude. $|\tilde{\psi}|_{\tilde{d}/2}$ denotes the order parameter magnitude at the normal barrier interface. $|\tilde{\psi}|_{\tilde{l}/2}$ denotes the order parameter magnitude in the bulk of the electrode; $|\tilde{\psi}|_{\tilde{l}/2}(\tilde{w}_s/2)$ denotes this magnitude at normal coating interface (located at $\tilde{y} = \tilde{w}_s/2$). Calculations make use of the FBH, Saint James (SJ) and FBHZM formalisms. The Josephson depairing current is then used in the Josephson relation (Section 2.5.2), as presented by Clem [72].

of the critical current density, $\tilde{J}_c$, requires the use of the Josephson relation (c.f. Eq. (2.5.66)) – the physical geometry of the system (w_s, l_s, d_n) in accounted for in the explicit result for the gauge invariant phase difference (Eq. (2.5.64)), whilst the material properties are contained in $\tilde{J}_{DJ}$. Specifically, the Josephson relation requires the variation of $\tilde{J}_{DJ}$ along the width of the normal barrier, $\tilde{J}_{DJ}(\tilde{y})$. Our new calculation of $\tilde{J}_{DJ}$ presented in Section 4.6 is for a single 1D narrow strip – we shall use this as our foundation to understand how we can obtain $\tilde{J}_{DJ}(\tilde{y})$. As shown in Section 4.6, our calculations of $\tilde{J}_{DJ}$ rely on an understanding of the order parameter at the centre of the normal barrier, $|\tilde{\psi}|_0$, which we can obtain trivially by knowing the variation of the order parameter along the interface, $|\tilde{\psi}|_{\tilde{d}_n/2}(\tilde{y})$. However, the procedure of calculating the spatial variation of the interfacial order parameter is dependent on the material properties – we shall outline the stages below.

We shall first consider the case where $\tilde{m}_n \leq 1$. In this instance, the normal barrier itself does not have a sheath – even though there are large counter-flowing currents flowing across the entire width of the junction, the majority of the width of the barrier does not carry a transport current. The distribution of current flow is set by the magnitude of the order parameter across the width according to GL2 – regions of low order parameter can only carry very little current. Therefore, the critical current is dominated by the current flowing near the edges of the system, which is dictated by the spatial variation of the order parameter across the width. We first calculate the order parameter magnitude at the interface in the bulk electrode, $|\tilde{\psi}|^2_{\tilde{l}/2}(\tilde{w}_s/2)$ – as in Section 4.3, the procedure for determining this is dependent on the presence/absence of an enhanced sheath, and therefore depends on the value of $\tilde{m}_c$ – in the case $\tilde{m}_c \leq 1$, the FBH framework is sufficient (Eq. (2.5.48)).

However, if $\tilde{m}_c > 1$, then a sheath emerges near the coating, and therefore the framework presented in Section 4.3 is adopted; the value of the order parameter magnitude at the coating interface is calculated using the double–linear approach. As discussed in Section 4.3, the sheath is correctly described by the Saint James formalism

alone. The knowledge of this interfacial order parameter allows us to calculate the full spatial variation of the order parameter in the bulk electrode using the Saint James formalism using the composite wavefunction in Eq. (4.3.24) – this yields an analytic calculation of $\left|\tilde{\psi}\right|^2_{\tilde{l}/2}(\tilde{y})$ for a coating with arbitrary mass. We shall make then use of the FBH machinery – for a given field value, at each point in the bulk, $\left|\tilde{\psi}\right|^2_{\tilde{l}/2}$, there is a unique corresponding magnitude at the interface, $\left|\tilde{\psi}\right|^2_{\tilde{d}_\mathrm{n}/2}$. Therefore, we can obtain $\left|\tilde{\psi}\right|^2_{\tilde{d}_\mathrm{n}/2}(\tilde{y})$ as required – knowledge of the interfacial order parameter allows us to use the results in Section 4.6 at each point along the width of the junction, and therefore obtain $\tilde{J}_\mathrm{DJ}(\tilde{y})$ as required.

Conversely, if the normal barrier is resistive ($\tilde{m}_\mathrm{n} > 1$), then the physics is very different. Since $\tilde{m}_\mathrm{n} > 1$, a sheath emerges along the junction above B_c2; the entire width of the barrier is able to carry current, and the entire core of the bulk superconductor is normal apart from the sheath near the edges of the system. Therefore, we cannot adopt the same philosophy that the behaviour in the bulk dictates the behaviour across the barrier. Instead, we can calculate the value of the order parameter magnitude at the barrier interface ($\left|\tilde{\psi}\right|_{\tilde{d}_\mathrm{n}/2}$) using the standard procedure as described in Section 4.3. However, since the sheath is uniform, this interfacial order parameter, $\left|\tilde{\psi}\right|^2_{\tilde{d}_\mathrm{n}/2}(\tilde{y})$, is also uniform along the width. We can then use this within the procedure in Section 4.6 to obtain $\tilde{J}_\mathrm{DJ}(\tilde{y})$ as required, which is therefore also uniform along the entire barrier width – each point carries the same amount of current. We have neglected the small corner effects here, where the order parameter near the corner is enhanced due to the proximity to the coating, which may have its own sheath, depending on the particular value of $\tilde{m}_\mathrm{c}$. However, above $\tilde{B}^*_\mathrm{c2}$, the entire system is normal other than these corners – there is no additional ability to carry current past $\tilde{B}^*_\mathrm{c2}$.

Finally, as presented in Fig. 4.16, we can then perform additional iterations. We will first calculate a initial prediction of the critical transport current, using an order parameter spatial variation calculated in zero transport current. We then obtain the spatial variation of both the transport current and the screening current following our results in Section 4.7, and understand the local current flowing at each point. Therefore, we can correspondingly suppress the order parameter as required using the FBH framework, since it provides a clear 1–to–1 correspondence between the order parameter spatial variation and a particular value of applied field and current. We can then use this suppressed order parameter to calculate a new value of the transport current, and iterate through this loop until convergence. In practice, the changes in the order parameter are small enough, so that the zero–transport current calculation is typically sufficient.

4.9 Conclusions

In this section, we have demonstrated how we can extend the formalism of Saint James to describe the behaviour near surfaces of arbitrary mass and $\tilde{\alpha}_\mathrm{n}$. We have shown how one can extract the effective upper critical field for S/N systems and identified the relevant dependencies on material parameters and electrode thickness. We have also related these results to existing known limits in the literature. This work serves as a generalisation of the previous results, which only considered insulating boundaries. We have also presented our new analytic solutions for the spatial variation of the order

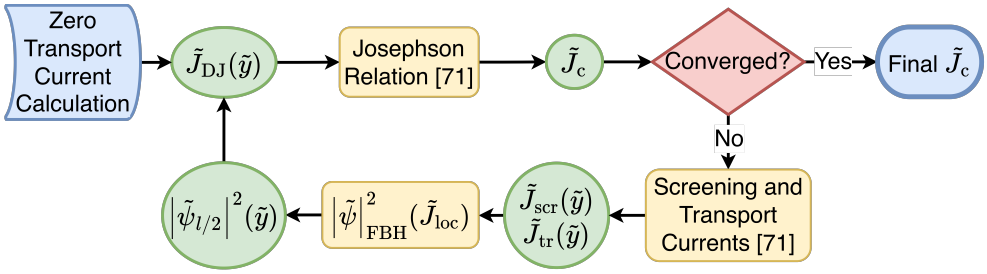

Figure 4.16: Flowchart for the iteration of the critical current density in the presence of a transport current. The zero transport current calculation is the output of Fig. 4.8. Here, $\tilde{F}_{l/2}(\tilde{y})$ denotes the spatial variation of the order parameter magnitude in the bulk of the electrode. Similarly, $\tilde{J}_{\mathrm{scr}}(\tilde{y})$ and $\tilde{J}_{\mathrm{tr}}(\tilde{y})$ denote the spatial variation of the screening and transport current densities respectively, calculated from the generalization of Clem to arbitrary width and κ_{s} (c.f Section 4.7).

parameter near boundaries of arbitrary mass, and the approaches we have adopted to determine the prefactor. We have demonstrated how the Abrikosov formalism can be used to derive the prefactor exactly in the high field regime, and have proposed an empirical double–linear approximation to extend this prefactor below B_{c2} for cases where a surface barrier is present ($\tilde{m}_{\mathrm{c}} > 1.0$). We have presented TDGL evidence for how the FBH interfacial order parameter may be used to describe the field dependence in systems where $\tilde{m}_{\mathrm{c}} < 1.0$ and no surface barrier exists.

We have also applied this framework in finite systems. In particular, we considered an SNS geometry, which is particularly relevant for the description of polycrystalline materials. We have identified the upper critical field in this geometry as a function of material parameters and normal barrier thickness, and demonstrated how they again reduce to known limiting values. Most interestingly for our application, we have also described a framework to extract the maximum current density that can pass through the barrier. We have demonstrated the dependence of this solution on the material parameters and system geometry, and explicitly identified how each parameter affects the maximum transport current through the order parameter at the centre of the junction.

We have presented an extension of the screening currents of Clem to arbitrary κ and width, and demonstrated the resulting spatial variations. We also present a use for this in ensuring that the Abrikosov field can be obtained in the bulk, in that we guarantee that the current flow partially screens out the applied field at the edge. We also provided an analytic form for the spatial variation of the transport currents present in the system.

Finally, we have presented our procedure for the determination of the critical current. The generalised theory presented in this chapter is formally in 1D – it is essential for obtaining more useful technological parameters, such as the critical current density in 2D for arbitrary systems. The flowchart presented here will form the backbone of our approach for obtaining analytic approximations of the critical current density over the entire field range for arbitrary Josephson junction systems that can be compared with our TDGL calculations.

Chapter 5

Critical Current Densities for Wide Junctions with Arbitrary Material Properties

5.1 Introduction

Although the effective upper critical field is an interesting and useful parameter, the main quantity of interest for future applications is the critical current density, $\tilde{J}_{\rm c}$. In particular, the most useful technological regime is certainly in the high–field regime; we are interested in capturing the behaviour of $\tilde{J}_{\rm c}\left(\tilde{B}_{\rm app}\right)$ accurately across this entire width. In the last chapter, we developed a framework that converts our understanding of the spatial variation of the order parameter near interfaces of arbitrary mass, the corresponding impact on $B^*_{\rm c2}$, and the Josephson depairing current density that can flow through a barrier with a given set of material properties.

In this chapter, we shall apply the prescription from the flowchart presented in Section 4.8 to provide analytical predictions of the critical current density in a variety of geometries. We will compare TDGL simulations for each different geometry described, and therefore validate the analytic prescription for $\tilde{J}_{\rm c}\left(\tilde{B}_{\rm app}\right)$. To the best of our knowledge, this is the first framework for providing an analytic prediction for the critical current density for systems with arbitrary width and geometry. Most importantly relevant for technological material, this is the first framework that provides an accurate description for systems where the grain boundary is more resistive than the grain. In fact, we will see that our framework is essential in this region of material parameter phase space – no other approach successfully captures the complexity of the physics near the surface barrier.

We shall first present some predictions of $\tilde{J}_{\rm c}\left(\tilde{B}_{\rm app}\right)$ generated from the three different analytic approaches of calculating $J_{\rm DJ}$ – the original FBH, our new Saint–James formalism, and the functional form approximation. Next, we shall apply the flowchart to the geometries with a normal barrier mass $\tilde{m}_{\rm n} = 1.0$ and with insulating coatings ($\tilde{m}_{\rm c} \to \infty$). In this particular geometry, a sheath exists only along the the horizontal edges of the coating, but not near the barrier. We shall observe the effect of the sheath emerging in these geometries, and compare our predictions to the equivalent FBH calculation. Crucially, we perform these comparisons for a range of superconducting widths, validating our approach to describe both narrow and wide Josephson junctions with arbitrary materials. Our next geometry then describes polycrystalline materials

more closely. We consider a junction geometry with both normal coatings and barriers ($\tilde{m}_{\mathrm{n}} = \tilde{m}_{\mathrm{c}} = 1.0$) – in this case, no surface sheath exists. Again, we perform simulations with a range of widths, and compare our calculation to FBH. Most importantly, we shall then consider our closest analogue for a real polycrystalline material, and study geometries where both the coating mass and the normal barrier mass are resistive ($\tilde{m}_{\mathrm{n}} = \tilde{m}_{\mathrm{c}} = 10.0$), and a sheath is present along all edges of the electrodes. We shall see how our new formalism is essential for capturing the behaviour of this system accurately. Finally, we provide some preliminary studies of junction array systems, which provides insight into how one can extend our study of a single junction system to describe a full polycrystalline material for arbitrary widths and material parameters.

5.2 Preliminary Data

Fig. 5.1 demonstrates the output of the flowchart shown in Fig. 4.15 – we have shown the specific case of a coated high–mass Josephson junction where $\tilde{m}_{\mathrm{n}} = \tilde{m}_{\mathrm{c}} = 10.0$. We have presented the calculations with the three different calculations of $\tilde{J}_{\mathrm{DJ}}$ presented in this thesis. The green dashed–dotted analytic line in Fig. 5.1 (the new Saint–James framework), finds an exact numerical solution of Eq. (4.5.7) (using Eqs. (4.5.16) and (4.5.17)) using the general forms of a_{n} and a_{s} (Eq. (4.6.11)), which has been cut off at the point which it becomes larger than the Fink value. The red solid line in Fig. 5.1 is the empirical functional form that provides a good agreement over the full field range (Eq. (4.6.14)). Finally, the blue dashed line is the equivalent calculation of $\tilde{J}_{\mathrm{DJ}}$ from FBH (Eq. (2.5.47)). Of course, all three approaches then follow Clem's work [72] to calculate J_{c} from J_{DJ}.

The Clem framework (as discussed in Section 2.5.2) contains oscillations, capturing the movement of fluxons through the junction. In a TDGL system, fluxons may also move into the bulk of the electrode, causing an additional phase shift across the junction and therefore leading to a sharp jump in the field dependence of the critical current density. This can be observed in Fig. 5.1 (top), where we see close agreement between the oscillations and the TDGL data in low field, until approximately $B_{\mathrm{app}} = 0.15B_{\mathrm{c2}}$, where the field is now sufficiently high that a fluxon has entered the bulk of the electrode. However, as seen in Fig. 5.1, even though fluxons can cause a phase shift, the magnitude of the field dependence remains broadly unchanged. This is particularly evident in higher fields and in wider systems (c.f. Sections 5.3, 5.4 and 5.5), where fluxons can enter the system much more easily, and these sharp jumps are much more frequent. Therefore, comparing the envelope of the analytic prediction to the TDGL data is perhaps much more useful, since the agreement of the specific positions of the maxima or minima between TDGL and analytic solutions are no longer important. Moreover, as we will discuss in Section 5.6, in a real 3D polycrystalline material, it is likely that any oscillations of a single SNS junction will be 'washed out', and so the remaining envelope is the most useful technological comparison.

Surprisingly, even though our analytic calculation has a discontinuous gradient at some field value, there is no corresponding sharp discontinuity in the critical current density trace, $\tilde{J}_{\mathrm{c}}\left(\tilde{B}_{\mathrm{app}}\right)$. However, the accuracy is clearly quite poor near $0.7B^{*}_{\mathrm{c2}}$; since the exact solution does tend to exceed the FBH solution, the solution is

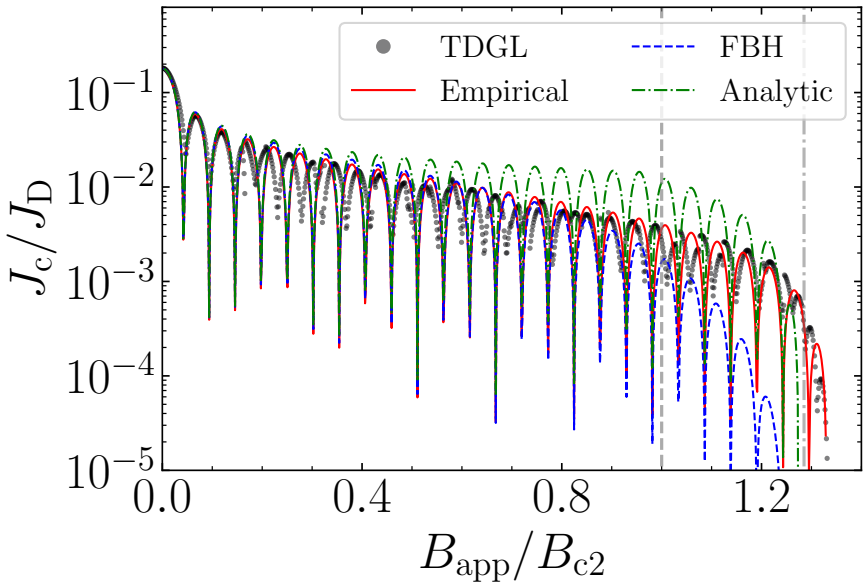

(a) Oscillations

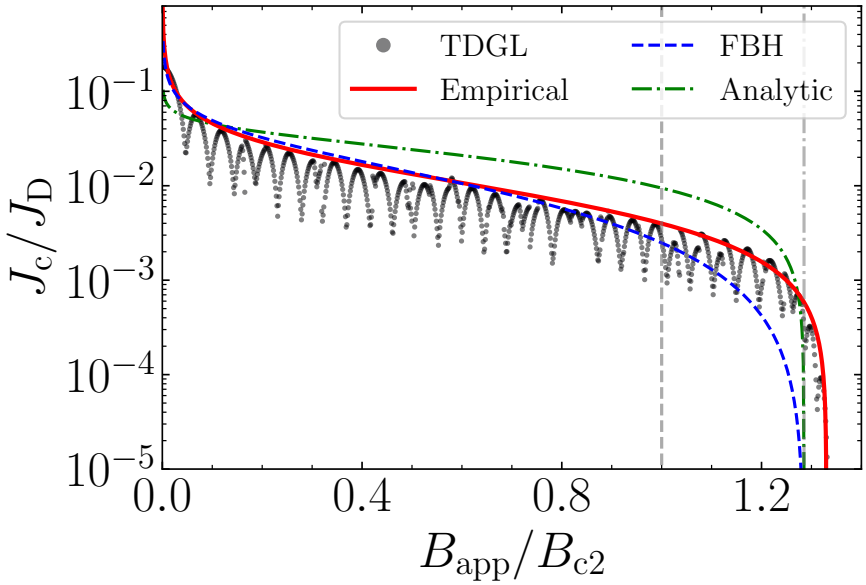

(b) Envelopes

Figure 5.1: Critical current density as a function of applied magnetic field for a SNS junction, where $\tilde{w}_s = 16.0$ and $\tilde{m}_n = \tilde{m}_c = 10.0$. In all cases, $\tilde{d}_n = 0.5$, $\tilde{\alpha}_n = -1.0$, $\tilde{\beta}_n = 1.0$ and $\kappa_s = 8.0$. The coating thickness was fixed to be $\tilde{w}_c = 3.0$. TDGL simulations are shown as solid markers, whilst various lines demonstrate different approaches of generating an analytic solution from the flowchart presented in Fig. 4.15. The solid and dashed–dotted lines use the new calculations of $\tilde{J}_{DJ}$ shown in Chapter 4 – the solid lines are using the empirical functional form (Eq. (4.6.14), with n and B^*_{c2} left as free parameters, fitted to be $n = 0.90$ and $B^*_{c2} = 1.33$), whilst the dashed–dotted lines are using the exact numerical solution (Eq. (4.5.7), using Eqs. (4.5.16) and (4.5.17)), cut off to remain physical (below the zero–field Fink value). The dashed lines are the equivalent envelopes using $\tilde{J}_{DJ}$ calculated from FBH shown in Eq. (2.5.47). The top figure presents the full analytic envelope, with the oscillations emerging from the Clem solution (c.f. Section (2.5.2)). The bottom figure presents the envelope to these oscillations, allowing a clearer comparison of the analytic prediction and the TDGL simulation. Vertical lines showing B_{c2} and B^*_{c2} are shown.

systematically higher than the TDGL simulation. Conversely, we can see that our empirical functional form actually provides excellent agreement across the entire field

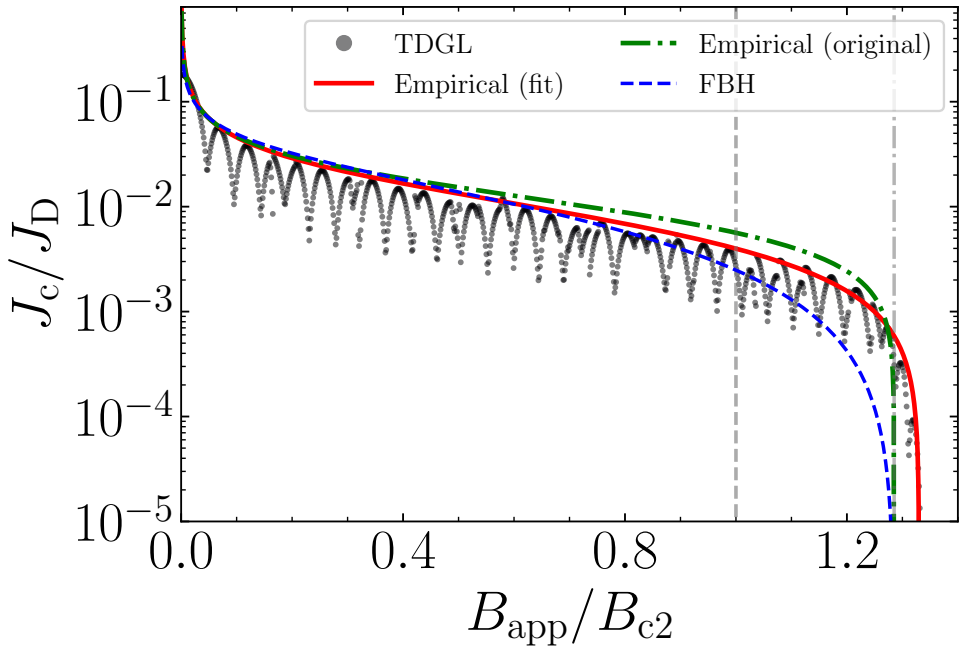

Figure 5.2: Critical current density as a function of applied magnetic field for a SNS junction, where $\tilde{w}_s = 16.0$ and $\tilde{m}_n = \tilde{m}_c = 10.0$. In all cases, $\tilde{d}_n = 0.5$, $\tilde{\alpha}_n = -1.0$, $\tilde{\beta}_n = 1.0$ and $\kappa_s = 8.0$. The coating thickness was fixed to be $\tilde{w}_c = 3.0$. TDGL simulations are shown as solid markers, whilst various lines demonstrate different approaches of generating an analytic solution from the flowchart presented in Fig. 4.15. The solid and dashed–dotted lines use the empirical functional form (Eq. (4.6.14) – the solid line left n and B^*_{c2} as free parameters, (fitted to be $n = 0.90$ and $B^*_{c2} = 1.33$), whilst the dashed–dotted line took the original calculations from Chapter 4 (with $n = 0.60$ from Table 4.1 and $B^*_{c2} = 1.28$ (c.f. Fig. 4.8)). The dashed lines are the equivalent envelopes using $\tilde{J}_{DJ}$ calculated from FBH shown in Eq. (2.5.47). The top figure presents the full analytic envelope, with the oscillations emerging from the Clem solution (c.f. Section (2.5.2)). The bottom figure presents the envelope to these oscillations, allowing a clearer comparison of the analytic prediction and the TDGL simulation. Vertical lines showing B_{c2} and B^*_{c2} are shown.

range. This functional form has better agreement with the TDGL calculation than the exact numerical calculation – this essentially has provided a good first order correction to the omission of the non–linear term. Moreover, it also does not require any additional cut off to remain physical, and by construction, has the correct limits in both zero field and in extremely high fields near B^*_{c2}. Of course, it has the drawback that we do not have full analytic understanding of the material parameter dependence of the power law exponent n. However, in the remaining sections, we will use this empirical functional form to compare with the TDGL data. Moreover, the calculation of the effective upper critical field remains exact, rather than an external parameter that is included in the FBH solution. As alluded to in Section 4.6, we can see that the solution using $\tilde{J}_{DJ}$ from FBH significantly underestimate J_c in Fig. 5.1.

We briefly discuss numerical artefacts in the TDGL data shown in Fig. 5.1; in particular, the oscillations in $\tilde{J}_c$ persist above B^*_{c2}. One possible explanation could be that the grid step used in these simulations ($h_x = 0.1\xi_s$) is too coarse – however, it is too computationally expensive to perform these simulations for the widths of interest unless one uses a more advanced method, such as a multigrid approach [118]. Another cause may be that the Saint–James formalism we have developed considers systems which are semi–infinite – however, the TDGL systems considered in the simulations

are finite. Notably, the construction of the coating geometry leads to additional enhancement near the corners. Physically, these corners should not provide any current since the bulk of the system is zero. However, although the order parameter in the TDGL simulation is small, it is finite, and therefore likely non–zero in the bulk of the system. Therefore, the system can indeed carry some transport current, which are so small and close to the noise floor of the TDGL system. Therefore, we regard these oscillations beyond B_{c2}^{*} as non–physical. As can be seen in Fig. 5.2, there is only a small difference in the resulting envelopes between the fitted values for B_{c2}^{*} and n compared to the results seen previously in Chapter 4.

5.3 Insulating Coatings: $\tilde{m}_{\mathrm{n}} = 1, \tilde{m}_{\mathrm{c}} = \infty$

We first consider the geometry which has been mostly commonly considered within existing analytic theory; the case of an SNS junction with insulating coatings. For this case, we consider the barrier to have the same mass as the superconductor; we set $\tilde{m}_{\mathrm{n}} = 1.0$, but allow the barrier to be non–superconducting and set $\tilde{\alpha}_{\mathrm{n}} = -1.0$. As we saw in Figs. 4.10 and 4.11, there was not a significant difference between the FBH calculation and our new calculation of $\tilde{J}_{\mathrm{DJ}}$, and so we do not expect a significant difference between the resulting behaviour in the critical current density trace, $\tilde{J}_{\mathrm{c}}\left(\tilde{B}_{\mathrm{app}}\right)$ – we attributed this to the lack of the sheath near the barrier. However, as discussed in Section 4.6.2, our method is implicitly rigorous since it does not require any input of the effective upper critical field as a free parameter, and the field dependence (proportional to $1 - \tilde{B}_{\mathrm{app}}/\tilde{B}_{\mathrm{c2}}^{*}$) is rigorously derived through the solution.

In Fig. 5.3, we provide the 2D spatial variation of the order parameter magnitude and magnetic field distribution with $\tilde{B}_{\mathrm{app}} = 0.8$ and zero transport current. With the insulating boundary conditions, we can clearly see the sheath region near the top and bottom edge, where the order parameter is significantly higher near the interface than in the bulk. We can see the obvious hexagonal vortex lattice structure deep in the bulk, and also observe disruptions to this structure near any surface barrier (such as the normal barrier or the insulating coating edge). We note that the magnetic field is actually lower than the applied field in the sheath region, associated with the counter rotating currents flowing within the sheath region that screen out the applied field. We also note that the density of the fluxons is significantly higher in the normal barrier, due to the lower energy barrier for a fluxon to nucleate in the normal region. We also note that despite the barrier thickness only being $\tilde{d}_{\mathrm{n}} = 0.5$, the fluxons are able to sit within the the barrier and extend far beyond this chemical thickness, similarly to that seen in Fig. 3.2.

Fig. 5.4 provides the spatial variation in the y–direction of the order parameter magnitude and the supercurrent density deep in the bulk of the electrode (at $\tilde{x} = \tilde{l}_{\mathrm{s}}/2$), at three different fields. As we saw in Fig. 5.3, if the field is sufficiently high, then many fluxons can exist in the electrode itself. To avoid taking a slice which is overly susceptible to the exact positions of the fluxons, we instead consider take an average over a fluxon spacing, a_0 – we consider all slices from $\tilde{x} \in \left[\tilde{l}_{\mathrm{s}}/2 - \tilde{a}_0/2, \tilde{l}_{\mathrm{s}}/2 + \tilde{a}_0/2\right]$, and then take an average at each y–coordinate. We consider three characteristic field regimes; 'high–field' (between $\tilde{B}_{\mathrm{c2}}$ and $\tilde{B}_{\mathrm{c2}}^{*}$), 'intermediate–field' (between $\tilde{B}_{\mathrm{c1}}$ and $\tilde{B}_{\mathrm{c2}}$), and low field (zero applied field). We shall discuss each in turn. The high–field

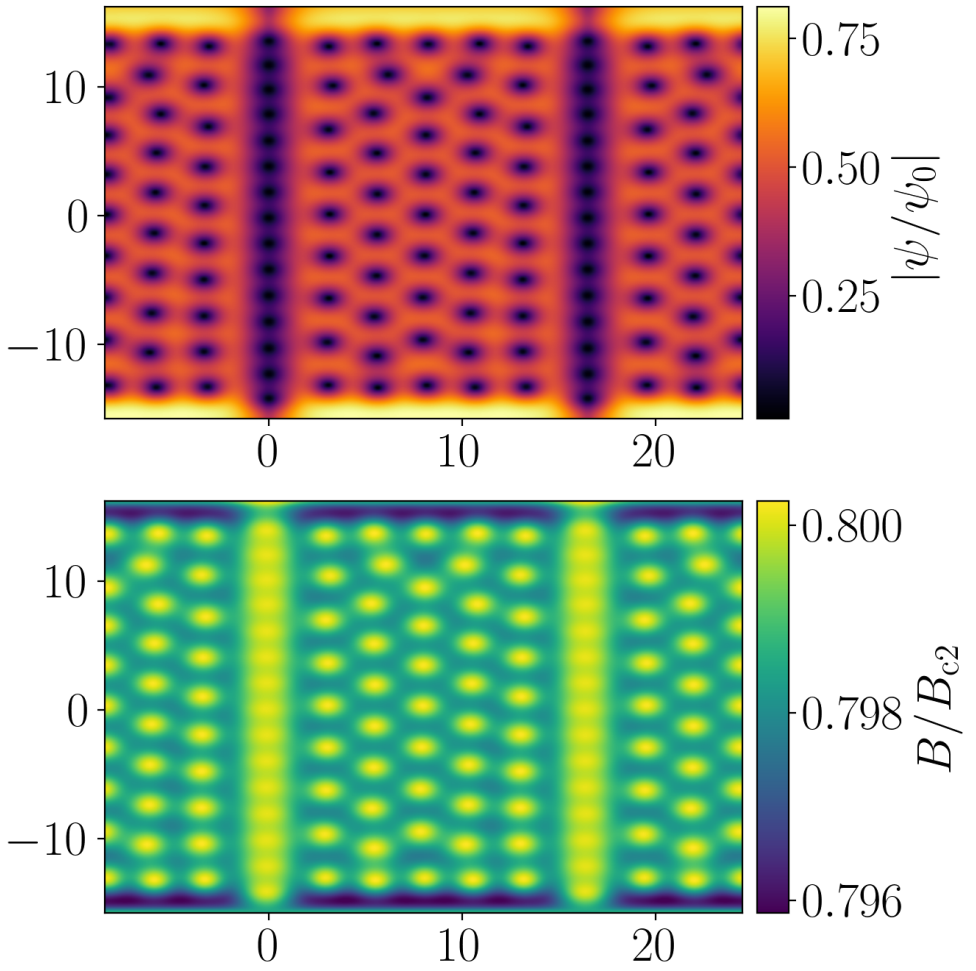

Figure 5.3: A snapshot of the normalized order parameter magnitude (top) and magnetic field distribution (bottom) for an SNS junction with insulating coatings, where the applied field $\tilde{B}_{\mathrm{app}} = 0.8$ and zero applied transport current. The TDGL simulation system has $\tilde{w}_{\mathrm{s}} = 32.0$, $\tilde{l}_{\mathrm{s}} = 16.0$, $\tilde{d}_{\mathrm{n}} = 0.5$, $\tilde{\alpha}_{\mathrm{n}} = -1.0$, $\tilde{m}_{\mathrm{n}} = 1.0$, $\tilde{\beta}_{\mathrm{n}} = 1.0$ and $\kappa_{\mathrm{s}} = 8.0$.

case is well–described by the Saint James formalism presented in Section 4.2 – the order parameter exists only in the insulating sheath, dropping to zero in the bulk of the electrode, and the screening currents are counter rotating in the sheath. We note that when a transport current flows, the order parameter is slightly asymmetric, due to the applied current producing an antisymmetric self-field in the system. However, in practice, these effects are marginal, particularly in high fields. The intermediate–field case is perhaps the most complex, since we not only have to account for the sheath near the edge, but also the fact that the bulk is no longer zero below $\tilde{B}_{\mathrm{c2}}$. In this case, following the flowchart in Fig. 4.15, we have used the composite wavefunction in Eq. (4.3.24), accounting for contribution from the both the Saint James framework which captures the enhancement near the edge, and the zero–mass FBH contribtion which captures the behaviour more accurately in the bulk. We can see that the TDGL data now contains oscillations due to the fluxons in the system. In particular, we can see that although the local currents near the fluxons are large, they are equal and opposite on each side of a given fluxon, and so their average contribution is close to zero; therefore, the counter rotating currents from the Saint James framework remains sufficient. Finally, we conclude with the spatial variation in zero–field: Since the Saint James formalism contains terms proportional to $1/\tilde{B}_{\mathrm{app}}$, the solution is

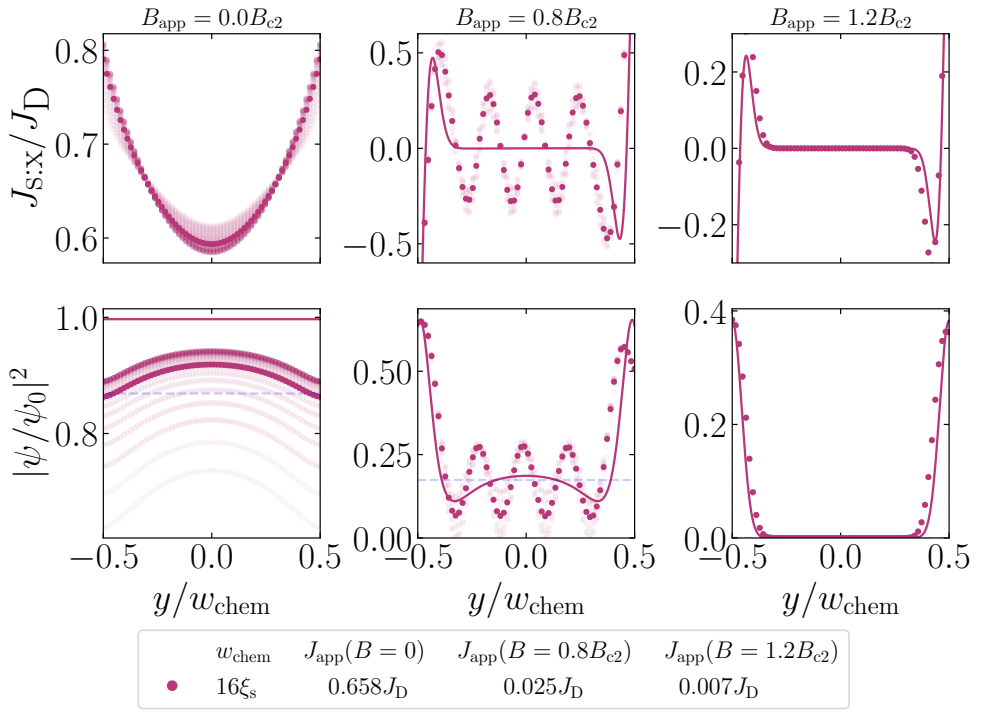

Figure 5.4: Spatial variation of the supercurrent density (top) and normalized order parameter magnitude (bottom) at three different applied magnetic fields and $J_{app} = 0.95J_c$, for an SNS junction with insulating coatings. The spatial variation is shown in the bulk of the electrode ($\tilde{x} = \tilde{l}_s/2$) – the faint dots are slices within a fluxon spacing of $\tilde{x} = \tilde{l}_s/2$, and the solid dots are the average over all at a given y–coordinate. The faint blue line is the Abrikosov prediction for the order parameter in the bulk (Eq. (2.3.33)). The solid lines denote analytic predictions for the screening current and the order parameter magnitude (Eq. (2.4.26) and Eq. (4.3.24)). The TDGL simulation system has $\tilde{w}_s = 16.0$, $\tilde{l}_s = 16.0$, $\tilde{d}_n = 0.5$, $\tilde{\alpha}_n = -1.0$, $\tilde{m}_n = 1.0$, $\tilde{\beta}_n = 1.0$ and $\kappa_s = 8.0$.

formally infinite in exactly zero–field - in this case, we use the FBH formalism alone. To first order, in zero field and zero transport current, there are no screening currents and the order parameter is completely uniform across the width of the system (c.f. Eq. (2.3.6)). However, with no applied field, the maximum current that can be passed through the system is largest, and so the suppression of the order parameter due to the transport current is significant. In the wide systems, the transport current follows a London–like distribution, as presented in Section 4.7, and so the current is larger near the edge. In this system, where $\tilde{w}_s = 16.0$ and $\kappa_s = 8.0$, we can see that the current density is still at a minima in the centre of the system, but is non–zero. Therefore, the order parameter is suppressed along the entire width; but the magnitude of the suppression is proportional to the local current flowing. In extremely wide systems, such as $\tilde{w}_s = 128.0$ and $\kappa_s = 8.0$, the current is very small far away from the surfaces, and so the order parameter in the bulk is essentially the Meissner value.

Finally, we present the results of the analytic prediction in Section 4.8 in Fig. 5.5. We provide the envelopes from both our new $\tilde{J}_{DJ}$ calculation, and the equivalent FBH calculation. As we already discussed, $\tilde{J}_{DJ}$ is not significantly different between the two, so the envelopes exhibit broadly similar behaviour. We can see that the agreement between the TDGL and our new analytic prediction is very good at high field; the FBH is quite reasonable as well. We have provided a comparison over a wide range of widths; we can see that our methodology presented in Fig. 4.15 provides a

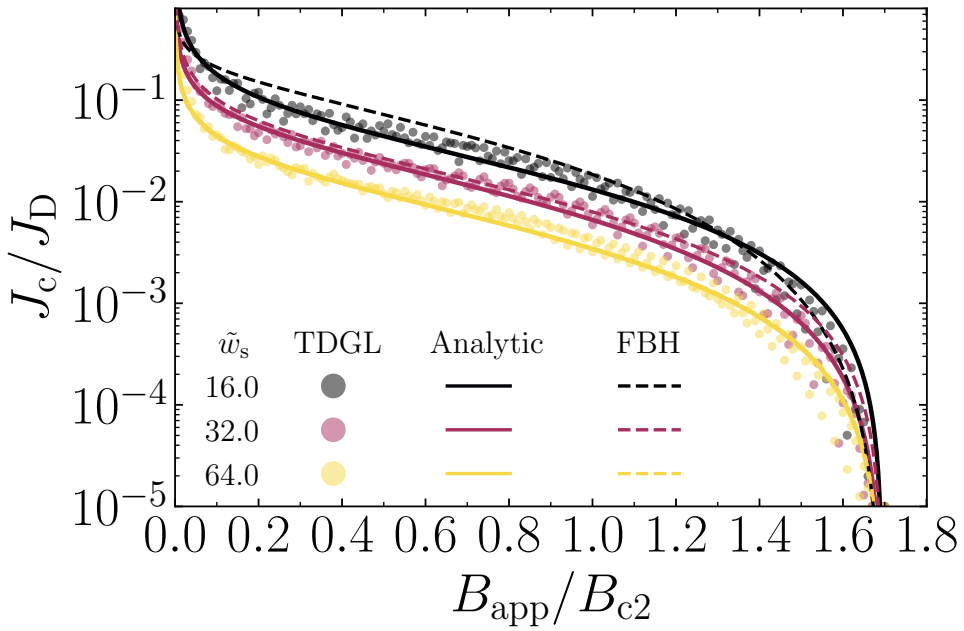

Figure 5.5: Critical current density as a function of applied magnetic field for a range of widths for a SNS junction with insulating coatings. In all cases, $\tilde{m}_n = 1.0$, $\tilde{d}_n = 0.5$, $\tilde{\alpha}_n = -1.0$, $\tilde{\beta}_n = 1.0$ and $\kappa_s = 8.0$. TDGL simulations are shown as solid markers. The solid lines are the envelopes generated from the flowchart presented in Fig. 4.15, using the new calculations of $\tilde{J}_{DJ}$ shown in Chapter 4 (Eq. (4.6.14) with $B_{c2} = 1.695$ and $n = 1.77$). Here, n has been fitted to optimise agreement with the TDGL data. The dashed lines are the equivalent envelopes using $\tilde{J}_{DJ}$ calculated from FBH shown in Eq. (2.5.47).

good description of the field dependence of the critical current density. Even though the Clem solution has little notion of the effective upper critical field (because it primarily addresses the phase of the order parameter rather than its magnitude), the field dependence of $\tilde{J}_{DJ}$ does, and so the solution contains the correct limits in both the high and low field extreme cases. Since $\tilde{m}_n = 1$, the general approach of treating the full 2D system as a sum of local slices performs well – in this case, the behaviour in the bulk electrode directly dictates the behaviour at the interface here. In this way, the total current density for any system where $\tilde{m}_n \leq 1$ (with no sheath along the normal barrier) can be well understood as a collection of local 1D slices.

5.4 Normal Coatings: $\tilde{m}_n = \tilde{m}_c = 1$

We now consider a geometry which brings us closer to the description of a real polycrystal – the case of an SNS junction where the coatings and the normal barrier have the same material properties. We will consider the barrier and the coating to have the same mass as the superconductor; we set $\tilde{m}_n = \tilde{m}_c = 1.0$ and $\tilde{\alpha}_n = -1.0$. As in Section 5.3, we are considering $\tilde{m}_n = 1.0$, and so again we do not have a significant difference between the FBH calculation and our new calculation of $\tilde{J}_{DJ}$.

In Fig. 5.6, we again provide the 2D spatial variation of the order parameter magnitude and magnetic field distribution with $\tilde{B}_{app} = 0.5$ and zero transport current. We can again see similar traits to the case of insulating coatings – the bulk has a clear vortex lattice structure, and the fluxons can again exceed the chemical thickness of the normal barrier, since the barrier is sufficiently strongly coupled. However, the

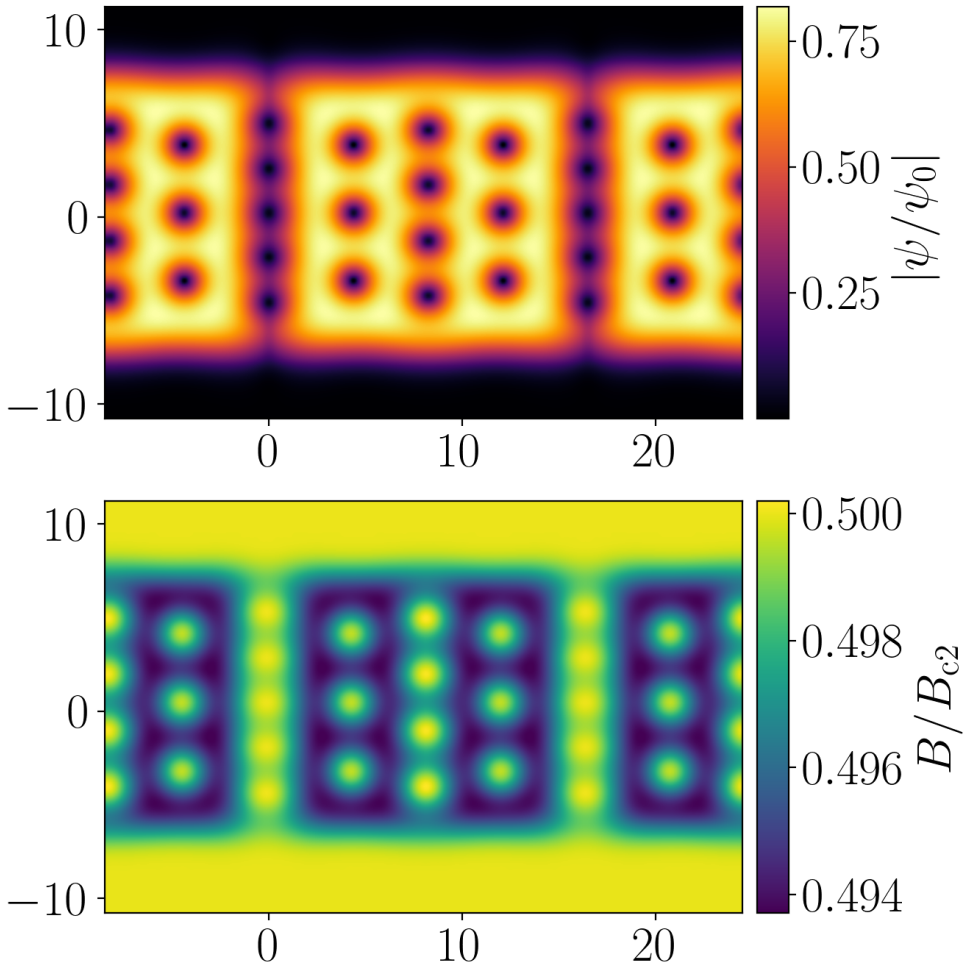

Figure 5.6: A snapshot of the normalized order parameter magnitude (top) and magnetic field distribution (bottom) for an SNS junction with normal coatings, where the applied field $\tilde{B}_{app} = 0.5$ and zero applied transport current. The coating thickness is set at $\tilde{w}_c = 3.0$, and $\tilde{m}_c = 1.0$. The TDGL simulation system has $\tilde{w}_s = 16.0$, $\tilde{l}_s = 16.0$, $\tilde{d}_n = 0.5$, $\tilde{\alpha}_n = -1.0$, $\tilde{m}_n = 1.0$, $\tilde{\beta}_n = 1.0$ and $\kappa_s = 8.0$.

key difference comes from the behaviour near the normal interface in accordance with the familiar boundary condition – instead of the order parameter being constant (and indeed, maximal) near the edge, we instead have a recovery of the order parameter away from the normal interface, over the length scale of the coherence length. This slight difference plays a crucial role; instead of the maximal current flowing near the edges, which decays as we move into the bulk, the current flow is minimal near the edge where the order parameter is small. As the order parameter recovers, the current flow increases, until a peak occurs, where the order parameter has recovered to the bulk value. Specifically, if we are sufficiently far away from the interface such that there is no coupling effects to the normal barrier, the system now behaves just as it did in the bulk of Fig. 5.3 – the screening currents now decay exponentially as before. Therefore, where the order parameter is smaller, the current carrying capacity is reduced. This can be related quite simply to the capacity of the insulating system, by accounting for the average of the order parameter recovery. However, with this understanding of the knowledge, we can proceed to understand the effect of this normal interface on the critical current density now.

Fig. 5.7 provides the spatial variation in the y–direction of the order parameter magnitude and the supercurrent density deep in the bulk of the electrode (at $\tilde{x} = \tilde{l}_s/2$),

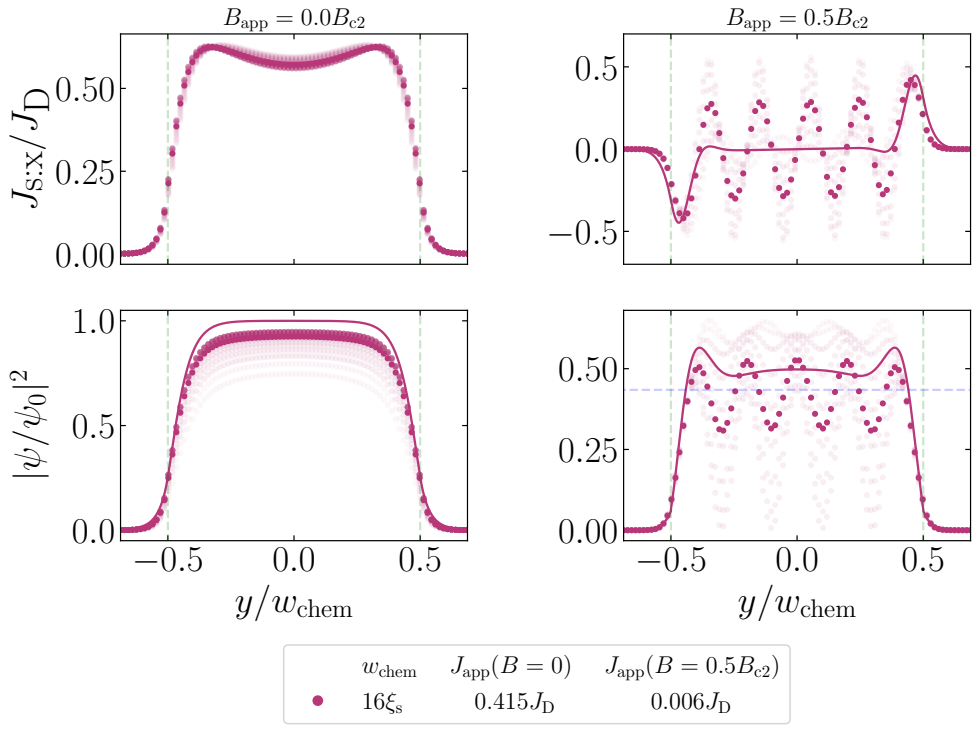

Figure 5.7: Spatial variation of the supercurrent density (top) and normalized order parameter magnitude (bottom) at two distinct applied magnetic fields and $J_{app} = 0.95J_c$, for an SNS junction with normal coatings ($\tilde{m}_c = 1$). The spatial variation is shown in the bulk of the electrode ($\tilde{x} = \tilde{l}_s/2$) – the faint dots are slices within a fluxon spacing of $\tilde{x} = \tilde{l}_s/2$, and the solid dots are the average over all at a given y–coordinate. The faint blue line is the Abrikosov prediction for the order parameter in the bulk (Eq. (2.3.33)). The solid lines denote analytic predictions for the screening current and the order parameter magnitude (Eq. (2.4.26) and Eq. (4.3.24)). The TDGL simulation system has $\tilde{w}_s = 16.0$, $\tilde{l}_s = 16.0$, $\tilde{d}_n = 0.5$, $\tilde{\alpha}_n = -1.0$, $\tilde{m}_n = 1.0$, $\tilde{\beta}_n = 1.0$ and $\kappa_s = 8.0$.

at zero field and at $\tilde{B}_{app} = 0.5$. Again, we see good agreement between the TDGL and the analytic distributions, where we use the composite wavefunction in Eq. (4.3.24). It is somewhat surprising that the FBH wavefunction alone does not provide a good approximation of the distribution in this case, since there is no sheath to accurately describe. However, this has provided poor agreement in high field, particularly close to the interface. We attribute this to the 1D nature of the FBH solution, which does not capture the non–uniformity of the screening current flowing near the interface – this is naturally incorporated in the Saint James formalism. Again, since the Saint James formalism is formally undefined in exactly zero–field, we use the FBH solution alone, which can capture the recovery away from the interface. As discussed above, we can see the corresponding spatial variation of the supercurrent density – we briefly note here than in the bulk, far away from the interface, both the order parameter and the supercurrent density are the same as in Fig. 5.4. This agreement with TDGL data is a key motivator in the formulation of the composite wavefunction in Eq. (4.3.24).

Finally, we present the critical current density as a function of field in Fig. 5.8. We can see that particularly for the wider widths, the FBH solution is too low in high fields, but too high in low fields. Although the differences in $\tilde{J}_{DJ}$ are slight, we can see that there is an improved agreement with the TDGL data from our new analytic calculation. In contrast to the data with insulating coatings, where the critical current dropped to zero very sharply near the effective upper critical field, the decrease in the

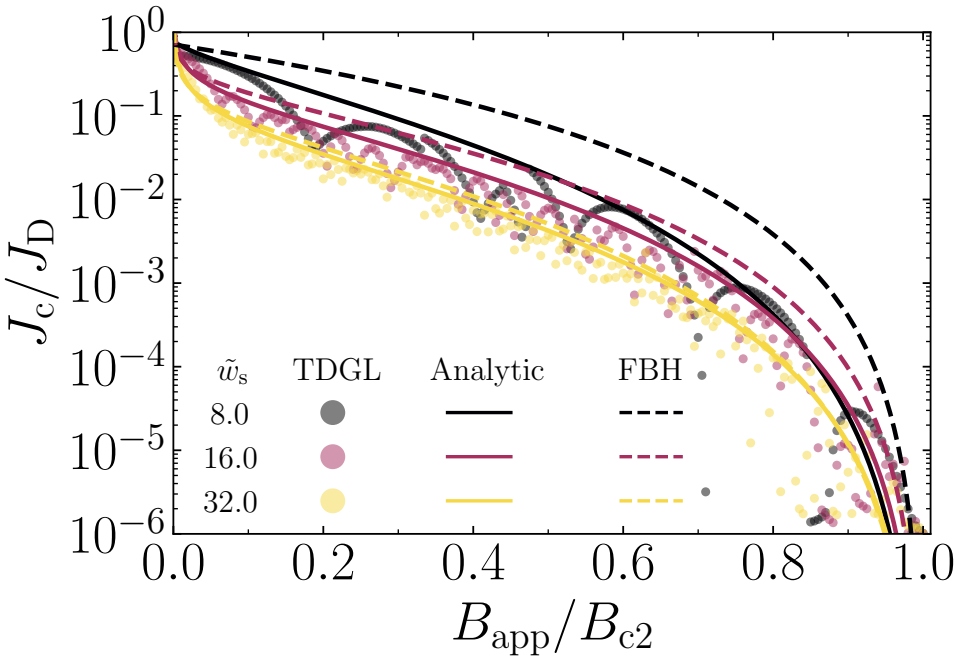

Figure 5.8: Critical current density as a function of applied magnetic field for a range of widths for a SNS junction, where $\tilde{m}_n = \tilde{m}_c = 1.0$. In all cases, $\tilde{d}_n = 0.5$ and $\tilde{\alpha}_n = -1.0$, $\tilde{\beta}_n = 1.0$ and $\kappa_s = 8.0$. The coating thickness was fixed to be $\tilde{w}_c = 3.0$. TDGL simulations are shown as solid markers. The solid lines are the envelopes generated from the flowchart presented in Fig. 4.15, using the new calculations of $\tilde{J}_{DJ}$ shown in Chapter 4 (Eq. (4.6.14), with $n = 2.2$ (taken from Table 4.1) and $B^*_{c2} = 1.0$ (taken from Fig. 4.8). The dashed lines are the equivalent envelopes using $\tilde{J}_{DJ}$ calculated from FBH shown in Eq. (2.5.47).

critical current near the upper critical field is much more gradual. As such, the TDGL data is much closer to the computational floor (set by the electric field criterion) – particularly for wider systems, where the critical current density is lower, we note that our simulation data becomes quite noisy, and the quality (and therefore, accuracy) of the data is reduced. Regardless, we can see good agreement overall; in particular, our new $\tilde{J}_{DJ}$ calculation appears to provide marginally better agreement that the FBH formalism – we can see that the FBH is too low in high fields, and too high in low fields. In particular, our solution provides a slightly better agreement with the TDGL data close to B_{c2}, particularly for the wider systems. Again, we observe the general principle that since $\tilde{m}_n \leq 1$, the behaviour in the bulk directly affects the behaviour at the interface, and the system can be treated as a sum of local 1D slices. However, the most extreme benefits of our new solution is reaped for systems where both the barrier and the coatings have high mass – fortunately, this region of phase space is most relevant for real materials. We discuss these geometries in the next section.

5.5 Polycrystalline Analogues: $\tilde{m}_n = \tilde{m}_c > 1$

Finally, we now consider the geometry which is closest to a real polycrystalline system and that incorporates the main contributions of this thesis – the case of an SNS junction where the coatings and the normal barrier have the same material properties, but the boundaries have a higher mass than the superconductor. We will set $\tilde{m}_n = \tilde{m}_c = 10.0$ and $\tilde{\alpha}_n = -1.0$. As we saw in Section 5.3, we now have a significant difference between the FBH calculation and our new calculation of $\tilde{J}_{DJ}$, due to the

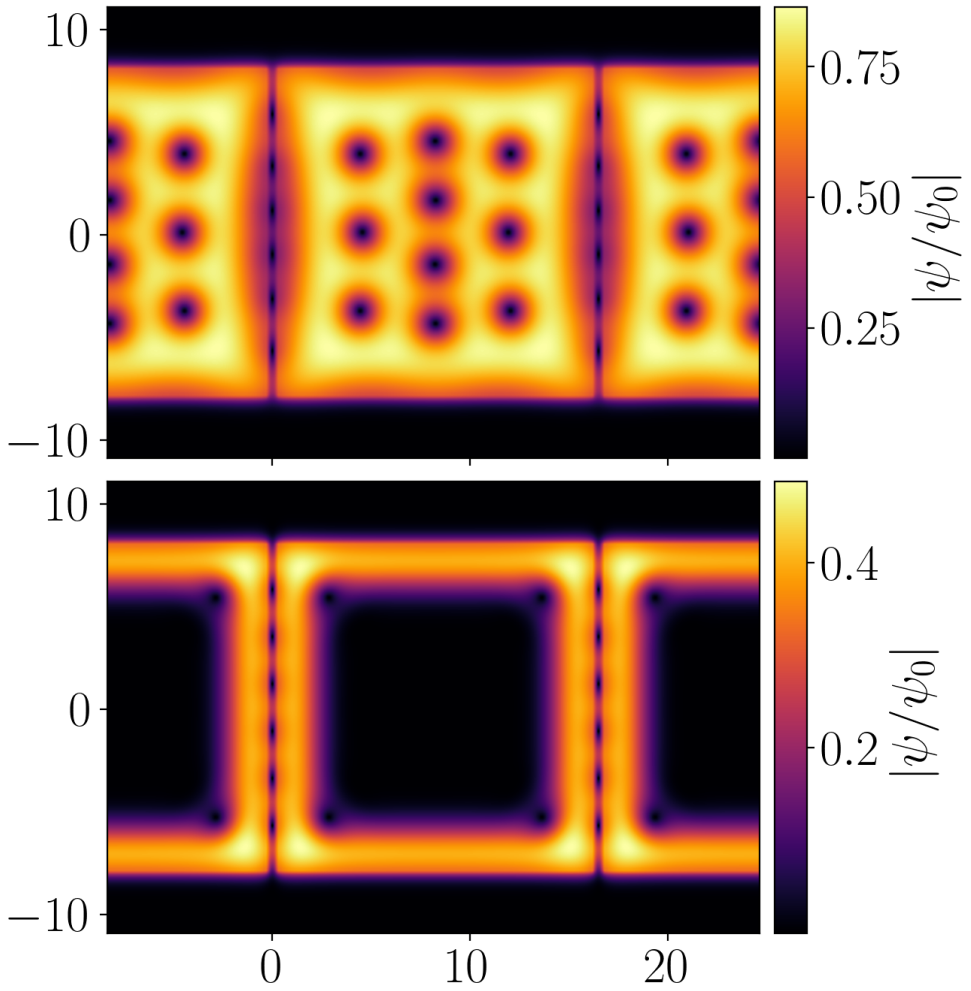

Figure 5.9: A snapshot of the normalized order parameter magnitude for an SNS junction with normal coatings, where the applied field is $\tilde{B}_{\mathrm{app}} = 0.5$ (top) and $\tilde{B}_{\mathrm{app}} = 1.1$ (bottom). In both cases, there is zero applied transport current. The coating thickness is set at $\tilde{w}_{\mathrm{c}} = 3.0$, and $\tilde{m}_{\mathrm{c}} = 10.0$. The TDGL simulation system has $\tilde{w}_{\mathrm{s}} = 16.0$, $\tilde{l}_{\mathrm{s}} = 16.0$, $\tilde{d}_{\mathrm{n}} = 0.5$, $\tilde{\alpha}_{\mathrm{n}} = -1.0$, $\tilde{m}_{\mathrm{n}} = 10.0$, $\tilde{\beta}_{\mathrm{n}} = 1.0$ and $\kappa_{\mathrm{s}} = 8.0$.

formal capturing of the increased effective upper critical field.

In Fig. 5.9, we provide the 2D spatial variation of the order parameter magnitude with $\tilde{B}_{\mathrm{app}} = 0.5$ and $\tilde{B}_{\mathrm{app}} = 1.1$ – in both cases, there is no transport current applied. This figure exemplifies the differences between the previous two sections, where $\tilde{m}_{\mathrm{n}} \leq 1$. Since the normal regions have high masses, the normal coherence length is smaller, and so the fluxons are significantly smaller (Eq. (2.5.49)). This leads to weaker coupling between the two superconducting electrodes across the normal region, even though the barrier is very thin – the fluxons in this case are distorted and 'squashed' along the junction, bearing some parallels to Clem's pancake vortices [159]. However, the most significant difference is that in this case where $\tilde{m}_{\mathrm{n}} > 1$, the philosophy that the bulk determines properties of the interface no longer holds – as we can see, if the system is above the upper critical field, then the bulk is clearly completely normal, but interface is superconducting along the entire width. Therefore, we are no longer able to treat the system as before, and cannot consider this geometry as a collection of 1D slices. The procedure presented in Fig. 4.15 is now motivated – to first order, the interfacial order parameter is uniform along the full width of the system. As mentioned, this neglects the secondary enhancement near the corners,

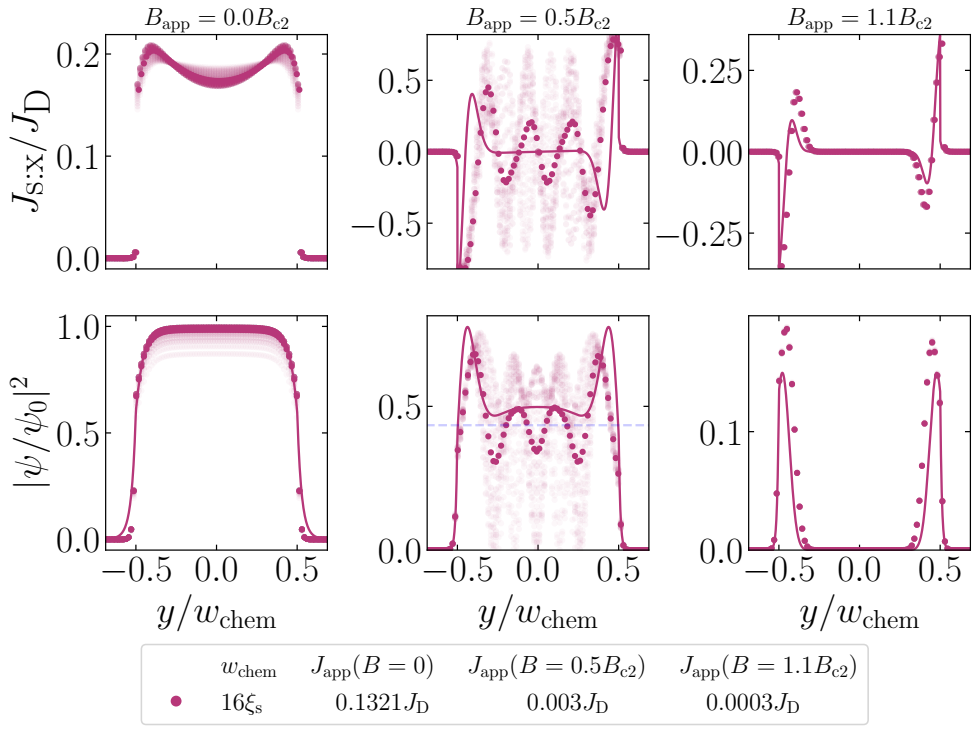

Figure 5.10: Spatial variation of the supercurrent density (top) and normalized order parameter magnitude (bottom) at three distinct applied magnetic fields and $J_{app} = 0.95J_c$, for an SNS junction with normal coatings ($\tilde{m}_c = 10$). The spatial variation is shown in the bulk of the electrode ($\tilde{x} = \tilde{l}_s/2$) – the faint dots are slices within a fluxon spacing of $\tilde{x} = \tilde{l}_s/2$, and the solid dots are the average over all at a given y–coordinate. The faint blue line is the Abrikosov prediction for the order parameter in the bulk (Eq. (2.3.33)). The solid lines denote analytic predictions for the screening current and the order parameter magnitude (Eq. (2.4.26) and Eq. (4.3.24)). The TDGL simulation system has $\tilde{w}_s = 16.0$, $\tilde{l}_s = 16.0$, $\tilde{d}_n = 0.5$, $\tilde{\alpha}_n = -1.0$, $\tilde{m}_n = 1.0$, $\tilde{\beta}_n = 1.0$ and $\kappa_s = 8.0$.

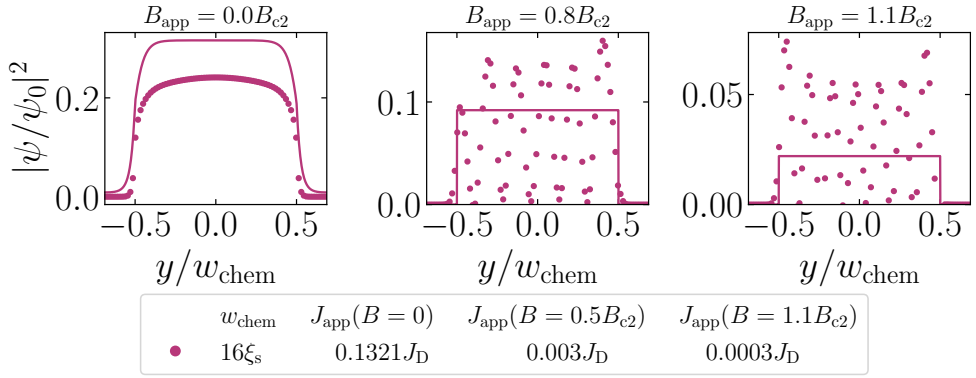

Figure 5.11: Spatial variation of the normalized order parameter magnitude at three distinct applied magnetic fields and $J_{app} = 0.95J_c$, for an SNS junction with normal coatings ($\tilde{m}_c = 10$). The spatial variation is shown in the centre of the barrier ($\tilde{x} = 0$). The solid lines denote analytic predictions for the order parameter magnitude, following the flowchart in Fig. 4.15. The TDGL simulation system has $\tilde{w}_s = 16.0$, $\tilde{l}_s = 16.0$, $\tilde{d}_n = 0.5$, $\tilde{\alpha}_n = -1.0$, $\tilde{m}_n = 1.0$, $\tilde{\beta}_n = 1.0$ and $\kappa_s = 8.0$.

but these regions do not increase the field range over which current may be carried. The spatial distributions of the order parameter across the electrode and the normal barrier are shown in Figs. 5.10 and 5.11 respectively.

Finally, we present the critical current density as a function of field in Fig. 5.12, which

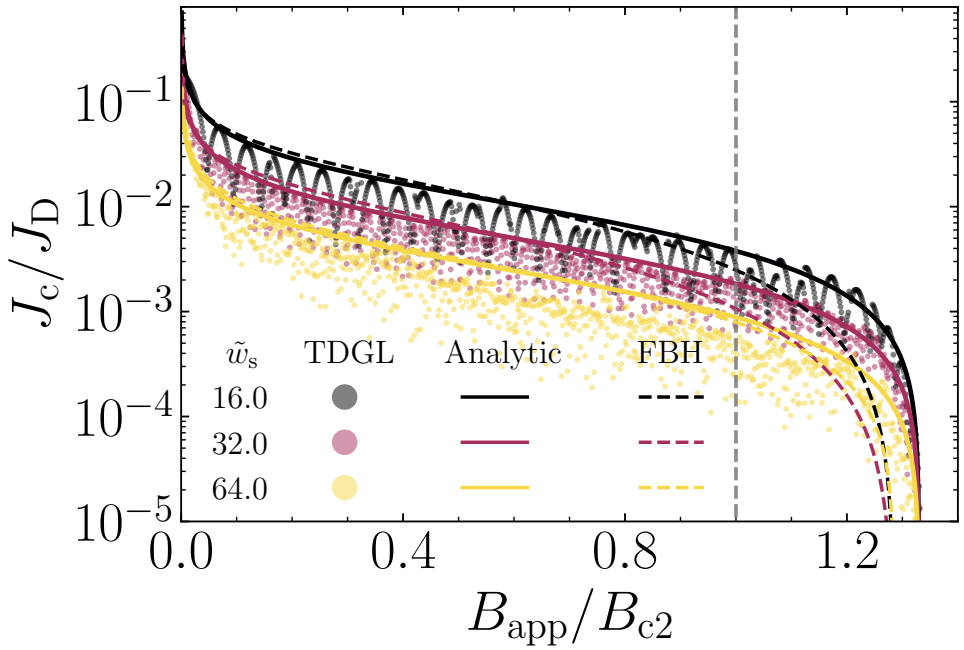

Figure 5.12: Critical current density as a function of applied magnetic field for a range of widths for a SNS junction, where $\tilde{m}_n = \tilde{m}_c = 10.0$. In all cases, $\tilde{d}_n = 0.5$, $\tilde{\alpha}_n = -1.0$, $\tilde{\beta}_n = 1.0$ and $\kappa_s = 8.0$. The coating thickness was fixed to be $\tilde{w}_c = 3.0$. TDGL simulations are shown as solid markers. The solid lines are the envelopes generated from the flowchart presented in Fig. 4.15, using the new calculations of $\tilde{J}_{DJ}$ shown in Chapter 4 (Eq. (4.6.14), with n and B^*_{c2} left as free parameters, fitted to be $n = 0.90$ and $B^*_{c2} = 1.33$). The dashed lines are the equivalent envelopes using $\tilde{J}_{DJ}$ calculated from FBH shown in Eq. (2.5.47).

is our key evidence and motivator for the use of our new $\tilde{J}_{DJ}$ calculation. We already observed in Figs. 4.12, and 4.13 how the FBH $\tilde{J}_{DJ}$ was systematically lower than the new Saint James calculation – this figure demonstrates how this difference manifests in the full $\tilde{J}_c\left(\tilde{B}_{app}\right)$ trace. We can see that the FBH prediction drops far below the TDGL data particularly in high fields and even in low fields. However, our framework has naturally captured behaviour near the interface, which allows for a much better approximation over the full field range. We can see that due to the larger widths leading an increased frequency of oscillations, the field resolution of the TDGL data may not reach the exact maximum, but the general envelope is still in much better agreement with our new calculation. In fact, one can see here that $\tilde{B}_{c2}$ is no longer a significant or special field value in any way, since again, the bulk behaviour does not affect the interface. For any case where $\tilde{m}_n > 1$, the sheath creates a natural uniformity in the current carrying capacity of the junction.

5.6 Junction Arrays

A natural extension is to question how relevant the study of a single junction is to developing our understanding of a full polycrystalline material. To this end, we have added some preliminary simulations of 'junction array systems'. These consist of multiple junctions stacked beside each other, separated by a barrier of a given thickness. We provide an example of the geometry in Fig. 5.13. In Fig. 5.14, we compare TDGL simulations of the critical current density of a triple junction array (diamond markers) to a single junction of equivalent width (circle markers). Here,

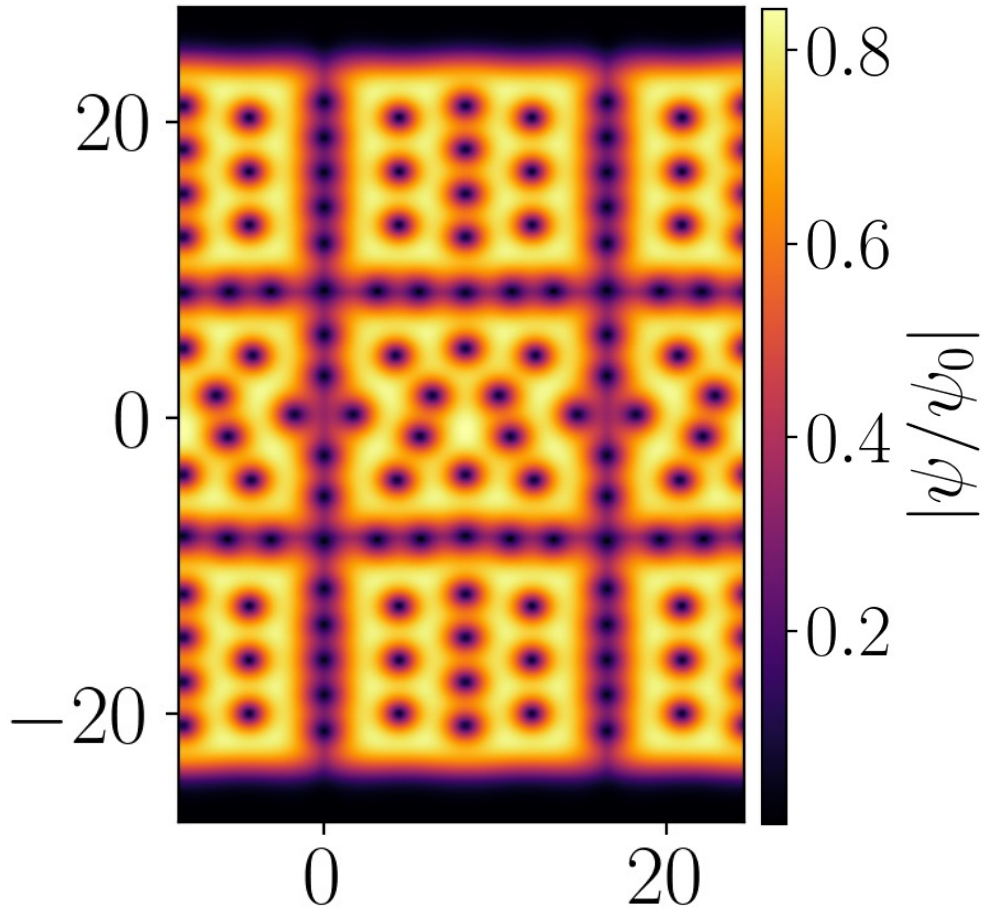

Figure 5.13: A snapshot of the normalized order parameter magnitude for a junction array with normal coatings, where the applied field is $\tilde{B}_{\rm app} = 0.5$ and there is zero applied transport current. The junction array had 3 junctions, each with $w_{\rm s} = 16.0\xi_{\rm s}$, separated by an internal coating of $0.5\xi_{\rm s}$, and an external coating of $w_{\rm c} = 3.0\xi_{\rm s}$, for a total width of $w = 55.0\xi_{\rm s}$. All normal barriers had a mass of $\tilde{m}_{\rm n} = 1.0$. The remaining TDGL simulation parameters are $\tilde{l}_{\rm s} = 16.0$, $\tilde{d}_{\rm n} = 0.5$, $\tilde{\alpha}_{\rm n} = -1.0$, $\tilde{\beta}_{\rm n} = 1.0$ and $\kappa_{\rm s} = 8.0$.

the single junction has a width of $w_{\rm s} = 16.0\xi_{\rm s}$ and a coating of $w_{\rm c} = 3.0\xi_{\rm s}$, for a total width of $w = 22.0\xi_{\rm s}$. Each junction within the triple junction array also has a width of $w_{\rm s} = 16.0\xi_{\rm s}$, but are separated by an internal coating of $0.5\xi_{\rm s}$. Again, this array has an external coating of $w_{\rm c} = 3.0\xi_{\rm s}$, for a total width of $w = 55.0\xi_{\rm s}$. In both cases, the properties of the coating were the same as that of the barrier – the mass was set to be $\tilde{m}_{\rm n} = 1.0$, but the junction condensation parameter $\tilde{\alpha}_{\rm n}$ was allowed to vary.

Fig. 5.14 provides some interesting and beautiful information. We first consider the black and grey data, where the junction condensation parameter was $\tilde{\alpha}_{\rm n} = -1.0$. We can see that in low field, the magnitude of $\tilde{J}_{\rm c}$ is significantly different – the junction array has a much lower $\tilde{J}_{\rm c}$ than the single array. Moreover, the frequency of the oscillations are also different. As the field is increased, we observe that the magnitudes become comparable as before, but the oscillation frequency remains different. We can understand this through the lens of coupling strength – since the magnitude of the junction condensation parameter is small, the junctions are strongly coupled to each other. The barrier parallel to current flow between each of the junctions therefore is subject to a significant proximity effect, and the order parameter magnitude remains large. Therefore, in low–field, the junction array acts like a single junction with a larger width – this is demonstrated in Fig. 5.15, where we see that the magnitude of

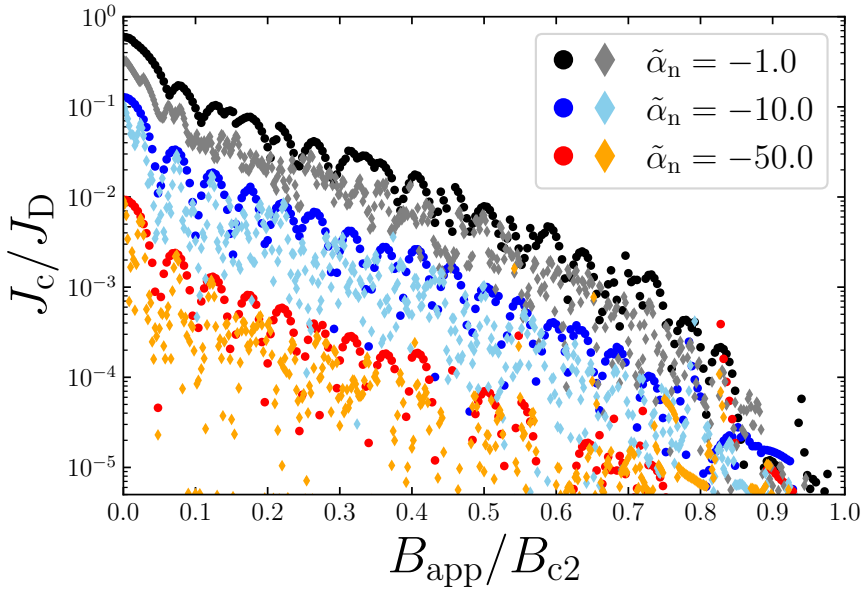

(a) Full Field Range

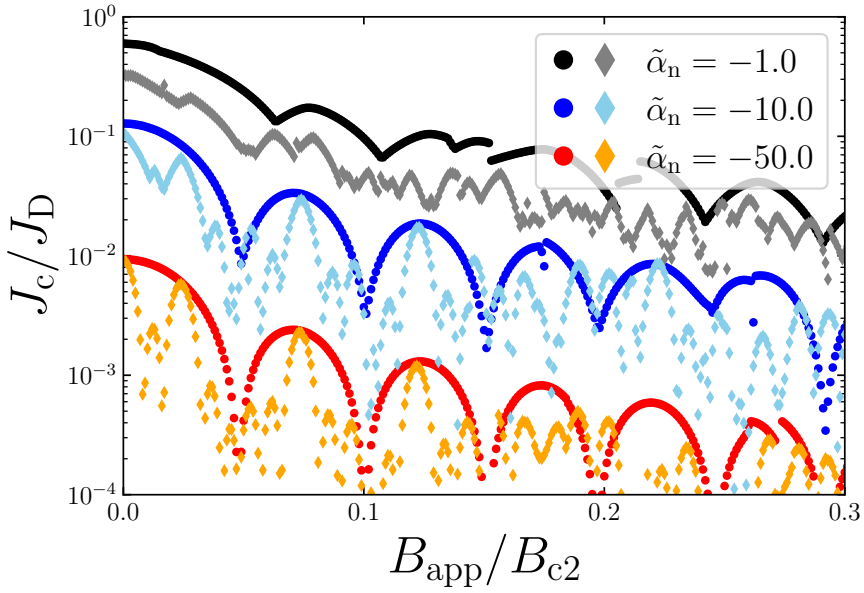

(b) Low Field

Figure 5.14: Critical current density as a function of field, across the entire field range (top) and in low field (bottom), for a single junction (circles) and a triple junction array (diamonds), with varying junction condensation parameters. In all simulations, the coating mass was $\tilde{m}_n = 1.0$ and the normal barrier thickness was $d_n = 0.5\xi_s$. The single junction had $w_s = 16.0\xi_s$ and a coating of $w_c = 3.0\xi_s$, for a total width of $w = 22.0\xi_s$. The junction array had 3 junctions, each with $w_s = 16.0\xi_s$, separated by an internal coating of $0.5\xi_s$, and an external coating of $w_c = 3.0\xi_s$, for a total width of $w = 55.0\xi_s$. In all simulations, $\tilde{\beta}_n = 1.0$.

$\tilde{J}_c$ looks much more like that of a single junction with an effective superconducting width of $49.0\xi_s$ (3 junctions of width $16.0\xi_s$ and 2 internal barriers of width $0.5\xi_s$). The frequency of the oscillations differs from that of a single barrier since fluxons are still able penetrate these normal regions more easily. However, in high field, where many fluxons have entered the normal barriers, the value of the junction condensation parameter becomes less important – the barriers all appear as if they are weakly coupled.

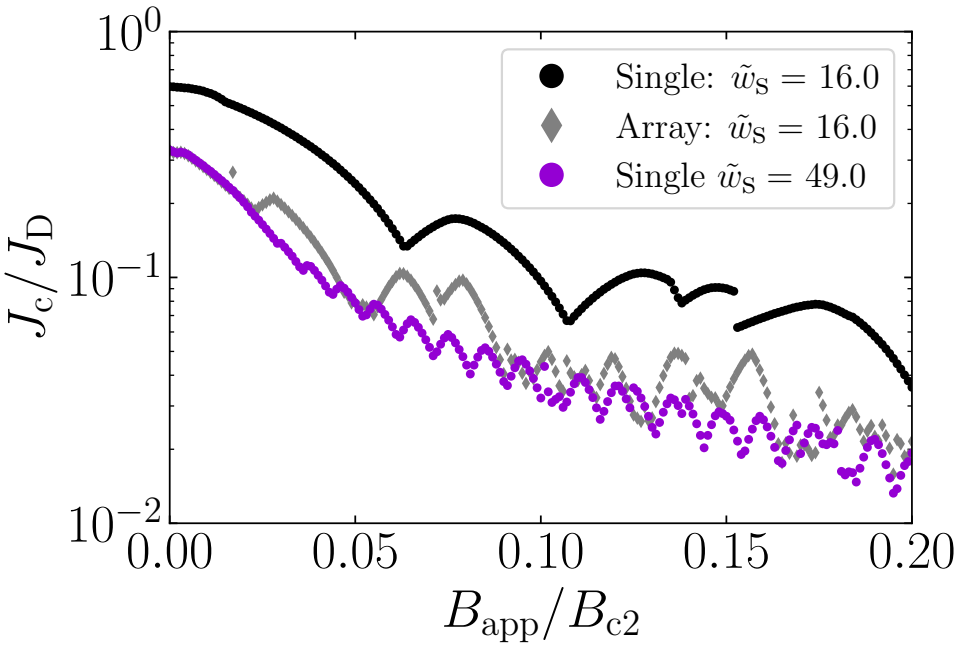

Figure 5.15: Critical current density in low field, for a strongly coupled triple junction array (diamonds), and strongly coupled single junctions of varying widths (circles). In all simulations, the coating mass was $\tilde{m}_n = 1.0$, the junction condensation parameter was $\tilde{\alpha}_n = -1.0$, and the normal barrier thickness was $d_n = 0.5\xi_s$. The junction array had 3 junctions, each with $w_s = 16.0\xi_s$, separated by an internal coating of $0.5\xi_s$, and an external coating of $w_c = 3.0\xi_s$, for a total width of $w = 55.0\xi_s$. The two single junctions shown both had a coating of $w_c = 3.0\xi_s$. The black and grey data are the same as seen in Fig. 5.14. In all simulations, $\tilde{\beta}_n = 1.0$.

We now consider arrays which are already weakly coupled – for example, the red and orange data in Fig. 5.14, where $\tilde{\alpha}_n = -50.0$. We can see here that the magnitude of $\tilde{J}_c\left(\tilde{B}_{app}\right)$ is similar across the entire field range, even in low field. The frequency of oscillations is again different, but there is a clear relationship between the two. The junction array data has more frequent minima (troughs) than the single array data – as to be expected since the minima in the critical current are associated with fluxons entering the barriers. However, the emergent field dependence of $\tilde{J}_c\left(\tilde{B}_{app}\right)$ looks like that of a triple slit diffraction pattern. The single junction provides the equivalent of the 'single slit envelope', with minima at specific values of field. The junction array also has these same values of the minima, but has additional minima/maxima in between. Since the internal barriers are so weakly coupled, there is very little interference between each of the junctions, and therefore each junction of width $16.0\xi_s$ to be isolated from one another – they can be viewed as similar to three identical optical slits separated by the internal barriers. Comparing the blue and light blue data in Fig. 5.14 where $\tilde{\alpha}_n = -10.0$ exhibits a similar behaviour.

Finally, we briefly note the effect of the junction array on the effective upper critical field. A snapshot of the order parameter magnitude for an array with thin normal barriers of mass $\tilde{m}_n = 10.0$ is shown in Fig. 5.16, demonstrating that the order parameter magnitude is significantly non–zero. From our results in Chapter 4, we expect the effective upper critical field to be approximately $1.278B_{c2}$. However, Fig. 5.16 shows a TDGL simulation performed with an applied field of $1.35B_{c2}$. Increasing the applied magnetic field further (e.g above $1.4B_{c2}$) leads to a negligible order parameter magnitude as expected. This suggests that the structure of the junction array produces a slight increase in the effective upper critical field. This is

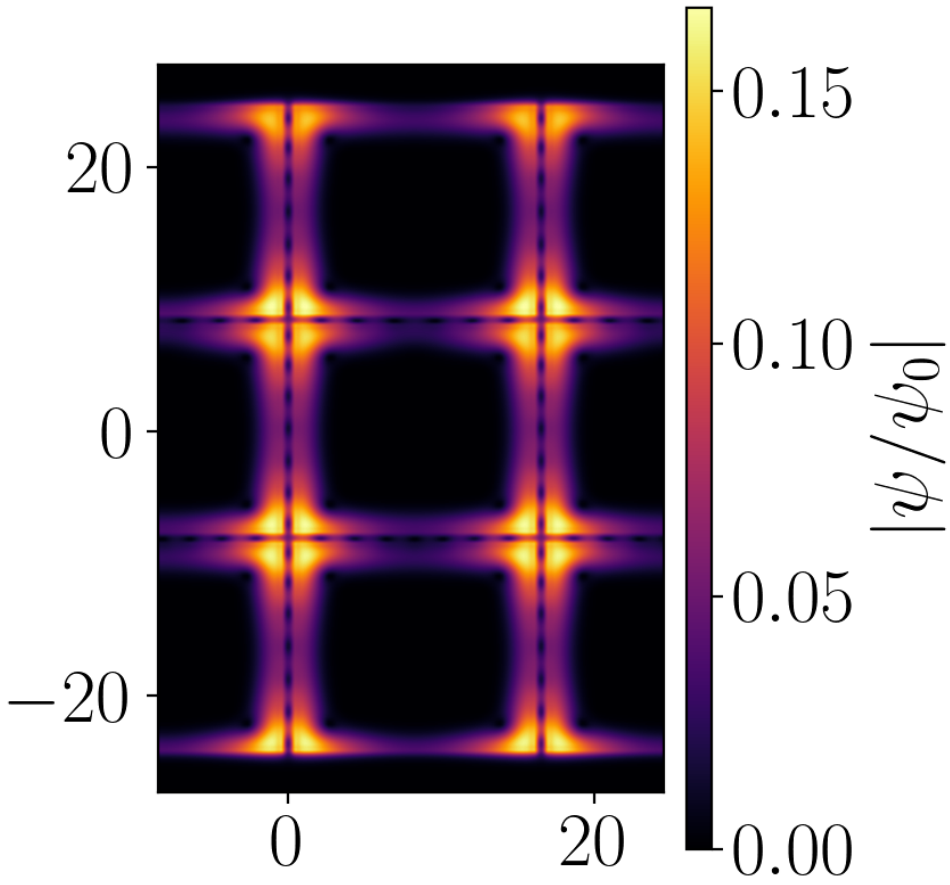

Figure 5.16: A snapshot of the normalized order parameter magnitude for a junction array with normal coatings, where the applied field is $\tilde{B}_{\mathrm{app}} = 1.35$ and there is zero applied transport current. The junction array had 3 junctions, each with $w_{\mathrm{s}} = 16.0\xi_{\mathrm{s}}$, separated by an internal coating of $0.5\xi_{\mathrm{s}}$, and an external coating of $w_{\mathrm{c}} = 3.0\xi_{\mathrm{s}}$, for a total width of $w = 55.0\xi_{\mathrm{s}}$. All normal barriers had a mass of $\tilde{m}_{\mathrm{n}} = 10.0$. The remaining TDGL simulation parameters are $\tilde{l}_{\mathrm{s}} = 16.0$, $\tilde{d}_{\mathrm{n}} = 0.5$, $\tilde{\alpha}_{\mathrm{n}} = -1.0$, $\tilde{\beta}_{\mathrm{n}} = 1.0$ and $\kappa_{\mathrm{s}} = 8.0$.

perhaps not a surprise given that our previous analytic framework considers only a single barrier, where interference between neighbouring arrays has not been accounted for, and may prove to be a significant challenge to solve algebraically. Nevertheless, we suggest that the previous framework still provides a good approximation to the junction array system.

Crucially, the envelope of these junction arrays in high field follows the envelope of the equivalent single junction. Therefore, even though the frequency of oscillations is different, the overall profile of the $\tilde{J}_{\mathrm{c}}\left(\tilde{B}_{\mathrm{app}}\right)$ behaviour remains similar – understanding a single junction is sufficient for understanding an entire array, and by extension, a full polycrystalline material. This picture provides a clear motivation for our interest in the envelope of the single junction. We have performed preliminary simulations with 5 junctions in the array, and observed a similar behaviour. These insights provide a useful first step towards understanding the envelope of a real polycrystalline material. However, there is still an extensive amount of research to be done to understand if this is a computationally or analytic approach - in Chapter 6, we shall discuss some of the remaining challenges to be addressed.

5.7 Conclusions

In this section, we have performed and presented 2D simulations of the critical current density as a function of applied magnetic field, for a variety of SNS Josephson junctions. The junctions considered had widths varying from narrow to wide junction systems, and also considered a range of normal barrier and coating masses. We then compared these TDGL simulations to our new analytic solutions using the procedure presented in Section 4.8. To our knowledge, this is the first rigorous analytic approach that is able to capture the behaviour near the interface accurately, and provide a prediction for the critical current density for both narrow and wide junctions. We applied this approach with existing analytic theory and our new analytic calculations for $\tilde{J}_{\mathrm{DJ}}$, presented in Section 4.6. In particular, we have demonstrated the applicability and necessity of our new analytic solutions for the accurate description of the critical current density for any range of material parameters. Most importantly, our new solutions perform very well for cases most relevant to real materials – we have demonstrated the limitations of existing analytic theory, and presented how our new solutions remedy these shortcomings. Moreover, our solution rigorously captures the full 2D nature of the solution, and does not require artificial corrections or free parameters.

Finally, we briefly presented TDGL simulations comparing a single SNS junction to a set of junctions arrays – this is important in extending analytic understanding of a single junction to a full 3D material. These simulations allowed a particularly aesthetic picture of how the material parameters affect the strength of coupling – depending on the normal region properties, these junction arrays can be viewed either as a collection of completely distinct junctions with no interaction (if the junctions are sufficiently weakly coupled), or almost as a single junction of a larger width with (if the junctions are sufficiently strongly coupled). Moreover, we demonstrated that if the junctions are indeed weakly coupled (which is most likely the regime of real materials), then the junction array exhibits a clear slit diffraction pattern, which sits within the envelope of a single junction. Specifically, even though the frequency of oscillations of the junction array is higher, the overall envelope is extremely close to that of a single junction. This is particularly important, because it implies that an understanding of a single junction does indeed provide the basic building block for understanding arrays, and in turn, a full 3D polycrystalline system.

We briefly note some numerical limitations of our results and the emergence of significant noise in the system. Our previous work already noted the importance of choosing a suitable grid step for simulations [116]; as the system becomes increasingly weakly coupled (either by increasing the mass of the barrier or choosing a larger and more negative junction condensation parameter), the normal coherence length becomes smaller (c.f. Eq. (2.5.49)) and it becomes harder to capture the essential physics occuring on a decreasing length scale. This problem is only excacerbated in higher fields, and failure to consider the relevant length scale can lead to massive overestimates of J_{c}. However, running simulations with a finer grid size requires more computational effort – quickly becoming unfeasible with many sets of material parameters, each requiring thousands of field points. Our choice of $0.1\xi_{\mathrm{s}}$ is a trade off between accuracy and computational efficiency – improved approaches such as a multigrid framework [118] would provide a clear improvement for this aspect. These more efficient solvers should also allow for an improved capacity to lower the noise

floor, allowing more weakly coupled systems to be studied and crucially capturing their behaviour more accurately in the high–field regime.

Chapter 6

Conclusions and Future Work

The contributions of our work are primarily in the analytic and computational descriptions of the order parameter near an interface with arbitrary material parameters, for three distinct geometries (SN, NSN and SNS). This naturally lead to a description of the effective upper critical field as a function of geometry and material parameters, and subsequently, the Josephson depairing current through the junction. Our results are formally analytic in that they provide an exact solution through a set of implicit equations. However, the necessity of solving implicit equations is an inherent limitation to the applicability of our results, despite being a relatively straightforward numerical task. Although this is equivalent to the conclusions of Saint James and de Gennes [79], it is somehow unsatisfactory, since any new geometry with an arbitrary difference in the material parameters requires a new calculation. To this end, an explicit solution (even as an approximate series solution) to our implicit equations would be desirable. In the interest of applicability to relevant polycrystalline materials, we note that our materials are effectively in the semi–infinite limit. We can see that for SNS geometries, if the thickness of the barrier is greater than $0.5\xi_s$, then the interaction of the interfaces is minimal (c.f. Fig. 4.7) – this condition is met for the majority of real polycrystalline materials. Therefore, the relevant problem is the same as in Section 4.2, which may simplify the necessary approximations. Standard series approximations of the parabolic cylinder functions include unphysical oscillations, and therefore care is needed to ensure that our solution remains physical. Moreover, the neglection of the non–linear terms inherently limits the formal validity of our solutions (despite the applicability of our results being validated by TDGL far beyond this limit). To this end, an analytic solution to the full non–linear equation would be desirable; we acknowledge that this is a difficult task for future work. Perhaps more realistically, some derivation of a functional form that covers the entire (reasonable) material parameter space would be sufficient. However, the physical basis for such a functional form is unclear, and would require further simulations or analytic investigation.

Next, we note that all of our considerations, both analytic and computational, consider a single field orientation, where the applied field is perpendicular to the plane of the junction. Since a real polycrystal contains many grains that are not perfectly orientated relative to the applied field, this would be an interesting and important direction for future computational and analytical work. The generalisation of the work of Saint James to include angular dependence for the ISI system has already been covered by Tinkham [82]. However, with our new developments, the natural question that follows is to ask if these results can be generalised for arbitrary field angle in

a similar way. This understanding would be particularly important for a complete understanding of a full 3D polycrystalline material. Careful averaging over all possible angles and field orientations may result in some non–trivial but analytic factor, which may allow for a simple relationship between the understanding of the critical current density for 1D systems with perpendicular field as considered here to the critical current density for full 3D systems. It is certainly not obvious how (or indeed, if) the geometry and properties of the normal barriers/grain boundaries would affect such a factor, if such a factor were to even exist. Further developments could be also considered to include the effect of finite systems – the Saint James derivation considers systems which are formally infinite in the y–direction; this property allows an infinite continuum of possible k_y values. However, in the case where the system is finite, we then have a discrete and countably finite set of k_y values permitted. Therefore, the specific value of the phase corresponding to the semi–infinite B_{c2} is not guaranteed to be in this set, and therefore, we no longer expect the semi–infinite behaviour. This physical behaviour may have a significant effect on TDGL simulations, which are by construction of finite width. Careful treatment of the boundary conditions may resolve this issue, but it is not obvious how to ensure consistency across the system.

Alongside the angular field dependence in the TDGL calculations, future work could also consider some non–trivial changes to increase the efficiency of the computational solvers. We have already discussed how multigrid implementations in Chapter 3 can serve to increase the effectiveness of the TDGL systems, which has mainly proved useful for increasing the capability of TDGL solver to explore larger 3D systems with arbitrary superconducting properties. However, the calculation of the critical current density is still slow – most of the simulation is spent in the resistive hold state after exceeding the E–field criterion. This is by far the slowest part of the simulation – it is particularly expensive to check that the E–field spike is truly persistent motion, rather than a transient spike. To overcome this, alternative current ramp schemes could be considered. One approach that has shown potential in preliminary simulations is a 'coarse then fine' scheme. In order to determine the critical current density accurately, one typically ramps the current in very fine steps. Instead, we could take very large current steps, allowing us to quickly obtain a lower and upper bound to the simulation. Then, one can restart the simulation, and quickly ramp up to the lower bound in large steps again, and then take the required fine steps after that. At worst, the true critical current is very close to the upper bound, and so there is little benefit to the approach other than the small benefit from the initial rapid ramp to the lower bound. At best, the true critical current is close to the lower bound, and the simulation is significantly more efficient. In preliminary testing, we found that this allowed simulations approximately 15x faster, but much more development is required to ensure the rigour of the implementation, the correctness of the numerical solution, and the correct range of computational parameters.

Next, we note that our simulations have considered simple representations of an SNS junction, where the only non–superconducting regions are the grain boundaries (the normal barriers and coatings). However, our simulations are limited by the noise floor of the computation. For very weakly coupled systems, such as geometries with thick grain boundaries or very large condensation parameter magnitudes, the critical current densities are very small, and so require very small E–field criterion. Although this is useful for high fields, it renders the low and intermediate field calculations intractably slow. One cannot simply perform the simulation with different E–field

criteria in different field regimes, since there is no guarantee that the resulting J_c trace will be continuous. Therefore, improving the speed of the low and intermediate field simulations with a lower E–field criterion, or developing a more general method of lowering the noise floor across the entire field range, would be particularly desirable, allowing simulations to efficiently cover a wide range of geometries. An additional interesting set of future simulations may be to consider these SNS systems with additional normal inclusions, which can model artificial pinning sites, impurities or defects from irradiation; these features are particularly important for real operation of superconducting materials [160]. Previous research has considered the effect of nanorod pinning and splay [117], but have not considered the combined effects from the surfaces and boundaries as well. These additional computational simulations should be relatively straightforward, and may provide interesting information in the optimization of LTS materials – however, providing an analytic understanding that includes these defects may prove to be much more challenging. HTS materials can also be modelled as Josephson junctions, and so our presented framework may also prove useful in the description of these materials.

Finally, in the interest of moving yet further towards real 3D systems, it would be interesting to extend the work in Section 5.6 further, and repeat the simulations for arrays with many junctions in the array – we expect that with an increasing number of junctions, the oscillations would become more frequent until we approach the envelope of the single junction. If we can conclude that the number of junctions within the array is not significantly important for determining the field dependence profile of the $\tilde{J}_c$, then the remaining aspect for understanding a real 3D polycrystal is to consider the relative angle of each of the grains to the field orientation. In our work so far, we have only considered junctions with the field perpendicular to the junction. If the full 3D system is large enough, then one can assume that there are sufficiently many grains such that every possible field orientation is considered – therefore, by taking the average over the entire polycrystal, one might expect to find a simple geometric factor that scales the single junction result. However, this is a significant claim which we do not have the evidence for – extensive further simulations and research would be necessary to validate this. In particular, the scale of the computational power needed to model an entire polycrystal of Nb_3Sn is unprecedented – even state–of–the–art simulations (e.g. multigrid methods) are significantly far away from being capable of performing simulations on this scale. It may be interesting to further develop analytic work for the junction array systems with different material properties – moreover, it would be interesting to see if one can find a theoretical basis which encapsulates the behaviour for any number of arrays and barrier properties. It would be particularly useful to consider the limit where we have an infinite number in the array, and if we indeed can find an analytic expression for the envelope of the single junction array. As discussed in Chapter 5, this envelope is more useful for comparison with real systems due to the spurious oscillations due to fluxon entry in the bulk – if this envelope is available analytically, then this could provide a huge improvement for our understanding of a full 3D polycrystal material.

Appendix A

Fusion CDT

The author is a member of the EPSRC Centre for Doctoral Training in the Science and Technology of Fusion Energy (Fusion CDT). The Fusion CDT is a collaboration between the universities of Durham, Liverpool, Manchester, Oxford and York, providing doctoral students with a broad basis in fusion disciplines to support their specialised research. Training courses and assignments are distributed through the first 9 months of the PhD, with courses on a range of topics delivered by each of the participating universities. Some courses are modules from the York University MSc in Fusion Energy, the others are bespoke courses for doctoral students. A summary of the courses taken is given in Table A.1. In addition to the training courses, the Fusion CDT organises a yearly student conference in York, Frontiers of Fusion.

Course Name	**Location**	**Result**
Introduction to Fusion Plasma	York	Distinction
Introduction to Materials	York	Distinction
Introduction to Computational Techniques	York	Distinction
Material Applications in Fusion	Oxford	Distinction
Plasma Surface Interactions	Liverpool	Distinction
Radiation Damage	York	Distinction
Materials for Nuclear Power	Oxford	Distinction
Characterisation and Analytic Tools	Manchester	Distinction
Finite Element Methods and Design Codes	Manchester	Distinction

Table A.1: First year courses attended as part of the Fusion CDT.

Appendix B

Software & GitHub Repositories

The important code used for the work presented in this thesis can be found on a git repository at `https://github.com/BradDin/thesis_code`. I have structured the Readme files and code by Chapters and Figures therein. It will enable future students to regenerate the data in the figures, from scratch as quickly and efficiently as possible.

The repository contains:

- TDGL2D Fortran solver
- Example slurm scripts and parameter initialisation scripts for local simulations or HPC usage
- All associated TDGL data
- Python code for generating Clem, FBH, and Saint James results

Bibliography

[1] D. Goodstein and J. Goodstein, "Richard Feynman and the history of superconductivity," *Physics in Perspective*, vol. 2, no. 1, pp. 30–47, 2000.

[2] H. K. Onnes, "Further experiments with Liquid Helium G. On the electrical resistance of Pure Metals etc. VI. On the Sudden Change in the Rate at which the Resistance of Mercury Disappears," in *KNAW, Proceedings*, vol. 14, pp. 1911–1912, 1911.

[3] H. K. Onnes, "Further experiments with liquid helium. H. On the electrical resistance of pure metals etc. VII. The potential difference necessary for the electric current through mercury below 4.19K," in *KNAW, Proceedings*, vol. 15, pp. 1406–1430, 1913.

[4] W. Meissner and R. Ochsenfeld, "Ein neuer effekt bei eintritt der supraleitfähigkeit," *Naturwissenschaften*, vol. 21, no. 44, pp. 787–788, 1933.

[5] F. London and H. London, "The electromagnetic equations of the supraconductor," *Proceedings of the Royal Society of London. Series A-Mathematical and Physical Sciences*, vol. 149, no. 866, pp. 71–88, 1935.

[6] V. Ginzburg and L. Landau, "On the Theory of superconductivity," *Zh. Eksp. Teor. Fiz.*, vol. 20, pp. 1064–1082, 1950.

[7] J. Bardeen, L. N. Cooper, and J. R. Schrieffer, "Theory of Superconductivity," *Phys. Rev.*, vol. 108, pp. 1175–1204, 1957.

[8] J. Bednorz and K. Muller, "Possible high Tc superconductivity in the Ba-La-Cu-O system," *Z. Phys. B*, vol. 64, pp. 189–193, 1986.

[9] M. K. Wu *et al.*, "Superconductivity at 93 K in a new mixed-phase Y-Ba-Cu-O compound system at ambient pressure," *Phys. Rev. Lett.*, vol. 58, pp. 908–910, 1987.

[10] A. P. Drozdov *et al.*, "Conventional superconductivity at 203 kelvin at high pressures in the sulfur hydride system," *Nature*, vol. 525, no. 7567, p. 73–76, 2015.

[11] A. P. Drozdov *et al.*, "Superconductivity at 250 K in lanthanum hydride under high pressures," *Nature*, vol. 569, no. 7757, p. 528–531, 2019.

[12] E. Snider *et al.*, "Synthesis of Yttrium Superhydride Superconductor with a Transition Temperature up to 262 K by Catalytic Hydrogenation at High Pressures," *Phys. Rev. Lett.*, vol. 126, p. 117003, 2021.

[13] N. Dasenbrock-Gammon *et al.*, "Evidence of near-ambient superconductivity in a N-doped lutetium hydride," *Nature*, vol. 615, no. 7951, pp. 244–250, 2023.

[14] X. Ming *et al.*, "Absence of near-ambient superconductivity in LuH2±xNy," *Nature*, pp. 1–3, 2023.

[15] N. P. Salke *et al.*, "Evidence for Near Ambient Superconductivity in the Lu-N-H System," 2023. Preprint, arXiv:2306.06301.

[16] S. Lee, J.-H. Kim, and Y.-W. Kwon, "The First Room-Temperature Ambient-Pressure Superconductor," 2023. Preprint, arXiv:2307.12008.

[17] S. Lee *et al.*, "Superconductor $Pb_{10-x}Cu_x(PO_4)_6O$ showing levitation at room temperature and atmospheric pressure and mechanism," 2023. Preprint, arXiv:2307.12037.

[18] W. D. D'haeseleer, "The importance of fusion development towards a future energy source," *Fusion Engineering and Design*, vol. 66-68, pp. 3 – 15, 2003. 22nd Symposium on Fusion Technology.

[19] J. F. Annett *et al.*, *Superconductivity, Superfluids and Condensates*, vol. 5. Oxford University Press, 2004.

[20] W. Han and D. Ward, "Revised assessments of the economics of fusion power," *Fusion Engineering and Design*, vol. 84, no. 2, pp. 895 – 898, 2009. Proceeding of the 25th Symposium on Fusion Technology.

[21] A. S. Eddington, "The internal constitution of the stars," *The Observatory*, vol. 43, pp. 341–358, 1920.

[22] P. Bruzzone, "Superconductivity and fusion energy—the inseparable companions," *Superconductor Science and Technology*, vol. 28, no. 2, p. 024001, 2014.

[23] F. F. Chen, *Introduction to plasma physics and controlled fusion; 3rd ed.* Cham: Springer, 2016.

[24] Y. Zhai, C. Kessel, L. El-guebaly, and P. Titus, "Magnet design considerations for fusion nuclear science facility," *IEEE Transactions on Applied Superconductivity*, vol. 06, no. 12, pp. 1–5, 2016.

[25] L. Muzzi *et al.*, "Cable-in-conduit conductors: Lessons from the recent past for future developments with low and high temperature superconductors," *Superconductor Science and Technology*, vol. 28, p. 053001, 2015.

[26] S. I. Schlachter *et al.*, "Coated Conductor Rutherford Cables (CCRC) for High-Current Applications: Concept and Properties," *IEEE Transactions on Applied Superconductivity*, vol. 21, pp. 3021–3024, 2011.

[27] H. Hashizume *et al.*, "Development of remountable joints and heat removable techniques for high-temperature superconducting magnets," *Nuclear Fusion*, vol. 58, no. 2, p. 026014, 2017.

[28] Z. Hartwig *et al.*, "VIPER: an industrially scalable high-current high-temperature superconductor cable," *Superconductor Science and Technology*, vol. 33, p. 11LT01, 2020.

[29] N. Mitchell, A. Devred, P. Libeyre, B. Lim, and F. Savary, "The ITER Magnets: Design and Construction Status," *IEEE Transactions on Applied Superconductivity*, vol. 22, no. 3, pp. 4200809–4200809, 2012.

[30] C. Barth, *High Temperature Superconductor Cable Concepts for Fusion Magnets*. 2013.

[31] C. Barth *et al.*, "Electro-mechanical properties of REBCO coated conductors from various industrial manufacturers at 77 K, self-field and 4.2 K, 19 T," *Superconductor Science and Technology 28(4):045011 (2015)*.

[32] P. Bruzzone, W. Fietz, J. Minervini, M. Novikov, N. Yanagi, Y. Zhai, and J. Zheng, "High temperature superconductors for fusion magnets," *Nuclear Fusion*, vol. 58, 2018.

[33] A. J. Creely *et al.*, "Overview of the SPARC tokamak," *Journal of Plasma Physics*, vol. 86, no. 5, p. 865860502, 2020.

[34] J. Morris, M. Coleman, S. Kahn, S. Muldrew, A. Pearce, D. Short, J. Cook, S. Desai, L. Humphrey, M. Kovari, J. Maddock, and D. Vaccaro, "Preparing systems codes for power plant conceptual design," *Nuclear Fusion*, vol. 61, 2021.

[35] A. Sykes *et al.*, "Compact fusion energy based on the spherical tokamak," *Nuclear Fusion*, vol. 58, no. 1, p. 016039, 2017.

[36] A. Sagara *et al.*, "Helical reactor design FFHR-d1 and c1 for steady-state DEMO," *Fusion Engineering and Design*, vol. 89, no. 9, pp. 2114–2120, 2014.

[37] L. Muzzi *et al.*, "Assessment Studies and Manufacturing Trials for the Conductors of DEMO TF Coils," *IEEE Transactions on Applied Superconductivity*, vol. 25, pp. 1–5, 2015.

[38] L. Zani *et al.*, "Overview of Progress on the EU DEMO Reactor Magnet System Design," *IEEE Transactions on Applied Superconductivity*, vol. 26, no. 4, pp. 1–5, 2016.

[39] G. Wang, M. J. Raine, and D. P. Hampshire, "How Resistive Must Grain-Boundaries be to Limit J_c in Polycrystalline Superconductors?," *Supercond. Sci. Technol.*, vol. 30, no. 10, 2017. Art. no. 104001.

[40] M. Parizh, Y. Lvovsky, and M. Sumption, "Conductors for commercial MRI magnets beyond NbTi: requirements and challenges," *Supercond Sci Technol*, vol. 30, no. 1, p. 014007, 2017.

[41] L. Rossi, "Superconductivity: its role, its success and its setbacks in the Large Hadron Collider of CERN," *Superconductor Science and Technology*, vol. 23, no. 3, p. 034001, 2010.

[42] D. Driscoll, "A review of superconducting motor technology development," in *2001 IEEE Power Engineering Society Winter Meeting. Conference Proceedings (Cat. No.01CH37194)*, vol. 2, pp. 438–441 vol.2, 2001.

[43] L. Ybanez *et al.*, "ASCEND: The first step towards cryogenic electric propulsion," *IOP Conference Series: Materials Science and Engineering*, vol. 1241, no. 1, p. 012034, 2022.

[44] W. Buckles and W. Hassenzahl, "Superconducting magnetic energy storage," *IEEE Power Engineering Review*, vol. 20, no. 5, pp. 16–20, 2000.

[45] R. C. Jaklevic *et al.*, "Quantum Interference Effects in Josephson Tunneling," *Phys. Rev. Lett.*, vol. 12, pp. 159–160, 1964.

[46] A. H. Silver and J. E. Zimmerman, "Quantum States and Transitions in Weakly Connected Superconducting Rings," *Phys. Rev.*, vol. 157, pp. 317–341, 1967.

[47] T. J. Quinn, "News from the BIPM," *Metrologia*, vol. 26, no. 1, p. 69, 1989.

[48] E. Maxwell, "Isotope Effect in the Superconductivity of Mercury," *Phys. Rev.*, vol. 78, pp. 477–477, 1950.

[49] H. Fröhlich, "Theory of the Superconducting State. I. The Ground State at the Absolute Zero of Temperature," *Phys. Rev.*, vol. 79, pp. 845–856, 1950.

[50] L. N. Cooper, "Bound Electron Pairs in a Degenerate Fermi Gas," *Phys. Rev.*, vol. 104, pp. 1189–1190, 1956.

[51] P. J. Ford and G. A. Saunders, *The Rise of the Superconductors*. CRC press, 2004.

[52] D. J. Thouless, "Perturbation theory in statistical mechanics and the theory of superconductivity," *Annals of Physics*, vol. 10, no. 4, pp. 553–588, 1960.

[53] D. Tilley and J. Tilley, *Superfluidity and Superconductivity*. Graduate Student Series in Physics, Taylor & Francis, 1990.

[54] G. Eliashberg, "Interactions between electrons and lattice vibrations in a superconductor," *Sov. Phys. JETP*, vol. 11, no. 3, pp. 696–702, 1960.

[55] J. Carbotte, "Properties of boson-exchange superconductors," *Reviews of Modern Physics*, vol. 62, no. 4, p. 1027, 1990.

[56] J. E. Hirsch, "BCS theory of superconductivity: the world's largest Madoff scheme?," *Physica Scripta*, vol. 80, no. 3, p. 035702, 2009.

[57] J. Hirsch, "Hole superconductivity," *Physics Letters A*, vol. 134, no. 7, pp. 451 – 455, 1989.

[58] L. P. Gor'kov, "Microscopic derivation of the Ginzburg-Landau equations in the theory of superconductivity," *Sov. Phys. JETP*, vol. 9, no. 6, pp. 1364–1367, 1959.

[59] L. Landau and E. Lifshitz, "Chapter XIV - Phase Transitions of the Second Kind and Critical Phenomena," in *Statistical Physics (Third Edition)*, vol. 5 of *Course of Theoretical Physics*, pp. 446–516, Pergamon, third edition ed., 1980.

[60] M. Tinkham, *Introduction to Superconductivity*, vol. 2. Mineola, New York: Dover Publications, 2004.

[61] N. Kopnin, *Theory of nonequilibrium superconductivity*, vol. 1. Oxford University Press, 2001.

[62] C. P. Poole, R. Prozorov, H. A. Farach, and R. J. Creswick, *Superconductivity (Third Edition)*. London: Elsevier, third edition ed., 2014.

[63] V. Ginzburg and L. Landau, "On the Theory of Superconductivity," *Zh. Eksp. Teor. Fiz.*, vol. 20, pp. 1064–1082, 1950.

[64] A. B. Pippard and W. L. Bragg, "An experimental and theoretical study of the relation between magnetic field and current in a superconductor," *Proceedings of the Royal Society of London. Series A. Mathematical and Physical Sciences*, vol. 216, no. 1127, pp. 547–568, 1953.

[65] R. D. Parks, *Superconductivity: In Two Volumes: Volume 2*, vol. 2. Routledge, 2018.

[66] A. A. Abrikosov, "On the magnetic properties of superconductors of the second group," *Sov. Phys. JETP*, vol. 5, pp. 1174–1182, 1957.

[67] M. J. Raine, *High Field Superconductors for Fusion Energy Application.* PhD thesis, Durham University, Durham, United Kingdom, 2015. Available at `http://etheses.dur.ac.uk/`.

[68] C. P. Poole, *Superconductivity.* London, UK: Elsevier Academic Press, 2nd ed., 2007.

[69] P. G. De Gennes, *Superconductivity of Metals and Alloys.* Boulder, Colorado: Perseus Books Group, 1999.

[70] W. H. Kleiner, L. M. Roth, and S. H. Autler, "Bulk Solution of Ginzburg-Landau Equations for Type II Superconductors: Upper Critical Field Region," *Phys. Rev.*, vol. 133, pp. A1226–A1227, 1964.

[71] U. Essmann and H. Träuble, "The direct observation of individual flux lines in type II superconductors," *Physics Letters A*, vol. 24, no. 10, pp. 526–527, 1967.

[72] J. R. Clem, "Josephson junctions in thin and narrow rectangular superconducting strips," *Phys. Rev. B*, vol. 81, no. 14, 2010. Art. no. 144515.

[73] D. A. Jacobson, "Ginzburg-Landau Equations and the Josephson Effect," *Phys. Rev.*, vol. 138, pp. A1066–A1070, 1965.

[74] H. J. Fink, "Supercurrents through superconducting-normal-superconducting proximity layers. I. Analytic solution," *Phys. Rev. B*, vol. 14, no. 3, pp. 1028–1038, 1976.

[75] A. I. Blair and D. P. Hampshire, "Critical current density of superconducting-normal-superconducting Josephson junctions and polycrystalline superconductors in high magnetic fields," *Phys. Rev. Research*, vol. 4, p. 023123, 2022.

[76] T. Matsushita and M. Kiuchi, "Depairing current density in superconductors," *Applied Physics Express*, vol. 12, no. 6, p. 063003, 2019.

[77] P. G. de Gennes, "Boundary Effects in Superconductors," *Rev. Mod. Phys.*, vol. 36, pp. 225–237, 1964.

[78] D. Saint-James and P. G. de Gennes, "Onset of superconductivity in decreasing fields," *Physics Letters*, vol. 7, no. 5, pp. 306–308, 1963.

[79] D. Saint-James and G. Sarma, *Type II Superconductivity.* Oxford, United Kingdom: Pergamon Press, 1969.

[80] "NIST Digital Library of Mathematical Functions." http://dlmf.nist.gov/, Release 1.1.1 of 2021-03-15. F. W. J. Olver, A. B. Olde Daalhuis, D. W. Lozier, B. I. Schneider, R. F. Boisvert, C. W. Clark, B. R. Miller, B. V. Saunders, H. S. Cohl, and M. A. McClain, eds.

[81] V. L. Ginzburg, "On the theory of superconductivity," *Il Nuovo Cimento (1955-1965)*, vol. 2, pp. 1234–1250, 1955.

[82] M. Tinkham, "Effect of Fluxoid Quantization on Transitions of Superconducting Films," *Phys. Rev.*, vol. 129, pp. 2413–2422, 1963.

[83] J. H. Durrell *et al.*, "The behavior of grain boundaries in the Fe-based superconductors," *Reports on Progress in Physics*, vol. 74, no. 12, p. 124511, 2011.

[84] G. J. Carty, M. Machida, and D. P. Hampshire, "Numerical studies on the effect of normal metal coatings on the magnetisation characteristics of type-II superconductors," *Physical Review B*, vol. 71, p. 144507, 2005.

[85] D. Dew-Hughes, "The critical current of superconductors: an historical review," *Low temperature physics*, vol. 27, no. 9, pp. 713–722, 2001.

[86] E. J. Kramer, "Summation curves for flux pinning in superconductors," *Journal of Applied Physics*, vol. 49, no. 2, pp. 742–748, 1978.

[87] T. Matsushita, *Flux Pinning Characteristics*, pp. 267–339. Berlin, Heidelberg: Springer Berlin Heidelberg, 2007.

[88] B. Josephson, "Possible new effects in superconductive tunnelling," *Physics Letters*, vol. 1, no. 7, p. 251–253, 1962.

[89] A. Barone and G. Paterno, *Physics and Applications of the Josephson Effect*. New York: Wiley, 1982.

[90] L. Fritzsch *et al.*, "SNS and SIS Josephson junctions with dimensions down to the submicron region prepared by a unified technology," *Superconductor Science and Technology*, vol. 12, no. 11, p. 880, 1999.

[91] S. Shapiro, "Josephson Currents in Superconducting Tunneling: The Effect of Microwaves and Other Observations," *Phys. Rev. Lett.*, vol. 11, pp. 80–82, 1963.

[92] B. D. Josephson, "The discovery of tunnelling supercurrents," *Reviews of Modern Physics*, vol. 46, no. 2, p. 251, 1974.

[93] R. P. Feynman, *The Feynman Lectures on Physics. Vol. III*. New York: Addison-Wesley, 1965.

[94] E. Neville, *Jacobian Elliptic Functions*. Clarendon Press, 1944.

[95] B. D. Josephson, "Supercurrents through barriers," *Advances in Physics*, vol. 14, no. 56, pp. 419–451, 1965.

[96] D. J. Griffiths, *Introduction to Electrodynamics*. Upper Saddle River, NJ: Pearson, 4 ed., 2012.

[97] R. Satariano *et al.*, "Inverse magnetic hysteresis of the Josephson supercurrent: Study of the magnetic properties of thin niobium/permalloy ($Fe_{20}Ni_{80}$) interfaces," *Physical Review B*, vol. 103, no. 22, p. 224521, 2021.

[98] H. J. Fink *et al.*, "Proximity effect and boundary conditions in superconducting-normal double layers," *Phys. Rev. B*, vol. 14, pp. 1052–1061, 1976.

[99] N. Giordano, "Evidence for Macroscopic Quantum Tunneling in One-Dimensional Superconductors," *Phys. Rev. Lett.*, vol. 61, pp. 2137–2140, 1988.

[100] L. Embon *et al.*, "Probing dynamics and pinning of single vortices in superconductors at nanometer scales," *Scientific reports*, vol. 5, no. 1, p. 7598, 2015.

[101] D. Roditchev *et al.*, "Direct observation of Josephson vortex cores," *Nature Physics*, vol. 11, no. 4, pp. 332–337, 2015.

[102] A. Kanda *et al.*, "Experimental Evidence for Giant Vortex States in a Mesoscopic Superconducting Disk," *Phys. Rev. Lett.*, vol. 93, p. 257002, 2004.

[103] A. Schmid, "A Time dependent Ginzburg-Landau Equation and its Application to the problem of resistivity in the Mixed State," *Physik der Kondensierte Materie*, vol. 5, no. 4, pp. 302–317, 1966.

[104] Q. Du and L. Ju, "Numerical simulations of the quantized vortices on a thin superconducting hollow sphere," *Journal of Computational Physics*, vol. 201, no. 2, pp. 511–530, 2004.

[105] H. Ding, G. D. Marzi, and Y. Gao, "Numerical simulation of mechanical behaviors and intergranular fracture of polycrystalline Nb3Sn and superconducting filaments," *Superconductor Science and Technology*, vol. 36, no. 9, p. 095001, 2023.

[106] M. Machida and H. Kaburaki, "Direct simulation of the time-dependent Ginzburg-Landau equation for type-II superconducting thin film: Vortex dynamics and V-I characteristics," *Phys. Rev. Lett.*, vol. 71, pp. 3206–3209, 1993.

[107] H. Gao and W. Sun, "An efficient fully linearized semi-implicit Galerkin-mixed FEM for the dynamical Ginzburg–Landau equations of superconductivity," *Journal of Computational Physics*, vol. 294, pp. 329–345, 2015.

[108] I. G. de Oliveira, "Instability in the magnetic field penetration in type II superconductors," *Physics Letters A*, vol. 379, no. 22, pp. 1486–1491, 2015.

[109] A. R. Pack *et al.*, "Vortex nucleation in superconductors within time-dependent Ginzburg-Landau theory in two and three dimensions: Role of surface defects and material inhomogeneities," *Phys. Rev. B*, vol. 101, p. 144504, 2020.

[110] B. Oripov and S. M. Anlage, "Time-dependent Ginzburg-Landau treatment of rf magnetic vortices in superconductors: Vortex semiloops in a spatially nonuniform magnetic field," *Phys. Rev. E*, vol. 101, p. 033306, 2020.

[111] J. Tinsley Oden, "Finite elements: An introduction," in *Finite Element Methods (Part 1)*, vol. 2 of *Handbook of Numerical Analysis*, pp. 3–15, Elsevier, 1991.

[112] G. J. Carty and D. P. Hampshire, "Visualising the mechanism that determines the critical current density in polycrystalline superconductors using time-dependent Ginzburg-Landau theory," *Physical Review B*, vol. 77, p. 172501, 2008.

[113] G. J. Carty and D. P. Hampshire, "The critical current density of an SNS Josephson-junction in high magnetic fields," *Superconductor Science and Technology*, vol. 26, no. 6, p. 065007, 2013.

[114] A. I. Blair and D. P. Hampshire, "Time-Dependent Ginzburg–Landau Simulations of the Critical Current in Superconducting Films and Junctions in Magnetic Fields," *IEEE Transactions on Applied Superconductivity*, vol. 28, no. 4, p. 1–5, 2018.

[115] A. I. Blair and D. P. Hampshire, "Modeling the Critical Current of Polycrystalline Superconducting Films in High Magnetic Fields," *IEEE Transactions on Applied Superconductivity*, vol. 29, no. 5, p. 1–5, 2019.

[116] B. P. Din, A. I. Blair, F. Schoofs, and D. P. Hampshire, "Critical Current Densities through Josephson Junctions in Low Magnetic Fields," *IEEE Transactions on Applied Superconductivity*, vol. 32, no. 4, pp. 1–5, 2022.

[117] C. W. W. Haddon, A. I. Blair, F. Schoofs, and D. P. Hampshire, "Computational Simulations Using Time-Dependent Ginzburg–Landau Theory for Nb–Ti-Like Microstructures," *IEEE Transactions on Applied Superconductivity*, vol. 32, no. 4, pp. 1–5, 2022.

[118] C. W. W. Haddon and D. P. Hampshire, "Fast Multigrid Simulations of Pinning in REBCO With Highly Resistive Nanorods," *IEEE Transactions on Applied Superconductivity*, vol. 33, no. 5, pp. 1–5, 2023.

[119] B. Ivlev and N. Kopnin, "Electric currents and resistive states in thin superconductors," *Advances in Physics*, vol. 33, no. 1, pp. 47–114, 1984.

[120] L. Kramer and R. J. Watts-Tobin, "Theory of Dissipative Current-Carrying States in Superconducting Filaments," *Phys. Rev. Lett.*, vol. 40, pp. 1041–1044, Apr 1978.

[121] R. J. Watts-Tobin, Y. Krähenbühl, and L. Kramer, "Nonequilibrium theory of dirty, current-carrying superconductors: Phase-slip oscillators in narrow filaments near Tc," *Journal of Low Temperature Physics*, vol. 42, no. 5, pp. 459–501, 1981.

[122] G. R. Berdiyorov, M. V. Milošević, and F. M. Peeters, "Kinematic vortex-antivortex lines in strongly driven superconducting stripes," *Phys. Rev. B*, vol. 79, p. 184506, May 2009.

[123] V. Souto, E. Duarte, E. Sardella, and R. Zadorosny, "Kinematic vortices induced by defects in gapless superconductors," *Physics Letters A*, vol. 419, p. 127742, 2021.

[124] M. Cyrot, "Ginzburg-Landau Theory for Superconductors," *Reports on Progress in Physics*, vol. 36, no. 2, p. 103, 1973.

[125] K. S. Grishakov *et al.*, "Time Dependent Ginzburg-Landau Equations for Modeling Vortices Dynamics in Type-II Superconductors with Defects Under A Transport Current," *Physics Procedia*, vol. 36, pp. 1206 – 1210, 2012. Superconductivity Centennial Conference 2011.

[126] Fleckinger-Pelle, Jacqueline and Kaper, Hans G, "Gauges for the Ginzburg-Landau equations of superconductivity," tech. rep., Argonne National Lab., IL (United States), 1995.

[127] L. P. Gor'kov and N. B. Kopnin, "Vortex motion and resistivity of type-II superconductors in a magnetic field," *Soviet Physics Uspekhi*, vol. 18, no. 7, pp. 496–513, 1975.

[128] I. A. Sadovskyy *et al.*, "Stable large-scale solver for Ginzburg—Landau equations for superconductors," *Journal of Computational Physics*, vol. 294, pp. 639 – 654, 2015.

[129] Q. Du, "Discrete Gauge Invariant Approximations of a Time Dependent Ginzburg-Landau Model of Superconductivity," *Mathematics of Computation*, vol. 67, no. 223, pp. 965–986, 1998.

[130] T. Winiecki and C. Adams, "A Fast Semi-Implicit Finite-Difference Method for the TDGL Equations," *Journal of Computational Physics*, vol. 179, no. 1, pp. 127 – 139, 2002.

[131] W. D. Gropp *et al.*, "Numerical Simulation of Vortex Dynamics in Type-II Superconductors," *Journal of Computational Physics*, vol. 123, no. 2, pp. 254 – 266, 1996.

[132] W. F. Ames, *Numerical Methods for Partial Differential Equations*. San Diego: Academic Press Inc, 3rd ed., 1992.

[133] J. Crank and P. Nicolson, "A practical method for numerical evaluation of solutions of partial differential equations of the heat-conduction type," *Mathematical Proceedings of the Cambridge Philosophical Society*, vol. 43, no. 1, p. 50–67, 1947.

[134] O. Schenk and K. Gärtner, "Solving unsymmetric sparse systems of linear equations with PARDISO," *Future Generation Computer Systems*, vol. 20, no. 3, p. 475–487, 2004.

[135] J. W. Ekin, *Experimental Techniques for Low-Temperature Measurements*. New York: Oxford University Press, 2007.

[136] W. B. Richardson *et al.*, "Numerical effects in the simulation of Ginzburg–Landau models for superconductivity," *International Journal for Numerical Methods in Engineering*, vol. 59, no. 9, pp. 1251–1272, 2004.

[137] Q. Du and P. Gray, "High-Kappa Limits of the Time-Dependent Ginzburg-Landau Model," *SIAM Journal on Applied Mathematics*, vol. 56, no. 4, pp. 1060–1093, 1996.

[138] H. Hilgenkamp and J. Mannhart, "Grain boundaries in high-T_c superconductors," *Rev. Mod. Phys.*, vol. 74, pp. 485–549, 2002.

[139] J. P. Hurault, "Surface nucleation in a superconductor coated with a normal metal," *Physics Letters*, vol. 20, no. 6, pp. 587–588, 1966.

[140] Y. V. Fominov and M. V. Feigel'man, "Superconductive properties of thin dirty superconductor–normal-metal bilayers," *Phys. Rev. B*, vol. 63, p. 094518, 2001.

[141] C. W. J. Beenakker, "Random-matrix theory of quantum transport," *Rev. Mod. Phys.*, vol. 69, pp. 731–808, 1997.

[142] V. Peña, Z. Sefrioui, D. Arias, C. Leon, J. Santamaria, M. Varela, S. J. Pennycook, and J. L. Martinez, "Coupling of superconductors through a half-metallic ferromagnet: Evidence for a long-range proximity effect," *Phys. Rev. B*, vol. 69, p. 224502, 2004.

[143] H. Meissner, "Superconductivity of Contacts with Interposed Barriers," *Phys. Rev.*, vol. 117, pp. 672–680, 1960.

[144] Y. Oda and H. Nagano, "Meissner effect in Cu of thick Cu clad Nb," *Solid State Communications*, vol. 35, no. 8, pp. 631–634, 1980.

[145] T. Bergmann *et al.*, "Proximity-effect-induced superconductivity at millikelvin temperatures," *Journal of Low Temperature Physics*, vol. 66, pp. 209–237, 1987.

[146] A. Mota, P. Visani, and A. Pollini, "Magnetic properties of proximity-induced superconducting copper and silver," *Journal of Low Temperature Physics*, vol. 76, pp. 465–512, 1989.

[147] D. Y. Vodolazov *et al.*, "Peculiar superconducting properties of a thin film superconductor–normal metal bilayer with large ratio of resistivities," *Superconductor Science and Technology*, vol. 31, no. 11, p. 115004, 2018.

[148] A. A. Golubov and M. Y. Kupriyanov, "Josephson effect in SNINS and SNIS tunnel structures with finite transparency of the SN boundaries," *Zh. Eksp. Teor. Fiz*, vol. 96, pp. 1420–1433, 1989.

[149] A. A. Golubov *et al.*, "Josephson effect in SS'IS'S tunnel structures," *Zh. Eksp. Teor. Fiz*, vol. 103, pp. 1851–1868, 1993.

[150] A. Godeke, "A review of the properties of Nb3Sn and their variation with A15 composition, morphology and strain state," *Superconductor Science and Technology*, vol. 19, no. 8, p. R68, 2006.

[151] J. Greenwood, *Percolative Current Flow through Anisotropic High-Field Superconductors under Strain*. PhD thesis, Durham University, Durham, United Kingdom, 2023. Available at `http://etheses.dur.ac.uk/`.

[152] L. Brillouin, *Wave Propagation in Periodic Structures: Electric Filters and Crystal Lattices*. International Series in Pure and Applied Physics, Dover Publications, 1953.

[153] R. G. Boyd, "Longitudinal Critical Current in Type-II Superconductors," *Phys. Rev.*, vol. 145, pp. 255–257, 1966.

[154] A. Abrikosov, "Concerning surface superconductivity in strong magnetic fields," *Sov. Phys. JETP*, vol. 20, no. 2, p. 480, 1965.

[155] A. Cuyt *et al.*, *Handbook of Continued Fractions for Special Functions*. New York: Springer, 2008.

[156] E. J. Kramer, "Scaling laws for flux pinning in hard superconductors," *Journal of Applied Physics*, vol. 44, no. 3, pp. 1360–1370, 1973.

[157] D. Dew-Hughes, "Flux pinning mechanisms in type II superconductors," *Philosophical Magazine*, vol. 30, no. 2, pp. 293–305, 1974.

[158] W. Schauer and W. Schelb, "Improvement of Nb_3Sn High Field Critical Current by a Two-stage Reaction," *IEEE Transactions on Magnetics*, vol. 17, pp. 374–377, 1981.

[159] J. R. Clem, "Two-dimensional vortices in a stack of thin superconducting films: A model for high-temperature superconducting multilayers," *Physical Review B*, vol. 43, no. 10, p. 7837–7846, 1991.

[160] S. B. L. Chislett-McDonald *et al.*, "In-situ critical current measurements of REBCO coated conductors during gamma irradiation," *Superconductor Science and Technology*, vol. 36, no. 9, p. 095019, 2023.

Colophon

This thesis is based on a template developed by Matthew Townson and Andrew Reeves. It was typeset with LaTeX 2_ε. It was created using the *memoir* package, maintained by Lars Madsen, with the *madsen* chapter style. The font used is Latin Modern, derived from fonts designed by Donald E. Knuth.